

1 LEVERAGING MULTI-MESSENGER ASTROPHYSICS FOR DARK MATTER SEARCHES

By

Daniel Nicholas Salazar-Gallegos

A DISSERTATION

Submitted to
Michigan State University
in partial fulfillment of the requirements
for the degree of

Physics—Doctor of Philosophy
Computational Mathematics in Science and Engineering—Dual Major

Today

ABSTRACT

3 I did Dark Matter with HAWC and IceCube. I also used Graph Neural Networks

ACKNOWLEDGMENTS

5 I love my friends. Thanks to everyone that helped me figure this out. Amazing thanks to the people
6 at LANL who supported me. Eames, etc Dinner Parties Jenny and her child Kaydince Kirsten, Pat,
7 Andrea Family. You're so far but so critical to my formation. Unconditional love. Roommate

TABLE OF CONTENTS

9	LIST OF TABLES	vi
10	LIST OF FIGURES	viii
11	CHAPTER 1 DARK MATTER IN THE COSMOS	1
12	1.1 Introduction	1
13	1.2 Dark Matter Basics	2
14	1.3 Evidence for Dark Matter	3
15	1.4 Searching for Dark Matter: Particle DM	10
16	1.5 Sources for Indirect Dark Matter Searches	15
17	1.6 Multi-Messenger Dark Matter	17
18	CHAPTER 2 HIGH ALTITUDE WATER CHERENKOV (HAWC) OBSERVATORY	20
19	2.1 The Detector	20
20	2.2 Event Reconstruction	25
21	2.3 Background Estimation: Direct Integration	33
22	CHAPTER 3 GLORY DUCK: MULTI-WAVELENGTH SEARCH FOR DARK MATTER ANNIHILATION TOWARDS DWARF SPHEROIDAL GALAXIES	35
25	3.1 Introduction	35
26	3.2 Dataset and Background	37
27	3.3 Analysis	39
28	3.4 Likelihood Methods	43
29	3.5 HAWC Results	50
30	3.6 Glory Duck Combined Results	52
31	3.7 HAWC Systematics	57
32	3.8 <i>J</i> -factor distributions	59
33	3.9 Discussion and Conclusions	65
34	CHAPTER 4 MULTITHREADING HAWC ANALYSES FOR DARK MATTER SEARCHES	69
36	4.1 Introduction	69
37	4.2 Dataset and Background	69
38	4.3 Analysis	71
39	4.4 Likelihood Methods	75
40	4.5 Computational Methods: Multithreading	75
41	4.6 Analysis Results	81
42	4.7 Systematics	86
43	4.8 Conclusion and Discussion	86
44	CHAPTER 5 ICECUBE NEUTRINO OBSERVATORY	88
45	5.1 The Detector	89
46	5.2 Event Reconstruction	93

47	5.3 Background	99
48	CHAPTER 6 HEAVY DARK MATTER ANNIHILATION SEARCH WITH ICE-	
49	CUBE'S NORTH SKY TRACK DATA	100
50	6.1 Introduction	100
51	6.2 Dataset and Background	100
52	6.3 Analysis	102
53	6.4 Likelihood Methods	111
54	6.5 Background Simulation	111
55	6.6 Signal Recovery	129
56	6.7 Systematics	132
57	6.8 Conclusions	135
58	CHAPTER 7 NU DUCK: CONCLUSIONS AND FUTURE DIRECTIONS	137
59	7.1 Conclusions	137
60	7.2 Future Directions: Multi-Messenger Dark Matter Search	138
61	APPENDIX A MULTI-EXPERIMENT SUPPLEMENTARY FIGURES	140
62	APPENDIX B MULTITHREADING DARK MATTER ANALYSES SUPPLEMEN-	
63	TARY MATERIAL	141
64	B.1 Remaining Spectral Models	141
65	B.2 <code>mpu_analysis.py</code>	142
66	B.3 Comparison with Glory Duck	151
67	APPENDIX C ICECUBE HEAVY DARK MATTER ANALYSIS SUPPLEMEN-	
68	TARY MATERIAL	154
69	C.1 Docker Image for Oscillating Neutrino Spectra	154
70	C.2 Spline Fitting Statuses	157
71	C.3 Neutrino Composite Spectra	158
72	C.4 Segue 1 And Ursa Major II Signal Recovery	159
73	C.5 n_s Sensitivities	165
74	BIBLIOGRAPHY	167

LIST OF TABLES

<p>76 Table 2.1 Definitions of f_{hit} energy estimator bins. Bins are defined by the fraction of 77 available PMTs that are triggered during an air shower event. The angular 78 resolution, Θ_{68}, is the bin containing 68% of events [34].</p> <p>79 Table 3.1 Summary of the relevant properties of the dSphs used in the present work. 80 Column 1 lists the dSphs. Columns 2 and 3 present their heliocentric distance 81 and galactic coordinates, respectively. Columns 4 and 5 report the J-factors of 82 each source given from the \mathcal{GS} and \mathcal{B} independent studies and their estimated 83 $\pm 1\sigma$ uncertainties. The values $\log_{10} J$ (\mathcal{GS} set) [59] correspond to the mean 84 J-factor values for a source extension truncated at the outermost observed star. 85 The values $\log_{10} J$ (\mathcal{B} set) [63] are provided for a source extension at the tidal 86 radius of each dSph. Bolded sources are within HAWC's field of view and 87 provided to the Glory Duck analysis.</p> <p>88 Table 3.2 Summary of dSph observations by each experiment used in this work. A 89 ‘-’ indicates the experiment did not observe the dSph for this study. For 90 Fermi-LAT, the exposure at 1 GeV is given. For HAWC, $\Delta\theta$ is the absolute 91 difference between the source declination and HAWC latitude. HAWC is more 92 sensitive to sources with smaller $\Delta\theta$. For IACTs, we show the zenith angle 93 range, the total exposure, the energy range, the angular radius θ of the signal or 94 ON region, the ratio of exposures between the background-control (OFF) and 95 signal (ON) regions (τ), and the significance of gamma-ray excess in standard 96 deviations, σ.</p> <p>97 Table 4.1 Summary of the relevant properties of the dSphs used in the present work. 98 Column 1 lists the dSphs. Columns 2 and 3 present their heliocentric distance 99 and galactic coordinates, respectively. Column 4 reports the J-factors of each 100 source given from the \mathcal{LS} studies and estimated $\pm 1\sigma$ uncertainties. The 101 values $\log_{10} J$ (\mathcal{LS} set) [80] correspond to the mean J-factor values for a 102 source extension truncated at 0.5°.</p> <p>103 Table 4.2 Timing summaries for analyses for serial and multithreaded processes. M 104 tasks is the number of functional-parallel tasks ran for the computation. $T_{p,c}$ 105 is a single run time in hours:minutes:seconds for runs utilizing p nodes and 106 c threads. Runs are run interactively on the same computer to maximize 107 consistency. Empty entries are indicated with ‘-’. (·) entries are estimated 108 entries extrapolated from data earlier in the column.</p> <p>109 Table 4.3 Speed up summaries for analyses for serial and multithreaded processes. M 110 tasks is the number of functional-parallel tasks ran for the computation. $S_{p,c}$ 111 is a single speedup comparison for runs utilizing p nodes and c threads. [·] 112 are the estimated speedups calculated from Tab. 4.2, Eq. (4.7), and Eq. (4.4). 113 Empty entries are indicated with ‘-’.</p>	<p>29</p> <p>44</p> <p>45</p> <p>75</p> <p>79</p> <p>81</p>
--	---

114	Table 6.1 Spline err tolerances used for input in particle physics component to Eq. (3.1).	
115	Column 1 is the DM annihilation channel being fit. Columns 2, 3, and 4	
116	are the tolerances for "GOOD" (pass), "OK" requires inspection, and "FAIL"	
117	(tune and refit) respectively. Column 5 has the X ranges over which the error	
118	is evaluated. MAX/MIN [.,.] takes the maximum or minimum of the two	
119	enclosed values.	108

LIST OF FIGURES

121	Figure 1.1	Rotation curve fit to NGC 6503 from [7]. Dashed line is the contribution 122 from visible matter. Dotted curves are from gas. Dash-dot curves are from 123 dark matter (DM). Solid line is the composite contribution from all matter 124 and DM sources. Data are indicated with bold dots with error bars. Data 125 agree strongly with a matter + DM composite prediction.	4
126	Figure 1.2	Light from distant galaxy is bent in unique ways depending on the distribution 127 of mass between the galaxy and Earth. Yellow dashed lines indicate where 128 the light would have gone if the matter were not present [8].	6
129	Figure 1.3	(left) Optical image of galactic cluster 1E0657-558. (right) X-ray image of the 130 cluster with redder meaning hotter and higher baryon density. (both) Green 131 contours are reconstruction of gravity contours from weak lensing. White 132 rings are the best fit mass maxima at 68.3%, 95.5%, and 99.7% confidence. 133 The matter maxima of the clusters are clearly separated from x-ray maxima. [9]	7
134	Figure 1.4	Plank CMB sky. Sky map features small variations in temperature in primor- 135 dial light. These anisotropies are used to make inferences about the universe's 136 energy budget and developmental history. [10]	8
137	Figure 1.5	Observed Cosmic Microwave Background power spectrum as a function of 138 multipole moment from Plank [10]. Blue line is best fit model from Λ CDM. 139 Red points and lines are data and error, respectively.	9
140	Figure 1.6	Predicted power spectra of CMB for different $\Omega_m h^2$ values for fixed baryon 141 density from [11]. (left) Low $\Omega_m h^2$ increases the prominence of first and 142 second peaks. (middle) $\Omega_m h^2$ is most similar to the observed power spectrum. 143 The second and third peaks are similar in height. (right) $\Omega_m h^2$ is large which 144 suppresses the first peak and raises the prominence of the third peak.	9
145	Figure 1.7	The Standard Model (SM) of particle physics. Figure taken from http://www.quantumdiaries.org/2014/03/14/the-standard-model-a-beautiful-but-flawed-theory/	11
148	Figure 1.8	Simplified Feynman diagram demonstrating with different ways DM can 149 interact with SM particles. The 'X's refer to the DM particles whereas the 150 SM refer to fundamental particles in the SM. The large circle in the center 151 indicates the vertex of interaction and is purposely left vague. The colored 152 arrows refer to different directions of time as well as their respective labels. 153 The arrows indicate the initial and final state of the DM -SM interaction in time.	12

154	Figure 1.9 A single jet event in ATLAS detector from 2017 [16]. Jet momentum was 155 observed to be 1.9 TeV. Missing transverse momentum was observed to be 156 1.9 TeV compared to the initial transverse momentum of the event was 0. 157 Implied MET is traced by a red dashed line in event display.	13
158	Figure 1.10 More detailed pseudo-Feynman diagram of particle cascade from dark matter 159 annihilation into 2 quarks. The quarks hadronize and down to stable particles 160 like γ or the anti-proton (p^-). Diagram pulled from ICRC 2021 presentation 161 on DM annihilation search [17].	14
162	Figure 1.11 Dark Matter (DM) decay spectrum for $b\bar{b}$ initial state and γ final state. Redder 163 spectra are for larger DM masses. Bluer spectra are light DM masses. x is a 164 unitless factor defined as the ratio of the mass of DM, m_χ , and the final state 165 particle energy E_γ . Figure from [19].	16
166	Figure 1.12 Different dark matter density profiles compared. Some models produce ex- 167 ceptionally large densities at small r [20].	17
168	Figure 1.13 The Milky Way Galaxy in photons (γ) and neutrinos (ν) [22]. The Galactic 169 center is at $l=0^\circ$ and is the brightest region in all panels. (top) An Optical 170 color image of the Milky Way galaxy seen from Earth. Clouds of gas and dust 171 obscure some light from stars. (2nd down) Integrated flux of γ -rays observed 172 by the Fermi-LAT telescope [23]. (middle) Expected neutrino emission 173 that corresponds with Fermi-LAT observations. (2nd up) Expected neutrino 174 emission profile after considering detector systematics of IceCube. (bottom) 175 Observed neutrino emission from region of the galactic plane. Substantial 176 neutrino emission was detected.	18
177	Figure 1.14 Dark Matter annihilation spectra for different final state particle and standard 178 model annihilation channels [24]. Photons (red), e^\pm (green), \bar{p} (blue), ν (black).	19
179	Figure 2.1 Photo of the HAWC detector that I took on May 17, 2023. Main array is 180 centered in the photo and comprised of the larger tanks. Outriggers are the 181 smaller tanks around the main array.	20
182	Figure 2.2 A particle physics illustration of high energy particle showers. Left shower is 183 an electromagnetic shower from a high energy gamma-ray. Most particles in 184 the shower will be a combination of photons and charged leptons, in this case 185 electrons (e). Right figure shows a cosmic ray particle shower. The cosmic 186 ray will produce many more types of particles including pions (π), neutrinos, 187 and charged leptons. Figure pulled from [26].	21
188	Figure 2.3 The WCDs. Left image features several WCDs looking from within the main 189 array of HAWC. Right image shows a schematic of a WCD pulled from [25].	22

190	Figure 2.4	Overview of HAWC control and data electronics. The LoToT and HiToT threshold signals are discussed in Section 2.1.2. Figure from [27]	23
192	Figure 2.5	Schematic of data flow in HAWC data acquisition and online processing system. Pulled from [29].	24
194	Figure 2.6	How HAWC FEB intially processes analog PMT signals. Signals are split through an amplifier and discriminator circuit. Each path is designated for ei- ther the HIGH or LOW threshold for the signal. The 2-edge event corresponds to LOW, while the 4 edge corresponds to HIGH.	24
198	Figure 2.7	An particle shower incident on WCDs. Secondary particles of an air shower travel in a cone centered on primary incident particle. Reconstruction of the initial angle is possible with arrival time of hits in PMTs inside WCDs. Figure from [33].	26
202	Figure 2.8	Charge deposition in each PMT for a reconstructed gamma-ray event. WCDs are outlined in black surrounding the 4 smaller circles that represent PMTs. The color scale indicates the charge deposition in each PMT. The best shower core fit from SFCF is noted with a red star in the center of the dashed circle [34].	27
206	Figure 2.9	Simulated normalized energy distribution of each f_{hit} bin defined in Tab. 2.1. Monte Carlo simulation of gamma-rays with $E^{-2.63}$ spectral shape and sim- ulated source at 20° declination. Figure from [34].	29
209	Figure 2.10	Neural Network energy estimator performance compared to true energy. The dotted line is the identity line where the estimator and injection agree. Gam- ma/hadron separation cuts were applied with the energy estimation. Figure pulled from [37]	31
213	Figure 2.11	Lateral distribution functions (LDFs) for cosmic ray (left) and a photon can- didate from the Crab Nebula (right). Cosmic ray LDF has clearly isolated hits far from the reconstructed shower core. Gamma-ray shower shows a more cuspy event [34].	32

217	Figure 3.1	Sensitivities of five gamma-ray experiments compared to percentages of the Crab nebula's emission and dark matter annihilation. Solid lines present estimated sensitivities to power law spectra [FACT CHECK THIS]for each experiment. Green lines are Fermi-LAT sensitivities where lighter green is the sensitivity to the galactic center and dark green is its sensitivity to higher declinations. Orange, red, and purple solid lines represent the MAGIC, HESS, and VERITAS 50 hour sensitivities respectively. The maroon and brown lines are the HAWC 1 year and 5 year sensitivities. Across four decades of gamma-ray energy, these experiments have similar sensitivities on the order 10^{-12} erg cm $^{-2}$ s $^{-1}$. The dotted lines are estimated dark matter fluxes assuming $m_\chi = 5$ TeV DM annihilating to bottom quarks (red), tau leptons (blue), and W bosons (green). Faded gray lines outline percentage flux of the Crab nebula. Figure is an augmented version of [40]	36
230	Figure 3.2	Effect of Electroweak (EW) corrections on expected DM annihilation spectrum for $\chi\chi \rightarrow W^-W^+$. Solid lines are spectral models that consider EW corrections. Dash-dot lines are spectral models without EW corrections. Red lines are models for $M_\chi = 1$ TeV. Blue lines represent models for $M_\chi = 100$ TeV. All models are sourced from the PPPC4DMID [58].	40
235	Figure 3.3	$\frac{dJ}{d\Omega}$ maps for Segue1 (top) and Coma Berenices (bottom). Origin is centered on the specific dwarf spheroidal galaxies (dSph). X and Y axes are the angular separation from the center of the dwarf. Profile is truncated at the scale radius. Plots of the remaining 11 dSph HAWC studied are linked in Fig. A.1.	42
239	Figure 3.4	Illustration of the combination technique showing a comparison between $-2 \ln \lambda$ provided by four instruments (colored lines) from the observation of the same dSph without any J nuisance and their sum, <i>i.e.</i> the resulting combined likelihood (thin black line). According to the test statistics of Equation (3.7), the intersection of the likelihood profiles with the line $-2 \ln \lambda = 2.71$ indicates the 95% C.L. upper limit on $\langle \sigma v \rangle$. The combined likelihood (thin black line) shows a smaller value of upper limit on $\langle \sigma v \rangle$ than those derived by individual instruments. We also show how the uncertainties on the J factor effects the combined likelihood and degrade the upper limit on $\langle \sigma v \rangle$ (thick black line). All likelihood profiles are normalized so that the global minimum $\widehat{\langle \sigma v \rangle}$ is 0. We note that each profile depends on the observational conditions in which a target object was observed. The sensitivity of a given instrument can be degraded and the upper limits less constraining if the observations are performed in non-optimal conditions such as a high zenith angle or a short exposure time.	48
254	Figure 3.5	51

255	Figure 3.6 HAWC TS values for best fit $\langle\sigma v\rangle$ versus m_χ for seven SM annihilation channels with J factors from \mathcal{GS} . The solid black line shows the combined best fit TS values. The colored, dashed lines are the TS values for each of the 13 sources HAWC studied.	52
259	Figure 3.7 HAWC Brazil bands at 95% confidence level on $\langle\sigma v\rangle$ versus DM mass for seven annihilation channels with J -factors from \mathcal{GS} [69]. The solid line represents the combined limit from 13 dSphs. The dashed line is the expected limit. The green band is the 68% containment. The yellow band is the 95% containment.	53
264	Figure 3.8 Upper limits at 95% confidence level on $\langle\sigma v\rangle$ in function of the DM mass for eight annihilation channels, using the set of J factors from Ref. [69] (\mathcal{GS} set in Table 3.1). The black solid line represents the observed combined limit, the black dashed line is the median of the null hypothesis corresponding to the expected limit, while the green and yellow bands show the 68% and 95% containment bands. Combined upper limits for each individual detector are also indicated as solid, colored lines. The value of the thermal relic cross-section in function of the DM mass is given as the red dotted-dashed line [70].	54
273	Figure 3.9 Same as Fig. 3.8, using the set of J factors from Ref. [63, 71] (\mathcal{B} set in Table 3.1).	55
274	Figure 3.10 Comparisons of the combined limits at 95% confidence level for each of the eight annihilation channels when using the J factors from Ref. [69] (\mathcal{GS} set in Table 3.1), plain lines, and the J factor from Ref. [63, 71] (\mathcal{B} set in Table 3.1), dashed lines. The cross-section given by the thermal relic is also indicated [70].	57
278	Figure 3.11 Comparisons of the combined limits at 95% confidence level for a point source analysis and extended source using [69] \mathcal{GS} J-factor distributions and PPPC [58] annihilation spectra. Shown are the limits for Segue1 which will have the most significant impact on the combined limit. 6 of the 7 DM annihilation channels are shown. Solid lines are extended source studies. Dashed lines are point source studies. Overall, the extended source analysis improves the limit by a factor of 2.	59
285	Figure 3.12 Same as Fig. 3.11 on Coma Berenices. This dSph also contributes significantly to the limit. The limits are identical in this case.	60
287	Figure 3.13 Comparison of combined limits when correcting for HAWC's pointing systematic. All DM annihilation channels are shown. The solid black line is the ratio between published limit to the declination corrected limit. The blue solid line or "Combined_og" represented the limits computed for Glory Duck. The solid orange line or "Combined_ad" represented the limits computed after correcting for the pointing systematic.	61

293	Figure 3.14 Differential map of dJ/Ω from model built in Section 3.8.1 and profiles provided directly from authors. (Top) Differential from Segue1. (bottom) Differential from Coma Berenices. Note that their scales are not the same. Segue1 shows the deepest discrepancies which is congruent with its large uncertainties. Both models show anuli where unique models become apparent.	62
298	Figure 3.15 HAWC limits for Coma Berenices (top) and Segue1 (bottom) for two different map sets. Blue lines are limits calculated on maps with poor model representation. Orange lines are limits calculated on spatial profiles provided by the authors of [59]. Black line is the ratio of the poor spatial model limits to the corrected spatial models. The left y-axis measures $\langle\sigma v\rangle$ for the blue and orange lines. The right y-axis measures the ratio and is unitless.	63
304	Figure 3.16 Comparisons between the J -factors versus the angular radius for the computation of J factors from Ref. [69] (\mathcal{GS} set in Table 3.1) in blue and for the computation from Ref. [63, 71] (\mathcal{B} set in Tab. 3.1) in orange. The solid lines represent the central value of the J -factors while the shaded regions correspond to the 1σ standard deviation.	65
309	Figure 3.17 Comparisons between the J -factors versus the angular radius for the computation of J factors from Ref. [69] (\mathcal{GS} set in Tab. 3.1) in blue and for the computation from Ref. [63, 71] (\mathcal{B} set in Tab. 3.1) in orange. The solid lines represent the central value of the J -factors while the shaded regions correspond to the 1σ standard deviation.	66
314	Figure 4.1 Spectral hypotheses from PPPC [58] and HDM [79] for DM annihilation: $\chi\chi \rightarrow W^-W^+$. Solid lines are spectral models with EW corrections from the PPPC. Dash-dot lines are spectral models from HDM. Red lines are models for $M_\chi = 1$ TeV. Blue lines represent models for $M_\chi = 100$ TeV.	71
318	Figure 4.2 Photon spectra for $\chi\chi \rightarrow \gamma\gamma$ (left) and $\chi\chi \rightarrow ZZ$ (right) after Gaussian convolution of line features. Both spectra have δ -features at photon energies equal to the DM mass. Bluer lines are annihilation spectra with lower DM mass. Redder lines are spectra from larger DM mass. All spectral models are sourced from the Heavy Dark Matter models [79]. Axes are drawn roughly according to the energy sensitivity of HAWC.	72
324	Figure 4.3 $\frac{dJ}{d\Omega}$ maps for Coma Berenices, Draco, Segue1, and Sextans. Columns are divided for the $\pm 1\sigma$ uncertainties in $dJ/d\Omega$ around the mean value from \mathcal{LS} [80]. Origin is centered on the specific dwarf spheroidal galaxies (dSph). θ and ϕ axes are the angular separation from the center of the dwarf. Profiles are truncated at 1° and flattened beyond.	74

329	Figure 4.4	Infographic on how jobs and DM computation was organized in Section 3.3. Jobs were built for each permutation of CHANS and SOURCES shown by the left block in the figure. Each job, which took on the order 2 hrs to compute, had the following work flow: 1. Import HAWC analysis software, 2 min to run. 2. Load HAWC count maps, 5 min to run. 3. Load HAWC energy and spatial resolutions, 4 min. 5. Load DM spatial source templates and spectral models, less than 1 s. 6. Perform likelihood fit on data and model, about 8 min per DM mass. 7. Write results to file, less than 1s.	76
337	Figure 4.5	Graphic of Gustafson parallel coding pattern. f_s is the fraction of a program, in time, spent on serial computation. f_p is the fraction of computing time that is parallelizable. T_p is the total time for a parallel program to run. T_1 is the total time for a parallel program to run if only 1 processor is allocated. P_N is the N -th processor where it's row is the computation the processor performs. The Gustafson pattern is most similar to what is implemented for this analysis. Figure is pulled from [82].	77
344	Figure 4.6	Task chart for one multithreaded job developed for this project. Green blocks indicate a shared resource across the threads AND computation performed serially. Red blocks indicate functional parallel processing within each thread. 3 threads are represented here, yet many more can be employed during the full analysis. Jobs are defined by the SOURCE as these require unique maps to be loaded into the likelihood estimator. The m_χ , CHAN, and $\langle\sigma v\rangle$ variables are entered into the thread pool and allocated as evenly as possible across the threads.	79
352	Figure 4.7	HAWC upper limits at 95% confidence level on $\langle\sigma v\rangle$ versus m_χ for $\chi\chi \rightarrow b\bar{b}$, $t\bar{t}$, $u\bar{u}$, $d\bar{d}$, $s\bar{s}$, $c\bar{c}$, gg , W^+W^- , and hh . Limits are with \mathcal{LS} J-factors [80]. The solid line represents the observed combined limit. Dashed lines represent limits from individual dSphs.	82
356	Figure 4.8	HAWC upper limits at 95% confidence level on $\langle\sigma v\rangle$ versus m_χ for $\chi\chi \rightarrow \nu_e \bar{\nu}_e$, $\nu_\mu \bar{\nu}_\mu$, $\nu_\tau \bar{\nu}_\tau$, $e\bar{e}$, $\mu\bar{\mu}$, $\tau\bar{\tau}$, $\gamma\gamma$ and ZZ . Limits use \mathcal{LS} J-factors [80]. The solid line represents the observed combined limit. Dashed lines represent limits from individual dSphs.	83
360	Figure 4.9	HAWC TS values for best fit $\langle\sigma v\rangle$ versus m_χ for SM annihilation channels: $\chi\chi \rightarrow b\bar{b}$, $t\bar{t}$, $u\bar{u}$, $d\bar{d}$, $s\bar{s}$, $c\bar{c}$, gg , W^+W^- , and hh . Limits use \mathcal{LS} J-factors. The solid black line shows the combined best fit TS values. The colored, dashed lines are the TS values from each dSph.	84
364	Figure 4.10	HAWC TS values for best fit $\langle\sigma v\rangle$ versus m_χ for SM annihilation channels: $\chi\chi \rightarrow \nu_e \bar{\nu}_e$, $\nu_\mu \bar{\nu}_\mu$, $\nu_\tau \bar{\nu}_\tau$, $e\bar{e}$, $\mu\bar{\mu}$, $\tau\bar{\tau}$, $\gamma\gamma$ and ZZ . Limits use \mathcal{LS} J-factors. The solid black line shows the combined best fit TS values. The colored, dashed lines are the TS values from each dSph.	85

368	Figure 4.11 Comparison of HAWC limits from this analysis to Glory Duck (Fig. 3.5) for 3 dSphs and 3 DM annihilation channels: $b\bar{b}$, $\tau\bar{\tau}$, and $e\bar{e}$. Each sector shows the 95% confidence limit from Glory Duck (blue line) and this analysis (orange line) in the top plot. The lower plot features the ratio in log scale of Glory Duck to this analysis in a red solid line. Horizontal dashed lines are for ratios of 1.0 (black) and $\sqrt{2}$ (blue). Ratios larger than 1.0 are for limits smaller, or stricter, than Glory Duck. Ratios larger than $\sqrt{2}$ indicates limits are stricter than a simple doubling of the Glory Duck data.	87
376	Figure 5.1 IceCube Neutrino observatory at the South Pole. Image from TODO: cite where you got this from	88
378	Figure 5.2 TODO: pasted Components of the DOM, showing mechanical layout (left) and functional connections (right). Figure from [83]	89
380	Figure 5.3 ICL. Picture from [84].	90
381	Figure 5.4 TODO: Copied Data flow diagram for recording and processing of PMT waveforms in the DOM to form “Hit Records” that are sent to the surface DAQ computers. As shown by dashes, full waveform data are only included when neighbor DOMs report time-coincident signals above the SPE discriminator threshold. Additionally, data from low-gain channels are omitted for waveforms that are within range of higher-gain channels.	91
387	Figure 5.5 TODO: copied . The parton level W (a/b) and Z (c/d) boson exchange between neutrinos and light quarks. Feynman diagrams for charged current interactions (a/b) and neutral current interactions (c/d) between neutrinos and quarks that make up nucleons in the ice. A W boson is exchanged in charged current interactions and produces an outgoing lepton corresponding to the neutrino flavor along with hadronic cascades. A Z boson is exchanged in neutral current interactions and only hadronic cascades are produced. Figure from [85]. a double cascade event topology, shown in Figure 5.9. If it has a lower energy, it will	93
396	Figure 5.6 TODO: copied . Event signature of high energy NC and CC neutrino interactions. The signature is decomposed in hadronic and electromagnetic cascades and Cherenkov radiation from a single long ranging particle. The type of cascade from the tau decay depends on the decay channel of the tau. For energies below a PeV the two cascades of the tau signature overlap and can not be distinguished. For a sparse instrumented detector like IceCube, the events can be classified in track-like and cascade-like. Figure from [86].	94

403	Figure 5.7 TODO: copied. A simulation of a track-like event in IceCube. Tracks are 404 produced when CC muon neutrino interactions occur and a muon is produced 405 in return. The color of the DOMs represent the arrival times of the photons 406 (red is early, green is late). The size of the DOM represents the amount of 407 charge that is seen in that DOM. The CC neutrino interaction occurred near 408 the red hits, with the muon exiting to the left. Figure taken from [87].	95
409	Figure 5.8 TODO: copied A simulation of a cascade-like event in IceCube. Cascades can 410 be produced by NC interactions for all flavors of neutrinos, for CC interactions 411 for electron neutrinos, and for CC interactions for tau neutrinos for energies 412 below 1 PeV. The color of the DOMs represent the arrival times of the photons 413 (red is early, green is late). The size of the DOM represents the amount of 414 charge that is seen in that DOM. Figure taken from [87].	96
415	Figure 5.9 TODO: copied. A simulation of a double-bang event in IceCube. Double- 416 bang events occur when CC tau neutrino interactions occur above 1 PeV 417 producing a g lepton. When these high-energy g leptons are produced, the g 418 leptons are able to travel over 50 m in IceCube before they decay. At these 419 distances, the light emission from the decays are distinguishable from the light 420 emission of the hadronic cascades from the initial tau neutrino interactions. 421 The color of the DOMs representthe arrival times of the photons (red is early, 422 green is late). The size of the DOM represents the amount of charge that is 423 seen in the DOM. Figure taken from [87].	97
424	Figure 6.1 Neutrino spectra at production (left panels) and after oscillation at Earth 425 (right panels). Blue, orange, and green lines are the ν_e , ν_μ , and ν_τ spectra 426 respectively. Top panels show the spectra in $\frac{dN}{dE}$. Lower panels plot the flavor 427 ratio to $\nu_e + \nu_\mu + \nu_\tau$. SM annihilation channels $b\bar{b}$, $\tau\bar{\tau}$, and $\nu_\mu\bar{\nu}_\mu$ are shown 428 for $M_\chi = 1$ Pev, TeV, and EeV.	104
429	Figure 6.2 Signal recovery for 100 TeV DM annihilation into $\nu_\mu\bar{\nu}_\mu$ for a source at Dec 430 = 16.06° . n_{inj} is the number of injected signal events in simulation. n_s is the 431 number of reconstructed signal events from the simulation data. Although 432 the uncertainties are small and tight, the reconstructed n_s are systematically 433 underestimated.	105
434	Figure 6.3 Left panel shows the two kernels overlaying the original spectrum from 435 χ arony after propagation to Earth [95]. The vertical red line indicates where 436 the original neutrino line is maximized. Blue line is the output from χ arony. 437 Green line is the spectrum after convolution with a flat kernel. Orange line 438 is the spectrum after Gaussian convolution. Right panel shows the signal 439 recovery of the spectral model using the Gaussian kernel with parameters 440 enumerated above.	106

441	Figure 6.4	Example spline that failed the fit. Failed splines are corrected on a case by case basis unless the SM channel has a systematic problem fitting the splines.	108
443		In this case, I made a bookkeeping error and loaded the incorrect spectral model	
444	Figure 6.5	Summary of input spectral models that were smoothed with Gaussian kernels. Spectral models are for $\chi\chi \rightarrow e\bar{e}$, $\mu\bar{\mu}$, $\tau\bar{\tau}$, $\nu_e\bar{\nu}_e$, $\nu_\mu\bar{\nu}_\mu$, and $\nu_\tau\bar{\nu}_\tau$. These spectra are the composite ($\nu_\mu + \nu_\tau$) of neutrino flavors. Every spectral model used for this analysis is featured as a colored solid line. Bluer lines are for low m_χ models. m_χ ranges from 681 GeV to 100 PeV. HDM [79], χ arov [95], and Photospline [99] are used to generate these spectra. Energy (x-axis) was chosen to roughly represent the energy sensitivity of NST.	109
451	Figure 6.6	Test statistic (TS) distributions for Segue 1 and $\chi\chi \rightarrow b\bar{b}$. Each subplot, except the final, is the TS distribution for a specific DM mass listed in the subplot. Orange dashed lines are the traces for a χ^2 distribution with 1 degree of freedom. $\epsilon[\cdot]$ is the fraction of trials smaller than the bracketed value. The final subplot features the all DM spectral models, similar to Fig. 6.5, used as input for the TS distributions.	112
457	Figure 6.7	Same as Fig. 6.6 for Segue 1 $\chi\chi \rightarrow \tau\bar{\tau}$.	113
458	Figure 6.8	Same as Fig. 6.6 for Segue 1 $\chi\chi \rightarrow \nu_\mu\bar{\nu}_\mu$.	114
459	Figure 6.9	Same as Fig. 6.6 for Ursa Major II 1 $\chi\chi \rightarrow b\bar{b}$.	115
460	Figure 6.10	Same as Fig. 6.6 for Ursa Major II 1 $\chi\chi \rightarrow \tau\bar{\tau}$.	116
461	Figure 6.11	Same as Fig. 6.6 for Ursa Major II 1 $\chi\chi \rightarrow \nu_\mu\bar{\nu}_\mu$.	117
462	Figure 6.12	Same as Fig. 6.6 for 15, \mathcal{GS} J-factor, stacked sources and $\chi\chi \rightarrow b\bar{b}$.	118
463	Figure 6.13	Same as Fig. 6.6 for 15, \mathcal{GS} J-factor, stacked sources and $\chi\chi \rightarrow t\bar{t}$.	119
464	Figure 6.14	Same as Fig. 6.6 for 15, \mathcal{GS} J-factor, stacked sources and $\chi\chi \rightarrow u\bar{u}$.	120
465	Figure 6.15	Same as Fig. 6.6 for 15, \mathcal{GS} J-factor, stacked sources and $\chi\chi \rightarrow d\bar{d}$.	121
466	Figure 6.16	Same as Fig. 6.6 for 15, \mathcal{GS} J-factor, stacked sources and $\chi\chi \rightarrow e\bar{e}$.	122
467	Figure 6.17	Same as Fig. 6.6 for 15, \mathcal{GS} J-factor, stacked sources and $\chi\chi \rightarrow \mu\bar{\mu}$.	123
468	Figure 6.18	Same as Fig. 6.6 for 15, \mathcal{GS} J-factor, stacked sources and $\chi\chi \rightarrow \tau\bar{\tau}$.	124
469	Figure 6.19	Same as Fig. 6.6 for 15, \mathcal{GS} J-factor, stacked sources and $\chi\chi \rightarrow W^+W^-$.	125
470	Figure 6.20	Same as Fig. 6.6 for 15, \mathcal{GS} J-factor, stacked sources and $\chi\chi \rightarrow ZZ$.	126

471	Figure 6.21 Same as Fig. 6.6 for 15, \mathcal{GS} J -factor, stacked sources and $\chi\chi \rightarrow \nu_e \bar{\nu}_e$	127
472	Figure 6.22 Same as Fig. 6.6 for 15, \mathcal{GS} J -factor, stacked sources and $\chi\chi \rightarrow \nu_\mu \bar{\nu}_\mu$	128
473	Figure 6.23 Signal Recovery study for an analysis with 15 stacked sources using the \mathcal{GS} J -factors [59]. Above shows 14 studies for DM mass ranging between 1 TeV and 20 PeV for $\chi\chi \rightarrow \mu_\mu \bar{\mu}_\mu$. The bottom right subplot features every spectral model used as input for the remaining subplots. The remaining subplots show n_{inj} as the number of signal events injected into background simulation. Whereas, n_s is the number of signal events recovered from analyzing the injected simulation. Blue line represents the median values of 100 simulations. Light blue bands show the 1σ statistical uncertainty around the median.	130
482	Figure 6.24 Same as Fig. 6.23 but for $\chi\chi \rightarrow t\bar{t}$ (top) and $b\bar{b}$ (bottom).	131
483	Figure 6.25 IceCube North Sky Track Sensitivities. Each panel shows sensitivity curves for various DM annihilation channels. Sensitivities are for the velocity-weighted cross-section $\langle\sigma v\rangle$ versus m_χ . Dotted, colored lines are sensitivities for individual sources. Solid white lines are for the combined sensitivity of all 15 \mathcal{GS} sources used in this study.	133
488	Figure 6.26 Same as Fig. 6.25 for three additional DM annihilation channels.	134
489	Figure 6.27 Panel A: Neutrino's from the Northern sky and incident on the IceCube detector will travel through the Earth. How much of the Earth these neutrinos travel is a function of zenith from the vertical axis. Panel B: SM prediction of neutrino transmission probabilities for neutrinos arriving at $90^\circ - 180^\circ$ zenith and with 100 GeV to 100 PeV energies. High-energy neutrinos traversing the whole Earth are completely absorbed, whereas low-energy neutrinos pass through unimpeded. Neutrinos coming from above the horizon will arrive unimpeded for all neutrino energies. Figure pulled from [102].	135
497	Figure 6.28 $\langle\sigma v\rangle$ sensitivities for 5 imaginary sources with $\log_{10} J = 19.42 \log_{10}(\text{GeV}^2 \text{cm}^{-5})$. Each imaginary source shares a declination with a source in Tab. 3.1	136
499	Figure 7.1 The prompt electron neutrino and photon spectrum resulting from the decay of a 2EeV DM particle to $\nu_e \bar{\nu}_e$, as currently being searched for at IceCube [5]. Solid curves represent the results of this work, and predict orders of magnitude more flux at certain energies than the dashed results of Pythia 8.2, one of the only existing methods to generate spectra at these masses. In both cases energy conservation is satisfied: there is a considerable contribution to a δ -function at $x = 1$, associated with events where an initial W or Z was never emitted and thus no subsequent shower developed. Large disagreements are generically observed at these masses for electroweak dominated channels, while the agreement is better for colored initial SM states.	138

509	Figure 7.2 TODO: neutrino and bb plot with nu Sensitivities[NEEDS A SOURCE][FACT 510 CHECK THIS]	139
511	Figure A.1 Sister figure to Figure 3.3. Sources in the first row from left to right: Bootes 512 I, Canes Venatici I, II. In second row: Draco, Hercules, Leo I. In the first row: 513 Leo II, Leo IV, Sextans. In the final row: Ursa Major I, Ursa Major II.	140
514	Figure B.1 Sister figure to Figure 4.2 for remaining SM primary annihilation channels 515 studied for this thesis. These did not require any post generation smoothing 516 and so are directly pulled from [79] with a binning scheme most helpful for a 517 HAWC analysis.	141
518	Figure B.2 Comparison of HAWC limits from this analysis to Glory Duck (Fig. 3.5) for 519 Coma Berenices and 7 DM annihilation channels.	151
520	Figure B.3 Same as Fig. B.2 but for Segue 1.	152
521	Figure B.4 Same as Fig. B.2 but for Sextans.	153
522	Figure C.1 Current status of spline tables according to constraints defined by Tab. 6.1. 523 Green splines are splines that passed under the GOOD tolerance. Yellow 524 are splines that are OK. Red are splines that FAIL. All yellow splines were 525 inspected individually before running the analysis. Splines were made for the 526 μ (PID 14; top panel) flavor and τ (PID 16; bottom panel) neutrino flavors.	157
527	Figure C.2 Sister figure to Fig. 6.5 for annihilation channels that did not require kernel 528 smoothing. These spectra are the composite ($\nu_\mu + \nu_\tau$) of neutrino flavors. 529 Every spectral model used for this analysis is featured as a colored solid line. 530 Bluer lines are for lower DM mass spectral models. DM masses range from 531 681 GeV to 100 PeV.	158
532	Figure C.3 Same as Fig. 6.23 but for Segue 1 and $\chi\chi \rightarrow b\bar{b}$	159
533	Figure C.4 Same as Fig. 6.23 but for Segue 1 and $\chi\chi \rightarrow t\bar{t}$	160
534	Figure C.5 Same as Fig. 6.23 but for Segue 1 and $\chi\chi \rightarrow \nu_\mu \overline{\nu_\mu}$	161
535	Figure C.6 Same as Fig. 6.23 but for Ursa Major II and $\chi\chi \rightarrow b\bar{b}$	162
536	Figure C.7 Same as Fig. 6.23 but for Ursa Major II and $\chi\chi \rightarrow t\bar{t}$	163
537	Figure C.8 Same as Fig. 6.23 but for Ursa Major II and $\chi\chi \rightarrow \nu_\mu \overline{\nu_\mu}$	164
538	Figure C.9 IceCube North Sky Track Sensitivities for $n_s/\langle N \rangle$. n_s values are the counts 539 fed into Eq. (6.8) to produce Fig. 6.26 and Fig. 6.25.	165
540	Figure C.10 Same as Fig. C.9 for three additional DM annihilation channels.	166

CHAPTER 1

541

DARK MATTER IN THE COSMOS

542 **1.1 Introduction**

543 The dark matter problem can be summarized in part by the following thought experiment.

544 Let us say you are the teacher for an elementary school classroom. You take them on a field
545 trip to your local science museum and among the exhibits is one for mass and weight. The exhibit
546 has a gigantic scale, and you come up with a fun problem for your class.

547 You ask your class, "What is the total weight of the classroom? Give your best estimation to
548 me in 30 minutes, and then we'll check your guess on the scale. If your guess is within 10% of the
549 right answer, we will stop for ice cream on the way back."

550 The students are ecstatic to hear this, and they get to work. The solution is some variation of
551 the following strategy. The students should give each other their weight or best guess if they do
552 not know. Then, all they must do is add each student's weight and get a grand total for the class.
553 The measurement on the giant scale should show the true weight of the class. When comparing
554 the measured weight to your estimation, multiply the measurement by 1.0 ± 0.1 to get the $\pm 10\%$
555 tolerances for your estimation.

556 Two of your students, Sandra and Mario, return to you with a solution.

557 They say, "We weren't sure of everyone's weight. We used 65 lbs. for the people we didn't
558 know and added everyone who does know. There are 30 of us, and we got 2,000 lbs.! That's a ton!"

559 You estimated 1,900 lbs. assuming the average weight of a student in your class was 60 lbs.
560 So, you are pleased with Sandra's and Mario's answer. You instruct your students to all gather on
561 the giant scale and read off the weight together. To all your surprise, the scale reads *10,000 lbs.*!
562 10,000 is significantly more than a 10% error from 2,000. In fact, it is approximately 5 times more
563 massive than either your or your students' estimates. You think to yourself and conclude there
564 must be something wrong with the scale. You ask an employee to check the scale and verify it is
565 well calibrated. They confirm that the scale is in working order. You weigh a couple of students
566 individually to assess that the scale is well calibrated. Sandra weighs 59 lbs., and Mario weighs

567 62 lbs., typical weights for their age. You then weigh each student individually and see that their
568 weights individually do not deviate greatly from 60 lbs. So, where does all the extra weight come
569 from?

570 This thought experiment serves as an analogy to the Dark Matter problem. The important
571 substitution to make however is to replace the students with stars and the classroom with a galaxy,
572 say the Milky Way. Individually the mass of stars is well measured and defined with the Sun as our
573 nearest test case. However, when we set out to measure the mass of a collection of stars as large as
574 galaxies, our well-motivated estimation is wildly incorrect. There simply is no way to account for
575 this discrepancy except without some unseen, or dark, contribution to mass and matter in galaxies.
576 I set out in my thesis to narrow the possibilities of what this Dark Matter could be.

577 This chapter is organized like the following... **TODO: Text should look like ... Chapter x has**
578 **blah blah blah.**

579 1.2 Dark Matter Basics

580 Presently, a more compelling theory of cosmology that includes Dark Matter (DM) in order
581 to explain a variety of observations is Λ Cold Dark Matter, or Λ CDM. I present the evidence
582 supporting Λ CDM in Section 1.3 yet discuss the conclusions of the Λ CDM model here. According
583 to Λ CDM fit to observations on the Cosmic Microwave Background (CMB), DM is 26.8% of the
584 universe's current energy budget. Baryonic matter, stuff like atoms, gas, and stars, contributes to
585 4.9% of the universe's current energy budget [1, 2, 3].

586 DM is dark; it does not interact readily with light at any wavelength. DM also does not interact
587 noticeably with the other standard model forces (Strong and Weak) at a rate that is readily observed
588 [3]. DM is cold, which is to say that the average velocity of DM is below relativistic speeds [1].
589 'Hot' DM would not likely manifest the dense structures we observe like galaxies, and instead
590 would produce much more diffuse galaxies than what is observed [3, 1]. DM is old; it played a
591 critical role in the formation of the universe and the structures within it [1, 2].

592 Observations of DM have so far been only gravitational. The parameter space available to what
593 DM could be therefore is extremely broad. The broad DM parameter space is iteratively tested in

594 DM searches by supposing a hypothesis that has not yet been ruled out and performing observations
595 to test them. When the observations yield a null result, the parameter space is constrained further.
596 I present some approaches for DM searches in Section 1.4.

597 **1.3 Evidence for Dark Matter**

598 Dark Matter (DM) has been a looming problem in physics for almost 100 years. Anomalies
599 have been observed by astrophysicists in galactic dynamics as early as 1933 when Fritz Zwicky
600 noticed unusually large velocity dispersion in the Coma cluster. Zwicky's measurement was the
601 first recorded to use the Virial theorem to measure the mass fraction of visible and invisible matter
602 in celestial bodies [4]. From Zwicky in [5], "*If this would be confirmed, we would get the surprising*
603 *result that dark matter is present in much greater amount than luminous matter.*" Zwicky's and
604 others' observation did not instigate a crisis in astrophysics because the measurements did not
605 entirely conflict with their understanding of galaxies [4]. In 1978, Rubin, Ford, and Norbert
606 measured rotation curves for ten spiral galaxies [6]. Rubin et al.'s 1978 publication presented a
607 major challenge to the conventional understanding of galaxies that could no longer be dismissed by
608 measurement uncertainties. Evidence has been mounting ever since for this exotic form of matter.
609 The following subsections provide three compelling pieces of evidence in support of the existence
610 of DM.

611 **1.3.1 First Clues: Stellar Velocities**

612 Zwicky, and later Rubin, measured the stellar velocities of various galaxies to estimate their
613 virial mass. The Virial Theorem upon which these observations are interpreted is written as

$$2T + V = 0. \quad (1.1)$$

614 Where T is the kinetic energy and V is the potential energy in a self-gravitating system. The
615 classical Newton's law of gravity from stars and gas was used for gravitational potential modeled in
616 the observed galaxies:

$$V = -\frac{1}{2} \sum_i \sum_{j \neq i} \frac{m_i m_j}{r_{ij}}. \quad (1.2)$$

617 Zwicky et al. measured just the velocities of stars apparent in optical wavelengths [5]. Rubin et al.
 618 added by measuring the velocity of the hydrogen gas via the 21 cm emission line of Hydrogen [6].
 619 The velocities of the stars and gas are used to infer the total mass of galaxies and galaxy clusters
 620 via Equation (1.1). An inferred mass is obtained from the luminosity of the selected sources. The
 621 two inferences are compared to each other as a luminosity to mass ratio which typically yielded [1]

$$\frac{M}{L} \sim 400 \frac{M_{\odot}}{L_{\odot}} \quad (1.3)$$

622 M_{\odot} and L_{\odot} referring to stellar mass and stellar luminosity, respectively. These ratios clearly indicate
 623 a discrepancy in apparent light and mass from stars and gas and their velocities.

624 Rubin et al. [6] demonstrated that the discrepancy was unlikely to be an underestimation of
 625 the mass of the stars and gas. The inferred "dark" mass was up to 5 times more than the luminous
 626 mass. This dark mass also needed to extend well beyond the extent of the luminous matter.

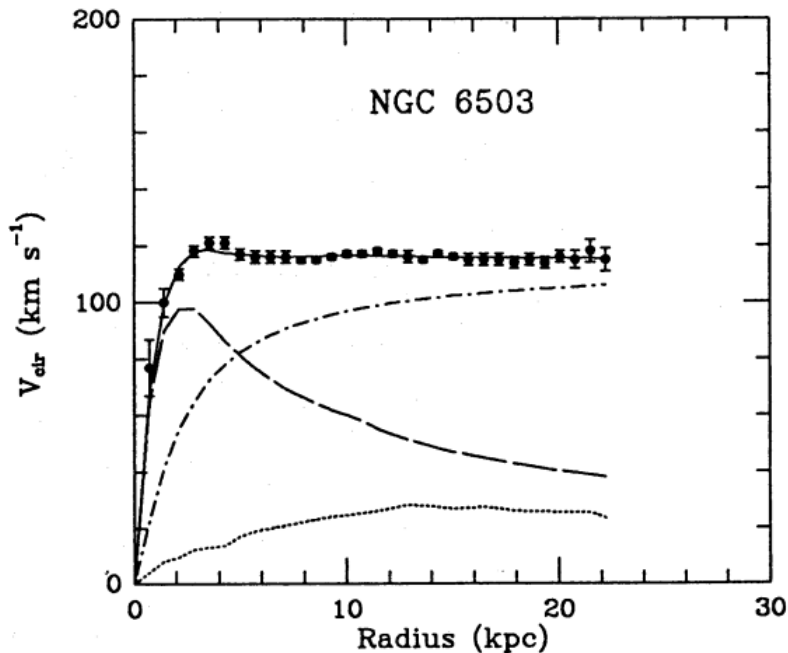


Figure 1.1 Rotation curve fit to NGC 6503 from [7]. Dashed line is the contribution from visible matter. Dotted curves are from gas. Dash-dot curves are from dark matter (DM). Solid line is the composite contribution from all matter and DM sources. Data are indicated with bold dots with error bars. Data agree strongly with a matter + DM composite prediction.

627 Figure 1.1 features one of many rotation curves plotted from the stellar velocities within galaxies.

628 The measured rotation curves mostly feature a flattening of velocities at higher radius which is not
629 expected if the gravity was only coming from gas and luminous matter. The extension of the
630 flat velocity region also indicates that the DM is distributed far from the center of the galaxy.
631 Modern velocity measurements include significantly larger objects, galactic clusters, and smaller
632 objects, dwarf galaxies. Yet, measurements along this regime are leveraging the Virial theorem
633 with Newtonian potential energies. We know Newtonian gravity is not a comprehensive description
634 of gravity. New observational techniques have been developed since 1978, and those are discussed
635 in the following sections.

636 1.3.2 Evidence for Dark Matter: Gravitational Lensing

637 Modern evidence for dark matter comes from new avenues beyond stellar velocities. Grav-
638 itational lensing from DM is a new channel from general relativity. General relativity predicts
639 aberrations in light caused by massive objects. In recent decades we have been able to measure the
640 lensing effects from compact objects and DM halos. Figure 1.2 shows how different massive ob-
641 jects change the final image of a faraway galaxy resulting from gravitational lensing. Gravitational
642 lensing developed our understanding of dark matter in two important ways.

643 Gravitational lensing provides additional compelling evidence for DM. The observation of two
644 merging galactic clusters in 2006, shown in Figure 1.3, provided a compelling argument for DM
645 outside the Standard Model. These clusters merged recently in astrophysical time scales. Galaxies
646 and star cluster have mostly passed by each other as the likelihood of their collision is low. Therefore,
647 these massive objects will mostly track the highest mass, dark and/or baryonic, density. Yet, the
648 intergalactic gas is responsible for the majority of the baryonic mass in the systems [4]. These gas
649 bodies will not phase through and will heat up as they collide together. The hot gas is located via
650 x-ray emission from the cluster. Two observations of the clusters were performed independently of
651 each other.

652 The first was the lensing of light around the galaxies due to their gravitational influences.
653 When celestial bodies are large enough, the gravity they exert bends space and time itself. The
654 warped space-time lenses light and will deflect in an analogous way to how glass lenses will bend

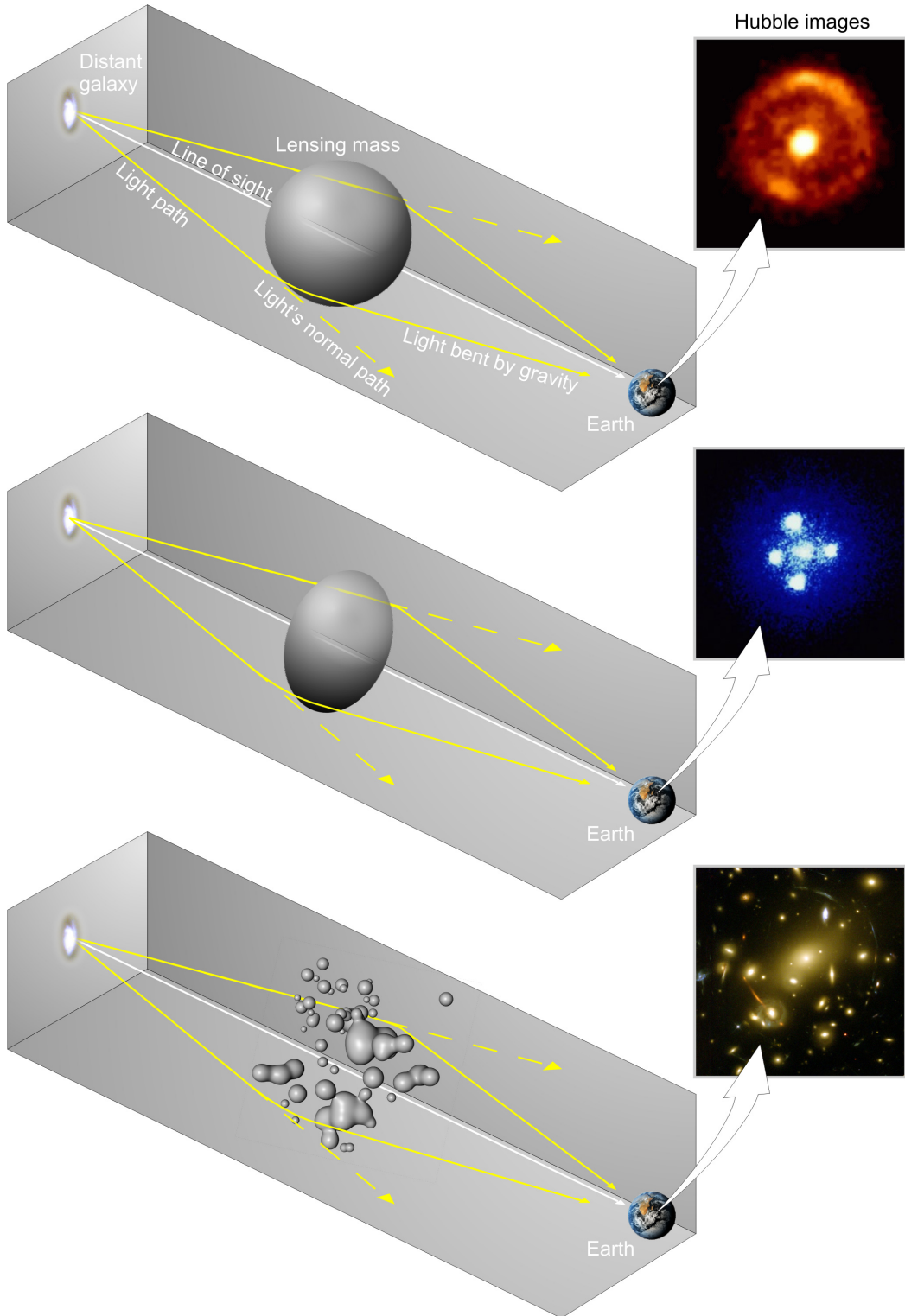


Figure 1.2 Light from distant galaxy is bent in unique ways depending on the distribution of mass between the galaxy and Earth. Yellow dashed lines indicate where the light would have gone if the matter were not present [8].

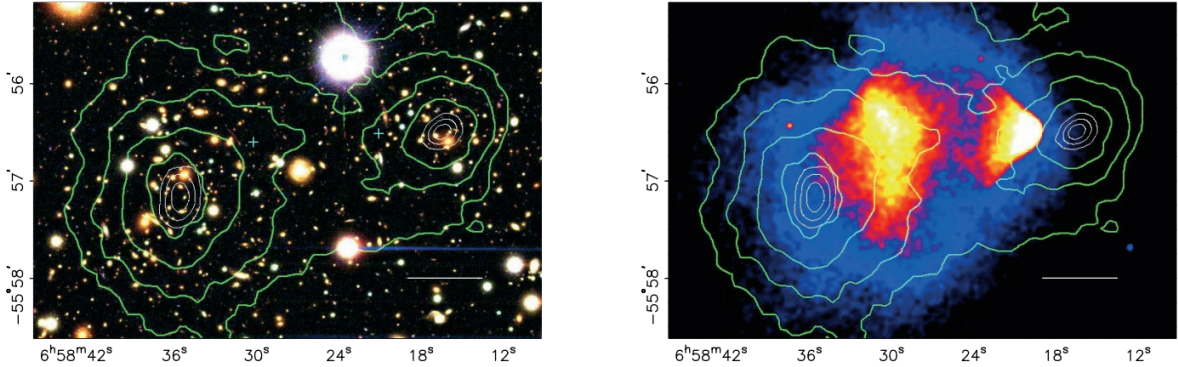


Figure 1.3 (left) Optical image of galactic cluster 1E0657-558. (right) X-ray image of the cluster with redder meaning hotter and higher baryon density. (both) Green contours are reconstruction of gravity contours from weak lensing. White rings are the best fit mass maxima at 68.3%, 95.5%, and 99.7% confidence. The matter maxima of the clusters are clearly separated from x-ray maxima. [9]

655 light, see Figure 1.2. With a sufficient understanding of light sources behind a massive object, we
 656 can reconstruct the contours of the gravitational lenses. The gradient of the contours shown in
 657 Figure 1.3 then indicates how dense the matter is and where it is.

658 The x-ray emission can then be observed from the clusters. Since these galaxies are mostly gas
 659 and are merging, then the gas should be getting hotter. If they are merging, the x-ray emissions
 660 should be the strongest where the gas is mostly moving through each other. Hence, X-ray emission
 661 maps out where the gas is in the merging galaxy cluster.

662 The lensing and x-ray observations were done on the Bullet cluster featured on Figure 1.3.
 663 The x-ray emissions do not align with the gravitational contours from lensing. The incongruence
 664 in mass density and baryon density suggests that there is a lot of matter somewhere that does
 665 not interact with light. Moreover, this dark matter cannot be baryonic [9]. The Bullet Cluster
 666 measurement did not really tell us what DM is exactly, but it did give the clue that DM also does
 667 not interact with itself very strongly. If DM did interact strongly with itself, then it would have been
 668 more aligned with the x-ray emission [9]. There have been follow-up studies of galaxy clusters with
 669 similar results. The Bullet Cluster and others like it provide a persuasive case against something
 670 possibly amiss in our gravitational theories.

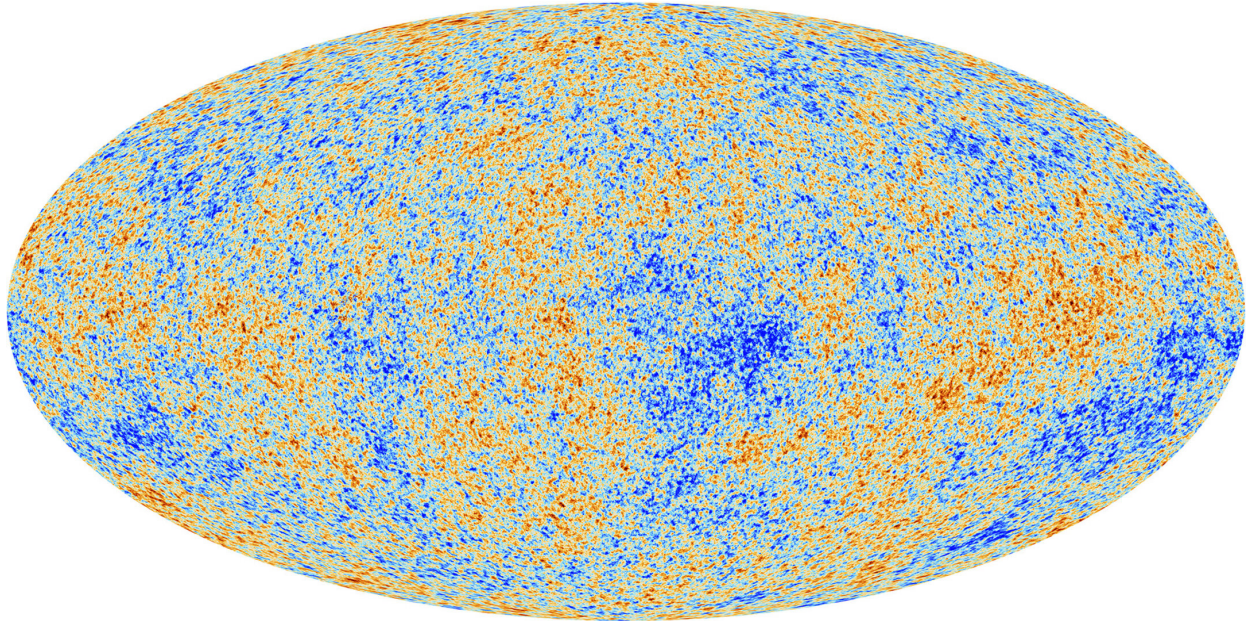


Figure 1.4 Plank CMB sky. Sky map features small variations in temperature in primordial light. These anisotropies are used to make inferences about the universe's energy budget and developmental history. [10]

671 **1.3.3 Evidence for Dark Matter: Cosmic Microwave Background**

672 The Cosmic Microwave Background (CMB) is the primordial light from the early universe
673 when Hydrogen atoms formed from the free electron and proton soup in the early universe. The
674 CMB is the earliest light we can observe; released when the universe was about 380,000 years old.
675 Then we look at how the simulated universes look like compared to what we see. Figure 1.4 is the
676 most recent CMB image from the Plank satellite after subtracting the average value and masking the
677 galactic plane [10]. Redder regions indicate a slightly hotter region in the CMB, and blue indicates
678 colder. The intensity variations are on the order of 1 in 1000 with respect to the average value.

679 The Cosmic Microwave Background shows that the universe had DM in it from an incredibly
680 early stage. To measure the DM, Dark Energy, and matter fractions of the universe from the CMB,
681 the image is analyzed into a power spectrum, which shows the amplitude of the fluctuations as
682 a function of spherical multipole moments. Λ CDM provides the best fit to the power spectra of
683 the CMB as shown in Figure 1.5. The CMB power spectrum is quite sensitive to the fraction
684 of each energy contribution in the early universe. Low l modes are dominated by variations
685 in gravitational potential. Intermediate l emerge from oscillations in photon-baryon fluid from

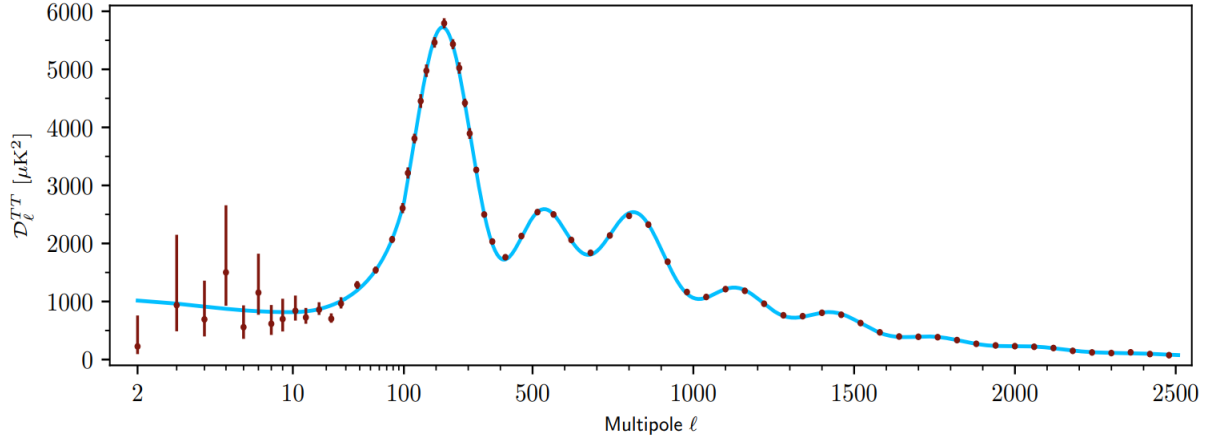


Figure 1.5 Observed Cosmic Microwave Background power spectrum as a function of multipole moment from Plank [10]. Blue line is best fit model from Λ CDM. Red points and lines are data and error, respectively.

686 competing baryon pressures and gravity. High l is a damped region from the diffusion of photons
 687 during electron-proton recombination. [1]

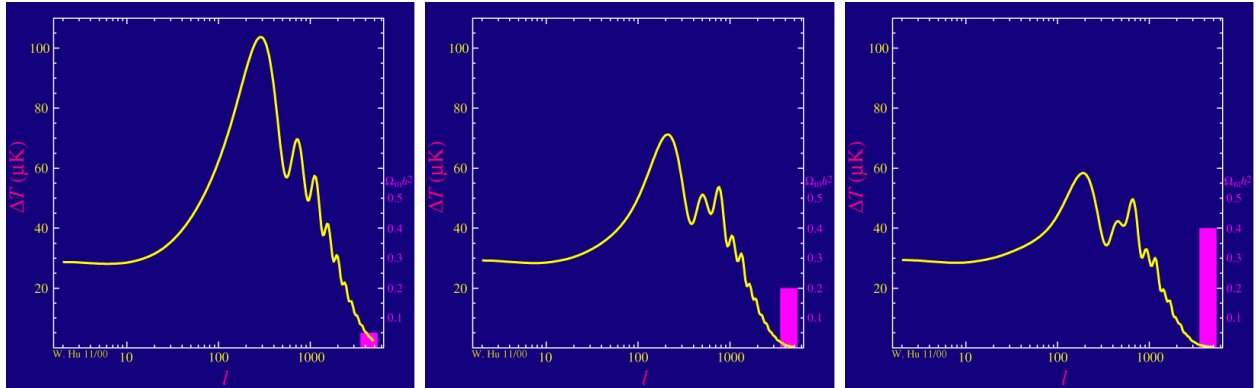


Figure 1.6 Predicted power spectra of CMB for different $\Omega_m h^2$ values for fixed baryon density from [11]. (left) Low $\Omega_m h^2$ increases the prominence of first and second peaks. (middle) $\Omega_m h^2$ is most similar to the observed power spectrum. The second and third peaks are similar in height. (right) $\Omega_m h^2$ is large which suppresses the first peak and raises the prominence of the third peak.

688 The harmonics would look quite different for a universe with less DM. Figure 1.6 demonstrates
 689 the effect $\Omega_m h^2$ has on the expected power spectrum for fixed baryon matter density. [11] Sweeping
 690 $\Omega_m h^2$ in this way clearly shows the effect dark matter has on the CMB power spectrum. The
 691 observations fit well with the Λ CDM model, and the derived fractions are as follows. The matter
 692 fraction: $\Omega_m = 0.3153$; and the baryon fraction: $\Omega_b = 0.04936$ [10]. Plank's observations also
 693 provide a measure of the Hubble constant, H_0 . H_0 especially has seen a growing tension in the

694 past decade that continues to deepened with observations from instruments like the James Webb
695 Telescope [12, 13]. As Hubble tensions deepen, we may find that perhaps Λ **CDM**, despite its
696 successes, is missing some critical physics.

697 Overall, the Newtonian motion of stars in galaxies, weak lensing from galactic clusters, and
698 power spectra from primordial light form a compelling body of research in favor of dark matter.
699 It takes another leap of theory and experimentation to make observations of DM that are non-
700 gravitational in nature. In Section 1.3, the evidence for DM implies strongly that the DM is matter
701 and not a lost parameter in the gravitational fields between massive objects. Finally, if we take one
702 axiom: that this matter has quantum behavior, such as being described by some Bohr wavelength
703 and abiding by some fermion or boson statistics; then we arrive at particle dark matter. One particle
704 DM hypothesis is the Weakly Interacting Massive Particle (WIMP). This DM candidate theory is
705 discussed further in the next section and is the focus of this thesis.

706 **1.4 Searching for Dark Matter: Particle DM**

707 Section 1.4 shows the Standard Model of particle physics and is currently the most accurate
708 model for the dynamics of fundamental particles like electrons and photons. The current status
709 of the SM does not have a viable DM candidate. When looking at the standard model, we can
710 immediately exclude any charged particle because charged particles interact strongly with light.
711 Specifically, this will rule out the following charged, fundamental particles: $e, \mu, \tau, W, u, d, s, c, t, b$
712 and their corresponding antiparticles. Recalling from Section 1.2 that DM must be long-lived and
713 stable over the age of the universe which excludes all SM particles with decay half-lives at or shorter
714 than the age of the universe. The lifetime constraint additionally eliminates the Z and H bosons.
715 Finally, the candidate DM needs to be somewhat massive. Recall from Section 1.2 that DM is cold
716 or not relativistic through the universe. This eliminates the remaining SM particles: $\nu_{e,\mu,\tau}, g, \gamma$ as
717 DM candidates. Because there are no DM candidates within the SM, the DM problem strongly
718 hints to physics beyond the SM (BSM).

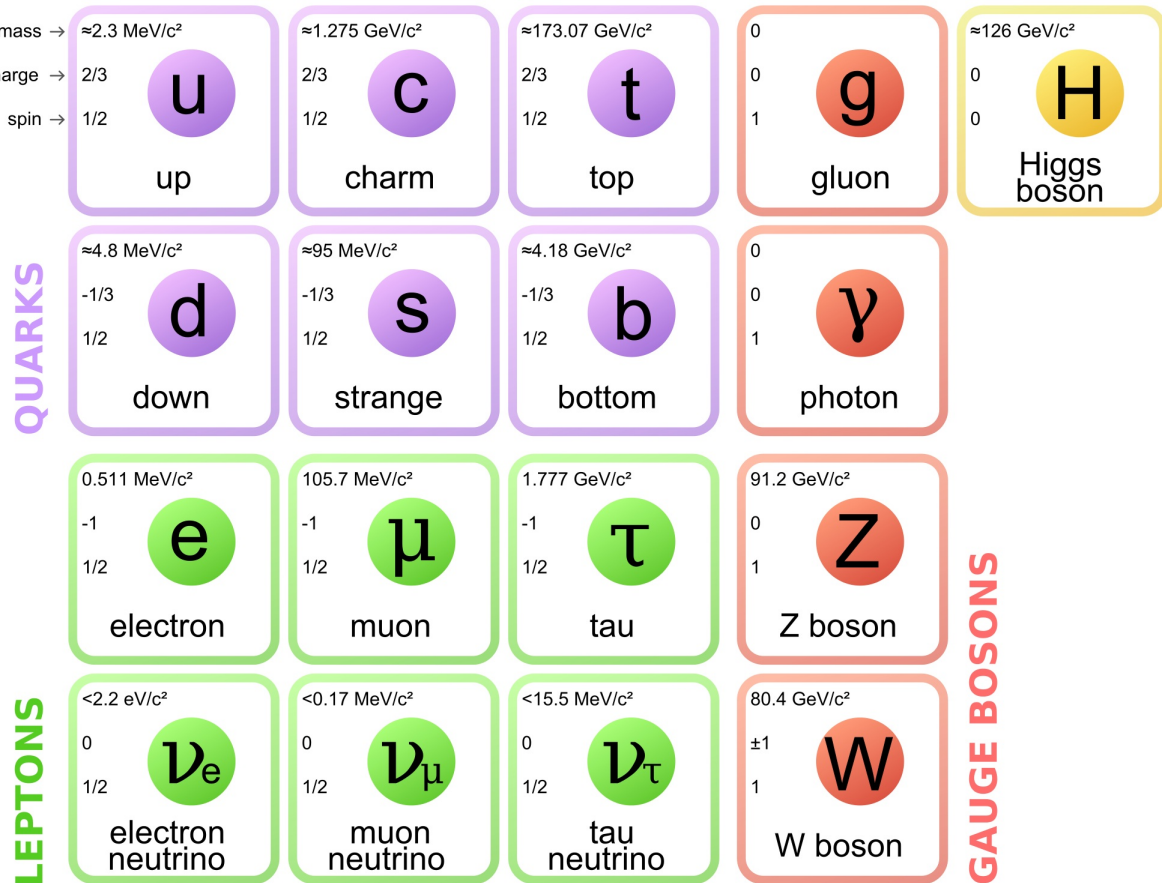


Figure 1.7 The Standard Model (SM) of particle physics. Figure taken from <http://www.quantumdiaries.org/2014/03/14/the-standard-model-a-beautiful-but-flawed-theory/>

719 1.4.1 Shake it, Break it, Make it

720 When considering DM that couples in some way with the SM, the interactions are roughly
 721 demonstrated by interaction demonstrated in Figure 1.8. The figure is a simplified Feynman
 722 diagram where the arrow of time represents the interaction modes of: **Shake it, Break it, Make it.**

723 **Shake it** refers to the direct detection of dark matter. Direct detection interactions start with
 724 a free DM particle and an SM particle. The DM and SM interact via elastic or inelastic collision
 725 and recoil away from each other. The DM remains in the dark sector and imparts some momentum
 726 onto the SM particle. The hope is that the momentum imparted onto the SM particle is sufficiently
 727 high enough to pick up with extremely sensitive instruments. Because we cannot create the DM in
 728 the lab, a direct detection experiment must wait until DM is incident on the detector. Most direct
 729 detection experiments are therefore placed in low-background environments with inert detection

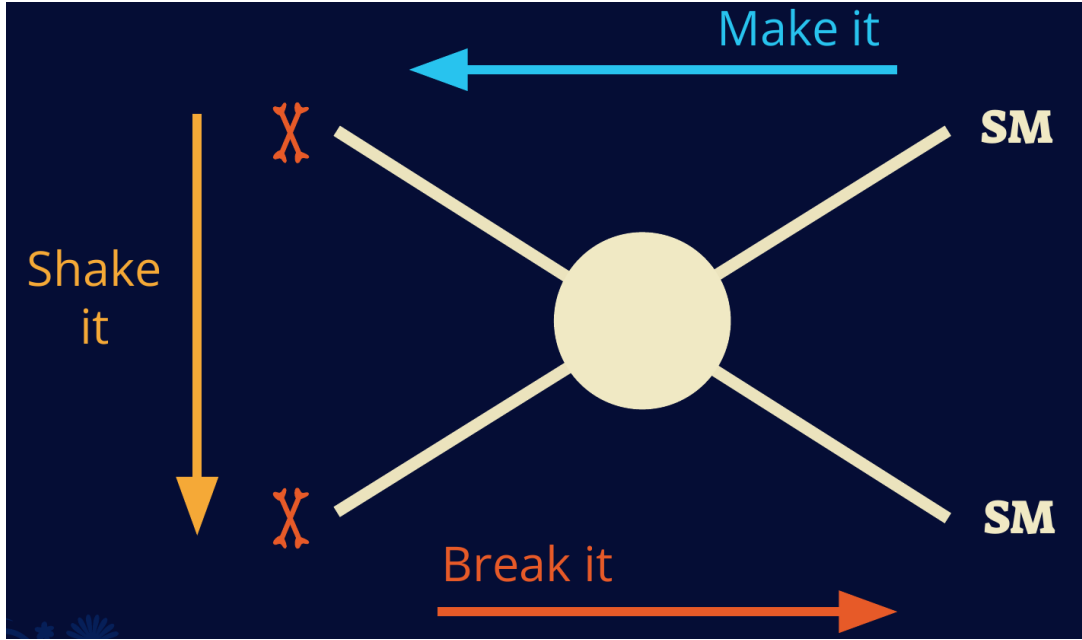


Figure 1.8 Simplified Feynman diagram demonstrating different ways DM can interact with SM particles. The 'X's refer to the DM particles whereas the SM refer to fundamental particles in the SM. The large circle in the center indicates the vertex of interaction and is purposely left vague. The colored arrows refer to different directions of time as well as their respective labels. The arrows indicate the initial and final state of the DM -SM interaction in time.

730 media like the noble gas Xenon. [14]

731 **Make it** refers to the production of DM from SM initial states. The experiment starts with
 732 particles in the SM. These SM particles are accelerated to incredibly high energies and then collide
 733 with each other. In the confluence of energy, DM hopefully emerges as a byproduct of the SM
 734 annihilation. Often it is the collider experiments that are energetic enough to hypothetically produce
 735 DM. These experiments include the world-wide collaborations ATLAS and CMS at CERN where
 736 proton collide together at extreme energies. The DM searches, however, are complex. DM likely
 737 does not interact with the detectors and lives long enough to escape the detection apparatus of
 738 CERN's colliders. This means any DM production experiment searches for an excess of events
 739 with missing momentum or energy in the events. An example event with missing transverse
 740 momentum is shown in Figure 1.9. The missing momentum with no particle tracks implies a
 741 neutral particle carried the energy out of the detector. However, there are other neutral particles
 742 in the SM, like neutrons or neutrinos, so any analysis has to account for SM signatures of missing

743 momentum. [15]

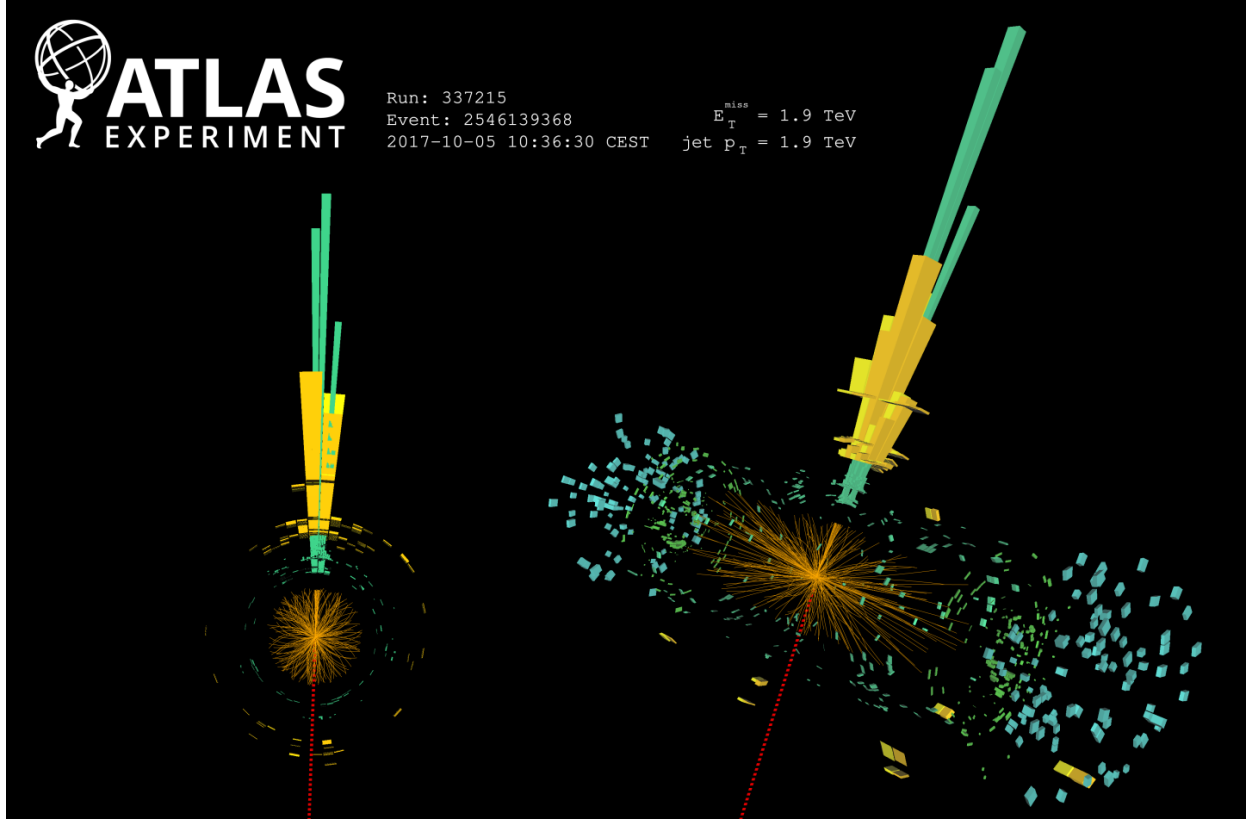


Figure 1.9 A single jet event in ATLAS detector from 2017 [16]. Jet momentum was observed to be 1.9 TeV. Missing transverse momentum was observed to be 1.9 TeV compared to the initial transverse momentum of the event was 0. Implied MET is traced by a red dashed line in event display.

744 1.4.2 Break it: Standard Model Signatures of Dark Matter through Indirect Searches

745 **Break it** refers to the creation of SM particles from the dark sector, and it is the primary focus
746 of this thesis. The interaction begins with DM or in the dark sector. The hypothesis is that this
747 DM will either annihilate with itself or decay and produce an SM byproduct. This method is
748 often referred to as the Indirect Detection of DM because we have no lab to directly control or
749 manipulate the DM. Therefore, most indirect DM searches are performed using observations of
750 known DM densities among the astrophysical sources. The strength is that we have the whole of the
751 universe and its 13.6-billion-year lifespan to use as a detector and particle accelerator. Additionally,
752 locations of dark matter are well cataloged since it was astrophysical observations that presented

753 the problem of DM in the first place.

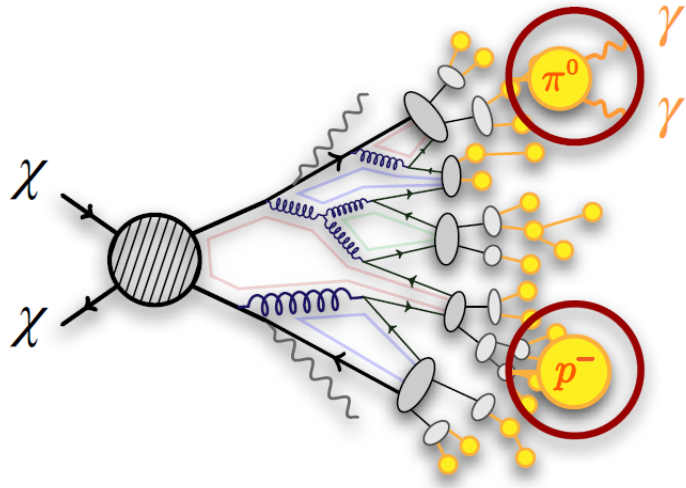


Figure 1.10 More detailed pseudo-Feynman diagram of particle cascade from dark matter annihilation into 2 quarks. The quarks hadronize and down to stable particles like γ or the anti-proton (p^-). Diagram pulled from ICRC 2021 presentation on DM annihilation search [17].

754 However, anything can happen in the universe. There are many difficult to deconvolve back-
755 grounds when searching for DM. One prominent example is the galactic center. We know the
756 galactic center has a large DM content because of stellar kinematics in our Milky Way and DM halo
757 simulations. Yet, any signal from the galactic center is challenging to parse apart from the extreme
758 environment of our supermassive black hole, unresolved sources, and diffuse emission from the
759 interstellar medium [18]. Despite the challenges, any DM model that yields evidence in the other
760 two observation methods, **Shake it or Make it** must be corroborated with indirect observations of
761 the known DM sources. Without corroborating evidence, DM observation in the lab is hard-pressed
762 to demonstrate that it is the model contributing to the DM seen at the universal scale.

763 In the case of WIMP DM, signals are described in terms of primary SM particles produced
764 from DM decay or annihilation. The SM initial state particles are then simulated down to stable
765 final states such as the γ , ν , p , or e which can traverse galactic lengths to reach Earth.

766 Figure 1.10 shows the quagmire of SM particles that emerges from SM initial states that are not
767 stable [17]. There are many SM particles with varying energies that can be produced in such an

768 interaction. For any arbitrary DM source and stable SM particle, the SM flux from DM annihilating
 769 to a neutral particle in the SM, ϕ , from a region in the sky is described by the following.

$$\frac{d\Phi_\gamma}{dE_\gamma} = \frac{\langle\sigma v\rangle}{8\pi m_\chi^2} \frac{dN_\gamma}{dE_\gamma} \times \int_{\text{source}} d\Omega \int_{l.o.s} \rho_\chi^2 dl(r, \theta') \quad (1.4)$$

770 In Equation (3.1), $\langle\sigma v\rangle$ is the velocity-weighted annihilation cross-section of DM to the SM. m_χ
 771 refers to the mass of DM, noted with Greek letter χ . $\frac{dN_\phi}{dE_\phi}$ is the N particle flux weighted by the
 772 particle energy. An example is provided in Figure 1.11 for the γ final state. The integrated terms
 773 are performed over the solid angle, $d\Omega$, and line of sight, l.o.s. ρ is the density of DM for a
 774 location (r, θ') in the sky. The terms left of the '×' are often referred to as the particle physics
 775 component. The terms on the right are referred to as the astrophysical component. For decaying
 776 DM, the equation changes to...

$$\frac{d\Phi_\phi}{dE_\phi} = \frac{1}{4\pi\tau m_\chi} \frac{dN_\phi}{dE_\phi} \times \int_{\text{source}} d\Omega \int_{l.o.s} \rho_\chi dl(r, \theta') \quad (1.5)$$

777 In Equation (1.5), τ is the decay lifetime of the DM. Just as in Equation (3.1), the left and right
 778 terms are the particle physics and the astrophysical components respectively. The integrated
 779 astrophysical component of Equation (3.1) is often called the J-Factor. Whereas the integrated
 780 astrophysical component of Equation (1.5) is often called the D-Factor.

781 Exact DM $\text{DM} \rightarrow \text{SM SM}$ branching ratios are not known, so it is usually assumed to go 100%
 782 into an SM particle/anti-particle. Additionally, when a DM annihilation or decay produces one of
 783 the neutral, long-lived SM particles (ν or γ), the particle is traced back to a DM source. For DM
 784 above GeV energies, there are very few SM processes that can produce particles with such a high
 785 energy. Seeing such a signal would almost certainly be an indication of the presence of dark matter.
 786 Fortunately, the universe provides us with the largest volume and lifetime ever for a particle physics
 787 experiment.

788 1.5 Sources for Indirect Dark Matter Searches

789 The first detection of DM relied on optical observations. Since then, we have developed new
 790 techniques to find DM dense regions. As described in Section 1.3.1, many DM dense regions were
 791 through observing galactic rotation curves. Our Milky Way galaxy is among DM dense regions

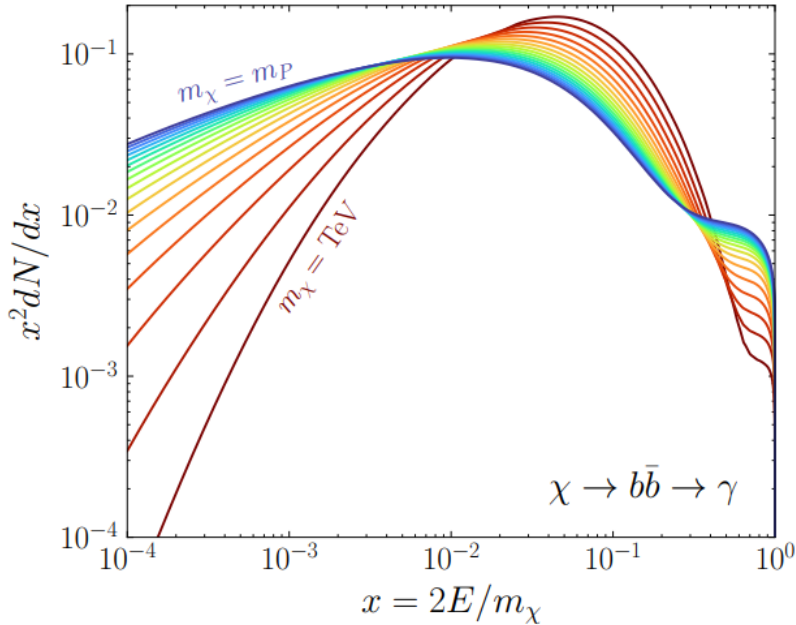


Figure 1.11 Dark Matter (DM) decay spectrum for $b\bar{b}$ initial state and γ final state. Redder spectra are for larger DM masses. Bluer spectra are light DM masses. x is a unitless factor defined as the ratio of the mass of DM, m_χ , and the final state particle energy E_γ . Figure from [19].

discovered, and it is the largest nearby DM dense region to look at. Additionally, the DM halo surrounding the Milky Way is clumpy [18]. There are regions in the DM halo of the Milky Way that have more DM than others that have captured gas over time. These sub-halos were dense enough to collapse gas and form stars. These apparent sub galaxies are known as dwarf spheroidal galaxies and are the main sources studied in this thesis. Each source type comes with different trade-offs. Galactic Center studies will be very sensitive to the assumed distribution of DM. The central DM density can vary substantially as demonstrated in Figure 1.12. At distances close to the center of the galaxy, or small r , the differences in DM densities can be 3-4 orders of magnitude. Searches toward the galactic center will therefore be quite sensitive to the assumed DM distribution.

Searches toward Dwarf Spheroidal Galaxies (dSph's) suffer from uncertainties in the DM density less than the galactic center studies. This is mostly from their diminutive size being smaller than the angular resolution of most γ -ray observatories [18]. The DM content dSph's are typically determined with the Virial theorem, Equation (1.1), and are usually majority DM [18] in mass. DSph's tend to be ideal sources to look at for DM searches. Their environments are quiet with little

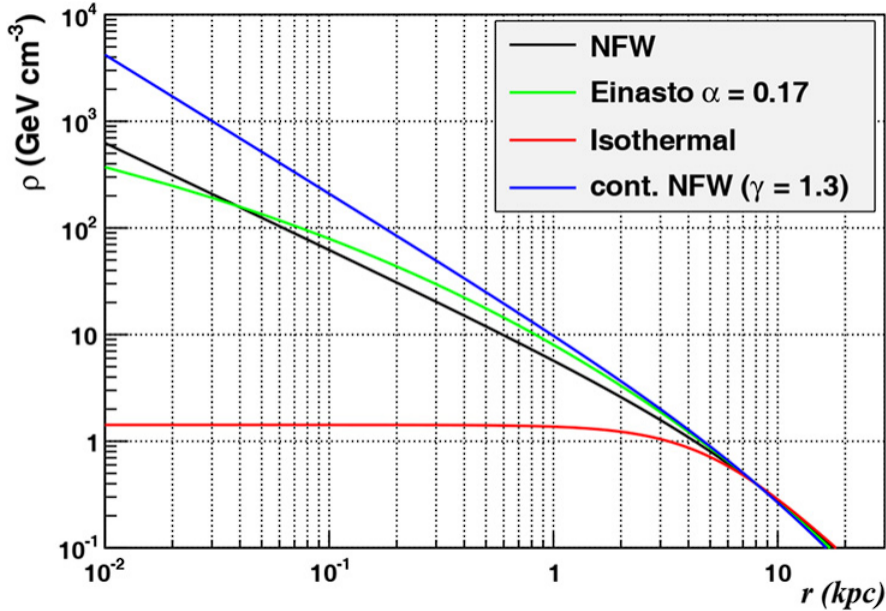


Figure 1.12 Different dark matter density profiles compared. Some models produce exceptionally large densities at small r [20].

806 astrophysical background. Unlike the galactic center, the most active components of dSph's are the
 807 stars within them versus a violent accretion disc around a black hole. All this together means that
 808 dSph's are among the best sources to look at for indirect DM searches. dSph's are the targets of
 809 focus for this thesis.

810 1.6 Multi-Messenger Dark Matter

811 Astrophysics entered a new phase in the past few decades that leverages our increasing sensitivity
 812 to SM channels and general relativity (GR). Up until the 21st century, astrophysical observations
 813 were performed with photons (γ) only. Astrophysics with this 'messenger' is fairly mature now.
 814 Novel observations of the universe have since only adjusted the sensitivity of the wavelength of
 815 light that is observed except at MeV energies. Gems like the CMB [10], and more have ultimately
 816 been observations of different wavelengths of light. Multi-messenger astrophysics proposes using
 817 other SM particles such the p^{+-} , or ν or gravitation waves predicted by general relativity.

818 The experiment LIGO had a revolutionary discovery in 2016 with the first detection of a binary
 819 black hole merger [21]. This opened the collective imagination to observing the universe through
 820 gravitational waves. There has also been a surge of interest in the neutrino (ν) sector. IceCube

821 demonstrated that we are sensitive to neutrinos in regions that correlate with significant photon
 822 emission like the galactic plane [22]. Neutrinos, like gravitational waves and light, travel mostly
 823 unimpeded from their source to our observatories. This makes pointing to the originating source
 824 of these messengers much easier than it is for cosmic rays which are deflected from their source by
 825 magnetic fields.

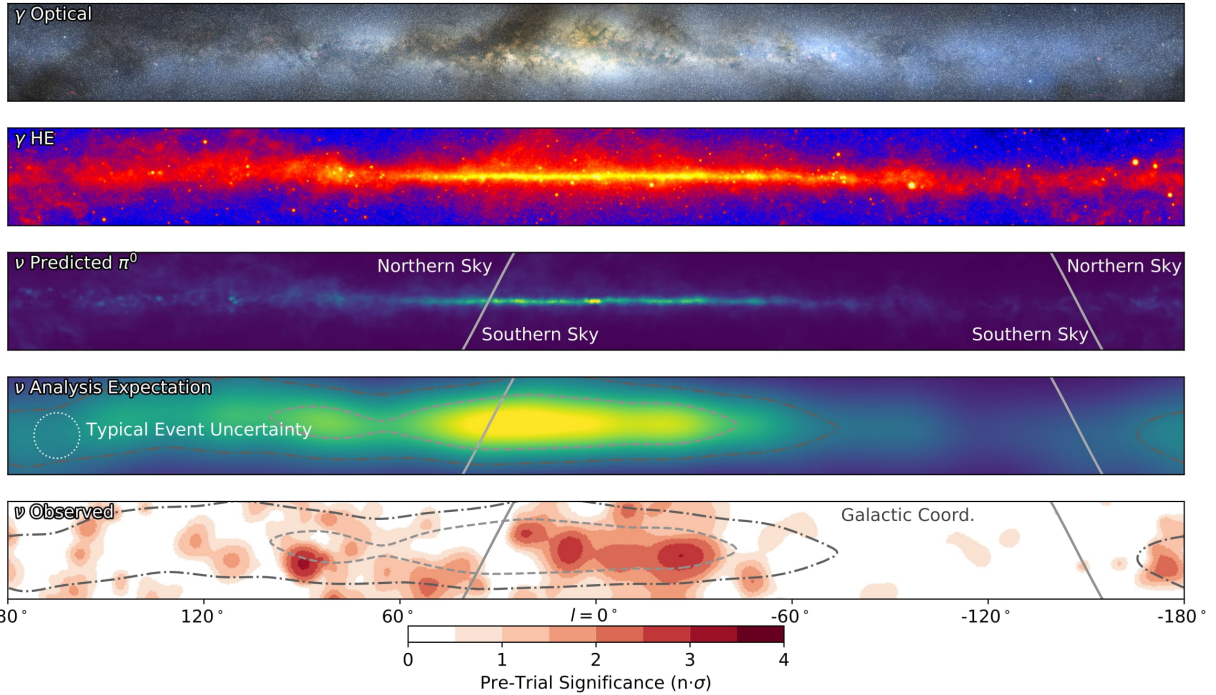


Figure 1.13 The Milky Way Galaxy in photons (γ) and neutrinos (ν) [22]. The Galactic center is at $l=0^\circ$ and is the brightest region in all panels. (top) An Optical color image of the Milky Way galaxy seen from Earth. Clouds of gas and dust obscure some light from stars. (2nd down) Integrated flux of γ -rays observed by the Fermi-LAT telescope [23]. (middle) Expected neutrino emission that corresponds with Fermi-LAT observations. (2nd up) Expected neutrino emission profile after considering detector systematics of IceCube. (bottom) Observed neutrino emission from region of the galactic plane. Substantial neutrino emission was detected.

826 The IceCube collaboration recently published a groundbreaking result of the Milky Way in
 827 neutrinos. The recent result from IceCube, shown in Figure 1.13, proves that we can make
 828 observations under different messenger regimes. The top two panels show the appearance of the
 829 galactic plane to different wavelengths of light. Some sources are more apparent in some panels,
 830 while others are not. This new channel is powerful because neutrinos are readily able to penetrate
 831 through gas and dust in the Milky Way. This new image also refines our understanding of how high

832 energy particles are produced. For example, the fit to IceCube data prefers neutrino production
 833 from the decay of π^0 [22].

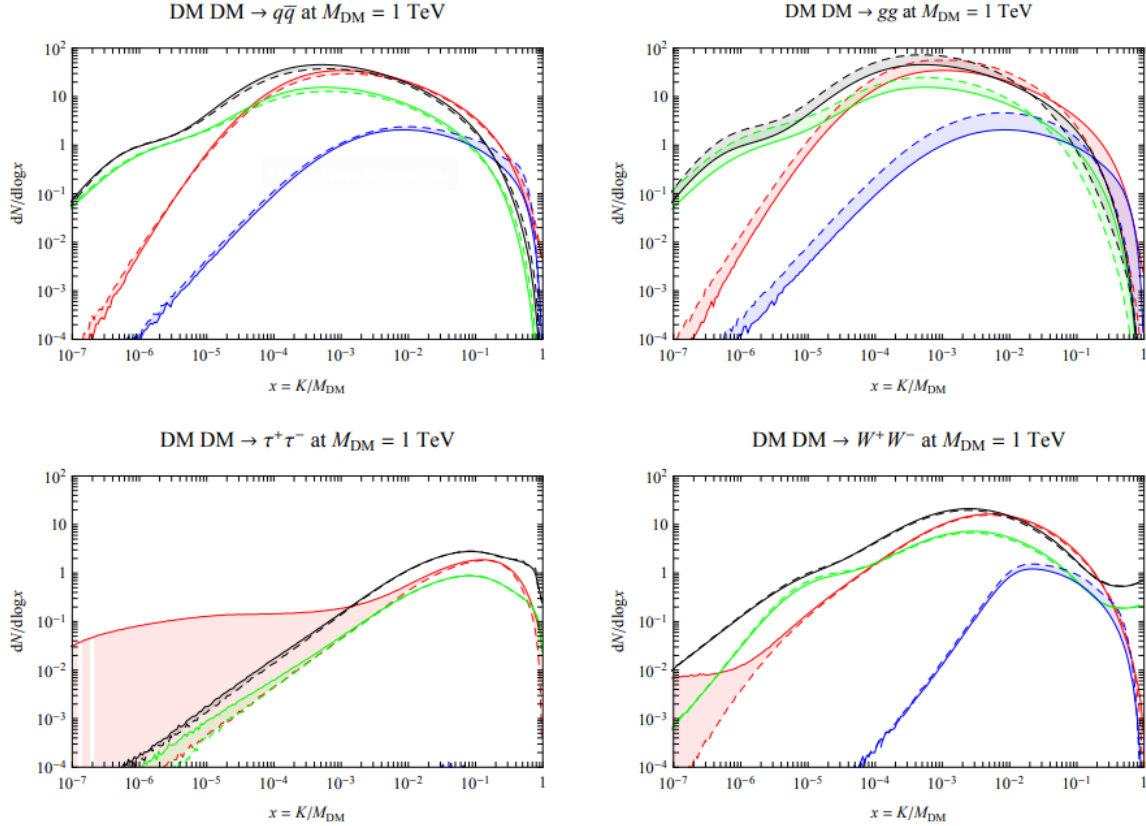


Figure 1.14 Dark Matter annihilation spectra for different final state particle and standard model annihilation channels [24]. Photons (red), e^\pm (green), \bar{p} (blue), ν (black).

834 Exposing our observations to more cosmic messengers greatly increases our sensitivity to
 835 rare processes. In the case of DM, Figure 1.14, there are many SM particles produced in DM
 836 annihilation. Among the final state fluxes are gammas and neutrinos. Charged particles are also
 837 produced however they would not likely make it to Earth since they will be deflected by magnetic
 838 fields between the source and Earth. This means observatories that can see the neutral messengers
 839 are especially good for DM searches and for combining data for a multi-messenger DM search.

CHAPTER 2

840

HIGH ALTITUDE WATER CHERENKOV (HAWC) OBSERVATORY

841



Figure 2.1 Photo of the HAWC detector that I took on May 17, 2023. Main array is centered in the photo and comprised of the larger tanks. Outriggers are the smaller tanks around the main array.

842

The High Altitude Water Cherenkov (HAWC) Observatory is a specialized instrument designed

843

for the observation of high energy gamma-rays and cosmic rays [25]. Located on the Sierra

844

Negra volcano in Mexico, HAWC observes gamma rays and cosmic rays in the energy range of

845

approximately 100 GeV to 100's of TeV. HAWC is strategically situated to maximize observational

846

efficiency due to its high altitude. At an elevation of 4,100 meters, it monitors about two-thirds of

847

the sky every day with an uptime above 90%. This capability is essential for studying high-energy

848

astrophysical phenomena.

849

HAWC consists of 300 water Cherenkov detectors (WCDs) spread over $22,000 \text{ m}^2$. Each main

850

array detector is filled with purified water and equipped with four, upward-facing photomultiplier

851

tubes (PMTs). See Fig. 2.3 for schematic of WCDs. These PMTs detect Cherenkov radiation from

852

charged particles passing through the tanks. These charged particles are generated when a high

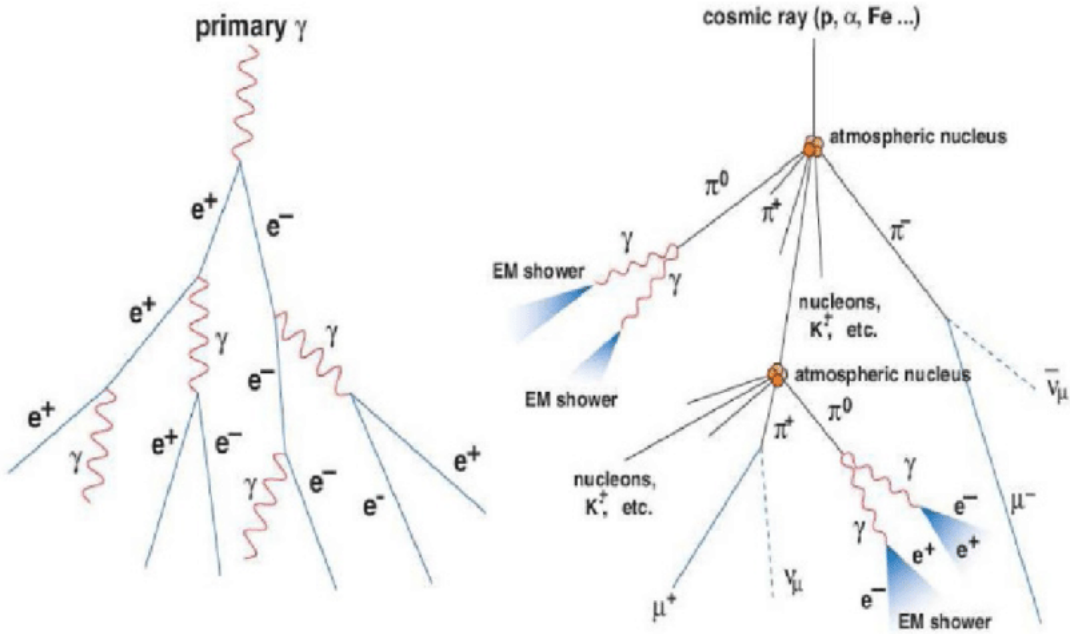


Figure 2.2 A particle physics illustration of high energy particle showers. Left shower is an electromagnetic shower from a high energy gamma-ray. Most particles in the shower will be a combination of photons and charged leptons, in this case electrons (e). Right figure shows a cosmic ray particle shower. The cosmic ray will produce many more types of particles including pions (π), neutrinos, and charged leptons. Figured pulled from [26].

853 energy gamma or cosmic ray collides with gas in the atmosphere to create a charged particle shower,
 854 see Fig. 2.2. The observatory includes a separate tank configuration which are referred to as the
 855 outriggers. They are a secondary array of 345 smaller WCD's. Surrounding the main array, each
 856 outrigger tank measures 1.55 meters in diameter and height and contain a single upward-facing
 857 eight-inch PMT. This add-on increases the instrumented footprint fourfold. The outriggers are
 858 meant to improve the reconstruction of showers extending beyond the main array, especially for
 859 events above 10 TeV. However, at the time of writing this thesis, the outriggers have not been fully
 860 integrated into HAWC's reconstruction software.

861 2.1.1 Construction and Hardware

862 Each main array WCD, see Fig. 2.3, is a cylindrical tank with dimensions of 7.3 m in diameter
 863 and 5.4 m in height and filled with 180,000 L of water [25]. The metal shell of these tanks is made
 864 from bolted together, corrugated, galvanized steel panels. The tanks are placed into 0.6 m deep

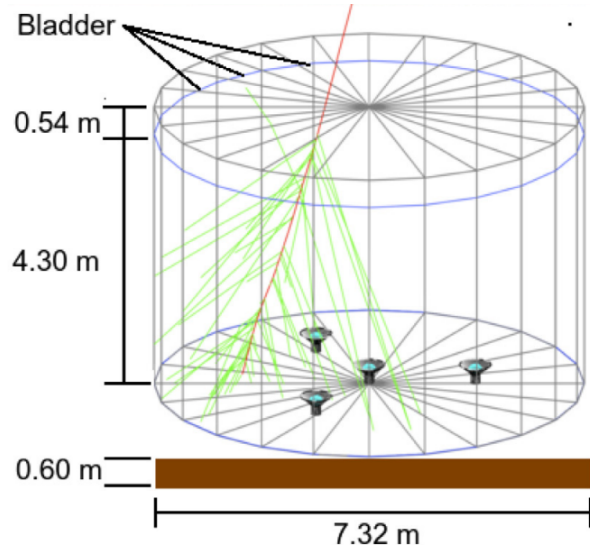


Figure 2.3 The WCDs. Left image features several WCDs looking from within the main array of HAWC. Right image shows a schematic of a WCD pulled from [25].

865 trenches filled with rammed earth to secure it against seismic activity [27]. The interior of each
 866 tank is lined with a black, low-density polyethylene bladder, designed to be impermeable to external
 867 light and to prevent reflection of Cherenkov light within the tank. This bladder is approximately 0.4
 868 mm thick and composed of two layers of three-substrate film. To further minimize light penetration,
 869 a black agricultural foil covers the bladder. The ground and walls inside the tank are protected
 870 with felt and sand to safeguard against punctures. The tanks are filled 4.5 m deep of purified water,
 871 achieving a photon attenuation length for Cherenkov photons that exceeds the tank's dimensions
 872 [27]. This purification level ensures the optimal detection environment for the photons generated
 873 by traversing charged particles.

874 At the base of each tank, four photomultiplier tubes (PMTs) are installed to detect the Cherenkov
 875 radiation emitted by charged particles in water. Three 8-inch diameter PMTs surround a larger
 876 10 inch PMT from Hamamatsu [28]. The variation in PMT response is carefully accounted for
 877 in event reconstruction algorithms. Signals from the PMTs traverse 610 ft cables to the counting
 878 house, where they are processed by Front-End Boards (FEBs), see Figs. 2.4 and 2.5. These FEBs,
 879 along with Time to Digital Converters (TDCs), digitize the signals and manage the high voltage
 880 supply to the PMTs.

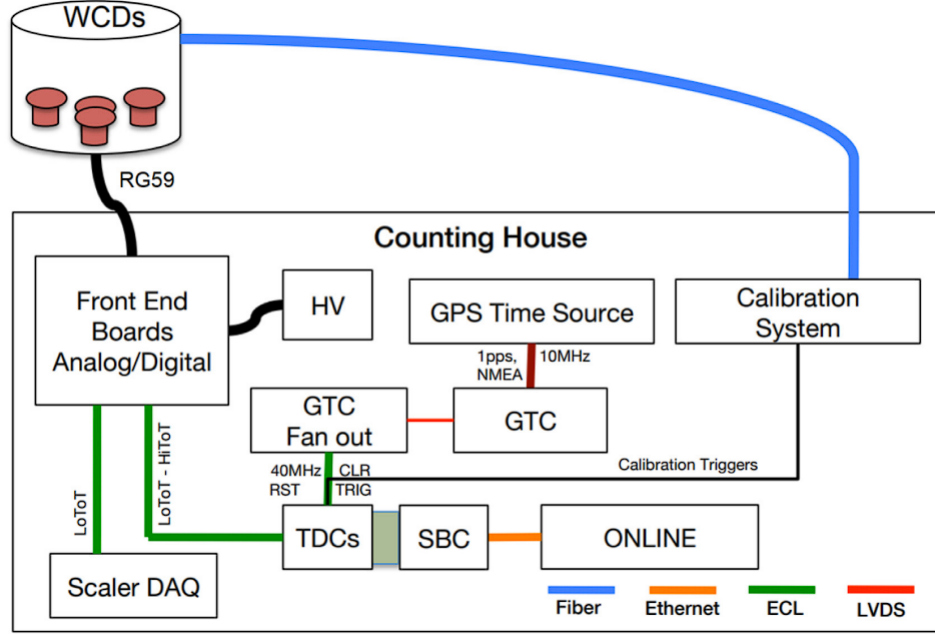


Figure 2.4 Overview of HAWC control and data electronics. The LoToT and HiToT threshold signals are discussed in Section 2.1.2. Figure from [27]

881 2.1.2 Data Acquisition and Signal Processing

882 The HAWC data acquisition (DAQ) and signal processing systems convert the physical detection
 883 of particles into analyzable data. This process involves a series of steps from initial signal detection
 884 by PMTs to digital conversion and preliminary analysis, see Figs. 2.5 and 2.6.

885 Once the signal from the PMTs arrive at the counting house, they enter the Front-End Boards
 886 (FEBs). The FEBs are responsible for the initial processing of these signals, which includes
 887 amplification and integration [30]. Each PMT signal is compared against preset LOW/HIGH
 888 voltage thresholds in the FEBs, see Fig. 2.6, identifying signals that correspond to about 1/4 and
 889 4 photoelectrons, respectively. This differentiation allows the system to gauge the strength of
 890 the detected Cherenkov radiation. The processed signals are then digitized by Time to Digital
 891 Converters (TDCs). These converters measure the time over threshold (ToT) for each signal, a
 892 parameter that reflects both the duration and amplitude of the signal. This digitization facilitates
 893 reconstruction of the original event for translating the physical interactions within the detectors into
 894 data [27, 29, 30].

895 Synchronization across the HAWC observatory is maintained by a central GPS Timing and

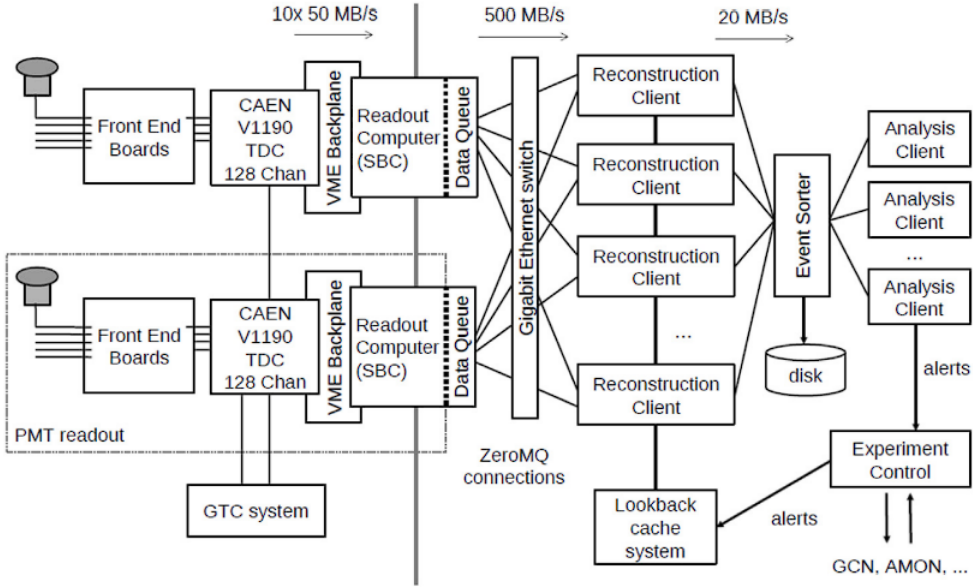


Figure 2.5 Schematic of data flow in HAWC data acquisition and online processing system. Pulled from [29].

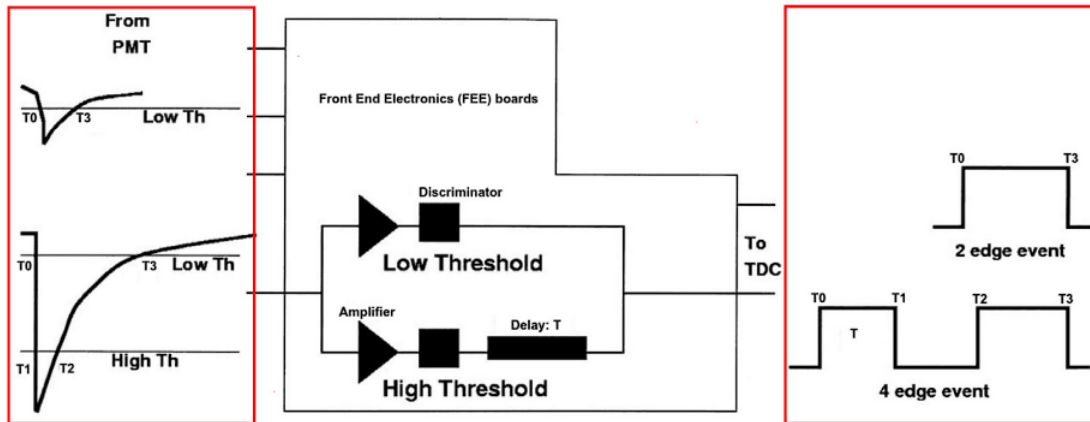


Figure 2.6 How HAWC FEB intially processes analog PMT signals. Signals are split through an amplifier and discriminator circuit. Each path is designated for either the HIGH or LOW threshold for the signal. The 2-edge event corresponds to LOW, while the 4 edge corresponds to HIGH.

896 Control (GTC) system, which achieves a timing resolution of 98 ps. This high-resolution timing
897 is vital for accurately reconstructing the timing and location of air showers initiated by cosmic
898 and gamma rays. The GTC system ensures that all components of the DAQ operate in unison to
899 preserve the temporal integrity of the detected events [27, 31].

900 Once digitized, the data are transferred to an online event reconstruction system. This system
901 runs the Reconstruction Client, which utilizes the raw PMT data to reconstruct the characteristics
902 of the air showers, such as their direction and energy [29]. The capacity for real-time analysis
903 allows HAWC to promptly respond to astrophysical phenomena like Gamma Ray Bursts (GRBs)
904 and to participate in multi-messenger astronomy by following up on alerts from other observatories.
905 This real-time processing system is designed to handle high data throughput, using ZeroMQ [32]
906 for efficient data transfer between software components. Analysis Clients perform specific online
907 analyses that require immediate data, including monitoring for GRBs, solar flare activity, and
908 participation in global efforts to track gravitational waves and neutrinos [27].

909 The DAQ system is overseen by an Experiment Control system and crew that manage the
910 operational aspects of data collection. This includes initiating and terminating data collection
911 runs and monitoring the experiment for errors. In the event of a system crash, often caused by
912 environmental factors such as lightning, the Experiment Control system is designed to automatically
913 restart the experiment and minimize downtime [27, 29].

914 2.2 Event Reconstruction

915 Event reconstruction at the HAWC Observatory is a critical procedure that converts the raw data
916 from the observatory’s WCDs into a coherent framework for understanding cosmic and gamma-
917 ray events. This process includes several distinct steps. Core Fitting determines the geometric
918 center of the air shower on the detector plane. Angle Reconstruction assesses the trajectory of the
919 incoming particle, revealing its origin in the sky. Energy Estimation is performed using both f -hit
920 and Neural Network (NN) methods to quantify the energy of the detected events. Gamma/Hadron
921 discrimination differentiates between gamma-ray and hadronic cosmic ray initiated showers, a vital
922 step for astrophysical interpretations. Each of these steps is integral to the observatory’s objective

923 of investigating the high-energy universe and enable the transformation of signals into detailed
 924 insights about high energy cosmic phenomena.

925 **2.2.1 Core Fitting**

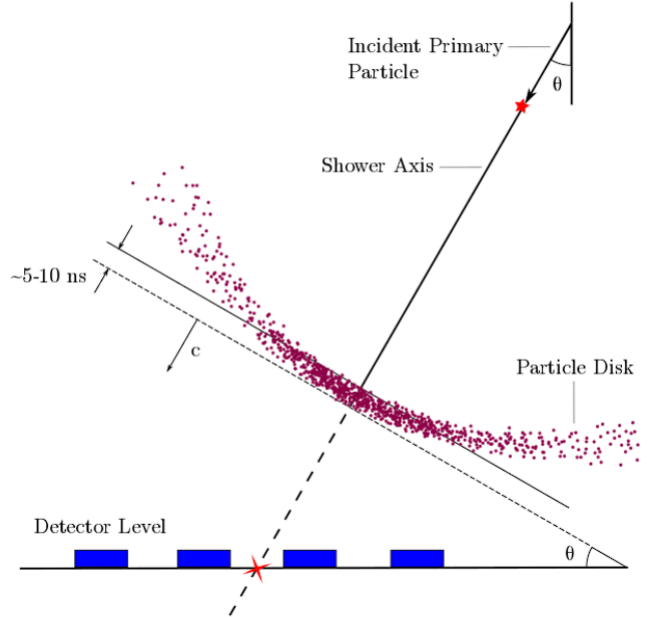


Figure 2.7 An air shower incident on WCDs. Secondary particles of an air shower travel in a cone centered on primary incident particle. Reconstruction of the initial angle is possible with arrival time of hits in PMTs inside WCDs. Figure from [33].

926 In the study of air showers, accurately determining the location of the air shower core on the
 927 ground is crucial for reconstructing the direction of the originating primary particle. An illustration
 928 of this can be seen in a HAWC event plot, Figs. 2.2 and 2.11, where the lateral charge distribution
 929 across the array is displayed. The core is identified and marked with a red star, reconstructed using
 930 a predetermined functional form, Eq. (2.1).

931 We model signal S_i from the i th PMT is given by the following equation:

$$S_i = S(A, \tilde{x}, \tilde{x}_i) = A \left(\frac{1}{2\pi\sigma^2} e^{-\frac{|\vec{x}_i - \vec{x}|^2}{2\sigma^2}} + \frac{N}{(0.5 + |\vec{x}_i - \vec{x}|/R_m)^3} \right) \quad (2.1)$$

932 In this model, \tilde{x} represents the core location and \tilde{x}_i is the position of the i th PMT. R_m stands for
 933 the Molière radius, which is approximately 120 meters at the altitude of HAWC. σ is the standard
 934 deviation of the Gaussian distribution. N is the normalization factor for the tail of the distribution.

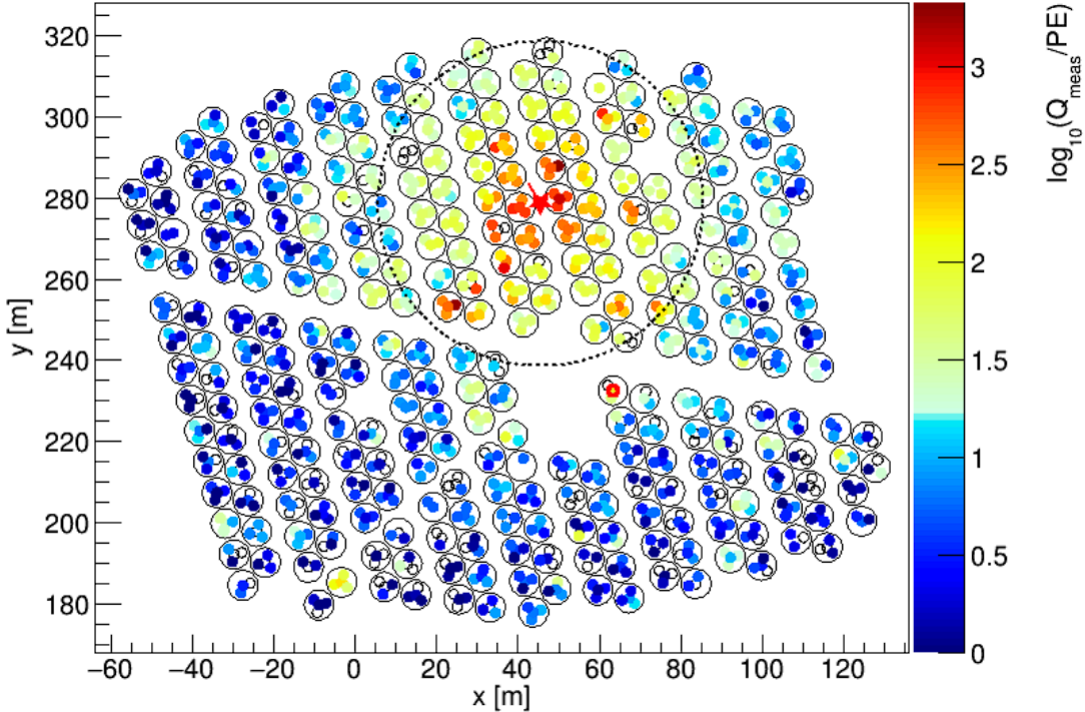


Figure 2.8 Charge deposition in each PMT for a reconstructed gamma-ray event. WCDs are outlined in black surrounding the 4 smaller circles that represent PMTs. The color scale indicates the charge deposition in each PMT. The best shower core fit from SFCF is noted with a red star in the center of the dashed circle [34].

935 The equation incorporates fixed values of $\sigma = 10$ m and $N = 5 \cdot 10^{-5}$. This leaves the core location
 936 and overall amplitude A as the free parameters to be determined during fitting.

937 The chosen functional form for the Super Fast Core Fit (SFCF) algorithm is a simplified version
 938 of a modified Nishimura-Kamata-Greisen (NKG) function [35], selected for its computational
 939 efficiency which is essential for rapid fitting of air shower cores. The SFCF form allows numerical
 940 minimization to converge more quickly due to the function's simplicity, the analytical computation
 941 of its derivatives, and the absence of a pole at the core location [34]. Figure 2.8 provides a
 942 visualization of a recorded event, with the plot depicting the charge recorded by each PMT as a
 943 function of the distance to the reconstructed shower core. Through the application of the SFCF,
 944 core locations can be identified with a median error of approximately 2 m for large events and about
 945 4 m for smaller ones, assuming the gamma-ray event core impacts directly upon the HAWC detector
 946 array [34]. It is noted that as the core's distance from the main array increases, the precision in

947 locating the core diminishes [34], highlighting the importance of proximity in the accuracy of core
948 reconstruction.

949 **2.2.2 Angle Reconstruction**

950 After establishing the core position, the next step is angle reconstruction. This process deter-
951 mines the primary particle's trajectory. The angle of arrival is indicative of the originating gamma
952 ray's direction. It correlates to the cosmic source of the gamma-ray. We deduce this angle using
953 the timing of PMT hits [34].

954 The air shower's front is conically shaped, not flat. This shape arises from the travel patterns
955 of secondary particles. An event example is illustrated in Fig. 2.7. Far from the core, secondary
956 particles undergo multiple scattering. They also travel longer distances [36]. Particle sampling
957 decreases with distance from the core. This decrease results in measurable delays in arrival times
958 [36, 34]. Simulations provide a corrective measure for these effects. The correction is a function of
959 shower parameters [34]. It adjusts both curvature and sampling. The distance from the shower core
960 and the charge recorded by PMTs are crucial to this correction. A function based on simulation
961 and Crab Nebula observations is used for this purpose [34]. This curvature correction allows us to
962 fit the particle front as a plane wave.

963 Corrections lead to the χ^2 minimization step. This technique fits a plane to the timing data of
964 the PMTs. It then calculates the shower's angle of arrival. The zenith and azimuth angles are the
965 results of this fit [36]. The local angles are converted to celestial coordinates. These coordinates
966 allow correlation with gamma-ray sources. Right ascension (RA) and declination (Dec) are used
967 for this purpose. RA is akin to longitude, and Dec to latitude.

968 The reconstructed angle's resolution ranges from 0.1° to 1° . This range depends on the incoming
969 particle's energy and zenith angle [36]. The analysis uses a curvature/sampling correction. This
970 correction applies a quadratic function based on distance from the core [34]. The adjustment
971 improves angular resolution. However, discrepancies between simulation and observation persist.
972 These discrepancies introduce systematic errors into HAWC analyses [34].

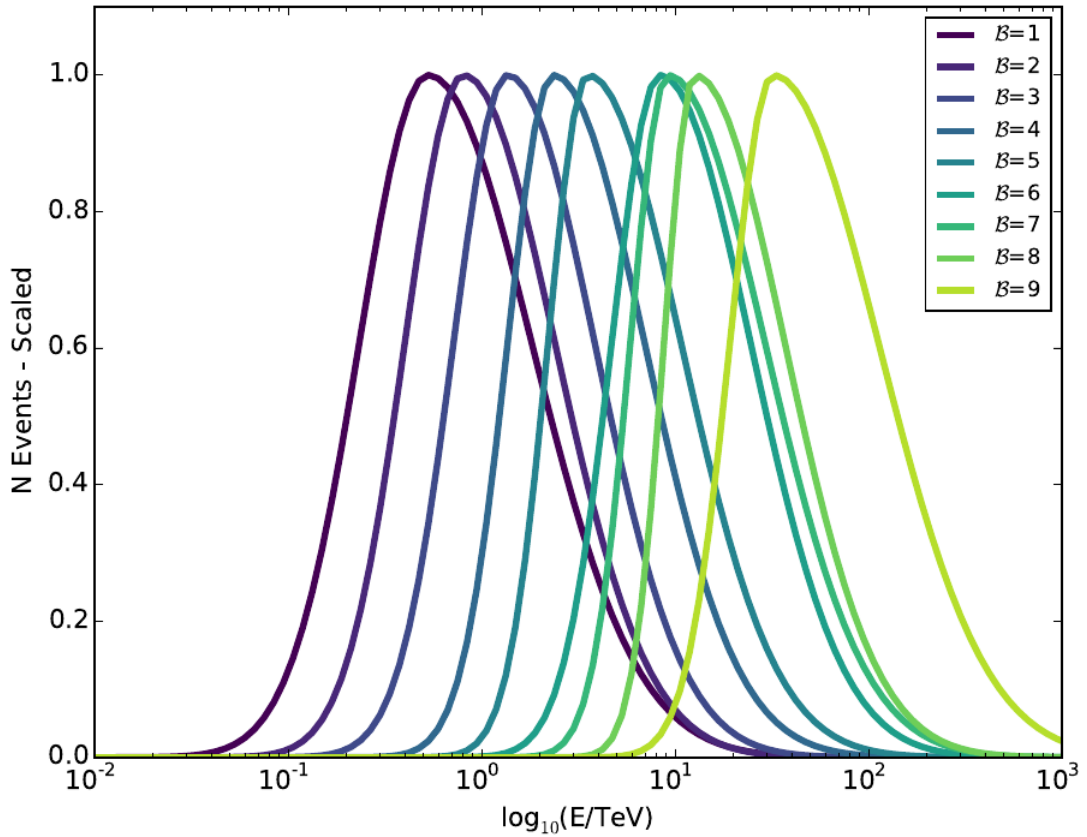


Figure 2.9 Simulated normalized energy distribution of each f_{hit} bin defined in Tab. 2.1. Monte Carlo simulation of gamma-rays with $E^{-2.63}$ spectral shape and simulated source at 20° declination. Figure from [34].

Bin	Lower Edge %	Upper Edge %	Θ_{68} ($^\circ$)
1	6.7	10.5	1.05
2	10.5	16.2	0.69
3	16.2	24.7	0.50
4	24.7	35.6	0.39
5	35.6	48.5	0.30
6	48.5	61.8	0.28
7	61.8	74.0	0.22
8	74.0	84.0	0.20
9	84.0	100	0.17

Table 2.1 Definitions of f_{hit} energy estimator bins. Bins are defined by the fraction of available PMTs that are triggered during an air shower event. The angular resolution, Θ_{68} , is the bin containing 68% of events [34].

973 **2.2.3 f_{hit} Energy Estimation**

974 The HAWC Observatory quantifies the primary particle energy of air showers using a metric
975 known as f_{hit} . This ratio compares the count of PMTs involved in the event reconstruction to the
976 total number of functional PMTs at the time [34]. The main array consists of about 1200 PMTs,
977 but the count may vary due to maintenance or other operational factors.

978 Events are stratified into several f_{hit} bins. Each bin corresponds to a specific range of angular
979 resolutions, enabling a structured approach to event analysis based on the extent of the shower
980 footprint, see Tab. 2.1. The f_{hit} metric, while effective, has several limitations. It is dependent on
981 the zenith angle and the spectral characteristics presumed for the observed source. The variable
982 also reaches a saturation point around 10 TeV, after which the detector's ability to discriminate
983 between higher energy levels diminishes [34]. Furthermore, the energy distribution for each f_{hit}
984 bin is notably broad, see Fig. 2.9. In response to these limitations, HAWC has developed more
985 intricate algorithms for energy estimation. These algorithms incorporate the zenith angle and
986 the distribution of charge around the shower core for a more accurate assessment of the primary
987 particle's energy, particularly at energies surpassing 10 TeV [36].

988 The relationship between f_{hit} and primary energy is complex. Atmospheric attenuation can
989 cause high-energy showers to present a smaller footprint, misrepresenting their energy in the f_{hit}
990 metric. This effect is captured in simulations that chart the actual energy distribution across f_{hit}
991 categories [36]. Such distributions vary with the declination of the source and the theoretical
992 energy spectrum used in the model.

993 **2.2.4 Neural Network Energy Estimation**

994 The energy estimation for photon events at the HAWC Observatory is refined through an
995 artificial neural network (NN) algorithm. This method, based on the Toolkit for Multivariate
996 Analysis NN, adopts a multilayer-perceptron model with logistic activation functions across its
997 layers. The structure includes two hidden layers, the first with 15 nodes and the second with 14,
998 designed to process input variables through a neural network optimized to estimate primary particle
999 energies [38].

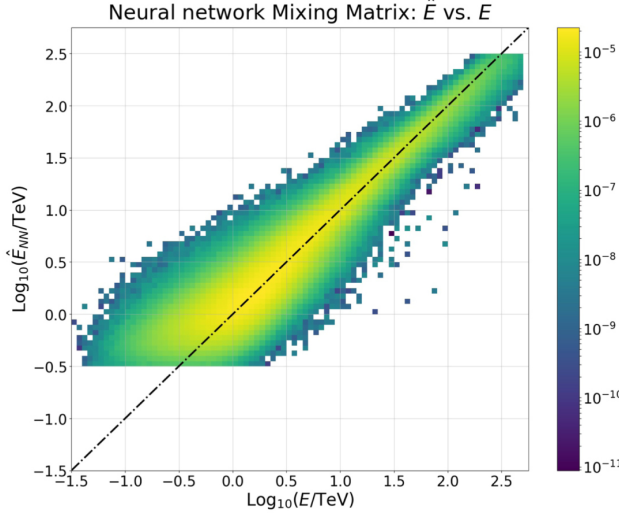


Figure 2.10 Neural Network energy estimator performance compared to true energy. The dotted line is the identity line where the estimator and injection agree. Gamma/hadron separation cuts were applied with the energy estimation. Figure pulled from [37]

1000 The NN is trained to minimize a specific error function that measures discrepancies between the
 1001 NN's energy predictions and the actual energies from Monte Carlo simulations. This minimization
 1002 targets an error function that incorporates the relative importance of each event, weighting more
 1003 the importance to mimic an E^{-2} power law spectrum. This approach helps achieve a uniform
 1004 error rate across energies ranging from 1 to 100 TeV. The optimization process leverages the
 1005 Broyden-Fletcher-Goldfarb-Shanno algorithm that calibrates the NN's 479 weights [37].

1006 The spectral analysis employs a binned likelihood method, using a forward-folding technique
 1007 to accommodate the energy estimate's bias and resolution [37]. This establishes a 2D binning
 1008 scheme that categorizes events by both their f_{hit} value and estimated energy. The decision to use
 1009 this scheme over a simple energy-based binning lies in the correlation between gamma/hadron
 1010 separation parameters and the angular resolution with both the size and energy of the event. The
 1011 spectrum of interest is partitioned into nine f_{hit} bins, each further divided into 12 energy bins,
 1012 spanning from 0.316 TeV to 316 TeV, encompassing a total of 108 bins [37]. However, not all
 1013 bins contribute to the final estimate. Bins with low event populations or insufficient Monte Carlo
 1014 simulation are excluded. This approach focuses on the central 99% of events by estimated energy
 1015 within each f_{hit} bin, effectively removing outliers [37].

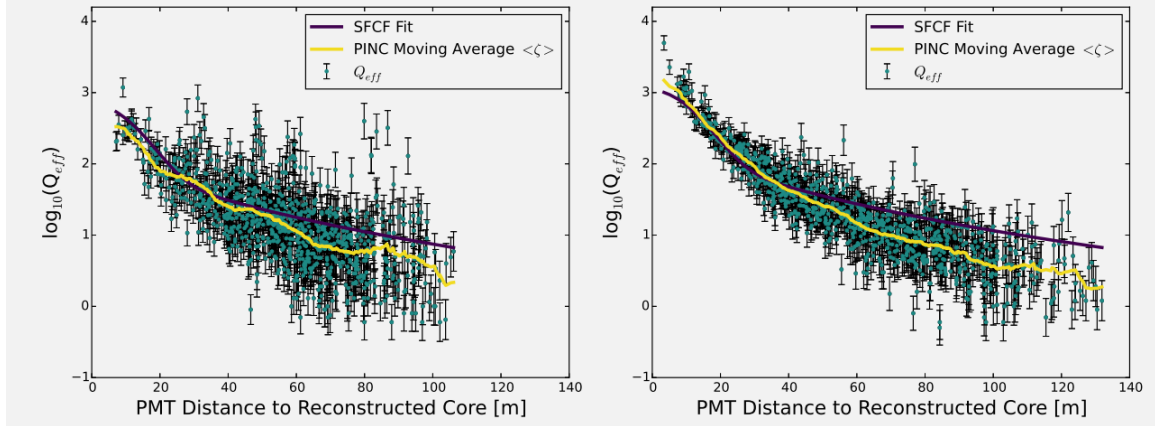


Figure 2.11 Lateral distribution functions (LDFs) for cosmic ray (left) and a photon candidate from the Crab Nebula (right). Cosmic ray LDF has clearly isolated hits far from the reconstructed shower core. Gamma-ray shower shows a more cuspy event [34].

1016 Input variables for the NN are selected to capture key characteristics of the air shower: energy
 1017 deposition, containment, and atmospheric attenuation. The algorithm calculates energy deposition
 1018 using the fraction of PMTs and tanks activated, alongside the logarithm of the normalization from
 1019 the lateral distribution fit. Containment is inferred from the distance between the shower core and
 1020 the array's center, while atmospheric attenuation is evaluated using the reconstructed zenith angle
 1021 and a detailed analysis of the shower's lateral charge distribution [38, 37].

1022 This refined NN energy estimation methodology is an integral component of HAWC's toolkit,
 1023 enabling precise analysis of high-energy gamma-ray events. It represents a significant advancement
 1024 in the field by more accurately mapping observed shower characteristics to primary particle energies.

1025 2.2.5 G/H Discrimination

1026 At the HAWC Observatory, distinguishing between air showers initiated by gamma rays and
 1027 those by hadronic cosmic rays is fundamental for astrophysical data purity. The separation process
 1028 leverages differences in shower characteristics: electromagnetic showers from gamma rays typically
 1029 display fewer muons and a smoother lateral distribution, whereas hadronic showers are more chaotic
 1030 due to the abundance of muons and hadronic sub-showers.

1031 Two primary parameters facilitate the identification of cosmic-ray events [34]:

1032 Compactness (C): This parameter evaluates the charge captured by PMTs, particularly focusing
 1033 on the PMT with the highest effective charge beyond a 40-meter radius from the shower core.

1034 Compactness is inversely proportional to this effective charge, as higher charges at extended
1035 distances from the core are indicative of hadronic showers. It is mathematically expressed as:

$$C = \frac{N_{\text{hit}}}{CxPE_{40}} \quad (2.2)$$

1036 where N_{hit} is the number of PMTs hit and $CxPE_{40}$ is the effective charge measured outside a 40 m
1037 radius from the shower cores [34].

1038 PINCness (P): PINCness quantifies the "clumpiness" of a shower using the charges recorded
1039 by PMTs and is short for Parameter for Identifying Nuclear Cosmic Rays. It is computed from the
1040 logarithm of the effective charge, $Q_{\text{eff},i}$, of each PMT hit, i , compared to an expected average for
1041 that annular region. A higher PINCness suggests a less smooth distribution, typical of hadronic
1042 showers. The formula is:

$$P = \frac{1}{N} \sum_{i=0}^N \frac{(\zeta_i - \langle \zeta \rangle)^2}{\sigma_{\zeta_i}^2} \quad (2.3)$$

1043 where $\zeta_i = \log_{10}(Q_{\text{eff},i})$. The average, $\langle \zeta \rangle$ is the average over an annular region surrounding the
1044 shower core. The errors, σ_{ζ_i} , are computed and allocated from gamma-ray candidates close to the
1045 Crab.

1046 These parameters are tested and modeled in simulations and with observational data near the
1047 Crab Nebula. Figure 2.11 illustrating the lateral distributions for representative cosmic-ray and
1048 photon candidate showers, as well as the distribution of these discrimination parameters, affirm
1049 their efficacy [34].

1050 The discrimination technique has remained consistent, but cut values have been reoptimized
1051 for the 2D bins based on f_{hit} and NN estimated energy. This refinement enhances the selection
1052 of high-energy events. Each bin ensures at least 50% efficiency for gamma-ray detection, with
1053 efficiencies extending up to nearly 100% in certain bins [34, 37].

1054 2.3 Background Estimation: Direct Integration

1055 The ratio of cosmic rays to gamma rays can be as high as 10,000 to 1, depending on the energy.
1056 At HAWC, we confront a significant challenge even after gamma/hadron cuts: our gamma-ray data
1057 is still inundated with cosmic-ray events. To tackle this, we rely on the direct integration method

1058 developed by Milagro [39]. This method capitalizes on the cosmic rays' isotropic nature resulting
1059 from their deflection by interstellar magnetic fields.

1060 The direct integration method estimates background events by integrating over a stable two-
1061 hour period of detector operation. The expected number of background events at a particular sky
1062 coordinate (ϕ, θ) is determined by integrating the normalized detector's efficiency with the all-sky
1063 event rate:

$$N_{\text{exp}}(\phi, \theta) = \int \int E(\text{ha}, \theta) \cdot R(t) dt \quad (2.4)$$

1064 Here, $E(\text{ha}, \theta)$, represents the detector's efficiency, which varies with local coordinates (hour angle
1065 and declination). $R(t)$ is the event rate as a function of time [39].

1066 Our background estimation is expected to falter in high-energy ranges where cosmic-ray events
1067 are less frequent due to enhanced gamma/hadron discrimination. Sparsity in our background and
1068 data also arise at the limits of HAWC's sensitivity and during short-term analyses of transient events.
1069 HAWC addresses these issues by using a pixel size of 0.5° in our direct integration to maintain
1070 robustness in our estimation [34, 36]. In constructing the background model, it's crucial to exclude
1071 areas of the sky with known gamma-ray sources. Regions containing the Crab Nebula, Mrk 421,
1072 Mrk 501, and the Galactic Plane are masked to prevent their significant gamma-ray signals from
1073 biasing our background estimate [34].

CHAPTER 3

GLORY DUCK: MULTI-WAVELENGTH SEARCH FOR DARK MATTTER ANNIHILATION TOWARDS DWARF SPHEROIDAL GALAXIES

3.1 Introduction

The field of astrophysics now has several instruments and observatories sensitive to high energy gamma-rays. The energy sensitivity for the modern gamma-ray program spans many orders of magnitude. Figure 3.1 demonstrates these comparable sensitivities across energies for the five experiments: Fermi-LAT, HAWC, HESS, MAGIC, and VERITAS.

Each of the five experiments featured in Figure 3.1 have independently searched for DM annihilation from dwarf spheroidal galaxies (dSph) and set limits on annihilation cross-section of WIMPs. Intriguingly, there are regions of substantial overlap in their energy sensitivities. This clearly motivates an analysis that combines data from these five. Each experiment has unique gamma-ray detection methods and their weaknesses and strengths can be leveraged with each other. The HAWC gamma-ray observatory is extensively introduced in chapter 2, so it is not introduced here. A brief description of the remaining experiments are in the following paragraphs.

The Large Area Telescope (LAT) is a pair conversion telescope mounted on the NASA Fermi satellite in orbit \sim 550 km above the Earth [41]. LAT's field of view covers about 20% of the whole sky, and it sweeps the whole sky approximately every 3 hours. LAT's gamma-ray energy sensitivity ranges from 20 MeV up to 1 TeV. Previous DM searches towards dSphs using Fermi-LAT are published in [42] and [43].

The High Energy Spectroscopic System (HESS), Major Atmospheric Gamma Imaging Cherenkov (MAGIC), and Very Energetic Radiation Imaging Telescope Array System (VERITAS) are arrays of Imaging Atmospheric Cherenkov Telescopes (IACT). These telescopes observe the Cherenkov light emitted from gamma-ray showers in the Earth's atmosphere. The field of view for these telescopes is no larger than 5° with energy sensitivities ranging from 30 GeV up to 100 TeV [44, 45, 46]. IACTs are able to make precise observations in selected regions of the sky, however can only be operated in ideal dark conditions. HESS's observations of the dwarves

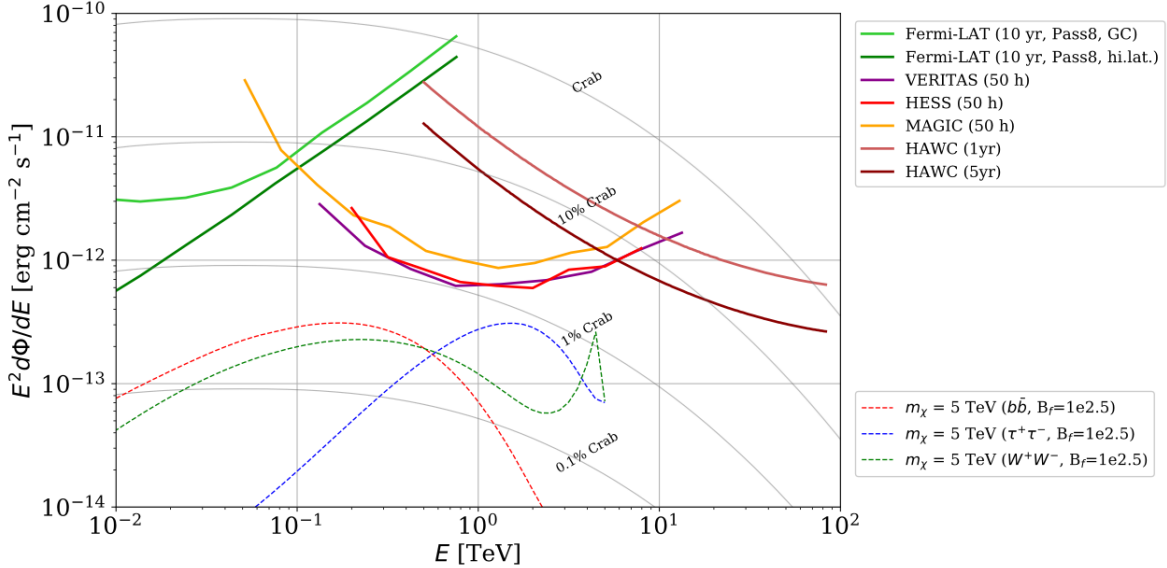


Figure 3.1 Sensitivities of five gamma-ray experiments compared to percentages of the Crab nebula’s emission and dark matter annihilation. Solid lines present estimated sensitivities to power law spectra [FACT CHECK THIS] for each experiment. Green lines are Fermi-LAT sensitivities where lighter green is the sensitivity to the galactic center and dark green is its sensitivity to higher declinations. Orange, red, and purple solid lines represent the MAGIC, HESS, and VERITAS 50 hour sensitivities respectively. The maroon and brown lines are the HAWC 1 year and 5 year sensitivities. Across four decades of gamma-ray energy, these experiments have similar sensitivities on the order 10^{-12} erg $\text{cm}^{-2}\text{s}^{-1}$. The dotted lines are estimated dark matter fluxes assuming $m_\chi = 5$ TeV DM annihilating to bottom quarks (red), tau leptons (blue), and W bosons (green). Faded gray lines outline percentage flux of the Crab nebula. Figure is an augmented version of [40]

1100 Sculptor and Carina were between January 2008 and December 2009. HESS’s observations of
 1101 Coma Berenices were taken from 2010 to 2013, and Fornax was observed in 2010 [47, 48, 49].
 1102 MAGIC provided deep observations of Segue1 between 2011 and 2013 [50]. MAGIC also provides
 1103 data for three additional dwarves: Coma Berenices, Draco, and Ursa Major II where observations
 1104 were made in: January - June 2019 [51], March - September 2018 [51], and 2014 - 2016 [52]
 1105 respectively. VERITAS provided data for Boötes I, Draco, Segue 1, and Ursa Minor from 2009 to
 1106 2016 [53].

1107 This chapter presents the Glory Duck analysis, the name given for the search for dark matter
 1108 annihilation from dSph by combining data from the five gamma-ray observatories: Fermi-LAT,
 1109 HAWC, HESS, MAGIC, and VERITAS. Specifically, the methods in analysis and modeling are
 1110 presented for the HAWC gamma-ray observatory. This work will be published in the Journal of

1111 Cosmology and Astroparticle Physics and presented at the International Cosmic Ray Conference
1112 in 2019, 2021, and 2023 [54, 55, 56] and others.

1113 **3.2 Dataset and Background**

1114 This section enumerates the data analysis and background estimation methods used for HAWC's
1115 study of dSphs. Section 3.2.1 and Section 3.2.2 are most useful for fellow HAWC collaborators
1116 looking to replicate the Glory Duck analysis.

1117 **3.2.1 Itemized HAWC files**

1118 These files are only available withing HAWC's internal documentation and collaborators. They
1119 are not meant for public access, and are presented here so that HAWC collaborators can reproduce
1120 results accurately.

- 1121 • Detector Response: `response_aerie_svn_27754_systematics_best_mc_test_noBr`
1122 `oadpulse\10pctlogchargesmearing_0.63qe_25kHzNoise_run5481_curvature`
1123 `0_index3.root`
- 1124 • Data Map: `maps-20180119/liff/maptree_1024.root`
- 1125 • Spectral Dictionary: `DM_CirrelliSpectrum_dict_gammas.npy`
- 1126 • Analysis wiki: https://private.hawc-observatory.org/wiki/index.php/Glory_Duck_Multi-Experiment_Dark_Matter_Search

1128 **3.2.2 Software Tools and Development**

1129 This analysis was performed using HAL and 3ML [34, 57] in Python version 2. I built software
1130 to implement the *A Poor Particle Physicist Cookbook for Dark Matter Indirect Detection* (PPPC)
1131 [58] DM spectral model and dSphs spatial model from [59] for HAWC analysis. A NumPy version
1132 of this dictionary was made for both Py2 and Py3. The code base for creating this dictionary is
1133 linked on my GitLab sandbox:

- 1134 • Py2: [Dictionary Generator \(Deprecated\)](#)

- 1135 • Py3: [PPPC2Dict](#)

1136 The analysis was performed using the f_{hit} framework as used and described in the HAWC Crab
1137 paper [34]. The Python2 NumPy dictionary file for gamma-ray final states is `dmCirSpecDict.npy`.
1138 The corresponding Python3 file is `DM_CirrelliSpectrum_dict_gammas.npy`. These files can
1139 also be used for decay channels and the PPPC describes how [58]. All other software used for data
1140 analysis, DM profile generation, and job submission to SLURM are also kept in my sandbox for
1141 [the Glory Duck](#) project.

1142 **3.2.3 Data Set and Background Description**

1143 The HAWC data maps used for this analysis contain 1017 days of data between runs 2104
1144 (2014-11-26) and 7476 (2017-12-20). They were generated from pass 4.0 reconstruction. The
1145 analysis is performed using the f_{hit} energy binning scheme with bins (1-9) similar to what was done
1146 for the Crab and previous HAWC dSph analysis [34, 60]. Bin 0 was excluded as it has substantial
1147 hadronic contamination and poor angular resolution.

1148 This analysis was done on dSphs because of their large DM mass content relative to baryonic
1149 mass. We consider the following to estimate the background to this study.

- 1150 • The dSphs' angular extent are small relative to HAWC's spatial resolution, so the analysis is
1151 not sensitive to large or small scale anisotropies.
- 1152 • The dSphs used in this analysis are off the galactic plane and therefore not contaminated by
1153 diffuse emission from the galaxy.
- 1154 • The dSphs are baryonically faint relative to their expected dark matter content and are not
1155 expected to contain high energy gamma-ray sources.

1156 Therefor we make no additional assumptions on the background from our sources and use
1157 HAWC's standard direct integration method for background estimation [34]. The largest background
1158 under this consideration is from an isotropic flux of cosmic rays. The contamination of this hadronic
1159 flux is worse at lower energies where HAWC's gamma/hadron discrimination worse. It is possible

1160 for gamma rays from DM annihilation to scatter in transit to HAWC via Inverse Compton Scattering
1161 (ICS). This was investigated and its impact on the flux is negligible. Supporting information on
1162 this is in Section 3.7.1

1163 **3.3 Analysis**

1164 The expected differential photon flux from DM-DM annihilation to standard model particles,
1165 $d\Phi_\gamma/dE_\gamma$, over solid angle, Ω , is described by the familiar equation.

$$\frac{d\Phi_\gamma}{dE_\gamma} = \frac{\langle\sigma v\rangle}{8\pi m_\chi^2} \frac{dN_\gamma}{dE_\gamma} \times \int_{\text{source}} d\Omega \int_{l.o.s} dl \rho_\chi^2 J(r, \theta') \quad (3.1)$$

1166 Where $\langle\sigma v\rangle$ is the velocity weighted annihilation cross-section. $\frac{dN}{dE}$ is the expected differential
1167 number of photons produced at each energy per annihilation. m_χ is the rest mass of the supposed
1168 DM particle. ρ_χ is the DM density. J is the astrophysical J-factor and is defined as

$$J = \int d\Omega \int_{l.o.s} dl \rho_\chi^2(r, \theta') \quad (3.2)$$

1169 l is the distance to the source from Earth. r is the radial distance from the center of the source. θ' is
1170 the half angle defining a cone containing the DM source. How each component is synthesized and
1171 considered for HAWC's analysis is presented in the following sections. Section 3.3.1 presents the
1172 particle physics model for DM annihilation. Section 3.3.2 presents the spatial distributions built
1173 for each dSph.

1174 **3.3.1 $\frac{dN_\gamma}{dE_\gamma}$ - Particle Physics Component**

1175 For these spectra, we import the PPPC with Electroweak (EW) corrections [58]. Public versions
1176 of the imported tables are provided by the [authors online](#). The spectrum is implemented as a model
1177 script in astromodels for 3ML. The EW corrections were previously not considered for HAWC and
1178 are significant for DM annihilating to EW coupled SM particles such as all leptons, and the γ ,
1179 Z , and W bosons [60]. Figure 3.2 demonstrates the significance of EW corrections for W boson
1180 annihilation. Across EW SM channels, the gamma-ray spectra become harder than spectra without
1181 EW corrections. Tables from the PPPC were reformatted into Python NumPy dictionaries for
1182 collaboration-wide use. A class in astromodels was developed to include the EW correction from
1183 the PPPC and is aptly named `PPPCSpectra` within `DM_models.py`.

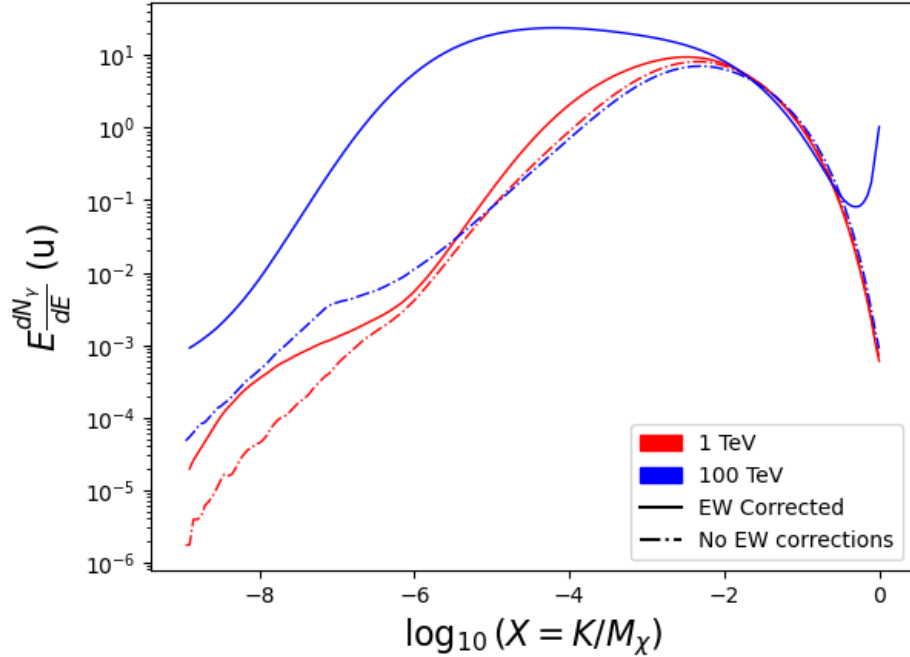


Figure 3.2 Effect of Electroweak (EW) corrections on expected DM annihilation spectrum for $\chi\chi \rightarrow W^-W^+$. Solid lines are spectral models that consider EW corrections. Dash-dot lines are spectral models without EW corrections. Red lines are models for $M_\chi = 1$ TeV. Blue lines represent models for $M_\chi = 100$ TeV. All models are sourced from the PPPC4DMID [58].

1184 3.3.2 J- Astrophysical Component

1185 The J-factor profiles for each source are imported from Geringer-Sameth (referred to with \mathcal{GS})

1186 [59]. \mathcal{GS} fits the Zhao DM profile to the dSphs which has a DM density described as [61]

$$\rho(r) = \frac{\rho_0}{(r/R_s)^\gamma (1 + (r/R_s)^\alpha)^{(\beta-\gamma)}}. \quad (3.3)$$

1187 R_s is the scale radius and free parameter in the model. γ is the logarithmic slope in the region

1188 $r \ll R_s$. β is the logarithmic slope in the region $r \gg R_s$. α is known as the sharpness of transition

1189 where $r \approx R_s$. The classic Navarro-Frenk-White [62] (NFW) can be retrieved from Zhao by fixing

1190 $(\alpha, \beta, \gamma) = (1, 3, 1)$.

1191 \mathcal{GS} best fits were pulled from the publication as $J(\theta)$, where θ is the angular separation from

1192 the center of the source. HAWC requires maps in terms of $\frac{dJ}{d\Omega}$, so the conversion from the maps

1193 was done in the following way...

1194 First, convert the angular distances to solid angles

$$\Omega = 2 \cdot \pi(1 - \cos(\theta)) \quad (3.4)$$

1195 which reduces with a small angle approximation to $\pi\theta^2$. Next, the central difference for both the
1196 ΔJ and $\Delta\Omega$ value were calculated from the discretized $J(\theta)$ with the central difference stencil:

$$\Delta\phi_i = \phi_{i+1} - \phi_{i-1} \quad (3.5)$$

1197 Where ϕ is either Ω or J . These were done separately in case the grid spacing in θ was not uniform.
1198 Finally, these lists are divided so that we are left with an approximation of the $dJ/d\Omega$ profile that
1199 is a function of θ . Admittedly, this is an approximation method for the map which introduces small
1200 errors compared to the true profile estimate. This was checked as a systematic against the author's
1201 profiling of the spatial distribution and is documented in Section 3.8.1.

1202 With $\frac{dJ}{d\Omega}(\theta)$, a map is generated, first by filling in the north-east quadrant of the map. This
1203 quadrant is then reflected twice, vertically then horizontally, to fill the full map. Maps are then
1204 normalized by dividing the discrete 2D integral of the map. The 2D integral was a simple height
1205 of bins, Newton's integral:

$$p^2 \cdot \sum_{i,j=0}^{N,M} \frac{dJ}{d\Omega}(\theta_{i,j}, \phi_{i,j}) \quad (3.6)$$

1206 These maps are HEALpix maps with NSIDE 16384 and saved in the .fits format. The hyper fine
1207 resolution was selected to better preserve the total expected counts after integrating Eq. (3.1) with
1208 the detector response.

1209 Another DM spatial distribution model from Bonnivard (\mathcal{B}) [63] was used for the Glory Duck
1210 study. However, to save computational time, limits from \mathcal{GS} were scaled to \mathcal{B} instead of each
1211 experiment performing a full study a second time. How these models compare is demonstrated
1212 for each dSph in Figure 3.16 and Figure 3.17 Plots of these maps are provided for each source
1213 in chapter A Examples of the two most impactful dSphs derived from \mathcal{GS} , Segue1 and Coma
1214 Berenices are featured in Figure 3.3

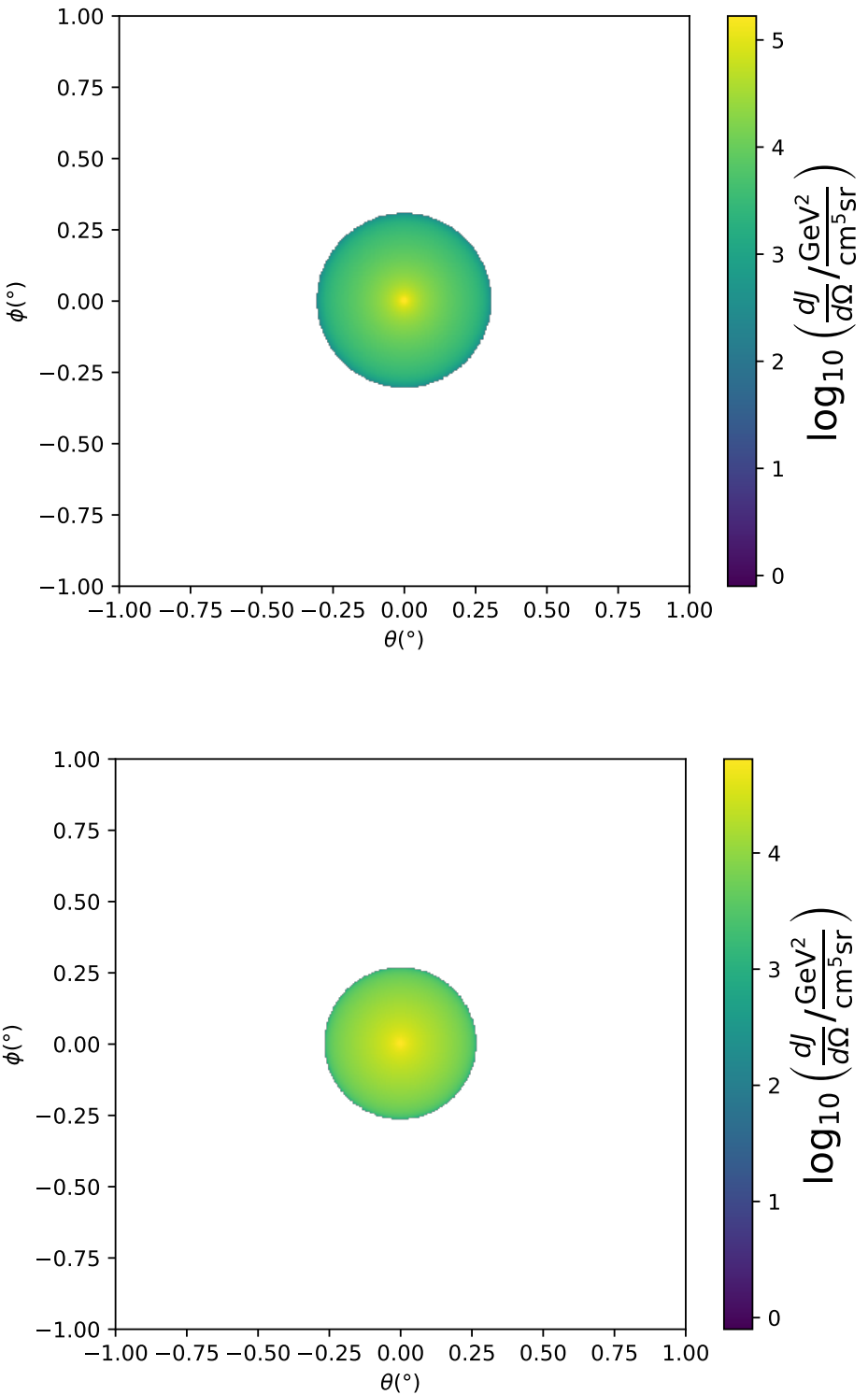


Figure 3.3 $\frac{dJ}{d\Omega}$ maps for Segue1 (top) and Coma Berenices (bottom). Origin is centered on the specific dwarf spheroidal galaxies (dSph). X and Y axes are the angular separation from the center of the dwarf. Profile is truncated at the scale radius. Plots of the remaining 11 dSph HAWC studied are linked in Fig. A.1.

1215 **3.3.3 Source Selection and Annihilation Channels**

1216 We use many of the dSphs presented in HAWC’s previous dSph DM search [60]. HAWC’s
1217 sources for Glory Duck include Boötes I, Coma Berenices, Canes Venatici I + II, Draco, Hercules,
1218 Leo I, II, + IV, Segue 1, Sextans, and Ursa Major I + II. A full description of all sources used
1219 in Glory Duck is found in Table 3.1. Triangulum II was excluded from the Glory Duck analysis
1220 because of large uncertainties in its J factor. Ursa Minor was excluded from HAWC’s contribution
1221 to the combination because the source extension model extended Ursa Minor beyond HAWC’s field
1222 of view. Ursa Minor was not expected to contribute significantly to the combined limit, so work
1223 was not invested in a solution to include Ursa Minor.

1224 This analysis improves on the previous HAWC dSph paper [60] in the following ways. Pre-
1225 viously, the dSphs were treated and implemented as point sources. For this analysis, dSphs are
1226 modeled and treated as extended source. The impact of this change with respect to the upper limit
1227 is source dependent and is explored in Section 3.7.2. Previously, the particle physics model used for
1228 gamma-ray spectra from DM annihilation did not have EW corrections where the PPPC includes
1229 them. Finally, the gamma-ray ray dataset is much larger. The study performed here analyzes over
1230 1000 days of data compared to 507.

1231 The SM annihilation channels probed for the Glory Duck combination include $b\bar{b}$, $e\bar{e}$, $\mu\bar{\mu}$, $\tau\bar{\tau}$,
1232 $t\bar{t}$, W^+W^- , and ZZ . A summary of all sources, with a description of each experiments’ sensitivity
1233 to the source, is provided in Table 3.2.

1234 **3.4 Likelihood Methods**

1235 **3.4.1 HAWC Likelihood**

1236 For every analysis bin in energy, f_{hit} bins (1-9), and location, we can expect N signal events and
1237 B background events. The expected number of excess signal events from dark matter annihilation,
1238 S , is estimated by convolving Equation (3.1) with HAWC’s energy response and pixel point spread
1239 functions. I then compute the test statistic (TS) with the log-likelihood ratio test,

$$TS_{\max} = -2 \ln \left(\frac{\mathcal{L}_0}{\mathcal{L}_{\max}} \right) \quad (3.7)$$

Table 3.1 Summary of the relevant properties of the dSphs used in the present work. Column 1 lists the dSphs. Columns 2 and 3 present their heliocentric distance and galactic coordinates, respectively. Columns 4 and 5 report the J -factors of each source given from the \mathcal{GS} and \mathcal{B} independent studies and their estimated $\pm 1\sigma$ uncertainties. The values $\log_{10} J$ (\mathcal{GS} set) [59] correspond to the mean J -factor values for a source extension truncated at the outermost observed star. The values $\log_{10} J$ (\mathcal{B} set) [63] are provided for a source extension at the tidal radius of each dSph. **Bolded sources are within HAWC's field of view and provided to the Glory Duck analysis.**

Name	Distance (kpc)	l, b ($^{\circ}$)	$\log_{10} J$ (\mathcal{GS} set) $\log_{10}(\text{GeV}^2\text{cm}^{-5}\text{sr})$	$\log_{10} J$ (\mathcal{B} set) $\log_{10}(\text{GeV}^2\text{cm}^{-5}\text{sr})$
Boötes I	66	358.08, 69.62	$18.24^{+0.40}_{-0.37}$	$18.85^{+1.10}_{-0.61}$
Canes Venatici I	218	74.31, 79.82	$17.44^{+0.37}_{-0.28}$	$17.63^{+0.50}_{-0.20}$
Canes Venatici II	160	113.58, 82.70	$17.65^{+0.45}_{-0.43}$	$18.67^{+1.54}_{-0.97}$
Carina	105	260.11, -22.22	$17.92^{+0.19}_{-0.11}$	$18.02^{+0.36}_{-0.15}$
Coma Berenices	44	241.89, 83.61	$19.02^{+0.37}_{-0.41}$	$20.13^{+1.56}_{-1.08}$
Draco	76	86.37, 34.72	$19.05^{+0.22}_{-0.21}$	$19.42^{+0.92}_{-0.47}$
Fornax	147	237.10, -65.65	$17.84^{+0.11}_{-0.06}$	$17.85^{+0.11}_{-0.08}$
Hercules	132	28.73, 36.87	$16.86^{+0.74}_{-0.68}$	$17.70^{+1.08}_{-0.73}$
Leo I	254	225.99, 49.11	$17.84^{+0.20}_{-0.16}$	$17.93^{+0.65}_{-0.25}$
Leo II	233	220.17, 67.23	$17.97^{+0.20}_{-0.18}$	$18.11^{+0.71}_{-0.25}$
Leo IV	154	265.44, 56.51	$16.32^{+1.06}_{-1.70}$	$16.36^{+1.44}_{-1.65}$
Leo V	178	261.86, 58.54	$16.37^{+0.94}_{-0.87}$	$16.30^{+1.33}_{-1.16}$
Leo T	417	214.85, 43.66	$17.11^{+0.44}_{-0.39}$	$17.67^{+1.01}_{-0.56}$
Sculptor	86	287.53, -83.16	$18.57^{+0.07}_{-0.05}$	$18.63^{+0.14}_{-0.08}$
Segue I	23	220.48, 50.43	$19.36^{+0.32}_{-0.35}$	$17.52^{+2.54}_{-2.65}$
Segue II	35	149.43, -38.14	$16.21^{+1.06}_{-0.98}$	$19.50^{+1.82}_{-1.48}$
Sextans	86	243.50, 42.27	$17.92^{+0.35}_{-0.29}$	$18.04^{+0.50}_{-0.28}$
Ursa Major I	97	159.43, 54.41	$17.87^{+0.56}_{-0.33}$	$18.84^{+0.97}_{-0.43}$
Ursa Major II	32	152.46, 37.44	$19.42^{+0.44}_{-0.42}$	$20.60^{+1.46}_{-0.95}$
Ursa Minor	76	104.97, 44.80	$18.95^{+0.26}_{-0.18}$	$19.08^{+0.21}_{-0.13}$

Table 3.2 Summary of dSph observations by each experiment used in this work. A ‘-’ indicates the experiment did not observe the dSph for this study. For Fermi-LAT, the exposure at 1 GeV is given. For HAWC, $|\Delta\theta|$ is the absolute difference between the source declination and HAWC latitude. HAWC is more sensitive to sources with smaller $|\Delta\theta|$. For IACTs, we show the zenith angle range, the total exposure, the energy range, the angular radius θ of the signal or ON region, the ratio of exposures between the background-control (OFF) and signal (ON) regions (τ), and the significance of gamma-ray excess in standard deviations, σ .

Source name	Fermi-LAT	HAWC	H.E.S.S, MAGIC, VERITAS						
	Exposure (10^{11} s m 2)	$ \Delta\theta $ (°)	IACT	Zenith (°)	Exposure (h)	Energy range (GeV)	θ (°)	τ	S (σ)
Boötes I	2.6	4.5	VERITAS	15 – 30	14.0	100–41000	0.10	8.6	-1.0
Canes Venatici I	2.9	14.6	–	–	–	–	–	–	–
Canes Venatici II	2.9	15.3	–	–	–	–	–	–	–
Carina	3.1	–	H.E.S.S.	27 – 46	23.7	310 – 70000	0.10	18.0	-0.3
Coma Berenices	2.7	4.9	H.E.S.S.	47 – 49	11.4	550 – 70000	0.10	14.4	-0.4
Draco	3.8	38.1	MAGIC	5 – 37	49.5	60 – 10000	0.17	1.0	–
			MAGIC	29 – 45	52.1	70 – 10000	0.22	1.0	–
			VERITAS	25 – 40	49.8	120 – 70000	0.10	9.0	-1.0
Fornax	2.7	–	H.E.S.S.	11 – 25	6.8	230 – 70000	0.10	45.5	-1.5
Hercules	2.8	6.3	–	–	–	–	–	–	–
Leo I	2.5	6.7	–	–	–	–	–	–	–
Leo II	2.6	3.1	–	–	–	–	–	–	–
Leo IV	2.4	19.5	–	–	–	–	–	–	–
Leo V	2.4	–	–	–	–	–	–	–	–
Leo T	2.6	–	–	–	–	–	–	–	–
Sculptor	2.7	–	H.E.S.S.	10 – 46	11.8	200 – 70000	0.10	19.8	-2.2
Segue I	2.5	2.9	MAGIC	13 – 37	158.0	60 – 10000	0.12	1.0	-0.5
			VERITAS	15 – 35	92.0	80 – 50000	0.10	7.6	0.7
Segue II	2.7	–	–	–	–	–	–	–	–
Sextans	2.4	20.6	–	–	–	–	–	–	–
Ursa Major I	3.4	32.9	–	–	–	–	–	–	–
Ursa Major II	4.0	44.1	MAGIC	35 – 45	94.8	120 – 10000	0.30	1.0	-2.1
Ursa Minor	4.1	–	VERITAS	35 – 45	60.4	160 – 93000	0.10	8.4	-0.1

1240 where \mathcal{L}_0 is the null hypothesis, or no DM emission, likelihood. \mathcal{L}^{\max} is the best fit signal
 1241 hypothesis where $\langle\sigma v\rangle$ maximizes the likelihood. We calculate the likelihood of each source and
 1242 model, assuming events are Poisson distributed, with

$$\mathcal{L} = \prod_i \frac{(B_i + S_i)^{N_i} e^{-(B_i + S_i)}}{N_i!} \quad (3.8)$$

1244 where S_i is the sum of expected number of signal counts. B_i is the number of background counts
 1245 observed. N_i is the total number of counts.

1246 I also calculate an upper limit on $\langle\sigma v\rangle$ by calculating the 95% confidence level (CL). For the
 1247 CL, we define a parameter, TS_{95} , as

$$TS_{95} \equiv \sum_{\text{bins}} \left[2N \ln \left(1 + \frac{\epsilon S_{\text{ref}}}{B} \right) - 2\epsilon S_{\text{ref}} \right] \quad (3.9)$$

1248 where the expected signal counts from a dSph is scaled by ϵ . S_{ref} is the expected number of excess
 1249 counts in a bin from DM emission from a dSph with a corresponding annihilation cross-section,
 1250 $\langle\sigma v\rangle$. We scan ϵ such that

$$2.71 = TS_{\max} - TS_{95} \quad (3.10)$$

1251 HAWC's exclusive results are provided in Section 3.5.

1252 3.4.2 Glory Duck Joint Likelihood

1253 The joint likelihood for the 5-experiment combination was done similarly as Section 3.4.1. We
 1254 calculate upper limits on $\langle\sigma v\rangle$ from the TS, Eq. (3.7), and define the likelihood ratio more generally

$$\lambda(\langle\sigma v\rangle | \mathcal{D}_{\text{dSphs}}) = \frac{\mathcal{L}(\langle\sigma v\rangle; \hat{\nu} | \mathcal{D}_{\text{dSphs}})}{\mathcal{L}(\widehat{\langle\sigma v\rangle}; \hat{\nu} | \mathcal{D}_{\text{dSphs}})} \quad (3.11)$$

1255 $\mathcal{D}_{\text{dSphs}}$ is the totality of observations across experiments and dSphs. ν are the nuisance parameters
 1256 which are the J factors in this study. $\widehat{\langle\sigma v\rangle}$ and $\hat{\nu}$ are the respective estimate that maximize \mathcal{L}
 1257 globally. Finally, $\hat{\nu}$ is the set of nuisance parameters that maximize \mathcal{L} for a fixed value of $\langle\sigma v\rangle$.

1258 The *complete* joint likelihood, \mathcal{L} that encompasses all observations from all instruments and
 1259 dSphs can be factorized into *partial* functions for each dSph l (with $\mathcal{L}_{\text{dSph},l}$) and its J factor (\mathcal{J}_l):

$$\mathcal{L}(\langle\sigma v\rangle; \nu | \mathcal{D}_{\text{dSphs}}) = \prod_{l=1}^{N_{\text{dSphs}}} \mathcal{L}_{\text{dSph},l}(\langle\sigma v\rangle; J_l, \nu_l | \mathcal{D}_l) \times \mathcal{J}_l(J_l | J_{l,\text{obs}}, \sigma_{\log J_l}). \quad (3.12)$$

1260 For this study, $N_{\text{dSphs}} = 20$ is the number of dSphs studied. \mathcal{D}_l are the gamma-ray observations
 1261 of dSph, l . ν_l are the nuisance parameters modifying the gamma-ray observations of dSph, l ,
 1262 but excludes \mathcal{J}_l . \mathcal{J}_l is the J factor for dSph, l , as defined in Equation (3.2), and it is a nuisance
 1263 parameter whose value is unknown. $\log_{10} J_{l,\text{obs}}$ and $\sigma_{\log J_l}$ are obtained by fitting a log-normal
 1264 function of $J_{l,\text{obs}}$ to the posterior distribution of J_l [64]. $\log_{10} J_{l,\text{obs}}$ and $\sigma_{\log J_l}$ values are provided
 1265 in Table 3.1. The term \mathcal{J}_l constraining J_l is written as:

$$\mathcal{J}_l(J_l | J_{l,\text{obs}}, \sigma_{\log J_l}) = \frac{1}{\ln(10)J_{l,\text{obs}}\sqrt{2\pi}\sigma_{\log J_l}} \exp\left(-\frac{(\log_{10} J_l - \log_{10} J_{l,\text{obs}})^2}{2\sigma_{\log J_l}^2}\right). \quad (3.13)$$

1266 Both the \mathcal{GS} and \mathcal{B} , displayed in Table 3.1, sets of J factors are used in this analysis. Equation (3.13)
 1267 is also normalized, so it can also be interpreted as a probability density function (PDF) for $J_{l,\text{obs}}$.
 1268 From Equation (3.1), we can also see that $\langle\sigma v\rangle$ and J_l are degenerate when computing $\mathcal{L}_{\text{dSph},l}$.
 1269 Therefore, as noted in [65], it is sufficient to compute $\mathcal{L}_{\text{dSph},l}$ versus $\langle\sigma v\rangle$ for a fixed value of J_l .
 1270 We used $J_{l,\text{obs}}(\mathcal{GS})$ reported in Tab. 3.1, in order to perform the profile of \mathcal{L} with respect to J_l .
 1271 The degeneracy implies that for any $J'_l \neq J_{l,\text{obs}}$ (in practice in our case we used $J'_l = J_{l,\text{obs}}(\mathcal{B})$ to
 1272 compute results from a different set of J factors):

$$\mathcal{L}_{\text{dSph},l}(\langle\sigma v\rangle; J'_l, \nu_l | \mathcal{D}_l) = \mathcal{L}_{\text{dSph},l}\left(\frac{J'_l}{J_{l,\text{obs}}} \langle\sigma v\rangle; J_{l,\text{obs}}, \nu_l | \mathcal{D}_l\right), \quad (3.14)$$

1273 which is a straightforward rescaling operation that reduces the computational needs of the profiling
 1274 operation since:

$$\mathcal{L}(\langle\sigma v\rangle; \hat{\nu} | \mathcal{D}_{\text{dSphs}}) = \prod_{l=1}^{N_{\text{dSphs}}} \max_{J_l} \left[\mathcal{L}_{\text{dSph},l}(\langle\sigma v\rangle; J_l, \hat{\nu}_l | \mathcal{D}_l) \times \mathcal{J}_l(J_l | J_{l,\text{obs}}, \sigma_{\log J_l}) \right]. \quad (3.15)$$

1275 In addition, Eq. (3.14) enables the combination of data from different gamma-ray instruments and
 1276 observed dSphs via tabulated values of $\mathcal{L}_{\text{dSph},l}$, or equivalently of λ from Eq. (3.11) as was done in
 1277 this work, versus $\langle\sigma v\rangle$. $\mathcal{L}_{\text{dSph},l}$ is computed for a fixed value of J_l and profiled with respect to all
 1278 instrumental nuisance parameters ν_l , these nuisance parameters are discussed in more detail below.
 1279 These values are produced by each detector independently and therefore there is no need to share
 1280 sensitive low-level information used to produce them, such as event lists. Figure 3.4 illustrates the
 1281 multi-instrument combination technique used in this study with a comparison of the upper limit

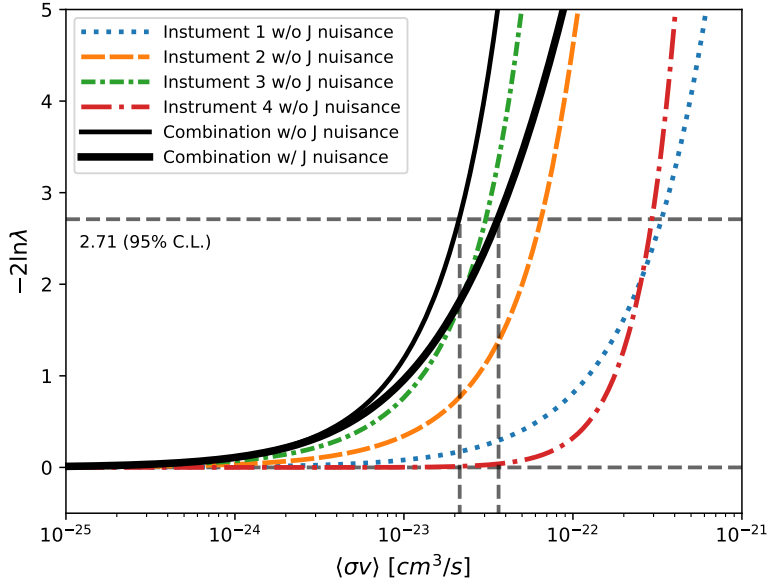


Figure 3.4 Illustration of the combination technique showing a comparison between $-2 \ln \lambda$ provided by four instruments (colored lines) from the observation of the same dSph without any J nuisance and their sum, *i.e.* the resulting combined likelihood (thin black line). According to the test statistics of Equation (3.7), the intersection of the likelihood profiles with the line $-2 \ln \lambda = 2.71$ indicates the 95% C.L. upper limit on $\langle\sigma v\rangle$. The combined likelihood (thin black line) shows a smaller value of upper limit on $\langle\sigma v\rangle$ than those derived by individual instruments. We also show how the uncertainties on the J factor effects the combined likelihood and degrade the upper limit on $\langle\sigma v\rangle$ (thick black line). All likelihood profiles are normalized so that the global minimum $\widehat{\langle\sigma v\rangle}$ is 0. We note that each profile depends on the observational conditions in which a target object was observed. The sensitivity of a given instrument can be degraded and the upper limits less constraining if the observations are performed in non-optimal conditions such as a high zenith angle or a short exposure time.

1282 on $\langle\sigma v\rangle$ obtained from the combination of the observations of four experiments towards one dSph
 1283 versus the upper limit from individual instruments. It also shows graphically the effect of the
 1284 J -factor uncertainty on the combined observations.

1285 The *partial* joint likelihood function for gamma-ray observations of each dSph ($\mathcal{L}_{\text{dSph},l}$) is
 1286 written as the product of the likelihood terms describing the $N_{\text{exp},l}$ observations performed with
 1287 any of our observatories:

$$\mathcal{L}_{\text{dSph},l} (\langle\sigma v\rangle; J_l, \nu_l | \mathcal{D}_l) = \prod_{k=1}^{N_{\text{exp},l}} \mathcal{L}_{lk} (\langle\sigma v\rangle; J_l, \nu_{lk} | \mathcal{D}_{lk}), \quad (3.16)$$

1288 where each \mathcal{L}_{lk} term refers to an observation of the l -th dSph with associated k -th instrument

1289 responses. $N_{\text{exp},l}$ varies from dSph to dSph and can be inferred from Table 3.2.

1290 Each collaboration separately analyzes their data for \mathcal{D}_{lk} corresponding to dSph l and gamma-
 1291 ray detector k , using as many common assumptions as possible in the analysis. HAWC's treatment
 1292 was described earlier in Section 3.4.1 whereas the specifics of the remaining experiments is left to
 1293 the publication. We compute the values for the likelihood functions \mathcal{L}_{lk} (see Eq. (3.16)) for a fixed
 1294 value of J_l and profile over the rest of the nuisance parameters ν_{lk} . Then, values of λ from Eq. (3.11)
 1295 are computed as a function of $\langle \sigma v \rangle$, and shared using a common format. Results are computed for
 1296 seven annihilation channels, W^+W^- , ZZ , $b\bar{b}$, $t\bar{t}$, e^+e^- , $\mu^+\mu^-$, and $\tau^+\tau^-$ over 62 m_χ values between
 1297 5 GeV and 100 TeV provided in [58]. The $\langle \sigma v \rangle$ range is defined between 10^{-28} and $10^{-18} \text{ cm}^3 \cdot \text{s}^{-1}$,
 1298 with 1001 logarithmically spaced values. The likelihood combination, i.e. Equation (3.12), and
 1299 profile over the J -factor to compute the profile likelihood ratio λ , Equation (3.11), are carried out
 1300 with two different public analysis software packages, namely `gLike` [66] and `LklCom` [67], that
 1301 provide the same results [68].

1302 As mentioned previously, each experiment computes the \mathcal{L}_{lk} from Equation (3.11) differently.
 1303 The remainder of this section highlights the differences in this calculation across the experiments.
 1304 Four experiments, namely *Fermi*-LAT, H.E.S.S., HAWC and MAGIC, use a binned likelihood to
 1305 compute the \mathcal{L}_{lk} . For these experiments, for each observation \mathcal{D}_{lk} of a given dSph l carried out
 1306 using a given gamma-ray detector k , the binned likelihood function is:

$$\mathcal{L}_{lk} (\langle \sigma v \rangle; J_l, \nu_{lk} | \mathcal{D}_{lk}) = \prod_{i=1}^{N_E} \prod_{j=1}^{N_P} \left[\mathcal{P}(s_{lk,ij}(\langle \sigma v \rangle, J_l, \nu_{lk}) + b_{lk,ij}(\nu_{lk}) | N_{lk,ij}) \right] \times \mathcal{L}_{lk,\nu} (\nu_{lk} | \mathcal{D}_{\nu_{lk}}) \quad (3.17)$$

1307 where N_E and N_P are the number of considered bins in reconstructed energy and arrival direction,
 1308 respectively; \mathcal{P} represents a Poisson PDF for the number of gamma-ray candidate events $N_{lk,ij}$
 1309 observed in the i -th bin in energy and j -th bin in arrival direction, when the expected number is
 1310 the sum of the expected mean number of signal events s_{ij} (produced by DM annihilation) and of
 1311 background events b_{ij} ; $\mathcal{L}_{lk,\nu}$ is the likelihood term for the extra ν_{lk} nuisance parameters that vary
 1312 from one instrument k to another. The expected counts for signal events s_{ij} for a given dSph l and

1313 detector k is given by:

$$s_{ij}(\langle\sigma\nu\rangle, J) = \int_{E'_{\min,i}}^{E'_{\max,i}} dE' \int_{P'_{\min,j}}^{P'_{\max,j}} d\Omega' \int_0^\infty dE \int_{\Delta\Omega_{tot}} d\Omega \int_0^{T_{\text{obs}}} dt \frac{d^2\Phi(\langle\sigma\nu\rangle, J)}{dEd\Omega} \text{IRF}(E', P' | E, P, t) \quad (3.18)$$

1314 where E' and E are the reconstructed and true energies, P' and P the reconstructed and true
1315 arrival directions; $E'_{\min,i}$, $P'_{\min,j}$, $E'_{\max,i}$, and $P'_{\max,j}$ are their lower and upper limits of the i -th
1316 energy bin and the j -th arrival direction bin; T_{obs} is the (dead-time corrected) total observation
1317 time; t is the time along the observations; $d^2\Phi/dEd\Omega$ is the DM flux in the source region (see
1318 Equation (3.1)); and $\text{IRF}(E', P' | E, P, t)$ is the IRF, which can be factorized as the product of the
1319 effective collection area of the detector $A_{\text{eff}}(E, P, t)$, the PDFs for the energy estimator $f_E(E' | E, t)$,
1320 and arrival direction $f_P(P' | E, P, t)$ estimators. Note that for Fermi-LAT, HAWC, MAGIC, and
1321 VERITAS the effect of the finite angular resolution is taken into account through the convolution
1322 of $d\Phi/dEd\Omega$ with f_P in Equation (3.18), whereas in the cases of H.E.S.S. f_P is approximated by a
1323 delta function. This approximation has been made in order to maintain compatibility of the result
1324 with what has been previously published. The difference introduced by this approximation is $< 5\%$
1325 for all considered dSphs. A more comprehensive review of the differences between the analyses of
1326 different instruments can be found in [40].

1327 3.5 HAWC Results

1328 13 of the 20 dSphs considered for the Glory Duck analysis are within HAWC's field of view.
1329 These dSph are analyzed for emission from DM annihilation according to the likelihood method
1330 described in Section 3.4. The 13 likelihood profiles are then stacked to synthesize a combined
1331 limit on the dark matter cross-section, $\langle\sigma\nu\rangle$. This combination is done for the 7 SM annihilation
1332 channels used in the Glory Duck analysis. Figure 3.5 shows the combined limit for all annihilation
1333 channels with HAWC only observations. We also perform 300 studies of Poisson trials on the
1334 background. These trials are used to produce HAWC sensitivities with $\pm 1\sigma$ and $\pm 2\sigma$ uncertainty
1335 bands which were shared with the other collaborators for combination. The results on fitting to
1336 HAWC's Poisson trials of the DM hypothesis is shown in Figure 3.7 for all the DM annihilation
1337 channels studied for Glory Duck.

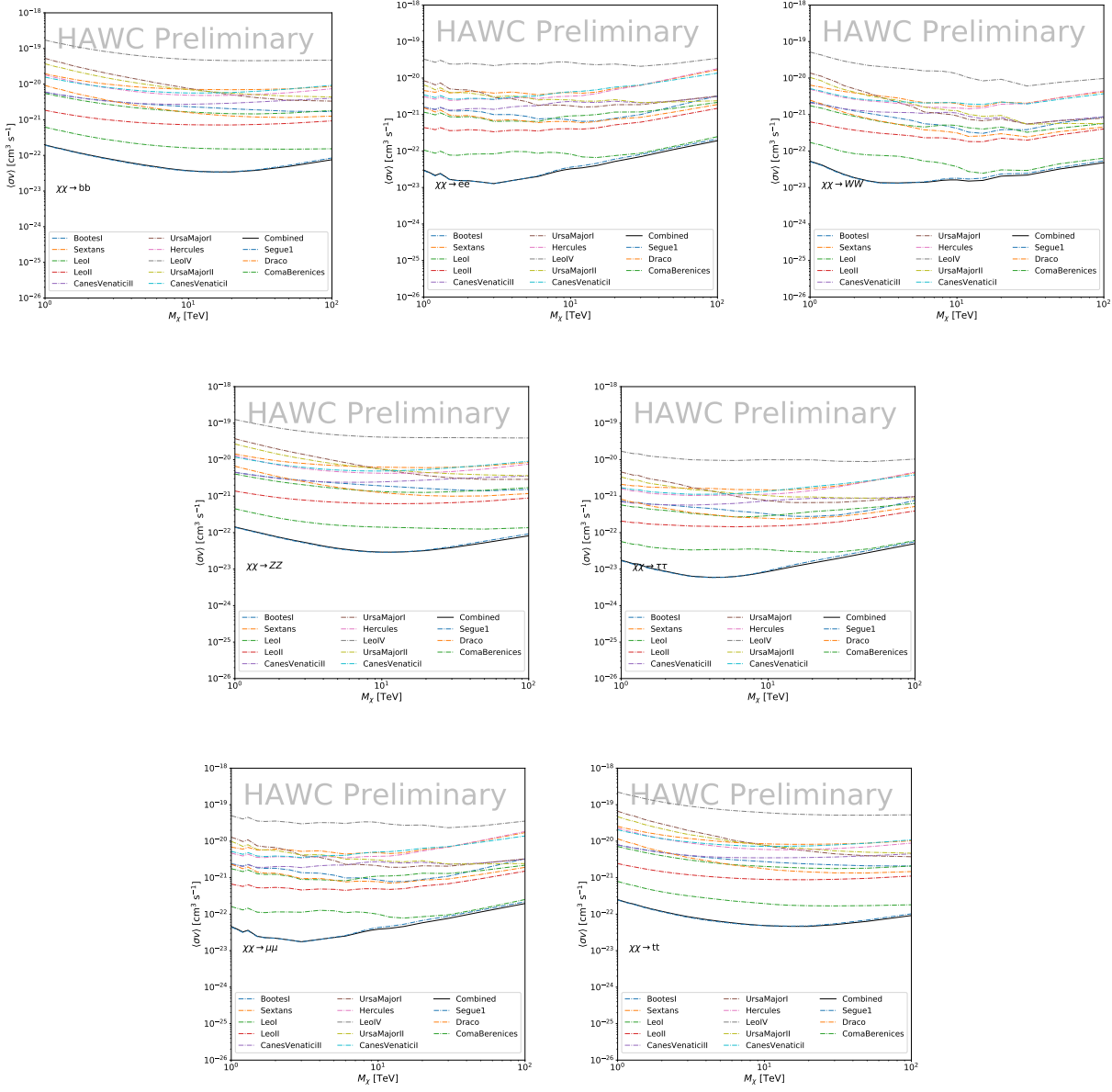


Figure 3.5

1338 No DM was found in HAWC observations. HAWC's limits are dominated by the dSphs Segue1
 1339 and Coma Berenices. The remaining 11 dSphs do not contribute significantly to the limit because
 1340 they are at high zenith and/or have much smaller J factors. Even though some remaining dSphs
 1341 have large J factors, they are towards the edge of HAWC's field of view where HAWC analysis is
 1342 less sensitive.

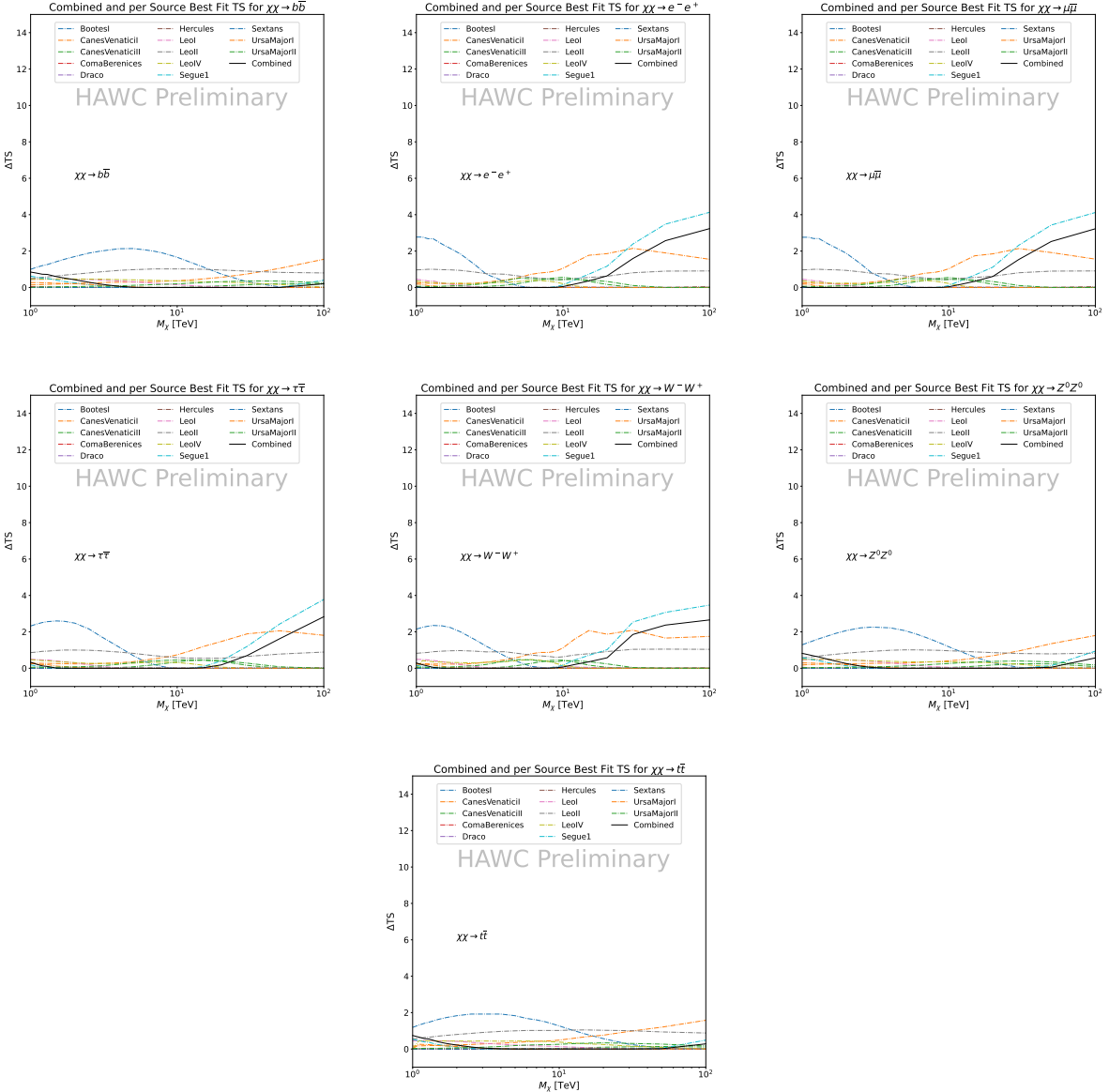


Figure 3.6 HAWC TS values for best fit $\langle\sigma v\rangle$ versus m_χ for seven SM annihilation channels with J factors from \mathcal{GS} . The solid black line shows the combined best fit TS values. The colored, dashed lines are the TS values for each of the 13 sources HAWC studied.

1343 3.6 Glory Duck Combined Results

1344 The crux of this analysis is that HAWC's results are combined with 4 other gamma-ray observa-
 1345 tories: Fermi-LAT, H.E.S.S., MAGIC, and VERITAS. No significant DM emission was observed
 1346 by any of the five instruments. We present the upper limits on $\langle\sigma v\rangle$ assuming seven independent
 1347 DM self annihilation channels, namely W^+W^- , Z^+Z^- , $b\bar{b}$, $t\bar{t}$, e^+e^- , $\mu^+\mu^-$, and $\tau^+\tau^-$. The 68%

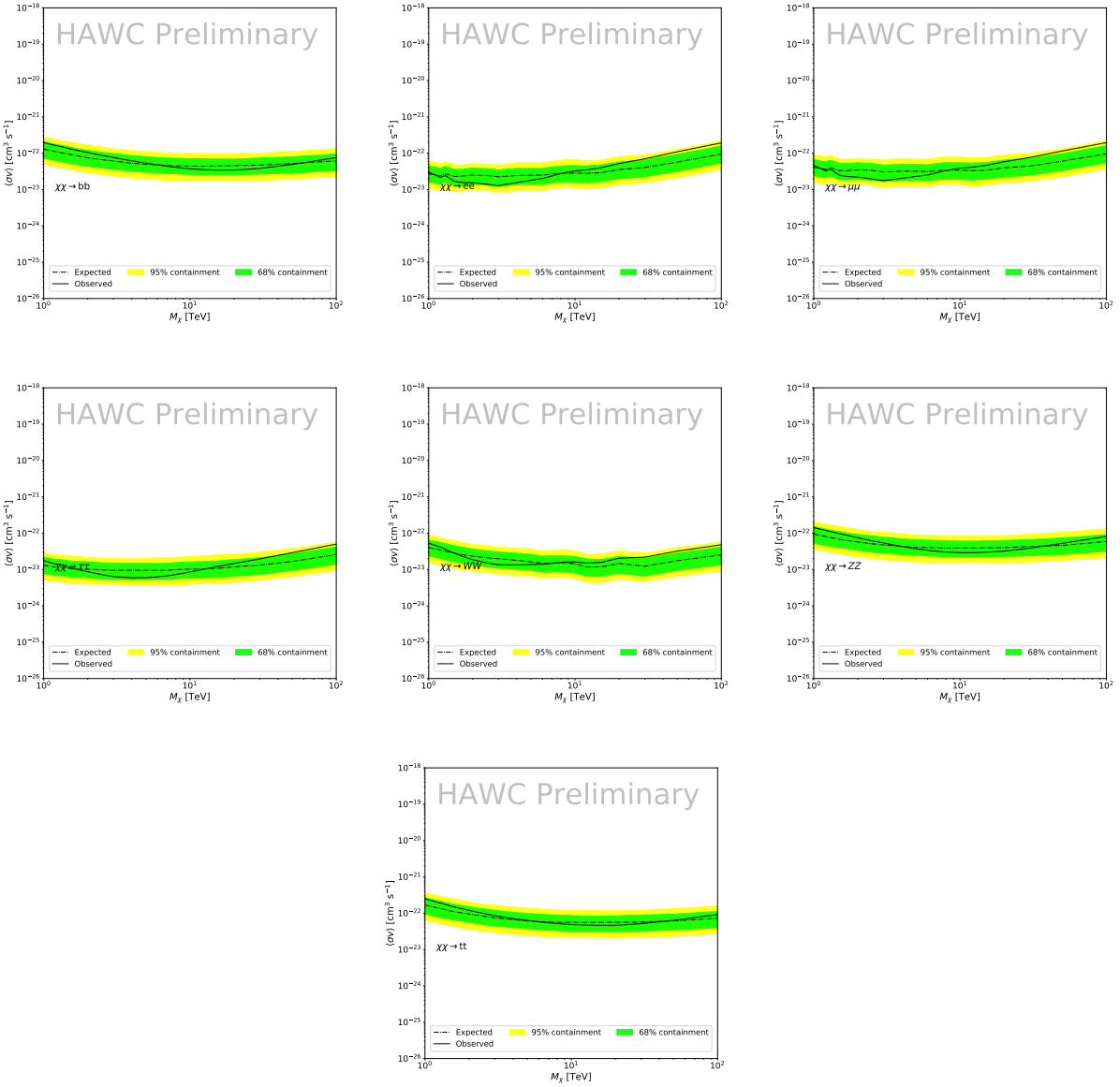


Figure 3.7 HAWC Brazil bands at 95% confidence level on $\langle\sigma v\rangle$ versus DM mass for seven annihilation channels with J -factors from \mathcal{GS} [69]. The solid line represents the combined limit from 13 dSphs. The dashed line is the expected limit. The green band is the 68% containment. The yellow band is the 95% containment.

1348 and 95% containment bands are produced from 300 Poisson realizations of the null hypothesis
 1349 corresponding to each of the combined datasets. These 300 realizations are combined identically
 1350 to dSph observations. The containment bands and the median are extracted from the distribution
 1351 of resulting limits on the null hypothesis. These 300 realizations are obtained either by fast simu-
 1352 lations of the OFF observations, for H.E.S.S., MAGIC, VERITAS, and HAWC, or taken from real

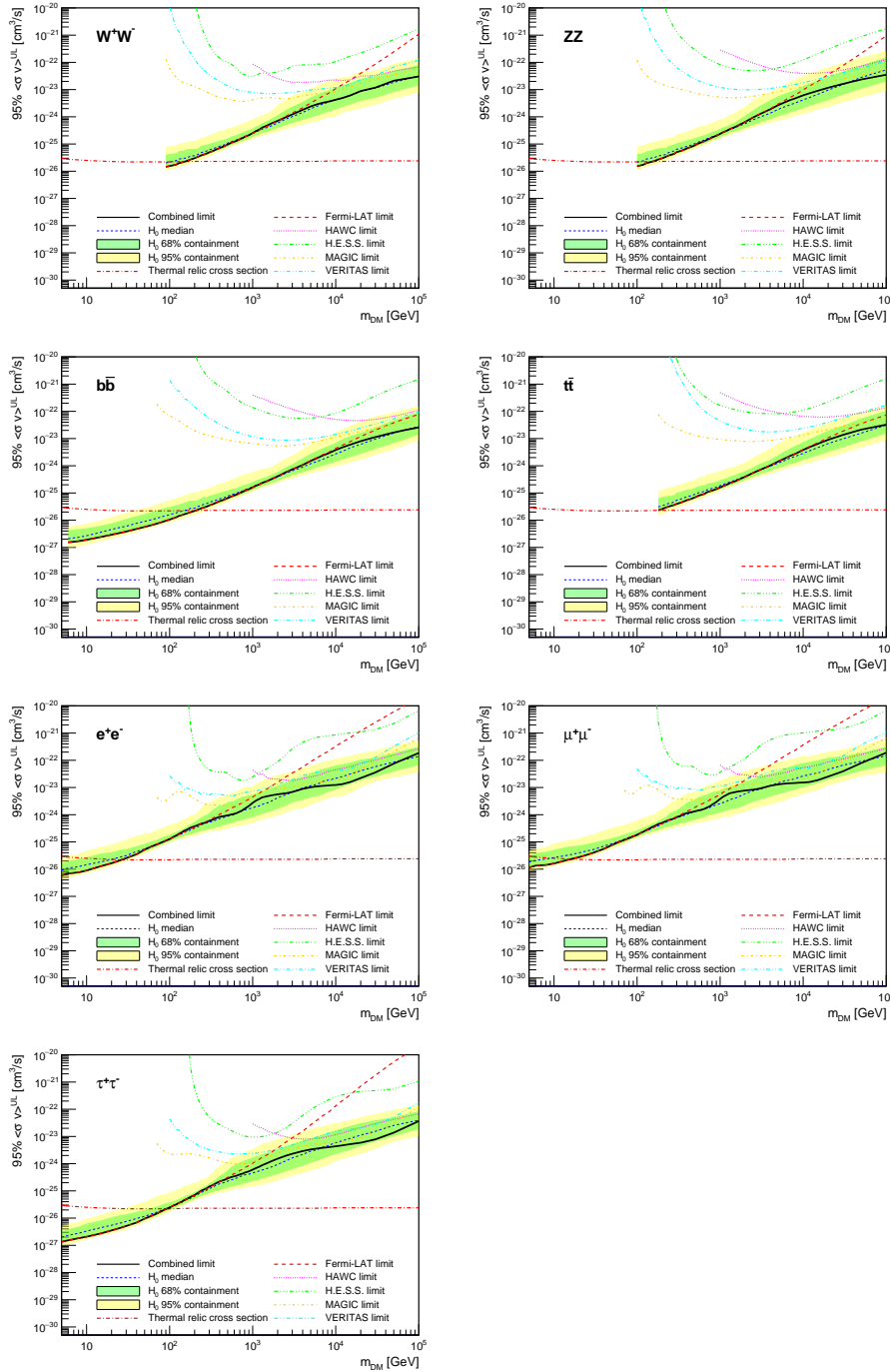


Figure 3.8 Upper limits at 95% confidence level on $\langle\sigma v\rangle$ in function of the DM mass for eight annihilation channels, using the set of J factors from Ref. [69] (\mathcal{GS} set in Table 3.1). The black solid line represents the observed combined limit, the black dashed line is the median of the null hypothesis corresponding to the expected limit, while the green and yellow bands show the 68% and 95% containment bands. Combined upper limits for each individual detector are also indicated as solid, colored lines. The value of the thermal relic cross-section in function of the DM mass is given as the red dotted-dashed line [70].

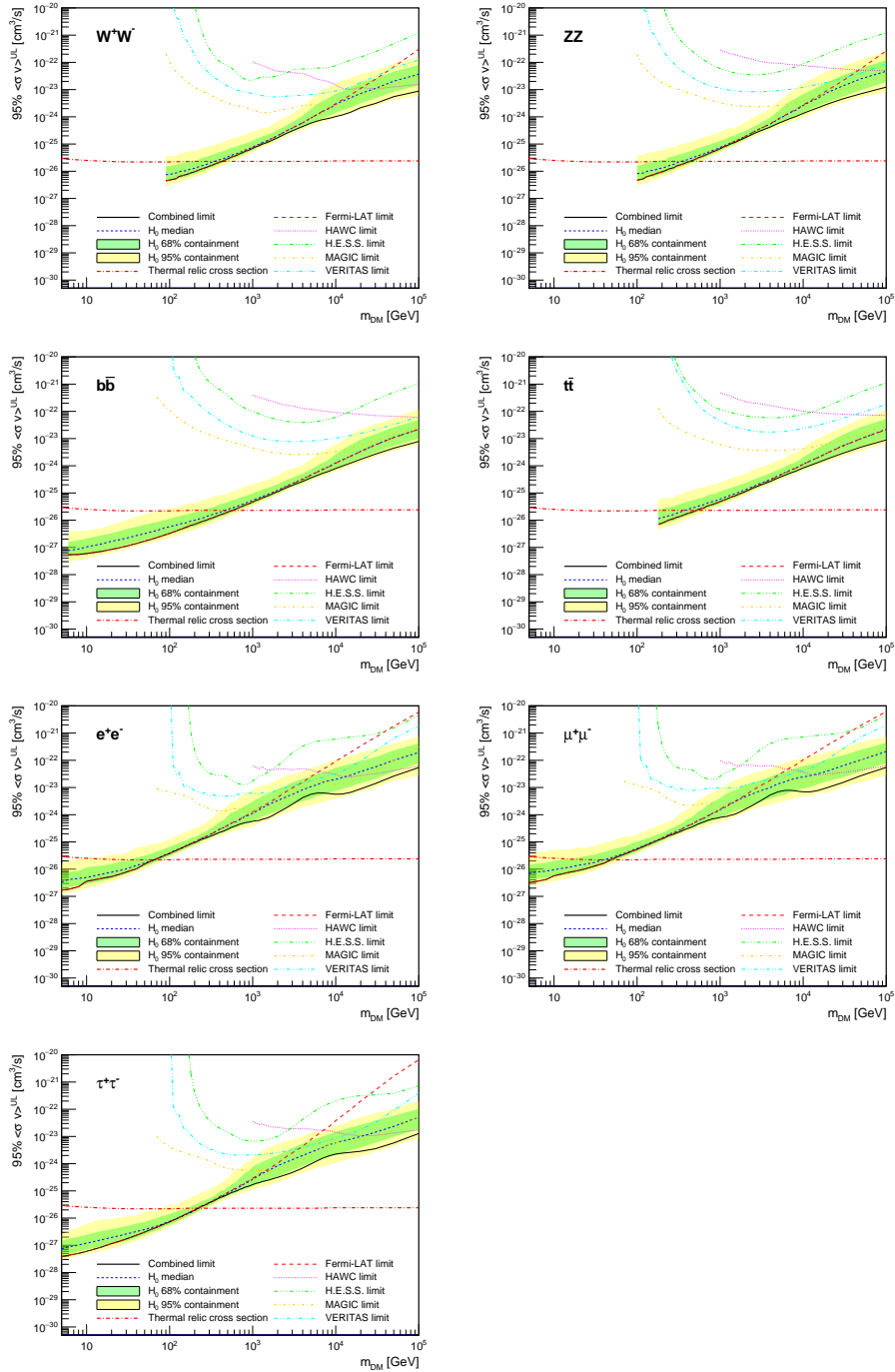


Figure 3.9 Same as Fig. 3.8, using the set of J factors from Ref. [63, 71] (\mathcal{B} set in Table 3.1).

1353 observations of empty fields of view in the case of Fermi-LAT [64, 72, 73].

1354 The obtained limits are shown in Figure 3.8 for the $\mathcal{G}\mathcal{S}$ set of J -factors [69] and in Figure 3.9
 1355 for the \mathcal{B} set of J -factors [63, 71]. The combined limits are presented with their 68% and 95%
 1356 containment bands, and are expected to be close to the median limit when no signal is present.

1357 We observe agreement with the null hypothesis for all channels, within 2σ standard deviations,
1358 between the observed limits and the expectations given by the median limits. Limits obtained from
1359 each detector are also indicated in the figures, where limits for all dSphs observed by the specific
1360 instrument have been combined.

1361 Below ~ 300 GeV, the *Fermi*-LAT dominates the DM limits for all annihilation channels. From
1362 ~ 300 GeV to ~ 2 TeV, *Fermi*-LAT continues to dominate for the hadronic and bosonic DM channels,
1363 yet the IACTs (H.E.S.S., MAGIC, and VERITAS) and *Fermi*-LAT all contribute to the limit for
1364 leptonic DM channels. For DM masses between ~ 2 TeV to ~ 10 TeV, the IACTs dominate leptonic
1365 DM annihilation channels, whereas both the *Fermi*-LAT and the IACTs dominate bosonic and
1366 hadronic DM annihilation channels. From ~ 10 TeV to ~ 100 TeV, both the IACTs and HAWC
1367 contribute significantly to the leptonic DM limit. For hadronic and bosonic DM, the IACTs and
1368 *Fermi*-LAT both contribute strongly.

1369 We notice that the limits computed using the \mathcal{B} set of J -factor are always better compared to the
1370 ones calculated with the \mathcal{GS} set. For the W^+W^- , Z^+Z^- , $b\bar{b}$, and $t\bar{t}$ channels, the ratio between the
1371 limits computed with the two sets of J -factor is varying between a factor of ~ 3 and ~ 5 depending
1372 on the energy, with the largest ratio around 10 TeV. For the channels e^+e^- , $\mu^+\mu^-$, and $\tau^+\tau^-$, the
1373 ratio lies between ~ 2 to ~ 6 , being maximum around 1 TeV. Examining Figure 3.16 and Figure 3.17
1374 in Section 3.8, these differences are explained by the fact that the \mathcal{B} set provides higher J -factors
1375 for the majority of the studied dSphs, with the notable exception of Segue I. The variation on the
1376 ratio of the limits for the two sets is due to different dSph dominating the limits depending on the
1377 energy. One set, \mathcal{B} , pushes the range of which thermal cross-section which can be excluded to
1378 higher mass. This comparison demonstrates the magnitude of systematic uncertainties associated
1379 with the choice of the J -factor calculation. The \mathcal{GS} and \mathcal{B} sets present a difference in the limits for
1380 all channels of about This difference is explained, see Figure 3.16 and Figure 3.17, by the fact that
1381 the \mathcal{B} set provides higher J -factors for all dSph except for Segue I.

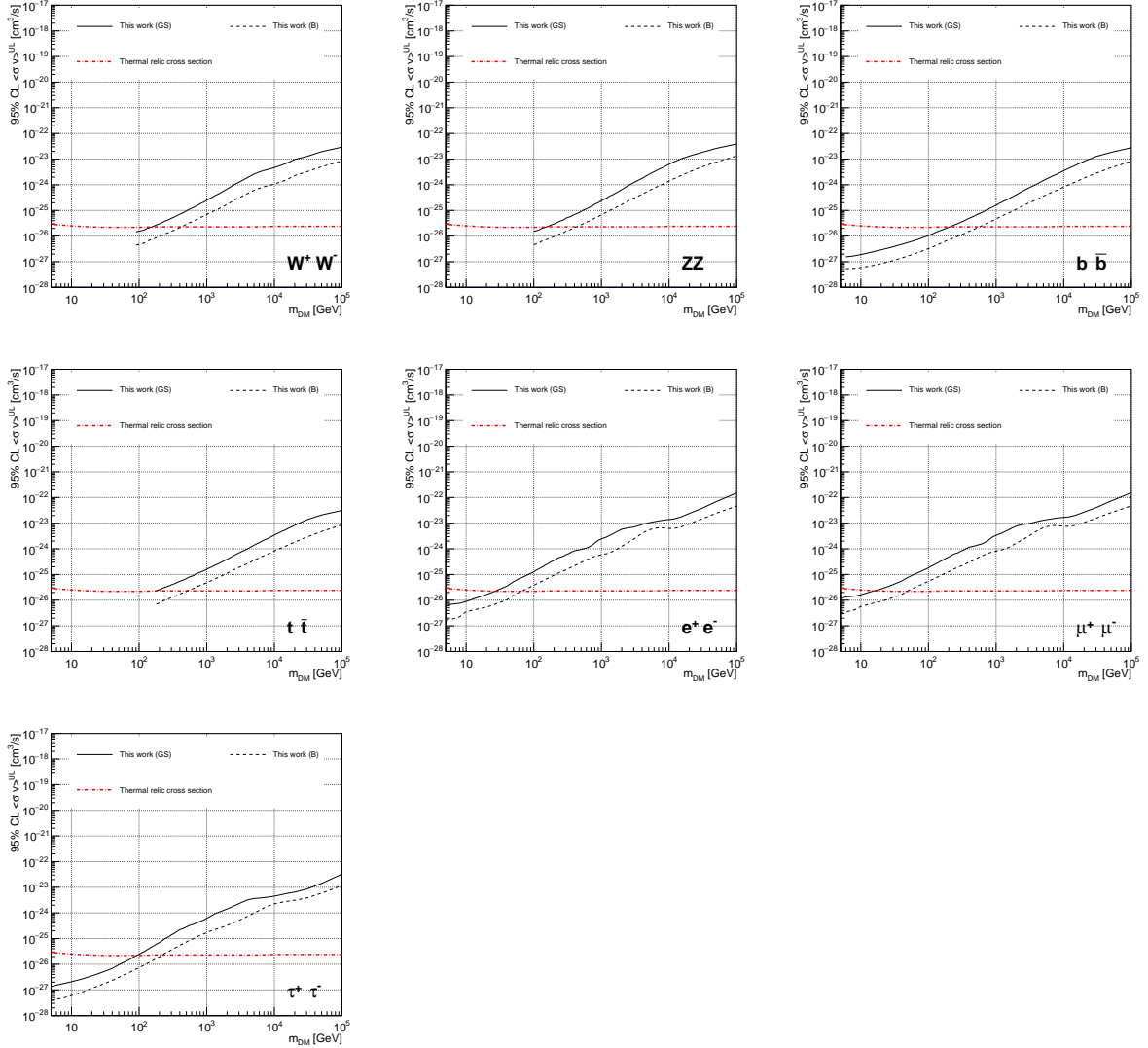


Figure 3.10 Comparisons of the combined limits at 95% confidence level for each of the eight annihilation channels when using the J factors from Ref. [69] (\mathcal{GS} set in Table 3.1), plain lines, and the J factor from Ref. [63, 71] (\mathcal{B} set in Table 3.1), dashed lines. The cross-section given by the thermal relic is also indicated [70].

1382 3.7 HAWC Systematics

1383 3.7.1 Inverse Compton Scattering

1384 The DM-DM annihilation channels produce many high energy electrons regardless of the
 1385 primary annihilation channel. These high energy electrons can produce high energy gamma-rays
 1386 through Inverse Compton Scattering (ICS). If this effect is strong, it would change the morphology
 1387 of the source and increase the total expected gamma-ray counts from any source. The PPPC [58]

1388 provides tools in Mathematica for calculating the impact of ICS for an arbitrary location in the
1389 sky for a specified annihilation channel. We calculated the change in gamma-ray counts for DM
1390 annihilation to primary $e\bar{e}$ for RA and Dec corresponding to Segue1 and Coma Berenices. These
1391 dSphs were chosen because they are the strongest contributors to the limit. $e\bar{e}$ was selected because
1392 it would have the largest number of high energy electrons. The effect was found to be on the order
1393 of 10^{-7} on the gamma-ray spectrum. As a result, this systematic is not considered in our analysis.

1394 **3.7.2 Point Source Versus Extended Source Limits**

1395 The previous DM search toward dSph approximated the dSphs as point sources [60]. In
1396 this analysis, the dSphs are implemented as extended with J-factor distributions following those
1397 produced by [69]. The resolution of the cited map is much finer than HAWC's angular resolution.
1398 The vast majority of the J-factor distribution is represented on the central HAWC pixel of the dSph
1399 spatial map. However, the neighboring 8 pixels are not negligible and contribute to our limit.

1400 Figure 3.11 shows a substantial improvement to the limit for Segue1. Fig. 3.12 however showed
1401 identical limits. These disparities are best explained by the relative difference in their J-Factors.
1402 Both dSphs pass almost overhead the HAWC detector, however Segue1 has the larger J-Factor
1403 between the two. Adjacent pixels to the central pixel will therefore contribute to the limits. This is
1404 the case for other dSph that are closer to the zenith of the HAWC detector.

1405 Comparison plots for all sources and the combined limit can be found in the sandbox for the
1406 Glory Duck project.

1407 **3.7.3 Impact of Pointing Systematic**

1408 During the analysis it was discovered that directional reconstruction of gamma-rays had a
1409 systematic bias at large zenith angles. Slides describing this systematic can be found [here](#). Shown
1410 on the presentation is dependence on the pointing systematic on declination. New spatial profiles
1411 were generated for every dSph and limits were computed for the adjusted declination.

1412 Section 3.7.3 demonstrates the impact of this systematic for all DM annihilation channels
1413 studied by HAWC. The impact is a tiny improvement, yet mostly identical, to the combined limits.

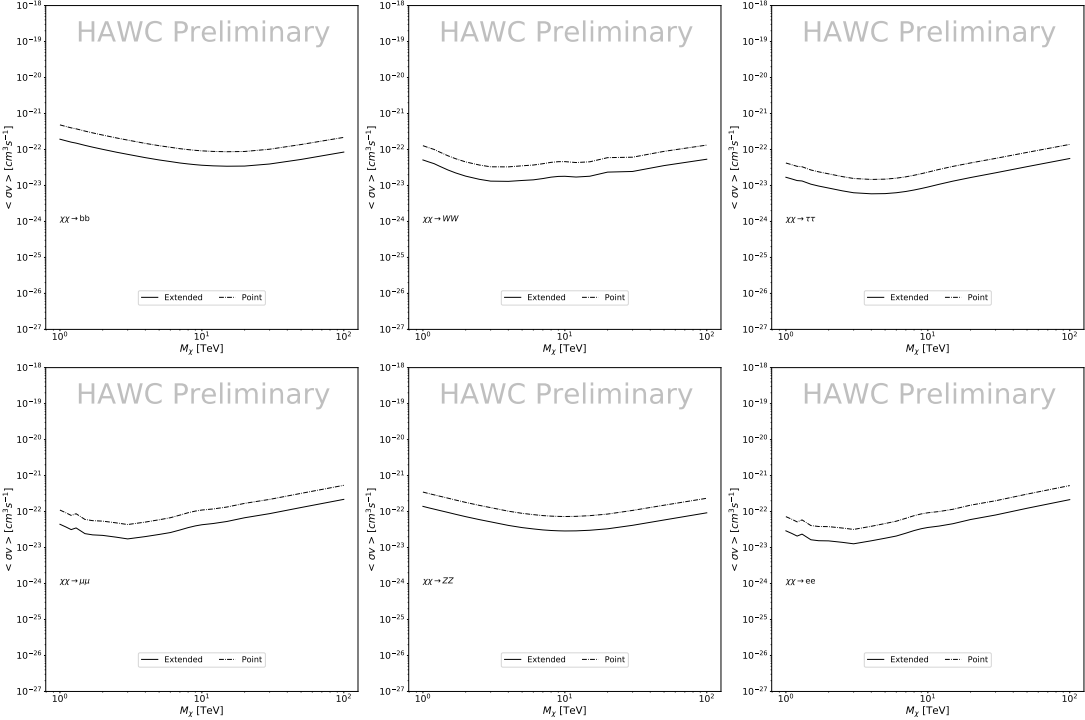


Figure 3.11 Comparisons of the combined limits at 95% confidence level for a point source analysis and extended source using [69] \mathcal{GS} J-factor distributions and PPPC [58] annihilation spectra. Shown are the limits for Segue1 which will have the most significant impact on the combined limit. 6 of the 7 DM annihilation channels are shown. Solid lines are extended source studies. Dashed lines are point source studies. Overall, the extended source analysis improves the limit by a factor of 2.

1414 3.8 J-factor distributions

1415 3.8.1 Numerical integration of \mathcal{GS} maps

1416 It was discovered well after the HAWC analysis was completed that the published tables from
 1417 \mathcal{GS} [59] quoted median J -factors were computed in a non-trivial manner. The assumption myself
 1418 and collaborators had been that the published tables represented the J -factor as a function of θ for
 1419 the best global fit model on a per-source basis. However, this is not the case. Instead, what is
 1420 published are the best fit model for each dwarf that only considers stars up to the angular separation
 1421 θ . Therefore, the model is changing for each value of θ for each dwarf. Yet, the introduced features
 1422 from unique models at each θ are much smaller than the angular resolution of HAWC. It is not
 1423 expected for these effects to impact the limits and TS greatly as a result.

1424 Median J -factor model profiles were provided by the authors. New maps were generated

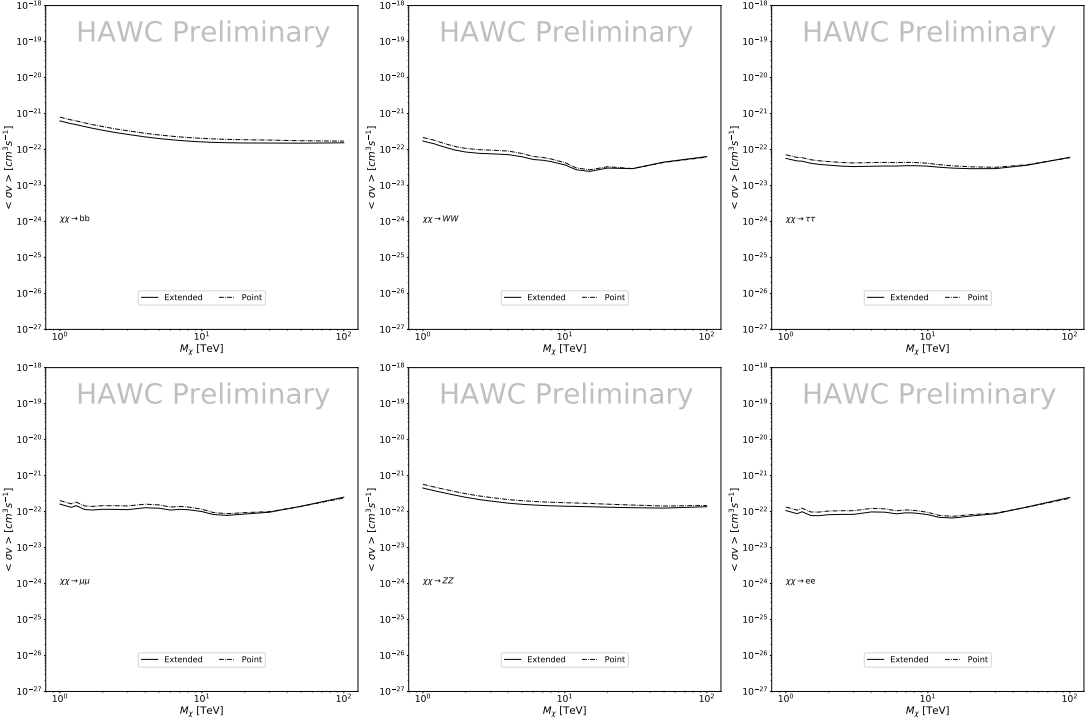


Figure 3.12 Same as Fig. 3.11 on Coma Berenices. This dSph also contributes significantly to the limit. The limits are identical in this case.

and analyzed for Segue1 and Coma Berenices. Figure 3.14 shows the differential between maps generated with the method from Section 3.8.1 and from the authors of [59]. These maps were reanalyzed for all SM DM annihilation channels. Upper limits for these channels are shown in Figure 3.15

From Figure 3.15, we can see that the impact of these model difference was no substantial. The observed impact was a fractional effect which is much smaller than the impact from selecting another DM spatial distribution model as was shown in Figure 3.10.

3.8.2 \mathcal{GS} Versus \mathcal{B} spatial models

We show in this appendix a comparison between the J -factors computed by Geringer-Sameth *et al.* [69] (the \mathcal{GS} set) and the ones computed by Bonnivard *et al.* [63, 71] (the \mathcal{B} set). The \mathcal{GS} J -factors are computed through a Jeans analysis of the kinematic stellar data of the selected dSphs, assuming a dynamic equilibrium and a spherical symmetry for the dSphs. They adopted the generalized DM density distribution, known as Zhao-Hernquist, introduced by [61], carrying

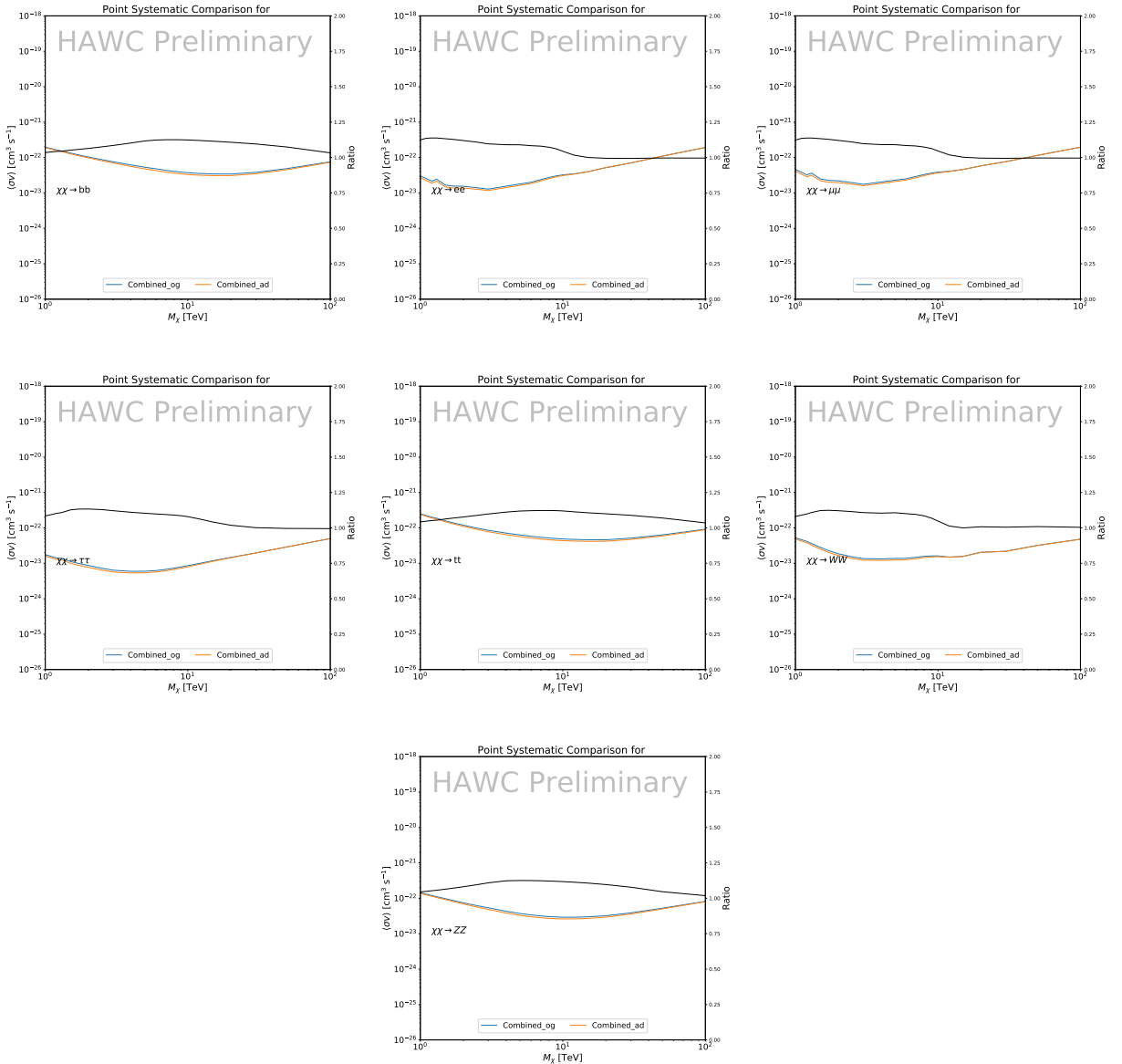


Figure 3.13 Comparison of combined limits when correcting for HAWC's pointing systematic. All DM annihilation channels are shown. The solid black line is the ratio between published limit to the declination corrected limit. The blue solid line or "Combined_og" represented the limits computed for Glory Duck. The solid orange line or "Combined_ad" represented the limits computed after correcting for the pointing systematic.

1438 three additional index parameters to describe the inner and outer slopes, and the break of the
 1439 density profile. Such a profile parametrization allows the reduction of the theoretical bias from
 1440 the choice of a specific radial dependency on the kinematic data. In other words, the increase of
 1441 free parameters with the use of the Zhao-Hernquist profile allows a better description of the mass

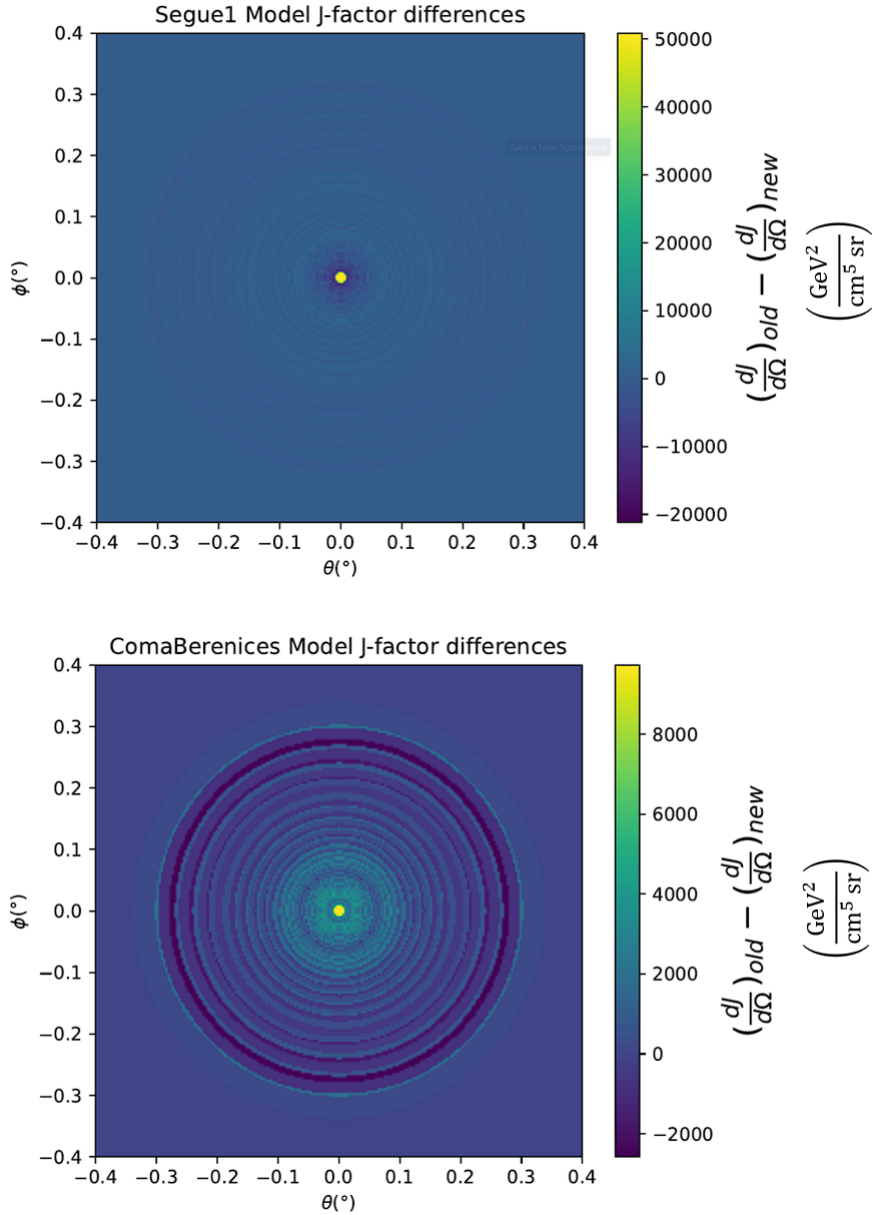


Figure 3.14 Differential map of dJ/Ω from model built in Section 3.8.1 and profiles provided directly from authors. (Top) Differential from Segue1. (bottom) Differential from Coma Berenices. Note that their scales are not the same. Segue1 shows the deepest discrepancies which is congruent with its large uncertainties. Both models show anuli where unique models become apparent.

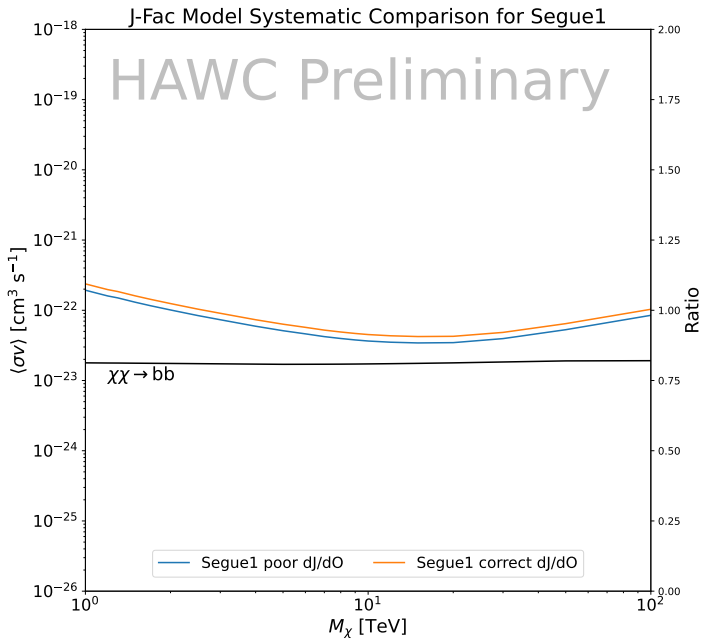
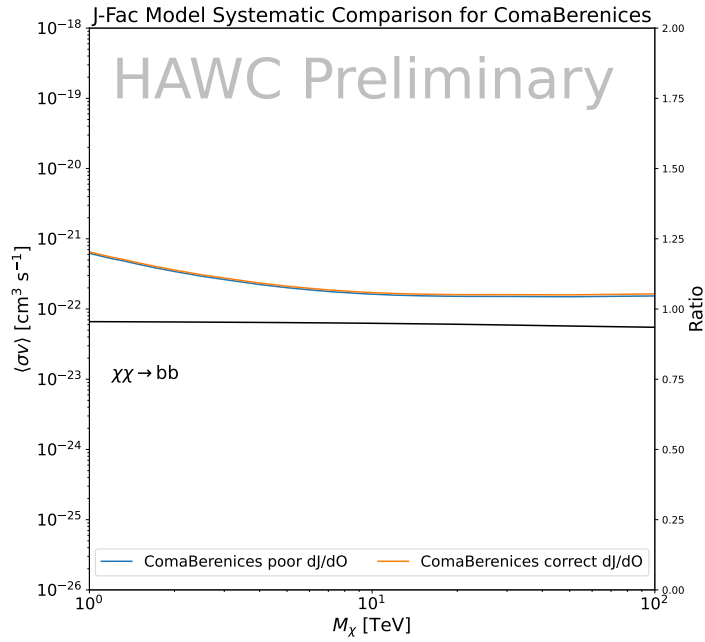


Figure 3.15 HAWC limits for Coma Berenices (top) and Segue1 (bottom) for two different map sets. Blue lines are limits calculated on maps with poor model representation. Orange lines are limits calculated on spatial profiles provided by the authors of [59]. Black line is the ratio of the poor spatial model limits to the corrected spatial models. The left y-axis measures $\langle\sigma v\rangle$ for the blue and orange lines. The right y-axis measures the ratio and is unitless.

1442 density distribution of dark matter.

1443 In addition, a constant velocity anisotropy profile and a Plummer light profile [74] for the stellar
1444 distribution were assumed. The velocity anisotropy profile depends on the radial and tangential
1445 velocity dispersion. However, its determination remains challenging since only the line-of-sight
1446 velocity dispersion can be derived from velocity measurements. Therefore, the parametrization of
1447 the anisotropy profile is obtained from simulated halos (see [75] for more details). They provide the
1448 values of the J -factors of regions extending to various angular radius up to the outermost member
1449 star.

1450 The \mathcal{B} J -factors were computed through a Jeans analysis taking into account the systematic
1451 uncertainties induced by the DM profile parametrization, the radial velocity anisotropy profile, and
1452 the triaxiality of the halo of the dwarf galaxies. They performed a more complete study of the dSph
1453 kinematics and dynamics than \mathcal{GS} for the determination of the J -factor. Conservative values of the
1454 J -factors where obtained using an Einasto DM density profile [76], a realistic anisotropy profile
1455 known as the Baes & Van Hese profile [77] which takes into account that the inner regions can be
1456 significantly non-isotropic, and a Zhao-Hernquist light profile [61].

1457 For both sets, J -factor values are provided for all dSphs as a function of the radius of the
1458 integration region [69, 63, 71]. Table 3.1 shows the heliocentric distance and Galactic coordinates
1459 of the twenty dSphs, together with the two sets of J -factor values integrated up to the outermost
1460 observed star for \mathcal{GS} and the tidal radius for \mathcal{B} . Both J -factor sets were derived through a Jeans
1461 analysis based on the same kinematic data, except for Draco where the measurements of [78] have
1462 been adopted in the computation of the \mathcal{B} value. The computations for producing the \mathcal{GS} and \mathcal{B}
1463 samples differ in the choice of the DM density, velocity anisotropy, and light profiles, for which the
1464 set \mathcal{B} takes into account some sources of systematic uncertainties.

1465 Figure 3.16 and Figure 3.17 show the comparisons for the J -factor versus the angular radius
1466 for each of the 20 dSphs used in this study. The uncertainties provided by the authors are also
1467 indicated in the figures. For the \mathcal{GS} set, the computation stops at the angular radius corresponding
1468 to the outermost observed star, while for the \mathcal{B} set, the computation stops at the angular radius

1469 corresponding to the tidal radius.

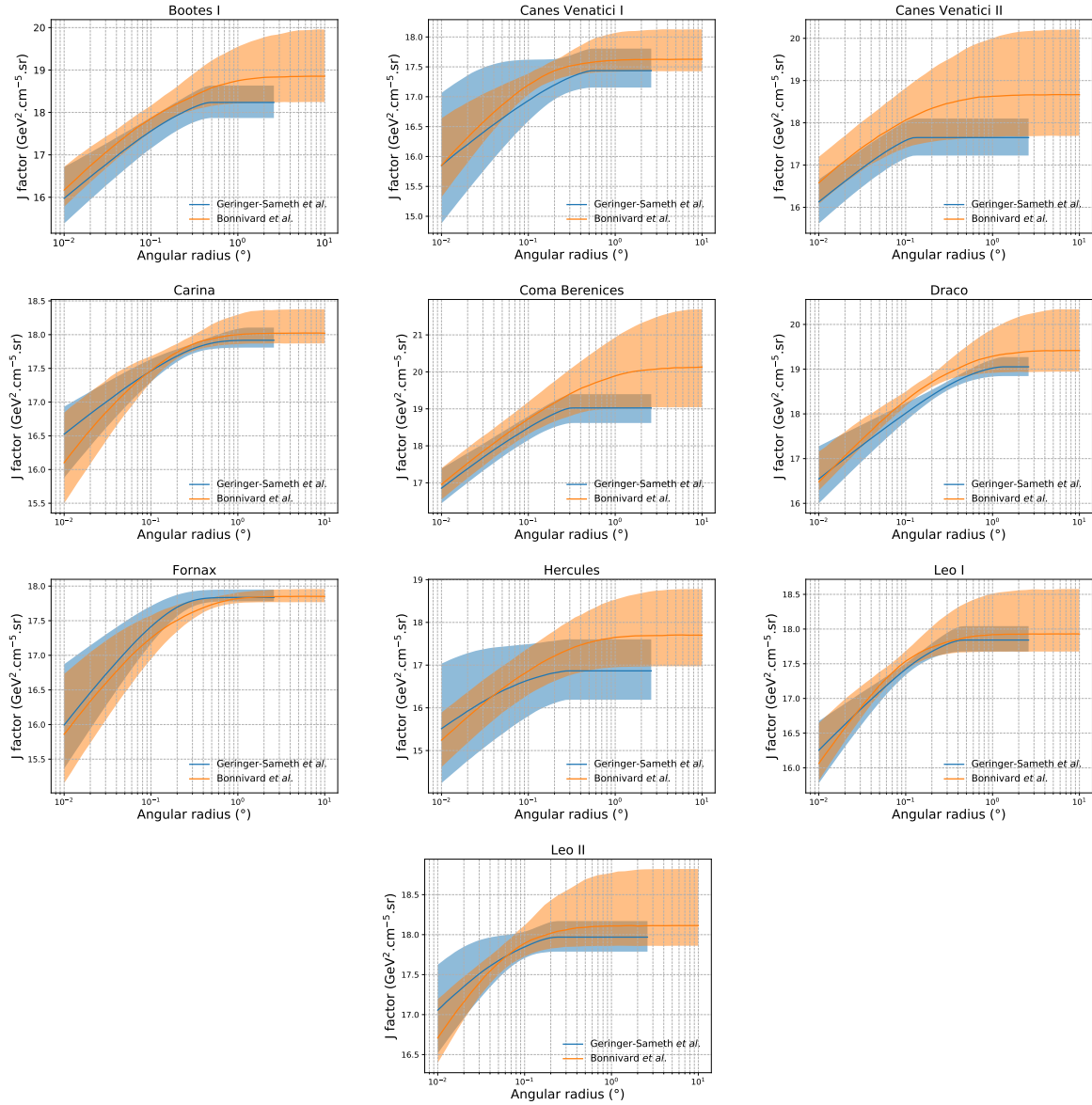


Figure 3.16 Comparisons between the J -factors versus the angular radius for the computation of J factors from Ref. [69] (\mathcal{GS} set in Table 3.1) in blue and for the computation from Ref. [63, 71] (\mathcal{B} set in Tab. 3.1) in orange. The solid lines represent the central value of the J -factors while the shaded regions correspond to the 1σ standard deviation.

1470 3.9 Discussion and Conclusions

1471 In this multi-instrument analysis, we have used observations of 20 dSphs from the gamma-ray
 1472 telescopes Fermi-LAT, H.E.S.S., MAGIC, VERITAS, and HAWC to perform a collective DM
 1473 search annihilation signals. The data were combined across sources and detectors to significantly

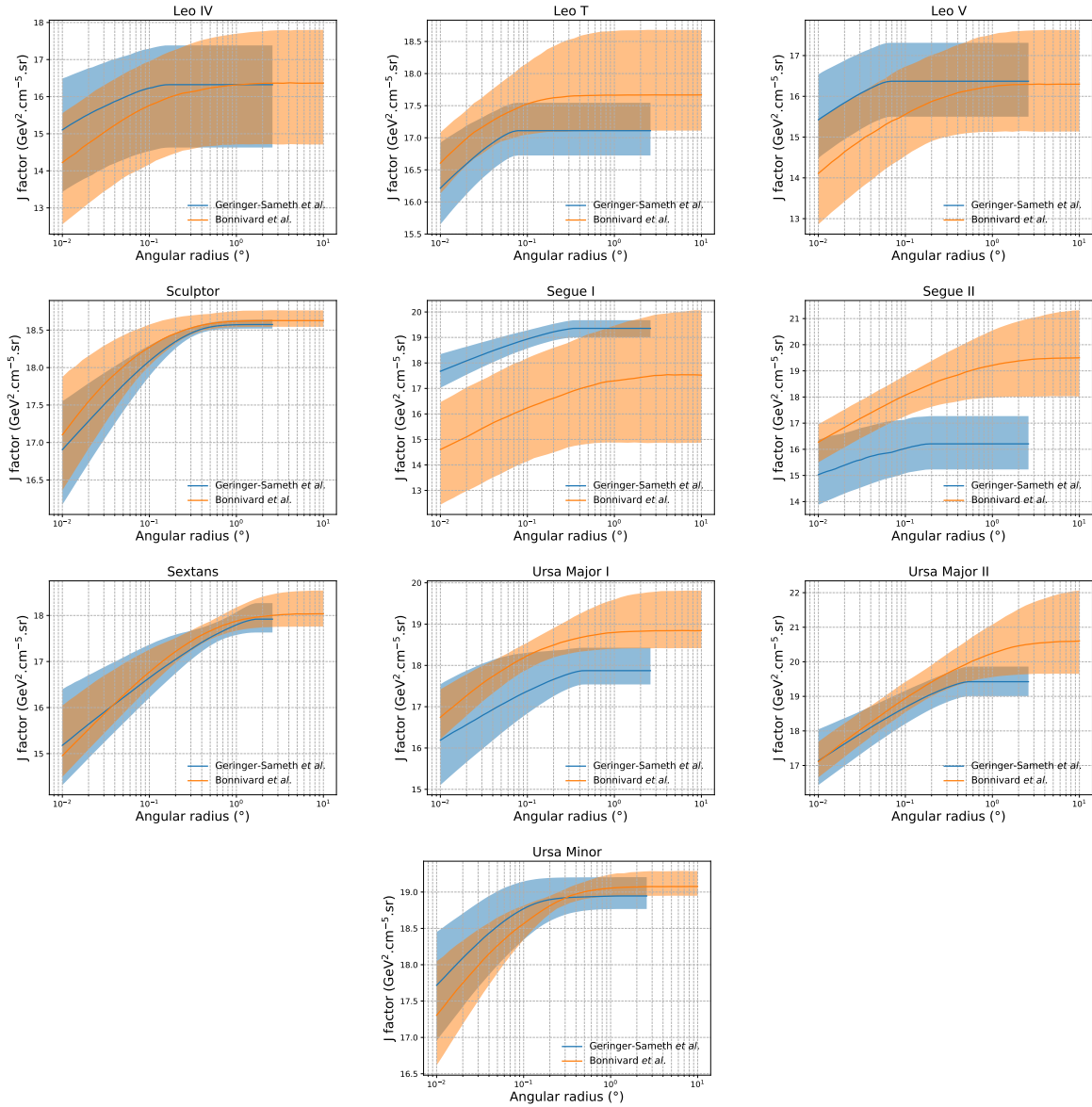


Figure 3.17 Comparisons between the J -factors versus the angular radius for the computation of J factors from Ref. [69] (\mathcal{GS} set in Tab. 3.1) in blue and for the computation from Ref. [63, 71] (\mathcal{B} set in Tab. 3.1) in orange. The solid lines represent the central value of the J -factors while the shaded regions correspond to the 1σ standard deviation.

increase the sensitivity of the search. We have observed no significant deviation from the null, no DM hypothesis, and so present our results in terms of upper limits on the annihilation cross-section for seven potential DM annihilation channels.

Fermi-LAT brings the most stringent constraints for continuum channels below approximately 1 TeV. The remaining detectors dominate at higher energies. Overall, for multi-TeV DM mass,

1479 the combined DM constraints from all five telescopes are 2-3 times stronger than any individual
1480 telescope for multi-TeV DM.

1481 Derived from observations of many dSphs, our results produce robust limits given the DM
1482 content of the dSphs is relatively well constrained. The obtained limits span the largest mass
1483 range of any WIMP DM search. Our combined analysis improves the sensitivity over previously
1484 published results from each detector which produces the most stringent limits on DM annihilation
1485 from dSphs. These results are based on deep exposures of the most promising known dSphs with
1486 the currently most sensitive gamma-ray instruments. Therefore, our results constitute a legacy of
1487 a generation of gamma-ray instruments on WIMP DM searches towards dSphs. Our results will
1488 remain the reference in the field until a new generation of more sensitive gamma-ray instruments
1489 begin operations, or until new dSphs with higher J -factors are discovered.

1490 This analysis serves as a proof of concept for future multi-instrument and multi-messenger
1491 combination analyses. With this collaborative effort, we have managed to sample over four orders
1492 in magnitude in gamma-ray energies with distinct observational techniques. Determining the nature
1493 of DM continues to be an elusive and difficult problem. Larger datasets with diverse measurement
1494 techniques could be essential to tackling the DM problem. A future collaboration using similar
1495 techniques as the ones described in this paper could grow even beyond gamma rays. The models we
1496 used for this study include annihilation channels with neutrinos in the final state. Advanced studies
1497 could aim to merge our results with those from neutrino observatories with large data sets. Efforts
1498 are already underway to add data from the IceCube, ANTARES, and KM3NeT observatories to
1499 these gamma-ray results.

1500 From this work, a selection of the best candidates for observations, according to the latest
1501 knowledge on stellar dynamics and modelling techniques for the derivation of the J -factors on
1502 the potential dSphs targets, is highly desirable at the time that new experiments are starting their
1503 dark matter programs using dSphs. Given the systematic uncertainty inherent to the derivation of
1504 the J -factors, an informed observational strategy would be to select both objects with the highest
1505 J -factors that could lead to DM signal detection, and objects with robust J -factor predictions, i.e.

1506 with kinematic measurements on many bright stars, which would strengthen the DM interpretation
1507 reliability of the observation outcome.

1508 This analysis combines data from multiple telescopes to produce strong constraints on astro-
1509 physical objects. From this perspective, these methods can be applied beyond just DM searches.
1510 Almost every astrophysical study can benefit from multi-telescope, multi-wavelength gamma-ray
1511 studies. We have enabled these telescopes to study the cosmos with greater precision and detail.
1512 Many astrophysical searches can benefit from multi-instrument gamma-ray studies, for which our
1513 analysis lays the foundation.

CHAPTER 4

1514 MULTITHREADING HAWC ANALYSES FOR DARK MATTER SEARCHES

1515 4.1 Introduction

1516 HAWC’s current software suite, plugins to 3ML and HAL [68, 34], do not fully utilize compu-
1517 tational advancements of recent decades. Said advancements include the proliferation of Graphical
1518 Processing Units (GPUs), and multithreading on multicore processors. The analysis described in
1519 chapter 3 took up to 3 months of wall time waiting for the full gambit of data analysis and simulation
1520 of background to compute. Additionally, with the updated 2D energy binning scheme, f_{hit} and
1521 Neural Network (NN), the time needed to compute expected to grow. Although excessive comput-
1522 ing time was, in part, from an intense use of a shared computing cluster, it was evident that there
1523 was room for improvement. In HAWC’s next generation dSph DM search, I decided to develop
1524 codes that would utilize the multicore processors on modern high performance computing clusters.
1525 The results of this work are featured in this chapter and brought a human timing improvement to
1526 computation that scales approximately as $1/N$ where N is the number of threads.

1527 4.2 Dataset and Background

1528 This section enumerates the data and background methods used for HAWC’s multithreaded
1529 study of dSphs. Section 4.2.1 and Section 4.2.2 are most useful for fellow HAWC collaborators
1530 looking to replicate a multithreaded dSph DM search.

1531 4.2.1 Itemized HAWC files

1532 These files are only available withing HAWC’s internal documentation and collaborators. They
1533 are not meant for public access, and are presented here so that HAWC collaborators can reproduce
1534 results accurately.

- 1535 • Detector Resolution: `refit-Pass5-Final-NN-detRes-zenith-dependent.root`
- 1536 • Data Map: `Pass5-Final-NN-maptree-ch103-ch1349-zenith-dependent.root`
- 1537 • Spectral Dictionary: `HDMspectra_dict_gamma.npy`

1538 **4.2.2 Software Tools and Development**

1539 This analysis was performed using HAL and 3ML [34, 57] in Python3. I built software
1540 in collaboration with Michael Martin and Letrell Harris to implement the *Dark Matter Spectra*
1541 *from the Electroweak to the Planck Scale* (HDM) [79] and dSphs spatial model from [80] for
1542 HAWC analysis. A NumPy dictionary of HDM, `HDMspectra_dict_gamma.npy`, was made for
1543 portability within the collaboration. These dictionaries were generated from the [git repository](#) [79].
1544 The analysis was performed using the Neural Network energy estimator for Pass 5.F. A description
1545 of this estimator was provided in chapter 2. [TODO: Define a subsection when it's written](#), and its
1546 key, relevant improvements are an improved energy estimation and improved sensitivities at higher
1547 zenith angles. All other software used for data analysis, DM profile generation, and job submission
1548 to SLURM are also kept in my sandbox in the [Dark Matter HAWC](#) project. The above repository
1549 also incorporates the model inputs used previously in Glory Duck, described in chapter 3, so Glory
1550 Duck remains compatible with modern software.

1551 **4.2.3 Data Set and Background Description**

1552 The HAWC data maps used for this analysis contain 2565 days of data between runs 2104 and
1553 7476. They were generated from pass 5.f reconstruction. The analysis is performed using the NN
1554 energy estimator with bin list:

1555 `B1C0Ea, B1C0Eb, B1C0Ec, B1C0Ed, B1C0Ee, B2C0Ea, B2C0Eb, B2C0Ec, B2C0Ed, B2C0Ee,`
1556 `B3C0Ea, B3C0Eb, B3C0Ec, B3C0Ed, B3C0Ee, B3C0Ef, B4C0Eb, B4C0Ec, B4C0Ed, B4C0Ee,`
1557 `B4C0Ef, B5C0Ec, B5C0Ed, B5C0Ee, B5C0Ef, B5C0Eg, B6C0Ed, B6C0Ee, B6C0Ef, B6C0Eg,`
1558 `B6C0Eh, B7C0Ee, B7C0Ef, B7C0Eg, B7C0Eh, B7C0Ei, B8C0Ee, B8C0Ef, B8C0Eg, B8C0Eh,`
1559 `B8C0Ei, B8C0Ej, B9C0Ef, B9C0Eg, B9C0Eh, B9C0Ei, B9C0Ej, B10C0Eg, B10C0Eh,`
1560 `B10C0Ei, B10C0Ej, B10C0Ek, B10C0El`

1561 Bin 0 was excluded as it has substantial hadronic contamination and poor angular resolution.

1562 Background considerations and source selection was identical to Section 3.2.3, and no additional
1563 arguments are provided here. Many of the HAWC systematics explored in Section 3.7 also apply

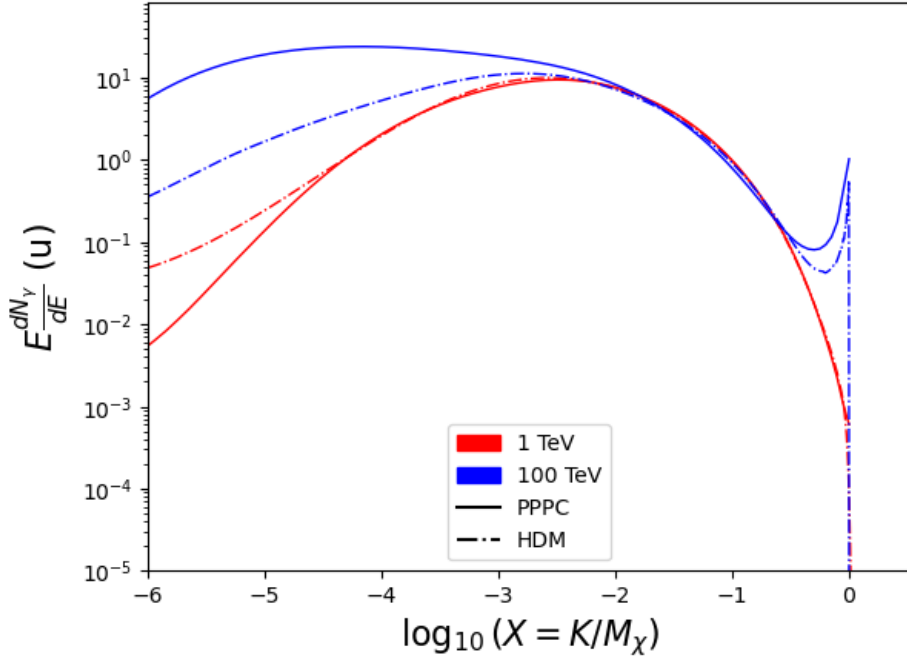


Figure 4.1 Spectral hypotheses from PPPC [58] and HDM [79] for DM annihilation: $\chi\chi \rightarrow W^-W^+$. Solid lines are spectral models with EW corrections from the PPPC. Dash-dot lines are spectral models from HDM. Red lines are models for $M_\chi = 1$ TeV. Blue lines represent models for $M_\chi = 100$ TeV.

1564 for this DM search and are not added upon here.

1565 **4.3 Analysis**

1566 The analysis and its systematics are almost identical to Section 3.3. Importantly, we use the
 1567 same **TODO: fix this ref** Equation (3.1) and Equation (3.2) for estimating the gamma-ray flux at
 1568 HAWC from our sources.

1569 **4.3.1 $\frac{dN_\gamma}{dE_\gamma}$ - Particle Physics Component**

1570 For these spectra, we import HDM with Electroweak (EW) corrections and additional correc-
 1571 tions for neutrinos above the EW scale [79]. The spectra are implemented as a model script in
 1572 astromodels for 3ML. A comprehensive description of EW corrections and neutrino considerations
 1573 are provided later in Sec. 7.

1574 Figure 4.1 demonstrates the impact of changes implemented in HDM on DM annihilation to W
 1575 bosons. A class in astromodels was developed to include HDM and is aptly named **HDMspectra**
 1576 within `DM_models.py`. The SM DM annihilation channels studied here are $\chi\chi \rightarrow$:

1577 e^+e^- , $\mu^+\mu^-$, $\tau^+\tau^-$, $b\bar{b}$, $t\bar{t}$, gg , W^+W^- , ZZ , $c\bar{c}$, $u\bar{u}$, $d\bar{d}$, $s\bar{s}$, $\nu_e\bar{\nu}_e$, $\nu_\mu\bar{\nu}_\mu$, $\nu_\tau\bar{\nu}_\tau$, $\gamma\gamma$, hh .

1578 For $\gamma\gamma$ and ZZ , a substantial fraction of the signal photons are expected to have $E_\gamma = m_\chi$ [79].
 1579 This introduces δ -function that is much narrower than the energy resolution of the HAWC detector.
 1580 To ensure that this feature is not lost in the likelihood fits, the 'line' feature is convolved with a
 1581 Gaussian kernel with a 1σ width of $0.05 \cdot m_\chi$ and total kernel window of $\pm 4\sigma$. This differs from
 1582 HAWC's previous line study where 30% of HAWC's energy resolution was used for the kernel [81].
 1583 The NN energy estimator's strength compared to f_{hit} at low gamma-ray energy enables narrower
 1584 kernels [79]. $\chi\chi \rightarrow \gamma\gamma$ and ZZ spectral hypotheses are shown in Figure 4.2. We did not explore
 1585 how well we reconstruct injected signal events for various kernels widths. This is a systematic
 1586 that should be tested before publication to journal. Spectral models for the remaining annihilation
 1587 channels are plotted for each m_χ in Figure B.1.

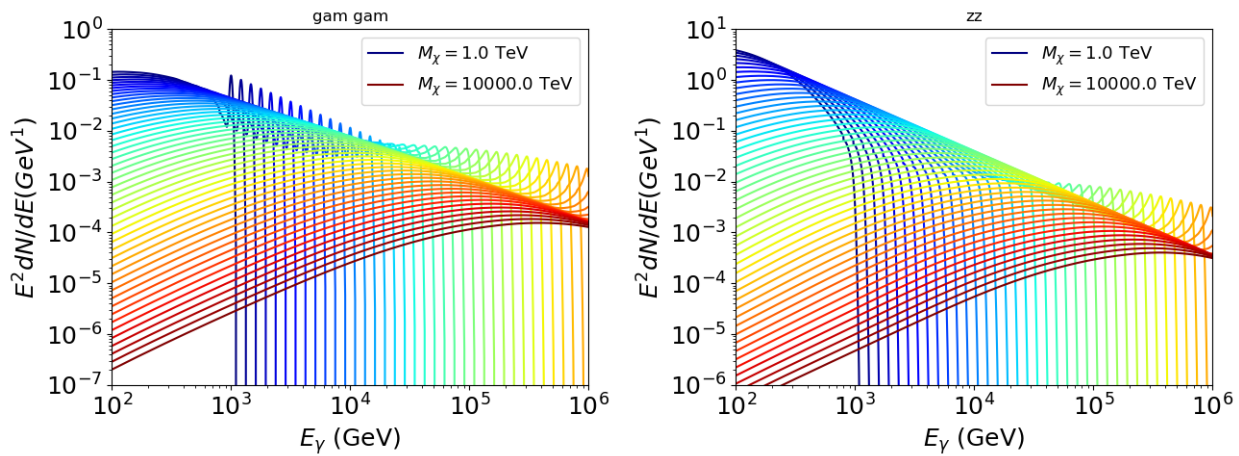


Figure 4.2 Photon spectra for $\chi\chi \rightarrow \gamma\gamma$ (left) and $\chi\chi \rightarrow ZZ$ (right) after Gaussian convolution of line features. Both spectra have δ -features at photon energies equal to the DM mass. Bluer lines are annihilation spectra with lower DM mass. Redder lines are spectra from larger DM mass. All spectral models are sourced from the Heavy Dark Matter models [79]. Axes are drawn roughly according to the energy sensitivity of HAWC.

1588 **4.3.2 J Astrophysical Components**

1589 The J-factor profiles for each source are imported from Louis Strigari et al. (referred to with
 1590 \mathcal{LS}) [80]. The \mathcal{LS} catalog fits a Navarro–Frenk–White (NFW) [62] spatial DM distributions to

1591 the dSphs which has a DM density of

$$\rho(r) = \frac{\rho_0}{\frac{r}{R_s} \left(1 + \frac{r}{R_s}\right)^2}. \quad (4.1)$$

1592 ρ_0 and the scale radius, R_s are free parameters fit for each dSph. r is the distance from the center
1593 of the dSph.

1594 Profiles in $\frac{dJ}{d\Omega}(\theta)$ up to an angular separation $\theta = 0.5^\circ$ were provided directly from the authors.

1595 Map generation from these profiles were almost identical to Section 3.3.2 except that a higher order
1596 trapezoidal integral was used for the normalization of the square, uniformly-spaced map:

$$p^2 \cdot \sum_{i=0}^N \sum_{j=0}^M w_{i,j} \frac{dJ}{d\Omega}(\theta_{i,j}, \phi_{i,j}) \quad (4.2)$$

1597 p is the angular side of one pixel in the map. $w_{i,j}$ is a weight assigned the following ways:

1598 $w_{i,j} = 1$ if $(\theta_{i,j}, \phi_{i,j})$ is fully within the region of integration

1599 $w_{i,j} = 1/2$ if $(\theta_{i,j}, \phi_{i,j})$ is on an edge of the region of integration

1600 $w_{i,j} = 1/4$ if $(\theta_{i,j}, \phi_{i,j})$ is on a corner of the region of integration

1601 Figure 4.3 shows the median and $\pm 1\sigma$ maps used as input for this DM annihilation study.

1602 4.3.3 Source Selection and Annihilation Channels

1603 HAWC's sources for this multithreaded analysis include Coma Berenices, Draco, Segue 1, and
1604 Sextans. \mathcal{LS} observed up to 43 sources in its publication, however only 4 of the best fit profiles
1605 were provided at the time this thesis was written. A full description of each source used in this
1606 analysis is found in Table 4.1.

1607 This analysis improves on chapter 3 in the following ways. Previously, the particle physics
1608 model used for gamma-ray spectra from DM annihilation was from the PPPC [58] which missed
1609 important considerations relevant for the neutrino sector. HDM is used to account for this shortfall
1610 [79]. HDM also models DM to the Planck scale which permits HAWC to probe PeV scale DM. For
1611 this study, we sample DM masses: 1 TeV - 10 PeV with 6 mass bins per decade in DM mass. In

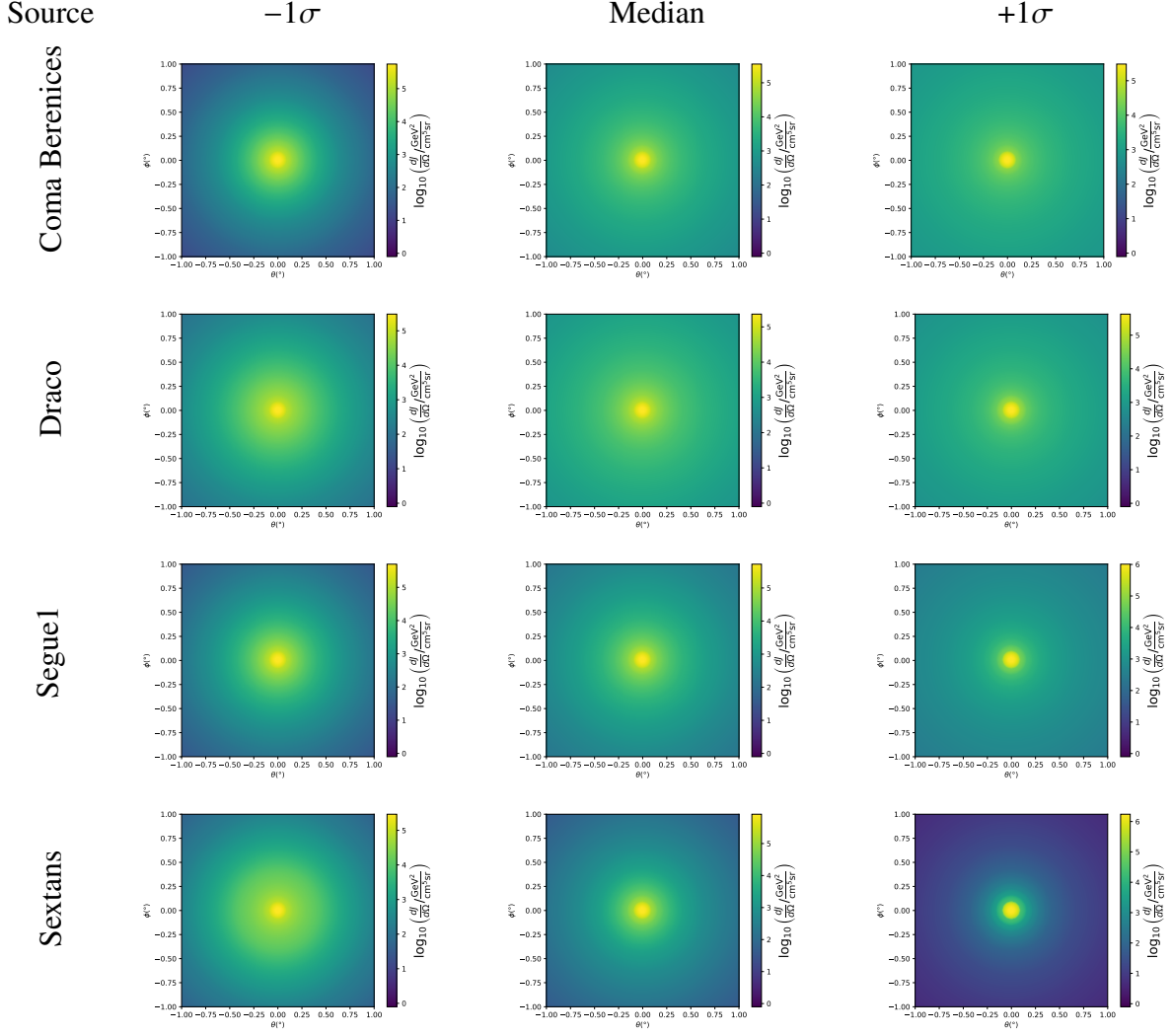


Figure 4.3 $\frac{dJ}{d\Omega}$ maps for Coma Berenices, Draco, Segue1, and Sextans. Columns are divided for the $\pm 1\sigma$ uncertainties in $dJ/d\Omega$ around the mean value from \mathcal{LS} [80]. Origin is centered on the specific dwarf spheroidal galaxies (dSph). θ and ϕ axes are the angular separation from the center of the dwarf. Profiles are truncated at 1° and flattened beyond.

the case of line spectra ($\chi\chi \rightarrow \gamma\gamma$, or ZZ), we double the mass binning to 12 DM mass bins per decade in DM mass.

\mathcal{LS} provides 25 sources within HAWC's field of view. Additionally, NFW [62] DM distributions have fewer parameters than Zhao [61], so \mathcal{LS} fits ultra-faint dwarves which expands the number of sources. However, all sources were not provided by the authors in time for the completion of this dissertation. Finally, the gamma-ray ray dataset is much larger. The study performed here analyzes 2565 days of data compared to 1017 days analyzed in chapter 3.

1619 **4.4 Likelihood Methods**

1620 These are identical to Section 3.4.1 and no additional changes are made to the likelihood. Bins
 1621 in this analysis are expanded to include HAWC’s NN energy estimator.

1622 **4.5 Computational Methods: Multithreading**

1623 Previously, as in Section 3.3, the likelihood was minimized for one model at a time. One model
 1624 in this case representing a DM annihilation channel (CHAN), DM mass (m_χ), and dSph ((SOURCE)).
 1625 In an effort to conserve human and CPU time, jobs submitted for high performance computing
 1626 contained a list of m_χ to iterate over for likelihood fitting. Jobs were then trivially parallelized
 1627 for each permutation of the two lists: CHANS and SOURCES. The lists for CHANS and SOURCES are
 1628 found in Section 4.3.1 and Table 4.1, respectively. Initially, 11 m_χ were serially sampled for one
 1629 job defined by a [CHAN, SOURCE] tuple. Computing the likelihoods would take between 1.5 to 2 hrs,
 1630 stochastically, for a job. We expect to compute likelihoods for data and 300 Poisson background
 1631 trials. The estimated CPU time based on the above for all CHAN (N = 17) and SOURCE (M = 25)
 1632 was estimated to 127,925 jobs. In total, 1,407,175 likelihood fits and profiles would be computed
 1633 for the 11 mass bins we wished to study. The estimated CPU time ranged between 8k CPU days
 1634 to 10k CPU days. Human time is more challenging to estimate as job allocation is stochastic and
 1635 highly dependent on what other users are submitting. Yet, it is unlikely that all jobs would run
 1636 simultaneously. Therefore, we can expect human time to be about as long as was seen in chapter 3

Name	Distance (kpc)	l, b ($^\circ$)	$\log_{10} J$ (\mathcal{LS} set) $\log_{10}(\text{GeV}^2\text{cm}^{-5}\text{sr})$
Coma Berenices	44	241.89, 83.61	$19.00^{+0.36}_{-0.35}$
Draco	76	86.37, 34.72	$18.83^{+0.12}_{-0.12}$
Segue I	23	220.48, 50.43	$19.12^{+0.49}_{-0.58}$
Sextans	86	243.50, 42.27	$17.73^{+0.13}_{-0.12}$

Table 4.1 Summary of the relevant properties of the dSphs used in the present work. Column 1 lists the dSphs. Columns 2 and 3 present their heliocentric distance and galactic coordinates, respectively. Column 4 reports the J -factors of each source given from the \mathcal{LS} studies and estimated $\pm 1\sigma$ uncertainties. The values $\log_{10} J$ (\mathcal{LS} set) [80] correspond to the mean J -factor values for a source extension truncated at 0.5° .

1637 which was on the order of months to fully compute on a smaller analysis. A visual aid to describe
1638 how jobs were organized is provided in Figure 4.4.

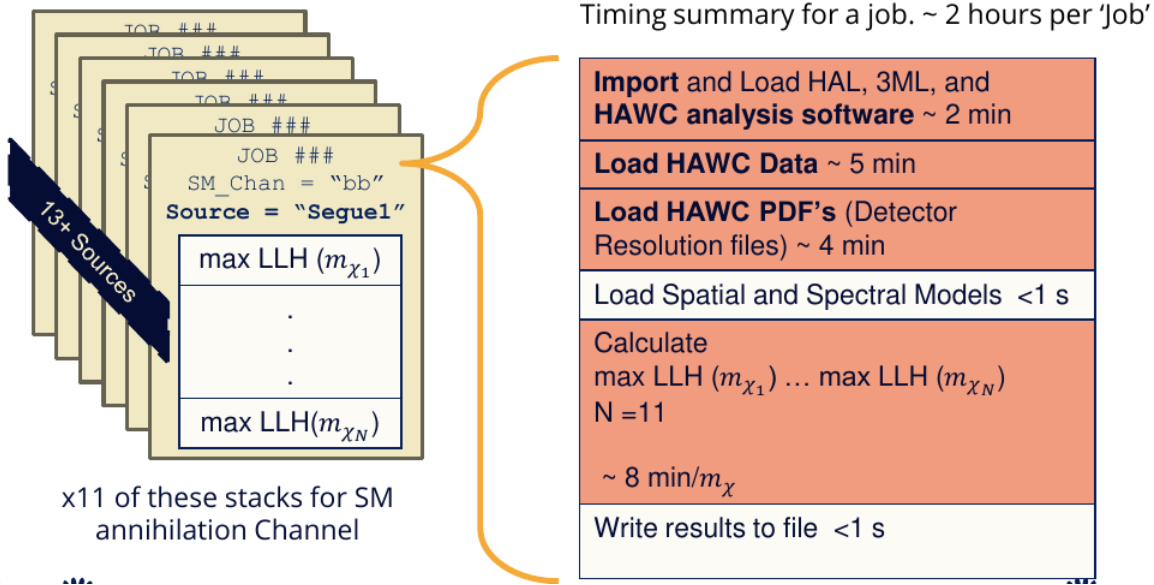


Figure 4.4 Infographic on how jobs and DM computation was organized in Section 3.3. Jobs were built for each permutation of CHANS and SOURCES shown by the left block in the figure. Each job, which took on the order 2 hrs to compute, had the following work flow: 1. Import HAWC analysis software, 2 min to run. 2. Load HAWC count maps, 5 min to run. 3. Load HAWC energy and spatial resolutions, 4 min. 5. Load DM spatial source templates and spectral models, less than 1 s. 6. Perform likelihood fit on data and model, about 8 min per DM mass. 7. Write results to file, less than 1s.

1639 The computational needs for this next generation DM analysis are extreme and is unlike other
1640 analyses performed on HAWC. It became clear that there was a lot to gain from optimizing how
1641 the likelihoods are computed. This section discusses how multi-threading was applied to solve and
1642 reduce HAWC's computing of likelihoods for large parameter spaces like in DM searches.

1643 4.5.1 Relevant Foundational Information

1644 The profiling of the likelihood for HAWC is done via gradient descent where the normalization
1645 of Equation (3.1) (linearly correlated with $\langle \sigma v \rangle$) is rescaled in the descent. Additionally, we sample
1646 the likelihood space for a defined list of $\langle \sigma v \rangle$'s described in Section 3.4.2. The time to compute
1647 these values is not predictable or consistent because many variables can change across the full
1648 model-space. Comprehensively, these variables are:

1649 • m_χ : DM rest mass
 1650 • CHAN : DM annihilation channel in SM.
 1651 • SOURCE : dSph. Involves a spatial template AND coordinate in HAWC data.
 1652 • $\langle\sigma v\rangle$: Effectively the flux normalization and free parameter in the likelihood fit.
 1653 Therefore, we develop an asynchronous, functional-parallel coding pattern. Asynchronous meaning
 1654 the instructions within a function are independent and permitted to be out of sync with sibling
 1655 computations. Functional-parallel meaning that instructions are the subject of parallelization
 1656 rather than threading the likelihood computation. This is close to trivial parallelization seen in
 1657 Figure 4.4 except that we seek to consolidate the loading stages (software, data, and detector
 1658 resolution loading). Multiple asynchronous threads are expected to reduce total serial processing
 1659 time and total overhead across the entire project in addition to saving human time.

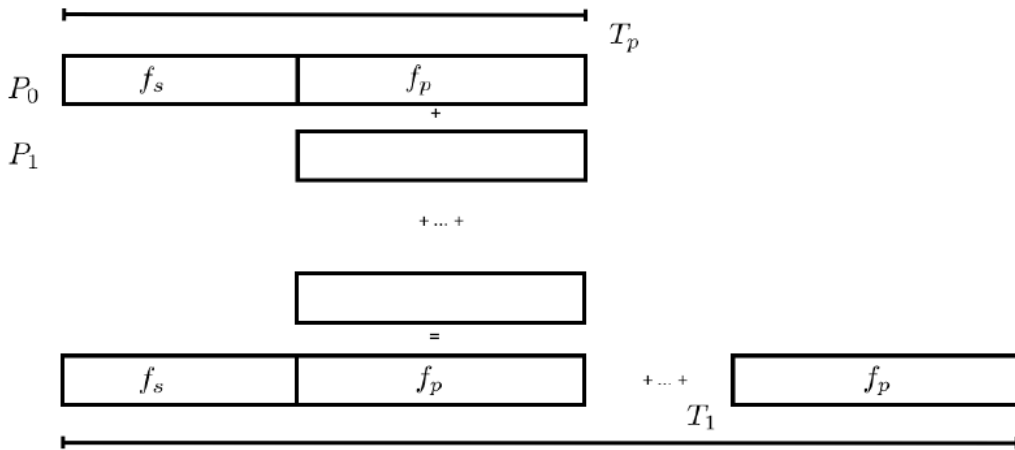


Figure 4.5 Graphic of Gustafson parallel coding pattern. f_s is the fraction of a program, in time, spent on serial computation. f_p is the fraction of computing time that is parallelizable. T_p is the total time for a parallel program to run. T_1 is the total time for a parallel program to run if only 1 processor is allocated. P_N is the N -th processor where it's row is the computation the processor performs. The Gustafson pattern is most similar to what is implemented for this analysis. Figure is pulled from [82].

1660 We need a way to measure and compare the expected speedup and efficiency gain for this
 1661 asynchronous coding pattern. I pull inspiration for timing measurement from [82] and use *Amdahl's*

1662 law with hybrid programming. Hybrid programming meaning that the computation is a mix of
 1663 distributed and shared memory programming. If we assume the code is fully parallelizable over p
 1664 processors and c threads, the ideal speedup is simply pc , and ideal run-time is $T_1/(pc)$. T_1 is the
 1665 total time for a parallel program to run if only 1 processor is allocated. However, the coding pattern
 1666 contains some amount of unavoidable serial computation, as shown in Figure 4.5. In our case, the
 1667 run time, $T_{p,c}$, is estimated to be

$$T_{p,c} = \frac{T_1}{pc} (1 + F_s(c - 1)). \quad (4.3)$$

1668 F_s is the fraction of CPU time dedicated to serial computation. The expected speedup, $S_{p,c}$, is

$$S_{p,c} \equiv \frac{T_1}{T_{p,c}} = \frac{pc}{1 + F_s(c - 1)}. \quad (4.4)$$

1669 From Equation (4.4), we can see that the speed-up scales with p/F_s . We are free to minimize F_s
 1670 asymptotically by enlarging the total models that are submitted to the thread pool, thereby shrinking
 1671 the CPU fraction dedicated to serial operation. We are also free to define exactly how many threads
 1672 and processors we utilize, yet eventually hit a hard cap at the hardware available on our computing
 1673 cluster. HAWC uses Intel Xeon™processors with 48 cores and 96 threads. We see that a successful
 1674 code will scale well as the expected speedup is inversely correlated with F_s . As the total number
 1675 of models sampled grows, the speedup will also.

1676 4.5.2 Implementation

1677 The multithreaded code was written in Python3 and is documented in the `dark_matter_hawc`
 1678 [repository](#) within the script named `mpu_analysis.py`. A version of the script as of April 25
 1679 **TODO: make sure to update on this date** is also provided in Section B.2. It has many dependencies
 1680 including the HAWC analysis software. Figure 4.6 displays the workflow of a job with 3 threads.
 1681 Within a job, SOURCE is kept fixed and CHANS remains 17 elements long. More m_χ are sampled
 1682 from 11 bins up to 49 (for $\gamma\gamma$ and ZZ) and 25 (for remaining CHANS) which amounts to 12 or 6
 1683 mass bins per decade. m_χ and CHANS are permuted into a 473 element list which is split evenly
 1684 across N threads where N is [2, 8, 16]. For each m_χ -CHAN tuple, 1001 $\langle\sigma v\rangle$ values are sampled in

Timing summary for a multi-threaded job.

Import and Load HAL, 3ML, and HAWC analysis software ~ 2 min		
Load HAWC Data ~ 5 min		
Load HAWC PDF's (Detector Resolution files) ~ 4 min		
Load Spatial Model < 1s		
Load Spectra Models <1 s	Load Spectra Models <1 s	Load Spectra Models <1 s
Calculate max LLH (Chan_0, m_{χ_1}) ... max LLH (Chan_?, m_{χ_N}) N = TOTAL/N_THREADS ~ 8 min/Spec_model	Calculate max LLH (Chan_?, m_{χ_1}) ... max LLH (Chan_?, m_{χ_N}) N = TOTAL/N_THREADS ~ 8 min/Spec_model	Calculate max LLH (Chan_?, m_{χ_1}) ... max LLH (Chan_?, m_{χ_N}) N = TOTAL/N_THREADS ~ 8 min/Spec_model
Write results to file <1 s	Write results to file <1 s	Write results to file <1 s
Join Threads and terminate < 1s		

Figure 4.6 Task chart for one multithreaded job developed for this project. Green blocks indicate a shared resource across the threads AND computation performed serially. Red blocks indicate functional parallel processing within each thread. 3 threads are represented here, yet many more can be employed during the full analysis. Jobs are defined by the SOURCE as these require unique maps to be loaded into the likelihood estimator. The m_{χ} , CHAN, and $\langle \sigma v \rangle$ variables are entered into the thread pool and allocated as evenly as possible across the threads.

1685 the likelihood, and the value of $\langle \sigma v \rangle$ that maximizes the likelihood is found. Although rare, fits
1686 that failed are handled on a case by case basis.

1687 4.5.3 Performance

M Tasks	$T_{p,c}$ (hr:min:s)			
	$T_{1,1}$	$T_{1,2}$	$T_{1,8}$	$T_{1,16}$
50	1:40:37.5	0:52:43.7	0:19:13.8	0:13:44.0
74	2:22:30.0	1:15:00.6	0:25:21.3	0:15:49.8
100	(3:07:51.9)	1:40:10.5	0:30:44.4	0:20:01.4
200	(6:02:20.6)	-	1:00:32.0	0:30:35.0
473	(13:58:40.3)	-	2:01:41.4	1:07:53.2

Table 4.2 Timing summaries for analyses for serial and multithreaded processes. M tasks is the number of functional-parallel tasks ran for the computation. $T_{p,c}$ is a single run time in hours:minutes:seconds for runs utilizing p nodes and c threads. Runs are run interactively on the same computer to maximize consistency. Empty entries are indicated with '-'. (·) entries are estimated entries extrapolated from data earlier in the column.

1688 We see a significant reduction to wall time needed for our dSph analyses to run. Table 4.2

1689 shows the timing summaries for analyses of different sizes and thread counts. Additionally, the
 1690 efficiency gained when consolidating the serial loading of data is also apparent in our ability to
 1691 study many more tasks in about the same amount of wall time as a smaller serial computation. Trials
 1692 represented in the table were run on an AMD Opteron® processor 6344 with 48 cores, 2 threads per
 1693 core; 2.6 GHz clock. This is not the same architecture used for analysis on the HAWC computing
 1694 cluster however they are similar enough that results shown here are reasonably representative of
 1695 computing on the HAWC computing cluster. I use Tab. 4.2 for the inferences and conclusions in
 1696 the following paragraphs.

1697 First, we want to find T_s , the time of serial computation. From Fig. 4.5, the timing for our
 1698 coding pattern can be written as

$$T_s + Mt_p = T_{1,1}^M. \quad (4.5)$$

1699 M is the number of functional-parallel tasks (represented as column 1 of Tab. 4.2), and t_p is the
 1700 average time to complete a single parallel task. $T_{1,1}^M$ is the total time for a parallel program to run if
 1701 only 1 processor is allocated for M parallel task. With two runs of different M (M_1 and M_2), we
 1702 can use a system of equations to compute

$$T_s = 803.1\text{s} \text{ and } t_p = 104.6\text{s} \quad (4.6)$$

1703 Now, we have specific estimation for the fraction of serial computing time, F_s :

$$F_s = \frac{803.1}{803.1 + 104.6 \cdot M}. \quad (4.7)$$

1704 The maximum M for this study is 473 which evaluates to: $F_s = 0.016$ or 1.6% of computing time.
 1705 Table 4.3 shows the resulting speedups.

1706 We see a speedup that generally exceeds expectations from Eq. (4.4) for real trail runs. We also
 1707 see that there are diminishing returns as the number of threads increases. For small jobs with large c ,
 1708 both the expected and observed speedup are significantly smaller than c . One thing not considered
 1709 in Eq. (4.4) is the time incurred via communication latency. Communication latency increases
 1710 with the number of threads and contributes to diminishing returns. Additionally, these values are

M Tasks	F_s	$S_{1,2}$	$S_{1,8}$	$S_{1,16}$
50	1.33 E-1	1.90 [1.76]	5.23 [4.14]	6.35 [5.34]
74	9.40 E-2	1.90 [1.83]	5.62 [4.82]	9.00 [6.64]
100	7.13 E-2	1.88 [1.87]	6.11 [5.34]	9.38 [7.73]
200	3.70 E-2	- [1.93]	5.98 [6.36]	11.85 [10.29]
473	1.60 E-2	- [1.97]	6.89 [7.20]	12.35 [12.91]

Table 4.3 Speed up summaries for analyses for serial and multithreaded processes. M tasks is the number of functional-parallel tasks ran for the computation. $S_{p,c}$ is a single speedup comparison for runs utilizing p nodes and c threads. [·] are the estimated speedups calculated from Tab. 4.2, Eq. (4.7), and Eq. (4.4). Empty entries are indicated with '-'.

1711 for single runs and do not consider the stochastic variation expected in a shared high performance
 1712 computing resource. Therefor, these results are not strictly conclusive, yet demonstrate the merits
 1713 of multi-threading. We see very clearly that there is a lot to gain, and this new coding pattern will
 1714 expand HAWC's analysis capabilities.

1715 **4.6 Analysis Results**

1716 3 of the 43 $\mathcal{L}\mathcal{S}$ dSphs considered for the multithreaded analysis. These dSph are analyzed
 1717 for emission from DM annihilation according to the likelihood method described in Section 3.4.
 1718 The three likelihood profiles are then stacked to synthesize a combined limit on the dark matter
 1719 annihilation cross-section, $\langle\sigma v\rangle$. This combination is done each of the 17 SM annihilation channels.
 1720 Figure 4.7 and Fig. 4.8 show the combined limits for all annihilation channels with HAWC's
 1721 observations. Test statistics of the best fit $\langle\sigma v\rangle$ values for each m_χ and CHAN are shown in Fig. 4.9
 1722 and Fig. 4.10. We also compare these limits to HAWC's Glory Duck limits shown in Section 3.5.
 1723 The comparison to Glory Duck are featured in Fig. 4.11 for all the DM annihilation channels studied
 1724 for Glory Duck. A full comparison is provided in the appendix in Fig. B.2, Fig. B.3, and Fig. B.4.
 1725 Here, we show updated limits for $\chi\chi \rightarrow b\bar{b}, e\bar{e}, \mu\bar{\mu}, \tau\bar{\tau}, t\bar{t}, W^+W^-$, $\gamma\gamma$ and ZZ . For the first time
 1726 ever, we show limits for $\chi\chi \rightarrow c\bar{c}, s\bar{s}, u\bar{u}, d\bar{d}, \nu_e\bar{\nu}_e, \nu_\mu\bar{\nu}_\mu, \nu_\tau\bar{\nu}_\tau, gg$, and hh .

1727 No DM was found in HAWC observations. The largest excess found in HAWC data was for DM
 1728 annihilating to W -bosons or $\nu_e\bar{\nu}_e$ for $m_\chi = 10$ TeV at significance 2.11σ and 2.14σ respectively.
 1729 HAWC's limits and excesses are dominated by Segue1. Coma Berenices shows excesses at higher
 1730 DM mass, yet no similar excesses were observed in Segue1 or Sextans. Sextans did not contribute

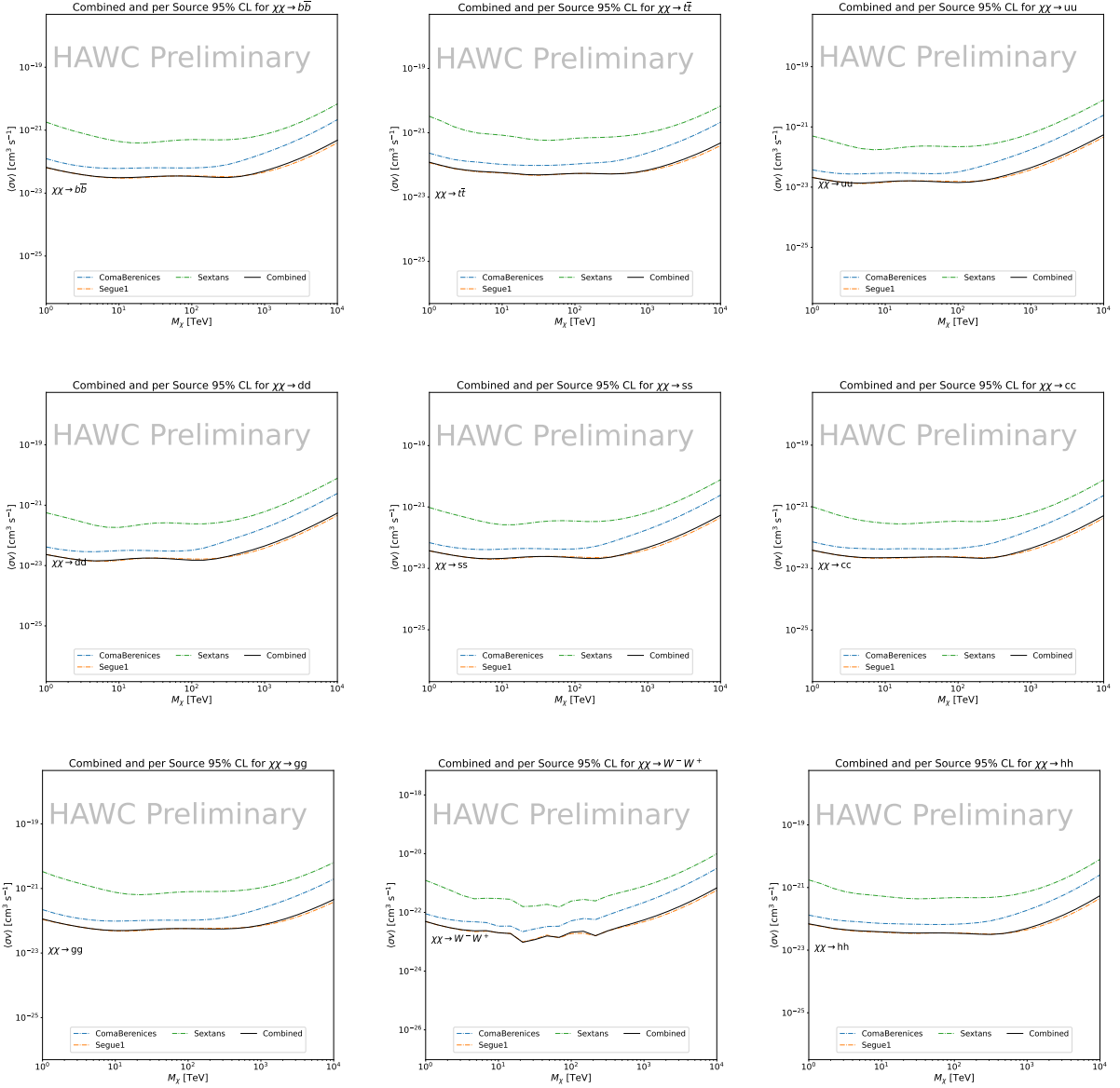


Figure 4.7 HAWC upper limits at 95% confidence level on $\langle\sigma v\rangle$ versus m_χ for $\chi\chi \rightarrow b\bar{b}$, $t\bar{t}$, $u\bar{u}$, $d\bar{d}$, $s\bar{s}$, $c\bar{c}$, gg , W^+W^- , and hh . Limits are with $\mathcal{L}\mathcal{S}$ J -factors [80]. The solid line represents the observed combined limit. Dashed lines represent limits from individual dSphs.

1731 significantly to signal excesses or the combined limit as it is at high zenith. Draco was not included
 1732 as the PDF of some of our analysis bins were wider than what is reasonable for a point source
 1733 analysis. Draco is at a high zenith for HAWC, so the effort required to include it was not justified
 1734 by the benefits.

1735 We did not generate background trials in time of writing this thesis. These are not shown and

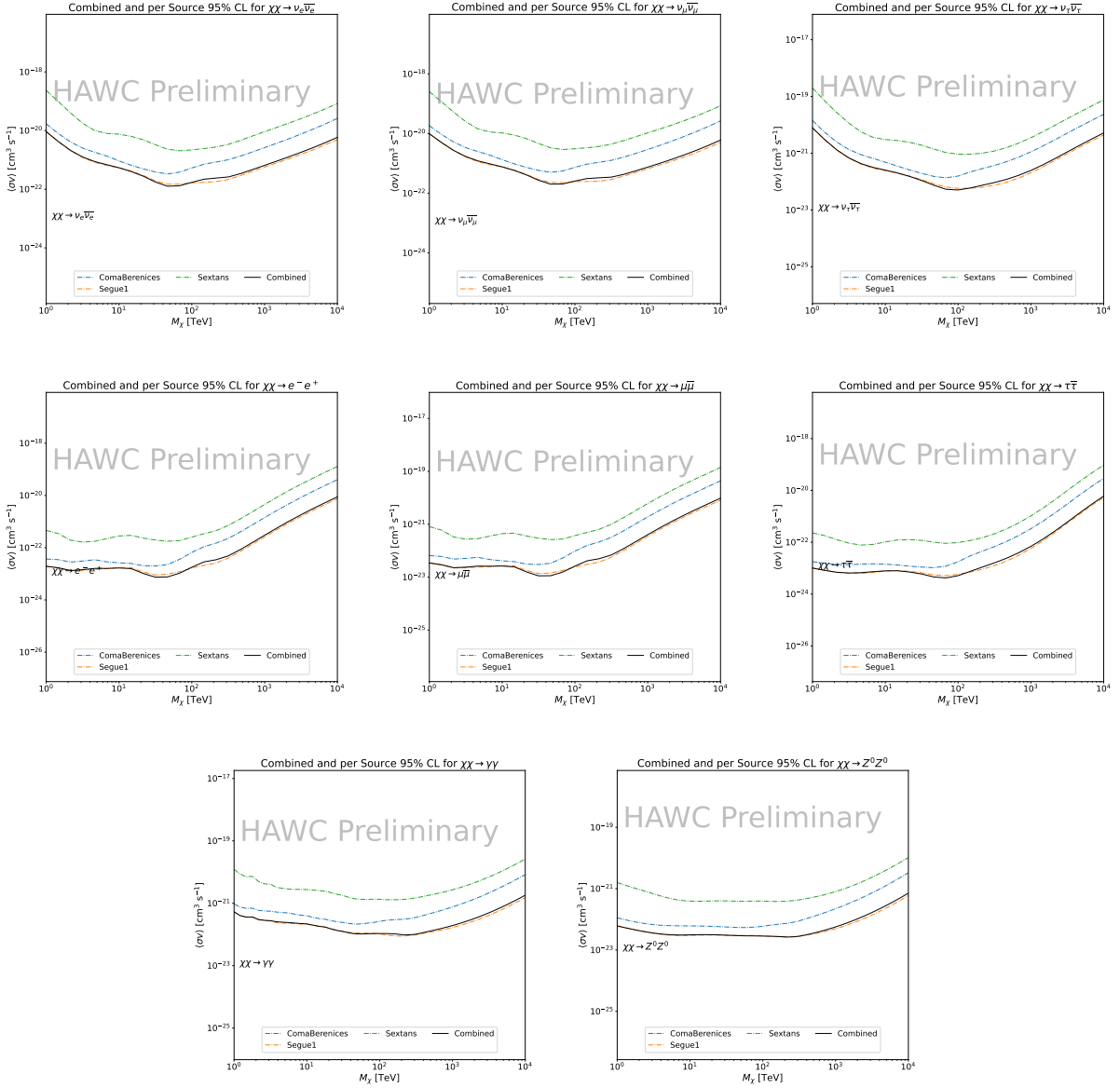


Figure 4.8 HAWC upper limits at 95% confidence level on $\langle\sigma v\rangle$ versus m_χ for $\chi\chi \rightarrow \nu_e \bar{\nu}_e$, $\nu_\mu \bar{\nu}_\mu$, $\nu_\tau \bar{\nu}_\tau$, $e \bar{e}$, $\mu \bar{\mu}$, $\tau \bar{\tau}$, $\gamma\gamma$ and ZZ . Limits use $\mathcal{L}S$ J -factors [80]. The solid line represents the observed combined limit. Dashed lines represent limits from individual dSphs.

1736 are an immediate next step for this analysis before publication.

1737 When comparing these results to Section 3.5, we see an overall decrease to the confidence limit
 1738 therefore improvement to HAWC's expected sensitivity. This improvement is generally stronger
 1739 than a doubling of data, or a factor $\sqrt{2}$ decrease. The comparison is somewhat complex and
 1740 dependent on the dSph and SM annihilation channel. Figure 4.11 shows the comparisons of limits

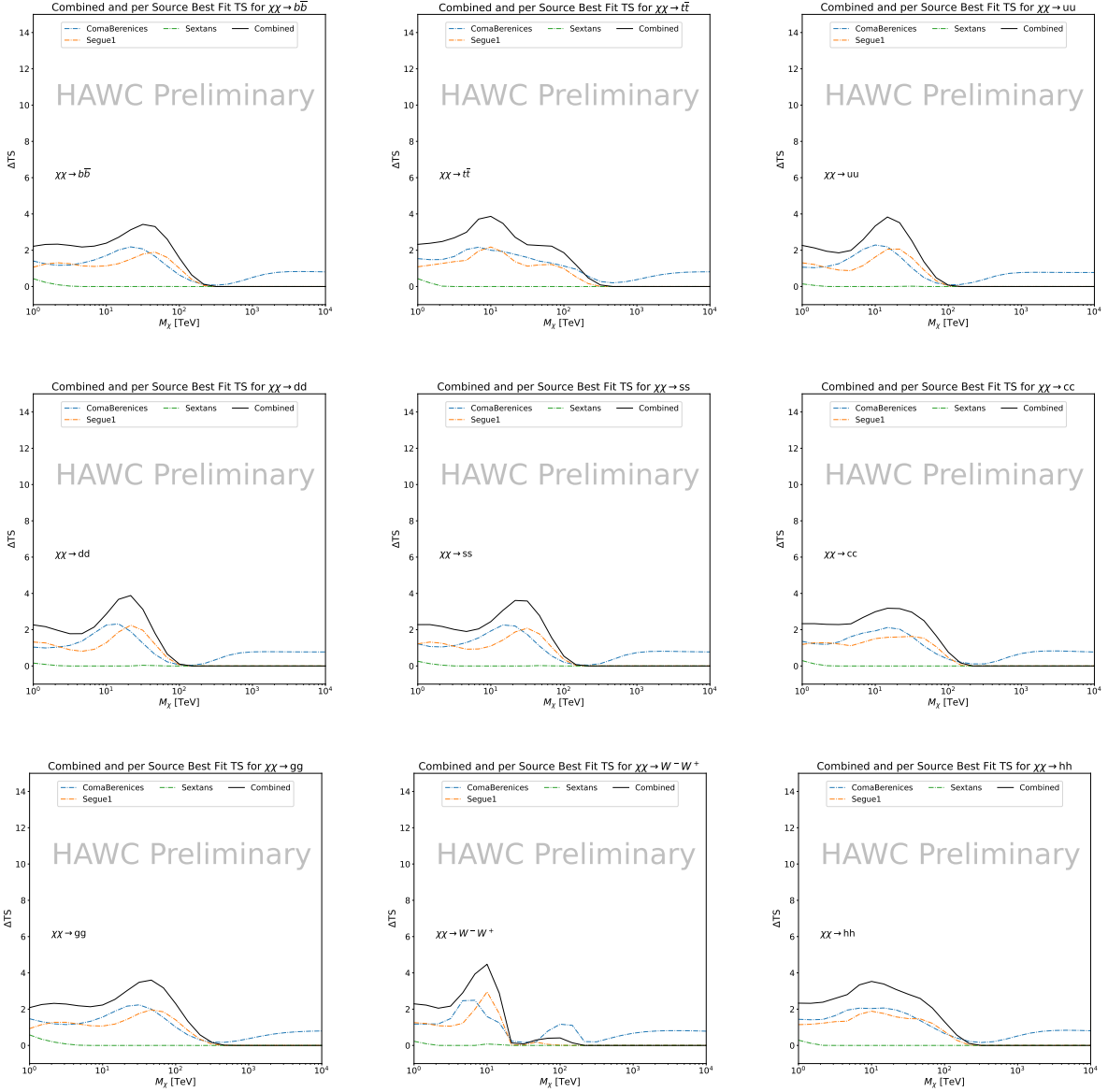


Figure 4.9 HAWC TS values for best fit $\langle\sigma v\rangle$ versus m_χ for SM annihilation channels: $\chi\chi \rightarrow b\bar{b}$, $t\bar{t}$, $u\bar{u}$, $d\bar{d}$, $s\bar{s}$, $c\bar{c}$, gg , W^-W^+ , and hh . Limits use \mathcal{LS} J -factors. The solid black line shows the combined best fit TS values. The colored, dashed lines are the TS values from each dSph.

1741 calculated for this analysis and Glory Duck (Section 3.5). Segue 1 and Coma Berenices are low
 1742 zenith where improvements to HAWC's analysis come only from energy estimation. Differences
 1743 between these two are dominantly from their differences in J -factor, half-light radii of the dSphs,
 1744 and the particle physics inputs. Substantial gains in HAWC's analysis methods (pass 5.F) were
 1745 made at high zenith which is important for sources like Sextans. The HDM particle physics model

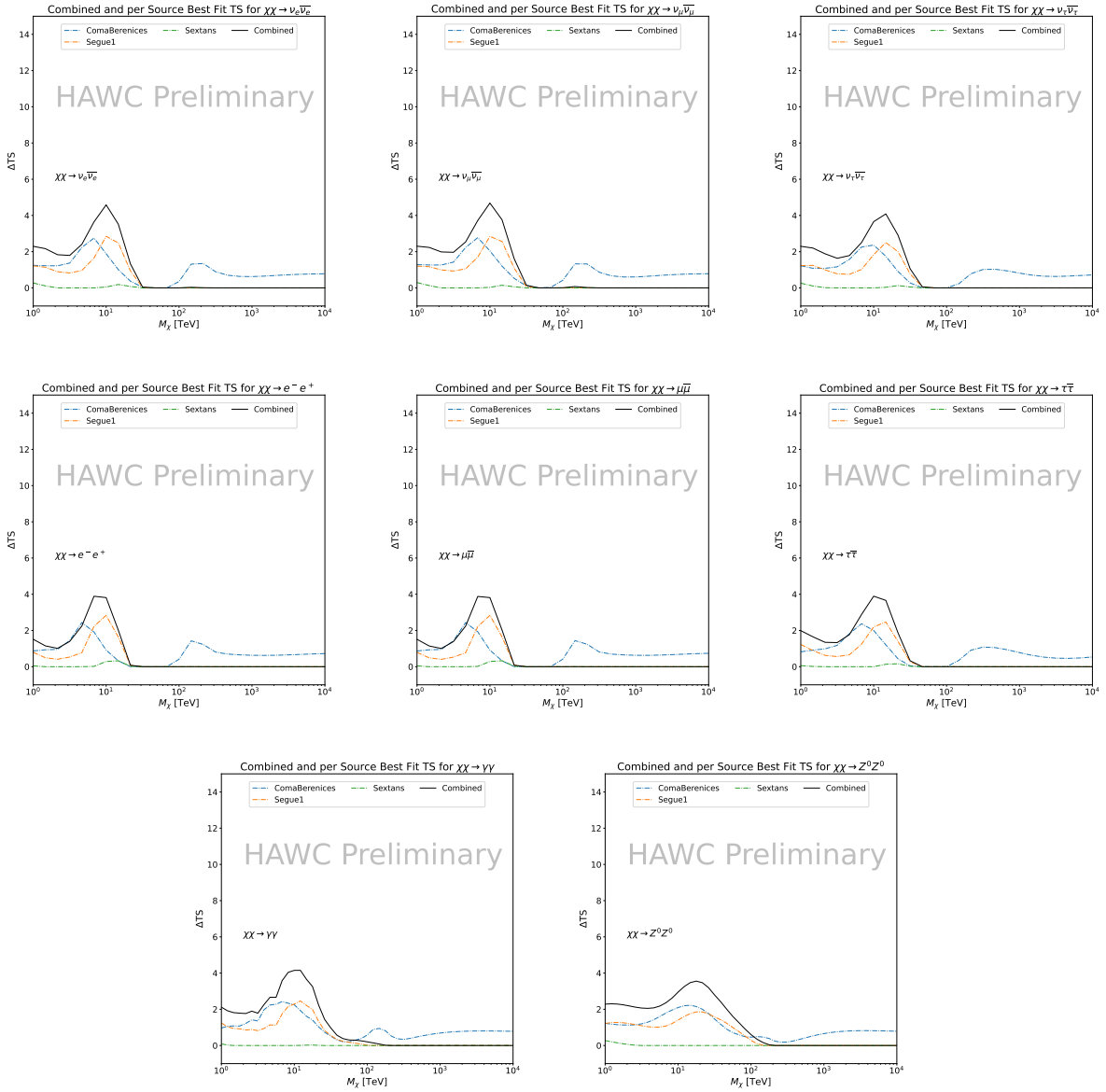


Figure 4.10 HAWC TS values for best fit $\langle \sigma v \rangle$ versus m_χ for SM annihilation channels: $\chi\chi \rightarrow \nu_e \bar{\nu}_e$, $\nu_\mu \bar{\nu}_\mu$, $\nu_\tau \bar{\nu}_\tau$, $e^- e^+$, $\mu \bar{\mu}$, $\tau \bar{\tau}$, $\gamma\gamma$ and ZZ . Limits use \mathcal{LS} J -factors. The solid black line shows the combined best fit TS values. The colored, dashed lines are the TS values from each dSph.

1746 produces almost identical spectra to the PPPC for $\chi\chi \rightarrow e^- e^+$. This channel can be used to
 1747 compare limits between dSph spatial models. Overhead sources see minimal improvement to the
 1748 limits, while high zenith sources see an order of magnitude improvement for all DM masses. Softer
 1749 SM annihilation channels see broad improvements to the limit compared to harder channels.

1750 **4.7 Systematics**

1751 Systematics to this analysis are identical to what was performed earlier in Glory Duck, Sec-
1752 tion 3.7. We are also sensitive to the choice in spatial template, and this was explored in Section 3.7.2
1753 and Section 3.8.2.

1754 **4.8 Conclusion and Discussion**

1755 In this multithreaded analysis, we have used observations of 3 dSphs from HAWC to perform
1756 a collective DM annihilation search towards dSphs. The data were combined across sources
1757 to significantly increase the sensitivity of the search. Advanced computational techniques were
1758 deployed to accelerate wall-time spent analyzing by an order of magnitude. We have observed
1759 no significant deviation from the null, no DM hypothesis, and so present our results in terms of
1760 upper limits on the velocity-weighted cross-section, $\langle\sigma v\rangle$, for seventeen potential DM annihilation
1761 channels across four decades of DM mass.

1762 This analysis serves as a proof of concept for multithreaded HAWC analyses with large parameter
1763 spaces. Larger datasets with fast techniques will be essential to tackling the DM problem. The
1764 models we used for this study include annihilation channels with neutrinos in the final state.
1765 Advanced studies could aim to merge our results with those from neutrino observatories with large
1766 data sets.

1767 A full HAWC analysis will include systematic studies of the J -factor distributions. Additionally,
1768 because of the timing reduction, the study can be doubled in size to include DM decay. We have not
1769 yet received the remaining spatial profiles to the \mathcal{LS} catalog, and limits can be quickly computed
1770 once these are received. Finally, statistical studies with Poisson variation of HAWC's background
1771 are essential to a comprehensive understanding of our observed excesses.

Segue1

Coma Berenices

Sextans

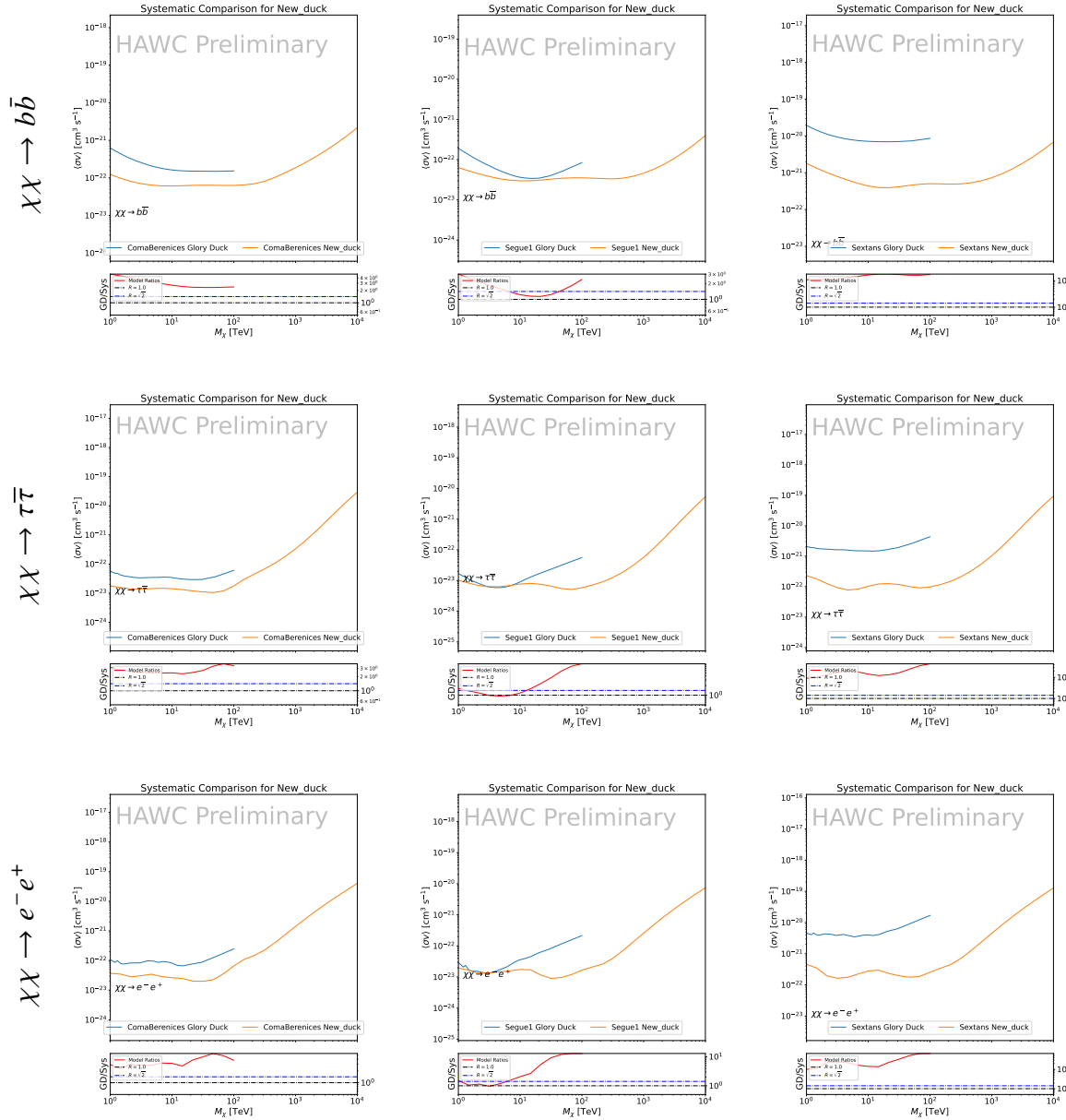


Figure 4.11 Comparison of HAWC limits from this analysis to Glory Duck (Fig. 3.5) for 3 dSphs and 3 DM annihilation channels: $b\bar{b}$, $\tau\bar{\tau}$, and $e\bar{e}$. Each sector shows the 95% confidence limit from Glory Duck (blue line) and this analysis (orange line) in the top plot. The lower plot features the ratio in log scale of Glory Duck to this analysis in a red solid line. Horizontal dashed lines are for ratios of 1.0 (black) and $\sqrt{2}$ (blue). Ratios larger than 1.0 are for limits smaller, or stricter, than Glory Duck. Ratios larger than $\sqrt{2}$ indicates limits are stricter than a simple doubling of the Glory Duck data.

1772

CHAPTER 5

ICECUBE NEUTRINO OBSERVATORY

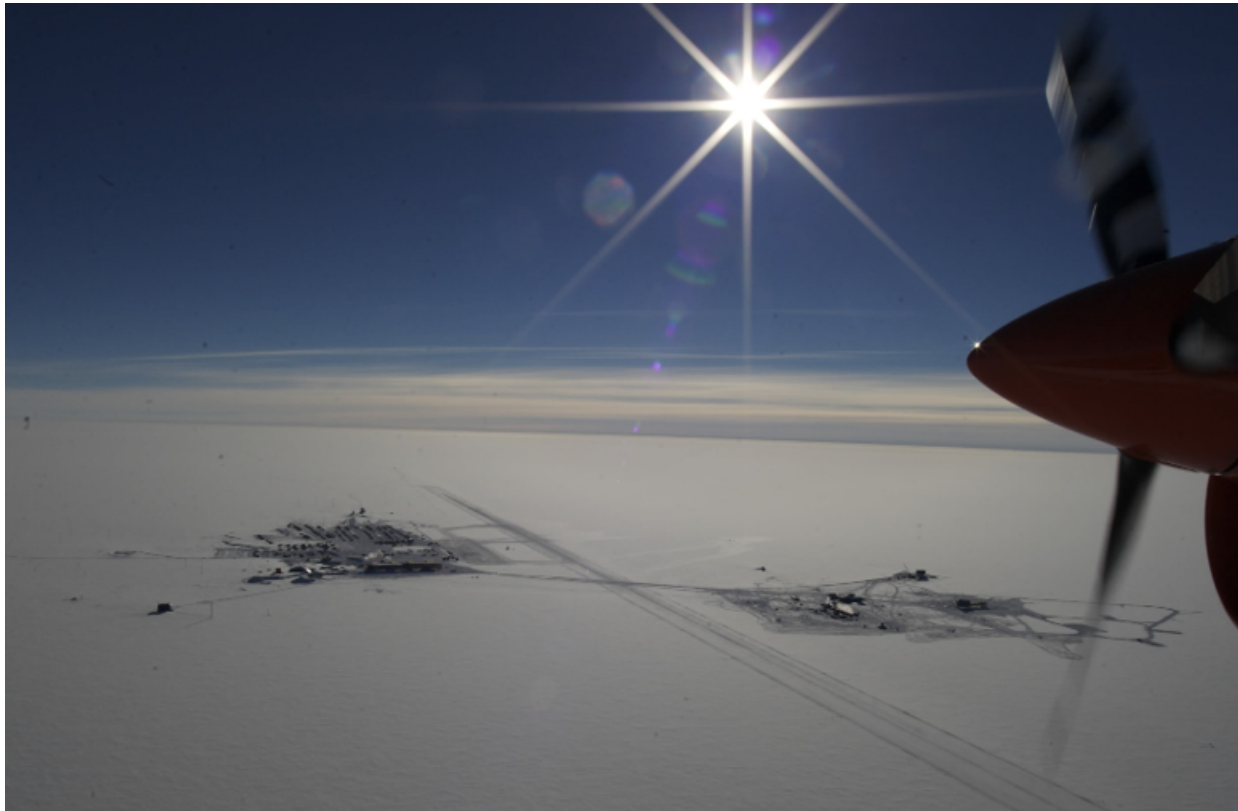


Figure 5.1 IceCube Neutrino observatory at the South Pole. Image from [TODO: cite where you got this from.](#)

1773 Located at the South Pole, the IceCube Neutrino Observatory is a pivotal instrument for
1774 neutrino astronomy. IceCube's primary function is the detection and analysis of elusive, high-
1775 energy neutrinos. These neutrinos carry information from the most energetic and distant cosmic
1776 phenomena. The observatory uses thousands of digital optical modules embedded in a cubic
1777 kilometer of Antarctic ice to detect Cherenkov radiation. This radiation occurs when neutrinos
1778 interact with the ice, revealing their origin and energy.

1779 IceCube is a critical component in the multi-messenger astrophysics toolkit, especially in the
1780 search for dark matter and beyond standard model (BSM) astrophysical processes. The observa-
1781 tory's analysis of neutrino signals enhances our understanding of the universe by correlating these
1782 signals with other cosmic messengers, including electromagnetic, gravitational waves, and cosmic

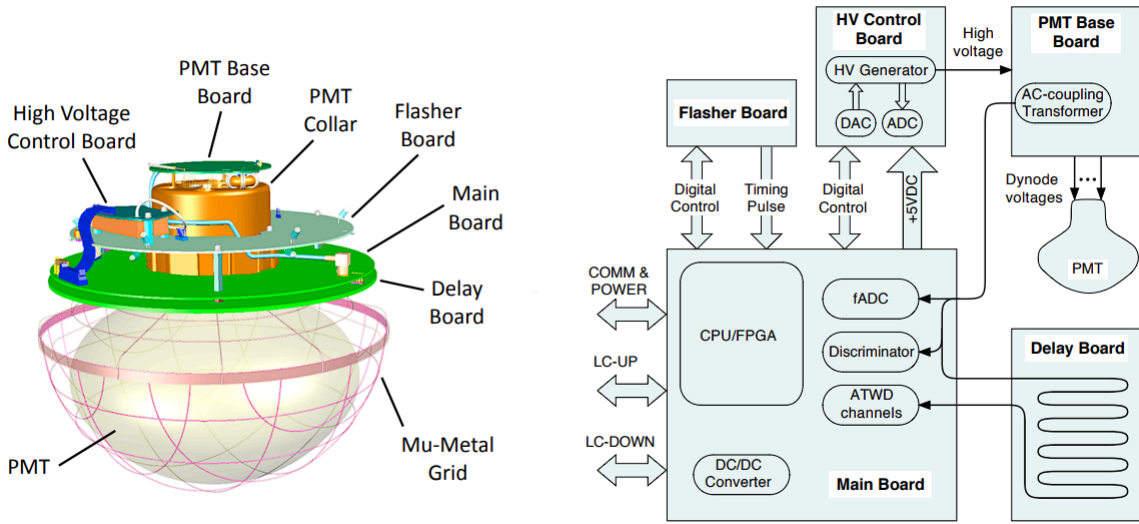


Figure 5.2 ~~TODO: pasted~~Components of the DOM, showing mechanical layout (left) and functional connections (right). Figure from [83]

1783 rays.

1784 The following sections will discuss the observatory's design, data acquisition, event recon-
 1785 struction methodologies, and its significance in observing the Northern Sky. These details will
 1786 underscore IceCube's role in advancing our understanding of the cosmos through data-driven
 1787 insights.

1788 5.1 The Detector

1789 The IceCube Neutrino Observatory is embedded within a cubic kilometer of Antarctic ice at
 1790 the South Pole. IceCube's modules are designed to detect neutrinos through Cherenkov radiation
 1791 emitted during neutrino interactions with the ice. It comprises 5160 Digital Optical Modules
 1792 (DOMs), arranged across 86 strings that span depths of 1450 m to 2450 m beneath the surface. This
 1793 arrangement allows IceCube to capture high-energy neutrinos across a broad neutrino spectrum.

1794 5.1.1 Hardware and Construction

1795 Digital Optical Modules (DOMs) are at the core of IceCube's detection technology, each encased
 1796 in a glass sphere to withstand deep-ice pressures. A DOM features a 10-inch photomultiplier tube
 1797 (PMT) for Cherenkov light detection, a high-voltage power supply for the PMT, and a Main



Figure 5.3 ICL. Picture from [84].

1798 Board for signal digitization and timestamping. An LED Flasher Board is included for calibration
1799 purposes, assisting in verifying DOM responses and measuring ice optical properties. The DOMs
1800 are deployed along cables on strings in a hexagonal grid pattern, which spans a cubic kilometer.
1801 Strings are placed with 125 meters of horizontal spacing, and DOMs are vertically separated
1802 by 17 meters on each string, chosen to optimize detection capability for neutrinos within the
1803 teraelectronvolt (TeV) to petaelectronvolt (PeV) energy range.

1804 DeepCore and IceTop, additional components of IceCube, extend its research capabilities.
1805 DeepCore, with its denser array of DOMs, targets lower energy neutrinos for studies such as
1806 neutrino oscillations and dark matter. IceTop, situated at the ice surface, measures cosmic rays,
1807 contributing data that complement the neutrino observations from below the ice.

1808 The central hub for IceCube's operations is the IceCube Laboratory (ICL), situated at the
1809 surface at the center of the array. This facility houses the servers and computers responsible for
1810 data acquisition and online filtering, connected to the DOMs via cables routed up from beneath the

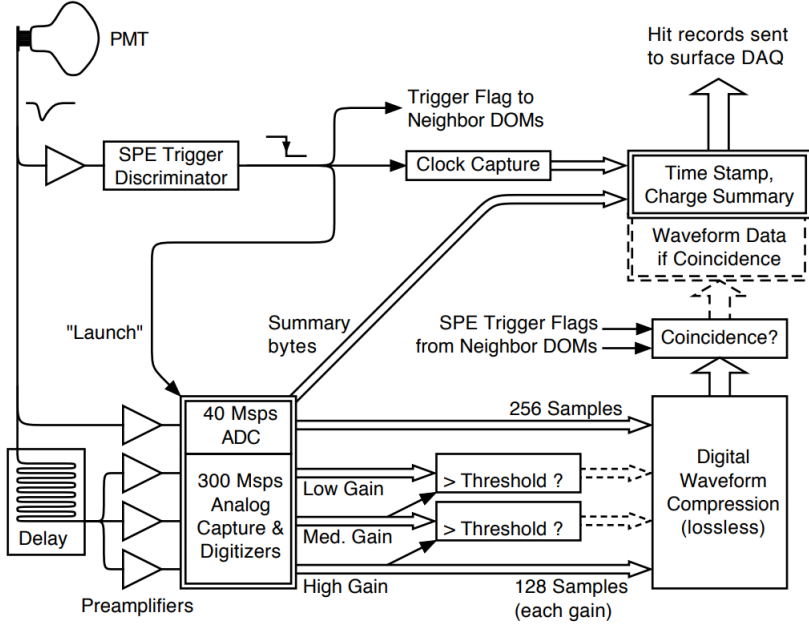


Figure 5.4 TODO: Copied Data flow diagram for recording and processing of PMT waveforms in the DOM to form “Hit Records” that are sent to the surface DAQ computers. As shown by dashes, full waveform data are only included when neighbor DOMs report time-coincident signals above the SPE discriminator threshold. Additionally, data from low-gain channels are omitted for waveforms that are within range of higher-gain channels.

1811 ice [83]. The ICL plays a crucial role in managing the data flow from the ice, ensuring continuous
 1812 operation and data integrity. It is designed to maintain optimal conditions for its electronic
 1813 equipment, including temperature control and protection against electromagnetic interference,
 1814 which is vital for the accurate processing and analysis of the collected data [83].

1815 5.1.2 Data Acquisition

1816 The data acquisition process in the IceCube Neutrino Observatory starts when a photomultiplier
 1817 tube (PMT) within a Digital Optical Module (DOM), distributed between 1450 m and 2450 m
 1818 beneath the ice, detects light surpassing a threshold of 0.25 photoelectrons. The importance of the
 1819 information transmitted to the surface computers depends on the detection of signals by neighboring
 1820 DOMs within a microsecond window. Isolated signals prompt a Soft Local Coincidence (SLC)
 1821 response, transmitting only a timestamp and a charge summary. In contrast, signals detected by
 1822 neighboring DOMs initiate a Hard Local Coincidence (HLC), resulting in the full waveform being
 1823 compressed and sent along with the timestamp and charge summary to the IceCube Laboratory

1824 (ICL), located at the surface at the center of the array [83].

1825 Achieving uniform timing across DOMs is essential for accurate event reconstruction. Each
1826 DOM's independent clock undergoes a rigorous calibration process to synchronize with the ICL's
1827 clocks, with the times further translated to Universal Coordinated Time (UTC). This calibration is
1828 critical, involving continuous pulses sent between the DOMs and the ICL to adjust the waveforms
1829 by subtracting the common baseline and applying the gain. This step is vital for the precise
1830 interpretation of the collected data [83].

1831 Within the ICL, the Data Acquisition (DAQ) system employs various trigger algorithms to
1832 discern neutrino events from the vast majority of DOM hits caused by dark noise. One such
1833 mechanism, the Simple Multiplicity Trigger (SMT), requires a specific number of HLC hits within
1834 a brief timeframe to recognize a series of hits as an event. This approach is pivotal for identifying
1835 sequences of detections likely resulting from neutrino interactions [83].

1836 Further refining the observatory's data, the Processing and Filtering (PnF) system, also housed
1837 within the ICL, applies around 25 different filters after initial event detection. Each filter is
1838 designed for specific physics analyses, significantly managing the observatory's data throughput
1839 by focusing on scientifically valuable information. The system employs filters like the Muon Track
1840 Filter to isolate high-quality track events crucial for neutrino source identification, the Shower
1841 Event Filter to select events with large energy deposits indicative of neutrino interactions, and the
1842 High-Charge Filter to highlight events with extensive photoelectron deposits, pointing to high-
1843 energy astrophysical neutrinos. These filters ensure that the data prepared for further analysis and
1844 transmission to researchers in the Northern Hemisphere contains the most significant scientific
1845 insights [83].

1846 The operational control of the observatory, maintained by the LiveControl system within the
1847 ICL, oversees the DAQ and PnF systems. It handles the initiation and conclusion of data-taking
1848 runs and maintains a database of operational parameters. Alerting operators to any deviations
1849 from expected conditions, this system is crucial for ensuring the observatory operates within its
1850 optimal parameters, highlighting the integrated effort required to manage and analyze the vast data

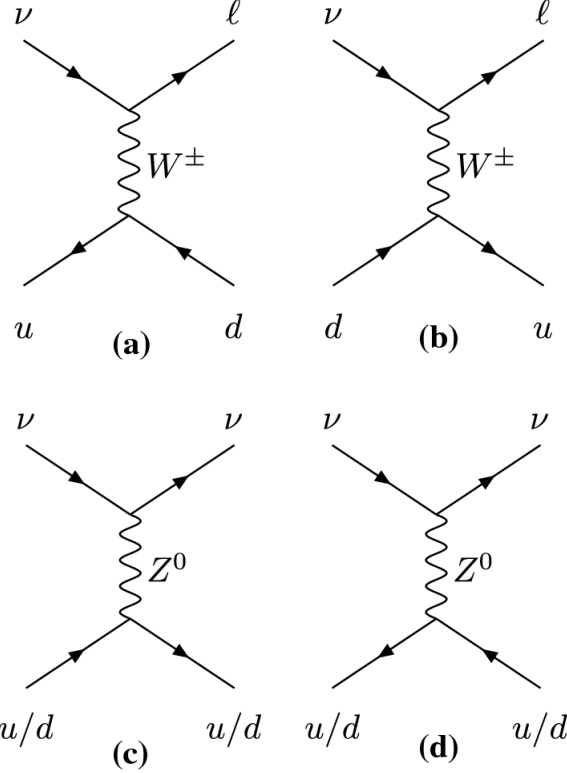


Figure 5.5 TODO: copied. The parton level W (a/b) and Z (c/d) boson exchange between neutrinos and light quarks. Feynman diagrams for charged current interactions (a/b) and neutral current interactions (c/d) between neutrinos and quarks that make up nucleons in the ice. A W boson is exchanged in charged current interactions and produces an outgoing lepton corresponding to the neutrino flavor along with hadronic cascades. A Z boson is exchanged in neutral current interactions and only hadronic cascades are produced. Figure from [85]. a double cascade event topology, shown in Figure 5.9. If it has a lower energy, it will

1851 generated by the IceCube Neutrino Observatory [83].

1852 5.2 Event Reconstruction

1853 Event Reconstruction within the IceCube Neutrino Observatory transforms signals captured by
 1854 Digital Optical Modules into quantifiable scientific insights. The goal of event reconstruction is
 1855 to ascertain the origin, trajectory, and strength of interacting neutrinos. This process is pivotal for
 1856 interpreting signals as either originating from celestial neutrino sources or other phenomena. I will
 1857 focus mostly on how IceCube reconstructs track-like events as these are the most relevant for this
 1858 dissertation.

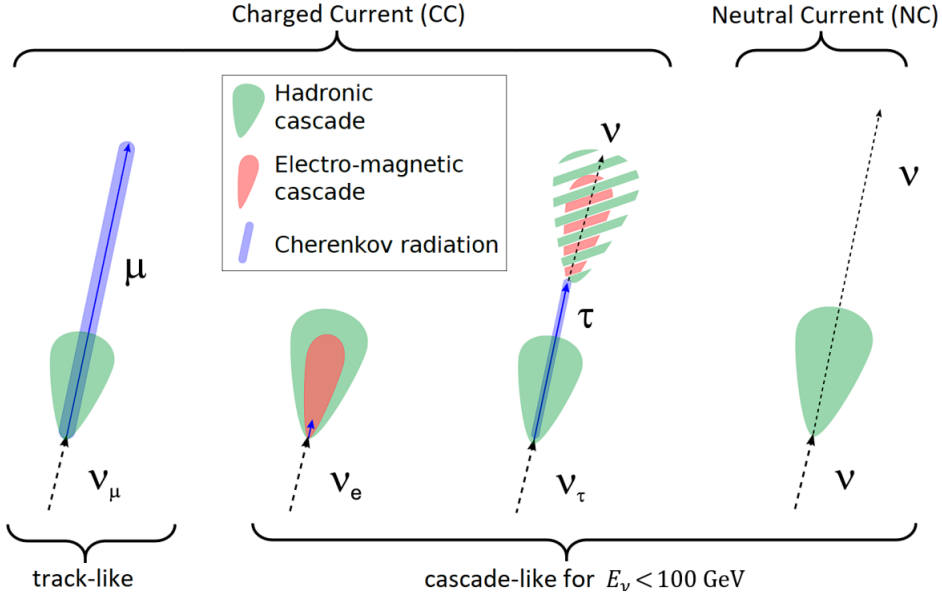


Figure 5.6 TODO: copied. Event signature of high energy NC and CC neutrino interactions. The signature is decomposed in hadronic and electromagnetic cascades and Cherenkov radiation from a single long ranging particle. The type of cascade from the tau decay depends on the decay channel of the tau. For energies below a PeV the two cascades of the tau signature overlap and can not be distinguished. For a sparse instrumented detector like IceCube, the events can be classified in track-like and cascade-like. Figure from [86].

1859 5.2.1 Tracks and Cascades

1860 Events in IceCube's detector volume manifest primarily as either tracks or cascades. The
 1861 primary cause of the event topology are both the neutrino flavor and the nature of the primary
 1862 neutrino's interaction with the ice.

1863 Tracks emerge from charged-current (CC) interactions involving muon neutrinos (ν_μ). These
 1864 events are characterized by the production of a high-energy muon (μ). These muons, due to its
 1865 relatively large mass compared to electrons, can traverse substantial distances through the ice,
 1866 exceeding kilometers. These long trajectories are obvious from continuous, distinct, and elongated
 1867 track of Cherenkov light in the ice. See Fig. 5.7 for a simulated track event. The angular deviation
 1868 between the incoming ν_μ and the secondary muon is notably slight, tapering to near 0.3° above
 1869 TeV energies. Therefore, muon tracks closely approximate the primary neutrino's path [85, 88].
 1870 Such precision affords angular resolutions finer than 1° for TeV neutrinos which facilitates the
 1871 determination of their cosmic origins [85].

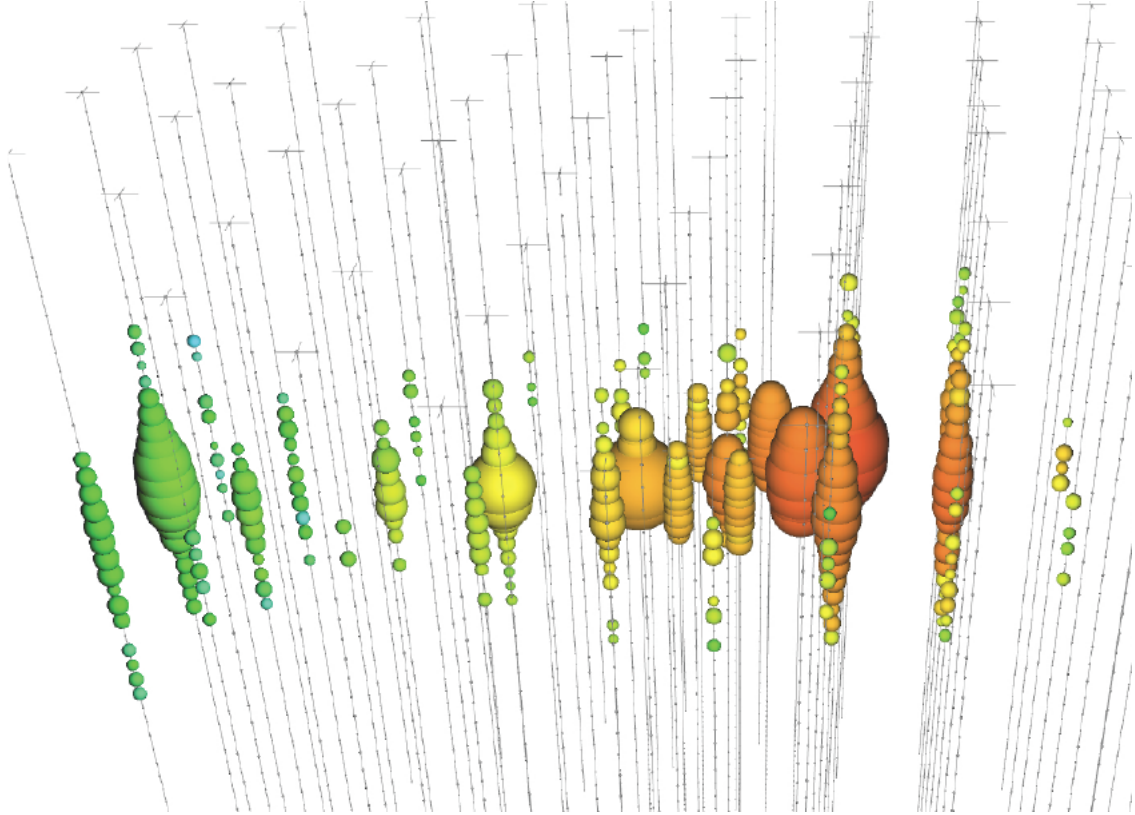


Figure 5.7 TODO: copied. A simulation of a track-like event in IceCube. Tracks are produced when CC muon neutrino interactions occur and a muon is produced in return. The color of the DOMs represent the arrival times of the photons (red is early, green is late). The size of the DOM represents the amount of charge that is seen in that DOM. The CC neutrino interaction occurred near the red hits, with the muon exiting to the left. Figure taken from [87].

1872 Cascades are products of both neutral-current (NC) interactions across all neutrino flavors and

1873 CC interactions involving electron or tau neutrinos, ν_e and ν_τ respectively. Unlike tracks, cascades

1874 result in a more localized burst of Cherenkov radiation. The burst imprints as a nearly spherical

1875 light pattern from the rapid dissipation of energy by the produced particles. This diffusion creates

1876 a distinct event signature with good energy estimation, but worse directional clarity compared to

1877 track events. The isotropic nature of cascades leads to larger angular uncertainties, typically around

1878 15°, Yet, cascades excel in providing energy measurements, with resolutions reaching as tight as

1879 15% from the contained nature of the energy deposition [85, 88].

1880 A rarely observed event type, the double-bang event, posited for ν_τ interacting via CC at energies

1881 above 1 PeV, would display as two distinct cascades within the detector. These events start from an

1882 initial interaction and subsequent decay of the τ lepton over a discernible distance. The double bang

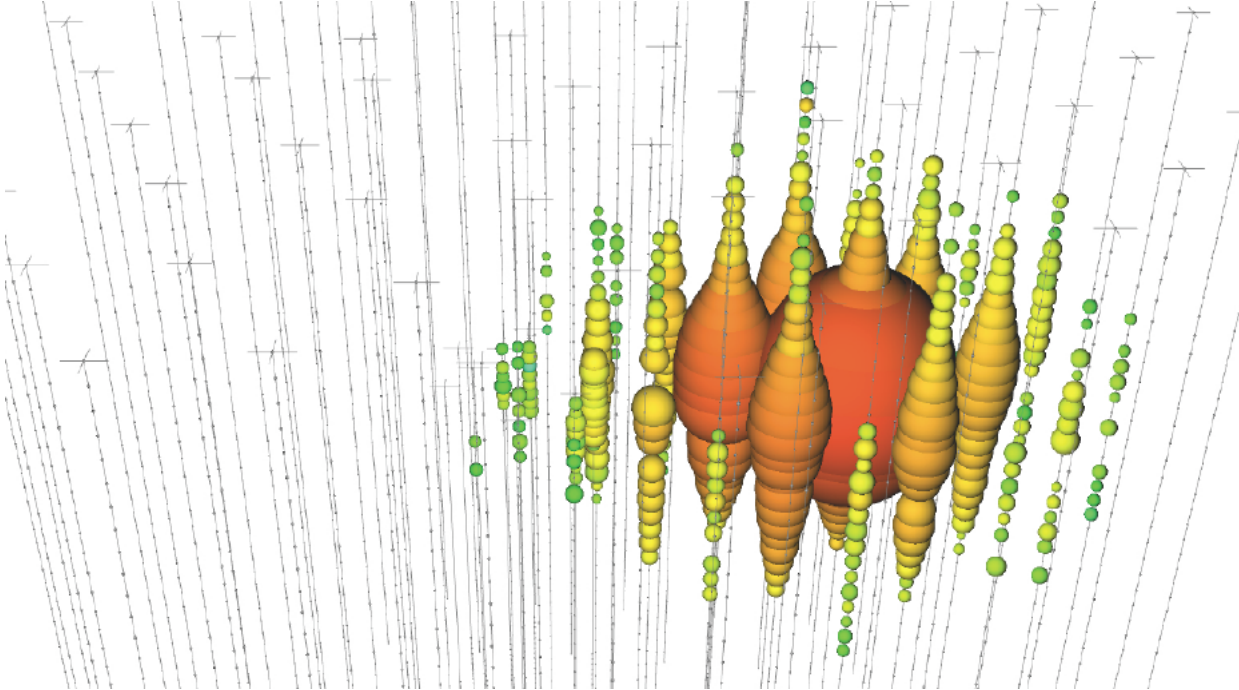


Figure 5.8 TODO: copied A simulation of a cascade-like event in IceCube. Cascades can be produced by NC interactions for all flavors of neutrinos, for CC interactions for electron neutrinos, and for CC interactions for tau neutrinos for energies below 1 PeV. The color of the DOMs represent the arrival times of the photons (red is early, green is late). The size of the DOM represents the amount of charge that is seen in that DOM. Figure taken from [87].

1883 offers a unique marker for high-energy ν_τ detection [85]. Preliminary whispers of double-bang
 1884 events IceCube have been observed [89]. Yet, efforts are ongoing to isolate such an event.

1885 5.2.2 Reconstruction of Track Direction

1886 Angular reconstruction for ν_μ induced tracks in the IceCube detector volume starts with the
 1887 LineFit algorithm [90]. LineFit estimates the muon's trajectory through a least squares fit to the
 1888 Cherenkov light hits on the DOMs. LineFit assumes the muon propagates with constant velocity
 1889 and treats its path as linear in order to simplify the emission patterns of Cherenkov radiation. To
 1890 improve this approximation, the Huber penalty function [91] is applied which distinguishes between
 1891 signal and noise by considering the spatial distribution of hits relative to the track [92].

1892 The reconstruction process is refined further by the Single Photoelectron (SPE) likelihood
 1893 method, which calculates the probability of photon arrival times at the DOMs [91]. It does so by

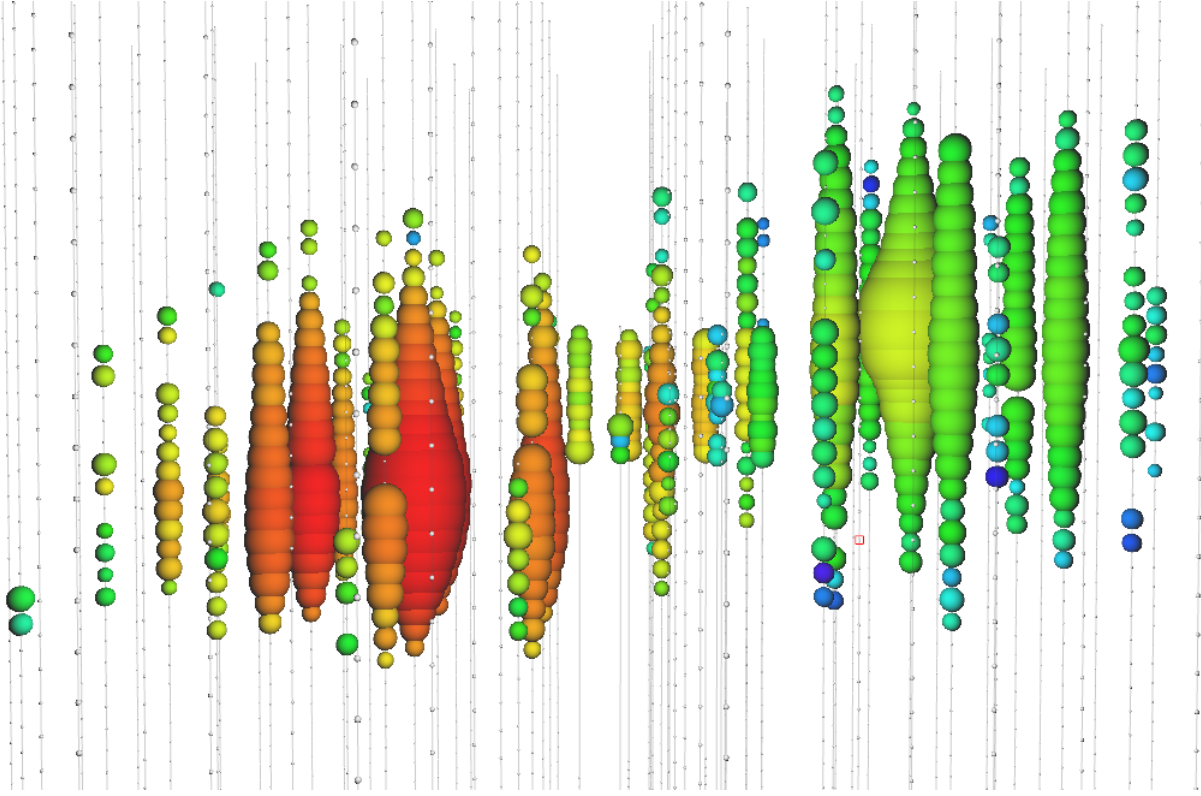


Figure 5.9 **TODO: copied.** A simulation of a double-bang event in IceCube. Double-bang events occur when CC tau neutrino interactions occur above 1 PeV producing a g lepton. When these high-energy g leptons are produced, the g leptons are able to travel over 50 m in IceCube before they decay. At these distances, the light emission from the decays are distinguishable from the light emission of the hadronic cascades from the initial tau neutrino interactions. The color of the DOMs represent the arrival times of the photons (red is early, green is late). The size of the DOM represents the amount of charge that is seen in the DOM. Figure taken from [87].

1894 taking into account the earliest detected photons as they are least likely to have been scattered:

$$L(\Theta) = \prod_{j=1}^{N_{\text{DOM}}} \prod_{i=1}^{N_{\text{hit}}} p_j(t_i)^{q_i} \quad (5.1)$$

1895 where N_{DOM} is the number of Digital Optical Modules involved in the event. N_{hit} is the number of
1896 hits registered [90]. The charge detected by each DOM, q_i , factors into the probability calculation,
1897 assuming that earlier photons provide more reliable directional information.

1898 An alternative to SPE, the Multi-Photoelectron (MPE) likelihood method accounts for all
1899 detected photons. MPE uses the total observed charge to weight the significance of each hit:

$$L(\Theta) = \prod_{j=1}^{N_{\text{DOM}}} \left[p_j(t_1)^{q_1} \cdot (1 - P_j(t_1))^{Q_j - q_1} \right], \quad (5.2)$$

1900 where Q_j is the sum of charges observed by the j-th DOM, providing a more detailed picture of the
1901 muon’s path [90].

1902 SplineMPE, is the final step and employs a spline-based parameterization of the photon arrival
1903 times. These spline fits encode a detailed understanding of the ice’s optical properties derived from
1904 calibration data [90]. This approach yields the following likelihood function for improved angular
1905 resolution:

$$L(\vec{r}_0, t_0, \theta, \phi) = \prod_k L_{\text{DOM}_k}(\vec{r}_0, t_0, \theta, \phi), \quad (5.3)$$

1906 where the parameters \vec{r}_0, t_0, θ , and ϕ describe the reconstructed track within IceCube’s voluminous
1907 array [90].

1908 From the light weight LineFit to the complex SplineMPE, each step incorporates more detailed
1909 physics to enhance the reconstruction’s accuracy. Each hones in on the muon track and revealing
1910 the muon’s origin from cosmic distances. This nuanced tracking is crucial for IceCube’s mission
1911 to map the universe through the lens of high-energy neutrino interactions.

1912 5.2.3 Energy

1913 After pinpointing the muon track’s direction, IceCube employs the MuEX algorithm to estimate
1914 the energy deposited by the muon inside the detector. The MuEX algorithm uses a Poisson
1915 likelihood model, comparing the observed photoelectrons k to the expected light output, Λ , which
1916 is directly related to the deposited energy E :

$$\ln \mathcal{L} = k \ln(\Lambda E + \rho) - (\Lambda E + \rho) - \ln(k!) \quad (5.4)$$

1917 where ρ is the number of expected noise photons, and Λ reflects the light yield per unit energy,
1918 taking into account the optical properties of the ice and the detector response. The logarithm of the
1919 likelihood is minimized with respect to the energy, resulting in the best-fit estimate [88].

1920 For a more detailed energy reconstruction, the Millipede algorithm unfolds the muon’s energy
1921 loss along its path by adapting the Poisson likelihood. This approach accounts for the stochas-
1922 tic energy losses due to Bremsstrahlung and pair production, treating the muon as a series of

1923 electromagnetic cascades:

$$\vec{k} - \vec{\rho} = \Lambda \cdot \vec{E} \quad (5.5)$$

1924

$$\mathcal{L} = \prod_j \int_0^\infty d\lambda_j G(\lambda_i, \lambda_j) \frac{\lambda_j^{k_i} e^{-\lambda_i}}{k_i!}, \quad (5.6)$$

1925 where k denotes the observed photons, ρ the noise, E the energy losses, and Λ the matrix of
1926 predicted light yields throughout the detector. By fitting the muon's position, direction, and the
1927 vector of energy losses, Millipede achieves a resolution on total deposited energy along the muon
1928 track of approximately 10-15% [88].

1929 IceCube's energy reconstruction techniques, from the direct approach of MuEX to the com-
1930 prehensive unfolding by Millipede, illustrate the observatory's robust analytical framework for
1931 interpreting the intricate signals of neutrino interactions [88].

1932 5.3 Background

1933 In IceCube, the primary challenge in detecting astrophysical neutrinos is the background noise
1934 from atmospheric neutrinos. These are produced from cosmic rays hitting the Earth's atmosphere,
1935 leading to a cascade that includes both neutrinos and muons (see Fig. 2.2). These particles
1936 sometimes generate detector signals similar to those from astrophysical sources.

1937 IceCube employs selective criteria to reduce this background. For instance, downward-moving
1938 tracks are scrutinized more heavily, as these are more likely to be related to atmospheric events.
1939 Upward-moving neutrinos, however, are less likely to be confused with this background because
1940 the Earth filters out most other particles, including muons.

1941 The detector uses the Earth itself as a filter to increase the purity of potential astrophysical
1942 neutrino signals. This differentiation between upgoing and downgoing events helps IceCube focus
1943 on the neutrinos that are of most interest for astronomical observations.

CHAPTER 6

HEAVY DARK MATTER ANNIHILATION SEARCH WITH ICECUBE'S NORTH SKY TRACK DATA

6.1 Introduction

Neutrinos are another astrophysical messenger than can travel long distances without significant attenuation or deflection. Additionally, Neutrinos come in three flavors which triples the multiplicity of the particles we are searching for. Uniquely, they interact less readily than photons especially above PeV energies. Neutrinos therefore provide another window through which we can perform dark matter searches.

The previous IceCube DM annihilation analysis towards dwarf galaxies was performed in 2013 [93] which, in technical terms, is more than a minute ago. This is in spite of IceCube's crucial sensitivity afforded from neutrino spectral lines [94]. A lot has changed in IceCube since its previous DM annihilation search such as, additional strings, more sophisticated analysis methods, and more accurate theory modeling. It has come time for IceCube to make a DM dSph contribution.

IceCube is sensitive to annihilating DM for DM masses above 1 TeV. Additionally, IceCube's sensitivity is comparable gamma-ray observatories in spectral models that produce hard neutrino features. The goal of this analysis is to perform a DM annihilation search using the Northern Sky Tracks datasets. The search will only be towards dwarf spheroidal galaxies (dSph) for the strengths mentioned in Section 3.3.3. These sources are treated as point sources for IceCube with little loss to sensitivity or model dependence on how the DM is distributed. DM masses from 500 GeV to 100 PeV are considered for this analysis. Several DM annihilation channels available from the HDMspectra [79] are studied in this analysis. This chapter presents the analysis work for IceCube to update our DM searches toward dSphs.

6.2 Dataset and Background

This section enumerates the data and background methods used for IceCube's study of dSphs. Section 6.2.1 and Section 6.2.2 are most useful for fellow IceCube collaborators looking to replicate this analysis.

1970 **6.2.1 Itemized IceCube files**

1971 These files are only available within IceCube’s internal documentation and wikis. They are not
1972 meant for public access, and are presented here so that IceCube collaborators can reproduce results
1973 accurately.

1974 • Software Environment: CVMFS Py3-v4.1.1

1975 • Data Sample: Northern Tracks NY86v5p1

1976 • Analysis Software: csky ([nu_dark_matter](#))

1977 • Analysis wiki: https://wiki.icecube.wisc.edu/index.php/Dark_Matter_Annihilation_Search_towards_dwarf_spheroidals_with_NST_and_DNN_Cascades

1979 • Project repository

1980 **6.2.2 Software Tools and Development**

1981 This analysis was performed inside IceCube’s CVMFS (3.4.1.1) software environment using
1982 csky for likelihood calculations. Csky at first did not come with dark matter spectral models nor
1983 could accommodate custom flux models. We developed these capacities for single source and
1984 stacked source studies for this analysis. The analysis code is held in a separate repository from
1985 csky. The [nu_dark_matter branch of csky](#) manages the input of custom dark matter spectra and
1986 accompanied DM astrophysical source. Csky also enables the use of multithreading which was
1987 shown to be crucial for DM searches (see Sec. 4). Csky then calculates likelihoods with a selected
1988 data sample. The [IceCube Dark Matter dSph repository](#) manages the generation of spectral models
1989 for neutrinos, physics parameter extraction from n_{sig} , J -factor per source inputs, and bookkeeping
1990 for the large parameter space. The project repository required a secondary software environment
1991 for neutrino oscillations. How to launch and run those calculations are documented in the project
1992 repository and the Docker image is additionally saved in Section C.1.

1993 **6.2.3 Data Set and Background Description**

1994 For this analysis, I use the Northern Sky Tracks (NST) Sample (Version V005-P01). The sample
1995 contains up-going track-like events, usually from ν_μ and ν_τ , with a superior angular resolution
1996 compared to the cascade dataset. This sample covers 10.4 years of data (IC86_2011-2021). The
1997 accepted neutrino energy range used for the analysis is unique from most other IceCube searches
1998 because DM spectra are hard with large contributions close to $E_\nu = m_\chi$. Therefore, the sampled
1999 energy range is $1 < \log(E_\nu/\text{GeV}) < 9.51$ with step size 0.125.

2000 The strengths of a dwarf analysis is that there are no additional background considerations
2001 beyond nominal, baseline background estimations (see Section 3.2.3). For NST, the nominal
2002 contributions come from atmospheric neutrinos and isotropic astrophysical neutrinos. We estimate
2003 the background by scrambling NST data along Right Ascension.

2004 **6.3 Analysis**

2005 The expected differential neutrino flux from DM-DM annihilation to standard model particles,
2006 $d\Phi_\nu/dE_\nu$, over solid angle, Ω is described by the familiar equation.

$$\frac{d\Phi_\nu}{dE_\nu} = \frac{\langle\sigma\nu\rangle}{8\pi m_\chi^2} \frac{dN_\nu}{dE_\nu} \times \int_{\text{source}} d\Omega \int_{l.o.s} \rho_\chi^2 dl(r, \theta') \quad (6.1)$$

2007 This is identical to Eq. (3.1) except that there are 3 neutrino flavors, so there are a corresponding
2008 3 flux equations. Section 3.3 has a complete description of each term in Eq. (6.1). Additionally,
2009 neutrinos oscillate between flavors which needs to be considered for the expected neutrino flux
2010 at Earth. Section 6.3.1 presents the particle physics model and processing for DM annihilation.
2011 Section 6.3.2 presents the spatial distributions built for each dSph.

2012 **6.3.1 $\frac{dN_\nu}{dE_\nu}$ - Particle Physics Component**

2013 Neutrino spectra from heavy DM annihilation were generated using HDMspectra [79] and
2014 χ arov [95]. HDMspectra has tables for the decay and annihilation of heavy DM for different
2015 dark DM and SM primary annihilation channels. The simulation includes electroweak or gluon
2016 radiative corrections and higher order loop corrections from the W and Z bosons (WWZ and $WW\gamma$).
2017 These corrections are especially important for accurately estimating the prompt neutrino flux. This

2018 publication also pushes the simulated DM mass to the Plank scale (1 EeV), however this study will
2019 not explore that high.

2020 An important feature in the spectra is that neutrino line channels will be accompanied by a low
2021 energy tail [79], see Fig. 6.1. Thus, the Earth will not fully attenuate a heavy neutrino line-like
2022 signal from high declination sources where the neutrino flux must first traverse through the Earth.
2023 The DM annihilation channels that feature lines include all leptonic channels: $\nu_{e,\mu,\tau}$, e , μ , and τ . We
2024 use the `xarov` software to propagate and oscillate the neutrinos from the source to Earth. Because
2025 these sources are quite large in absolute terms, and also far (order 10 kpc or more), the resulting
2026 flavor spectra are the averages of the transition probabilities [95]:

$$P(\nu_\alpha \rightarrow \nu_\beta) \approx \begin{bmatrix} 0.55 & 0.18 & 0.27 \\ 0.18 & 0.44 & 0.38 \\ 0.27 & 0.38 & 0.35 \end{bmatrix} \quad (6.2)$$

2027 Examples of the spectra before and after propagation are shown in Fig. 6.1.

2028 When calculating the expected contribution to n_s , only ν_μ and ν_τ are considered as NST's
2029 effective area to ν_e is negligible [96]. Therefore, the expected composite neutrino spectrum is the
2030 sum of the two flavors: $\frac{dN\nu_\mu}{dE\nu_\mu} + \frac{dN\nu_\tau}{dE\nu_\tau}$. The spectral tables are then converted to splines to condense
2031 information, enable random sampling of the spectra, and reduce computing times. The spectral
2032 splines are finally implemented as a DM class in csky.

2033 6.3.1.1 Treatment of Neutrino Line Features

2034 All DM annihilation channels into leptons $\chi\chi \rightarrow [\nu_{e,\mu,\tau}, e, \mu, \tau]$ develop a prominent and
2035 narrow spectral line feature. For all neutrino flavors, this line is visible and prominent in all m_χ
2036 studied in this analysis. For charged leptons, the feature typically manifests at $m_{ch}hi > 10$ TeV, yet
2037 its prominence varies slightly between the flavors. Examples for lines in the annihilation spectra
2038 with neutrinos or charged leptons are provided in Fig. 6.1.

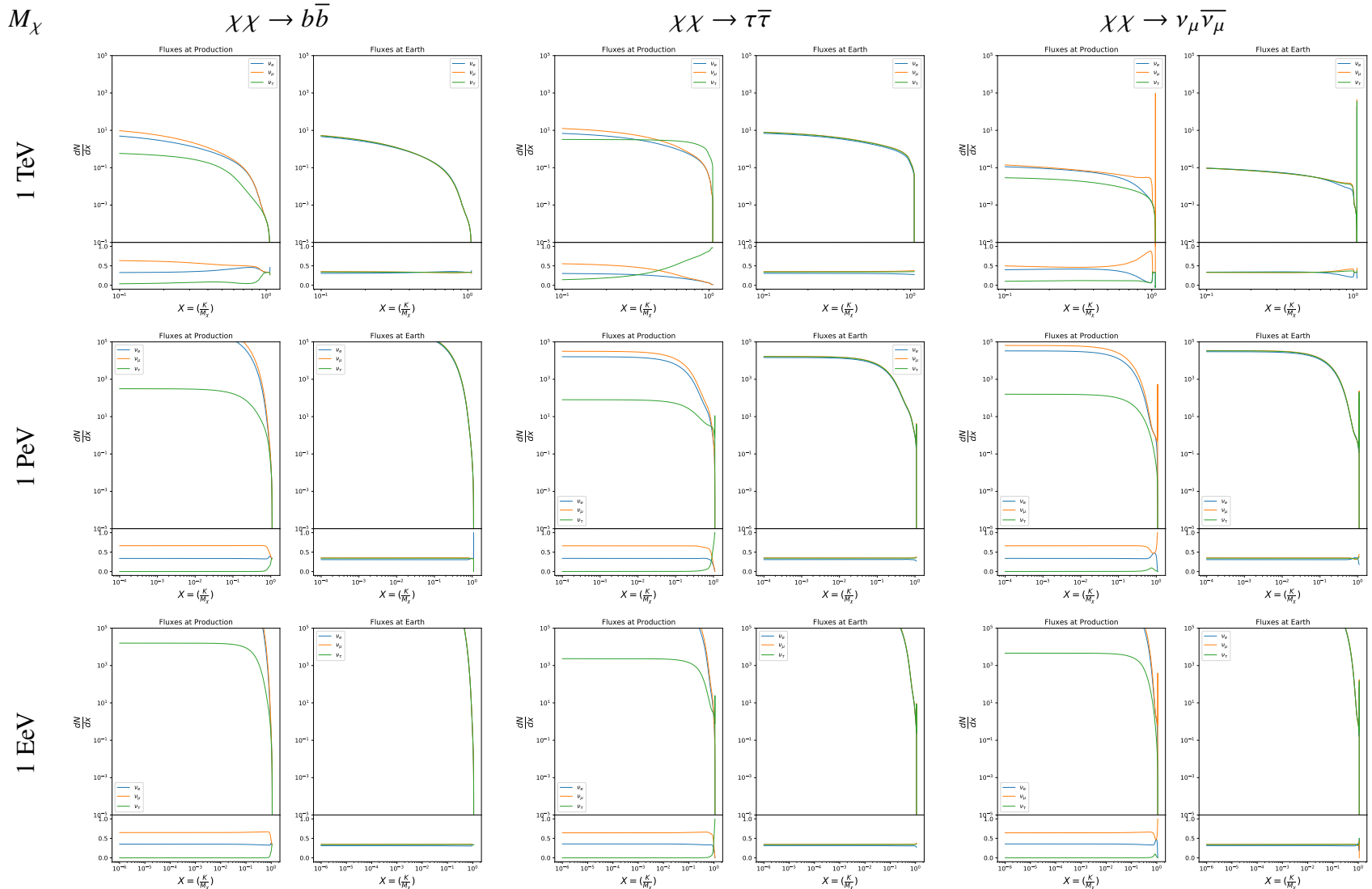


Figure 6.1 Neutrino spectra at production (left panels) and after oscillation at Earth (right panels). Blue, orange, and green lines are the ν_e , ν_μ , and ν_τ spectra respectively. Top panels show the spectra in $\frac{dN}{dE}$. Lower panels plot the flavor ratio to $\nu_e + \nu_\mu + \nu_\tau$. SM annihilation channels $b\bar{b}$, $\tau\bar{\tau}$, and $\nu_\mu \bar{\nu}_\mu$ are shown for $M_\chi = 1 \text{ PeV}$, TeV , and EeV .

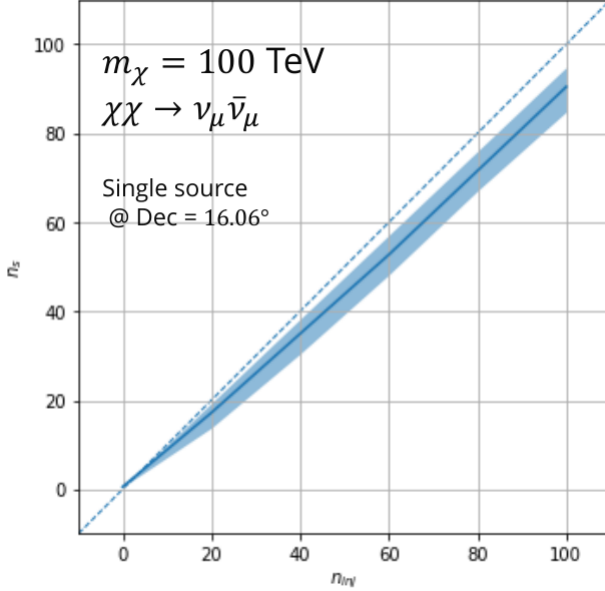


Figure 6.2 Signal recovery for 100 TeV DM annihilation into $\nu_\mu \bar{\nu}_\mu$ for a source at Dec = 16.06°. n_{inj} is the number of injected signal events in simulation. n_s is the number of reconstructed signal events from the simulation data. Although the uncertainties are small and tight, the reconstructed n_s are systematically underestimated.

2039 The neutrino line feature is so narrow relative the sampled energy range that the random
 2040 sampling of the spectra and likelihood fitting rarely capture the line in computation. As a result,
 2041 often the best fit to simulation of background will always floor to TS = 0 and the signal recovery
 2042 systematically underestimates the signal (see Fig. 6.2).

2043 To remedy this, we take a similar approach to the IceCube’s decay analysis [97] and the previous
 2044 gamma-ray study in Section 4.3.1. Two smoothing kernels were tested (Gaussian and uniform)
 2045 to widen the line feature. The widths were tuned such that the signal recovery approached unity
 2046 for DM mass 100 TeV to 1 PeV for a source at Segue 1’s declination, 16.06°. Near horizon
 2047 was chosen in order to isolate loss in signal recovery away from Earth’s attenuation of very high
 2048 energy neutrinos and atmospheric backgrounds. The kernel convolution needed closely preserve
 2049 the integrated counts of neutrinos. The optimized kernel parameters for all lines are summarized
 2050 as:

- 2051 • Gaussian kernel with 1σ width = $1.75\text{E-}3 \cdot m_\chi$
- 2052 • Minimum energy included in convolution = $\text{MIN}[0.995 \cdot m_\chi, E(\nu_{\text{line}}) - 4\sigma]$

- 2053 • Maximum energy included in convolution = $\text{MAX}[1.005 \cdot m_\chi, E(\nu_{\text{line}}) + 4\sigma]$

2054 where $E(\nu_{\text{line}})$ is the neutrino energy where the neutrino line is at the maximum.

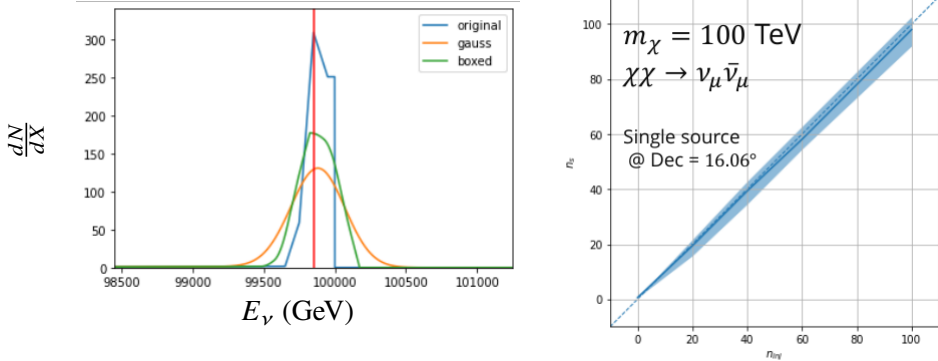


Figure 6.3 Left panel shows the two kernels overlaying the original spectrum from $\chi\text{aron}\nu$ after propagation to Earth [95]. The vertical red line indicates where the original neutrino line is maximized. Blue line is the output from $\chi\text{aron}\nu$. Green line is the spectrum after convolution with a flat kernel. Orange line is the spectrum after Gaussian convolution. Right panel shows the signal recovery of the spectral model using the Gaussian kernel with parameters enumerated above.

2055 These parameters broadly improved the signal recovery of the line spectra. An example is in
2056 Fig. 6.3. Analysis level signal recovery studies are expanded upon in Section 6.6.

2057 6.3.1.2 Spline Fitting

2058 In an effort to reduce computational work, memory burden, and align with point source methods
2059 used for NGC1068 [98], spectral splines were created and adopted for estimating the neutrino flux
2060 for the different spectral models. Software was written to generate, book keep, and calculate values
2061 on the splines.

2062 When using splines, one has to be careful of the goodness to fit. The spline software used here,
2063 Photospline [99], uses the penalized spline technique [100]. Through the penalized technique,
2064 poor fits are penalized according to the accuracy of the nominal value, and the smoothness of the
2065 first and second derivatives. However, this construction does not penalize on the integral of the
2066 fit distribution which is critical in low signal studies, such as DM searches. There are additional
2067 caveats when testing the goodness to fit to the MC generated above for all DM annihilation channels.

- 2068 • The splines must be Log10(*) in Energy and dN/dX to account for the exponential nature of
 2069 the flux.
- 2070 • The fidelity of the fit matters more at $E_\nu \approx m_\chi$ where the model uncertainties are minimal
 2071 and physical considerations (like the cut-off) are most important.
- 2072 • The fidelity of the fit matters less at low E_ν as the model uncertainties are large AND
 2073 IceCube's sensitivity diminishes significantly below 500 GeV.
- 2074 • Total integrated counts should be well-preserved.

2075 The resulting cost function was built to evaluate the goodness of spline fits to account for the above
 2076 considerations.

$$e_i = x_i \cdot \left(\frac{dN_i}{dX_i} - 10^{\hat{e}_i} \right) \quad (6.3)$$

2077 Where \hat{e}_i is the spline estimator's value for x_i . $x_i = E_{\nu_i}/m_\chi$. $\frac{dN_i}{dX_i}$ is the flux value from MC. I then
 2078 take the RMS of the error distribution and the resulting value, err, is used to evaluate the fidelity of
 2079 the spectral spline.

$$\text{err} = \sqrt{\frac{1}{x_{\max} - x_{\min}} \int_{x_{\min}}^{x_{\max}} e^2 dx} \quad (6.4)$$

2080 x_{\min} and x_{\max} are the scope of the error evaluation and are provided in Tab. 6.1.

2081 Each SM channel had unique tolerances for 'err'. Channels with very hard cut-offs had looser
 2082 tolerance for err because a significant error would be generated from single counts over/underes-
 2083 timated at the cut-off. Soft channels do not share this issue, so the tolerance is much stricter. All
 2084 annihilation channels from HDM are modeled well below IceCube's NST sensitivity which falls
 2085 off substantially below 100 GeV [96]. We do not think it is necessary to evaluate the spline fits
 2086 below 100 GeV and use this value as the default lower cut-off. Yet, HDM's model uncertainties
 2087 at $E_\nu < 10^{-6} \cdot m_\chi$ span an order of magnitude [79]. We also choose not to evaluate the splines
 2088 below this critical value if it is within IceCube's sensitivity. Finally, the smoothing of the spectral
 2089 lines in leptonic annihilation channels are ignored for evaluating the fit. We used the lower limit of

$\chi\chi \rightarrow$	GOOD	OK	FAIL	Limits of err calc [X_{min}, X_{max}]
$Z^0 Z^0, W^+ W^-$	1.0E-3	1.0E-3, 1.0E-2	1.0E-2	MAX[100GeV/ m_χ , 10^{-6}], 1.0
$t\bar{t}, hh$	1.0E-5	1.0E-5, 1.0E-4	1.0E-4	MAX[100GeV/ m_χ , 10^{-6}], 1.0
$b\bar{b}, d\bar{d}, u\bar{u}$	9.0E-7	9.0E-7, 9.0E-6	9.0E-6	MAX[100GeV/ m_χ , 10^{-6}], 1.0
$\nu\bar{\nu}_{e,\mu,\tau}$	1.0E-3	1.0E-3, 1.0E-2	1.0E-2	MAX[100GeV/ m_χ , 10^{-6}], MIN[0.995, ($E_n(\nu_{line}) - 4\sigma$)/ M_χ]
$e\bar{e}, \mu\bar{\mu}, \tau\bar{\tau}$	1.0E-3	1.0E-3, 1.0E-2	1.0E-2	MAX[100GeV/ m_χ , 10^{-6}], MIN[0.995, ($E_n(\nu_{line}) - 4\sigma$)/ M_χ]

Table 6.1 Spline err tolerances used for input in particle physics component to Eq. (3.1). Column 1 is the DM annihilation channel being fit. Columns 2, 3, and 4 are the tolerances for "GOOD" (pass), "OK" requires inspection, and "FAIL" (tune and refit) respectively. Column 5 has the X ranges over which the error is evaluated. MAX/MIN [·, ·] takes the maximum or minimum of the two enclosed values.

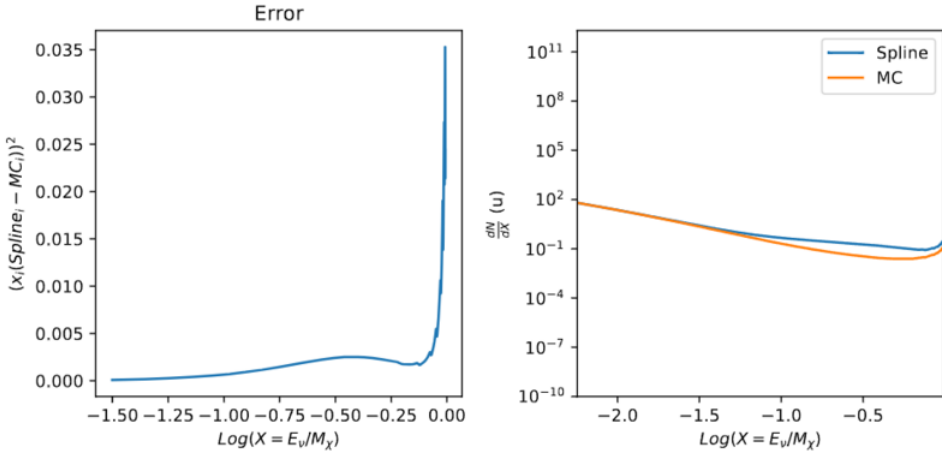


Figure 6.4 Example spline that failed the fit. Failed splines are corrected on a case by case basis unless the SM channel has a systematic problem fitting the splines. In this case, I made a bookkeeping error and loaded the incorrect spectral model

2090 the kernel mask as the upper limit of evaluation. Table 6.1 summarizes the tolerances for the DM
 2091 annihilation channels used for this analysis.

2092 The errors are then assesed in two ways. First, FAIL and OK are directly plotted with e_i as a
 2093 function of x with the full spline and MC. An example of a single failure is provided in Fig. 6.4.
 2094 Second, a summary plot of all the splines is plotted and colors coded. Figure C.1 are the spline
 2095 summaries as of writing this thesis. The goal broadly is to eliminate all red and inspect yellow
 2096 statuses.

2097 The ν_e spectra at Earth are not considered in this analysis, so no work was done to refine the

2098 spline fits for this flavor. Finally, I perform a visual inspection of the splines to verify that the spline
 2099 fitting did not introduce spurious features that would corrupt the likelihood fitting.

2100 **6.3.1.3 Composite Neutrino Spectra**

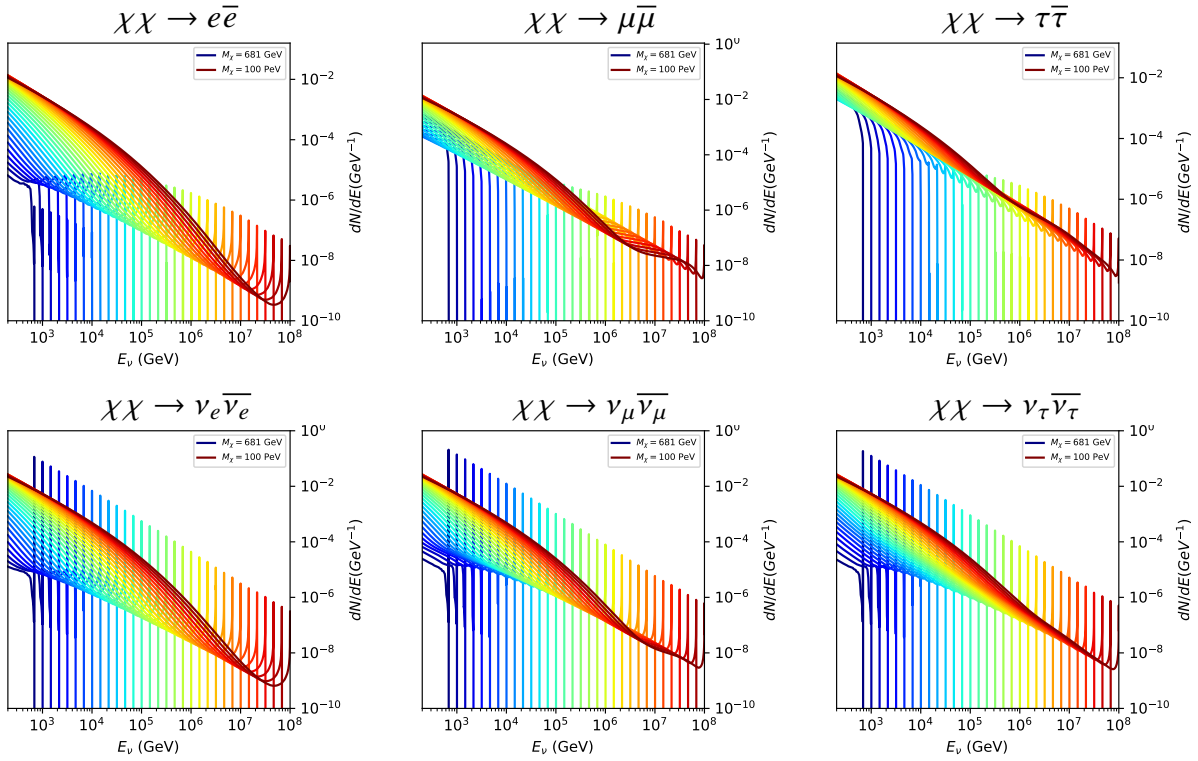


Figure 6.5 Summary of input spectral models that were smoothed with Gaussian kernels. Spectral models are for $\chi\chi \rightarrow e\bar{e}$, $\mu\bar{\mu}$, $\tau\bar{\tau}$, $\nu_e\bar{\nu}_e$, $\nu_\mu\bar{\nu}_\mu$, and $\nu_\tau\bar{\nu}_\tau$. These spectra are the composite ($\nu_\mu + \nu_\tau$) of neutrino flavors. Every spectral model used for this analysis is featured as a colored solid line. Bluer lines are for low m_χ models. m_χ ranges from 681 GeV to 100 PeV. HDM [79], χ arov [95], and Photospline [99] are used to generate these spectra. Energy (x-axis) was chosen to roughly represent the energy sensitivity of NST.

2101 With all the previously mentioned pieces, we are ready to fully assemble a comprehensive
 2102 description of the particle physics term dN/dE in Eq. (6.1).

$$\frac{dN_\nu}{dE_\nu \oplus} = \left(\frac{dN_{\nu_e}}{dE_{\nu_e}} + \frac{dN_{\nu_\mu}}{dE_{\nu_\mu}} + \frac{dN_{\nu_\tau}}{dE_{\nu_\tau}} \right)_{\text{src}} \cdot \mathbf{P}(\nu_\alpha \rightarrow \nu_\beta) \quad (6.5)$$

2103 Figure 6.5 shows the spectral models that required Gaussian smoothing, the leptonic annihilation
 2104 channels. The remaining models where the only processing were spline fitting and neutrino
 2105 oscillation are documented in Section C.3. Notice that the different neutrino flavors are unique,

2106 especially in their low energy tails. Therefore, this analysis will be sensitive to DM annihilating to
2107 the distinct neutrino flavors.

2108 **6.3.2 *J*- Astrophysical Component**

2109 For this analysis, we re-adopt the \mathcal{GS} model [59] used in Sec. 3 for dSphs. These models
2110 are based on a modified Navarro-Frenk-White (NFW) profile where the indices of the NFW
2111 (traditionally 1,3,1) are allowed to float. The angular width of these sources is much smaller than
2112 the angular resolution of IceCube NST [98]. We therefore treat these sources as point sources
2113 in this analysis, and forgo generating maps. These sources and the \mathcal{GS} model have already been
2114 discussed at length in Section 3.3.2 and is not repeated here. IceCube uses identical sources to
2115 Tab. 3.1 except we analyze source with declinations above 0.0° .

2116 **6.3.3 Source Selection and Annihilation Channels**

2117 We use all the dSphs presented in IceCube’s previous dSph DM search [93] and expand beyond
2118 it. IceCube’s sources for this analysis studies include Boötes I, Canes Venatici I, Canes Venatici II,
2119 Coma Berenices, Draco, Hercules, Leo I, Leo II, Leo V, Leo T, Segue 1, Segue 2, Ursa Major I,
2120 Ursa Major II, and Ursa Minor. A full description of all sources used is in Table 3.1. Sources with
2121 declinations less than 0.0 are excluded from this analysis.

2122 This analysis improves on the previous IceCube dSph paper [93] in the following ways. Previ-
2123 ously, the IceCube detector was not yet completed to the 86 string configuration. Many more dSphs
2124 will be observed, from 4 to 15. Previously, the particle physics model used for neutrino spectra
2125 from DM annihilation did not have EW corrections where they are now included [79]. The spectral
2126 models also predict substantial differences between the neutrino flavors, so this analysis will be the
2127 first DM dwarf analysis to discriminate between primary neutrino flavors. The study performed
2128 here studies 10.4 years of data.

2129 The SM annihilation channels probed for this study include $\chi\chi \rightarrow$

2130 $b\bar{b}, t\bar{t}, u\bar{u}, d\bar{d}, e\bar{e}, \mu\bar{\mu}, \tau\bar{\tau}, ZZ, W^+W^-, \nu_e\bar{\nu}_e, \nu_\mu\bar{\nu}_\mu$, and $\nu_\tau\bar{\nu}_\tau$

2131 **6.4 Likelihood Methods**

2132 I use the Point-Source search likelihood which is widely used in IceCube analyses. The
2133 likelihood function is defined as the following:

$$L(n_s) = \prod_{i=1}^N \left[\frac{n_s}{N} S_i + \left(1 - \frac{n_s}{N}\right) B_i \right] \quad (6.6)$$

2134 where i is an event index, S and B are the signal PDF and background PDF respectively. For a joint
2135 analysis where the sources are stacked the likelihood is expanded in the simplified way:

$$L(n_s) = \prod_{i=1}^{N_{\text{sources}}} L_i(n_s) \quad (6.7)$$

2136 Where L_i is the likelihood from the i -th source in the stacked analysis. The Test Statistic (TS)
2137 definition remains the same as Eq. (3.7)

2138 **6.5 Background Simulation**

2139 Before we look at data, we must first analyze background and signal injection to validate our
2140 analysis. We set out to characterize the TS distributions for each source, annihilation channel,
2141 and m_χ . Previous IceCube DM searches [97, 101] showed TS distributions that did not behave
2142 according to a χ^2 distribution with 1 degree of freedom. TS distributions can also vary significantly
2143 between DM mass and annihilation models. Therefore, Wilk's theorem may not be applicable to
2144 the analysis. Instead, a critical value is defined from many background trials. We study the TS
2145 distributions first for each source, then for the stacked analysis. The following sections show the
2146 results of the likelihood fitting for a suite of background trials.

2147 I assume that TS values are physical: $TS \geq 0$. $\epsilon[x]$ indicate the fraction of events where $TS < x$.
2148 For TS plots shown here, the decimal values of x are 1.0e-2 and 1.0e-3. Each subplot represents
2149 a simulation of 100,000 data-scrambled background trials. Section 6.5.1 show the background TS
2150 distributions obtained from Segue 1, a source with little Earth attenuation and large J -factor, and
2151 Ursa Major II, which has similarly large J -factor but significantly more Earth attenuation, assuming
2152 DM annihilation into $b\bar{b}$, $\tau\bar{\tau}$, and $\nu_\mu\bar{\nu}_\mu$. I show the TS distributions of a stacked study of 15 sources
2153 for all DM annihilation channels.

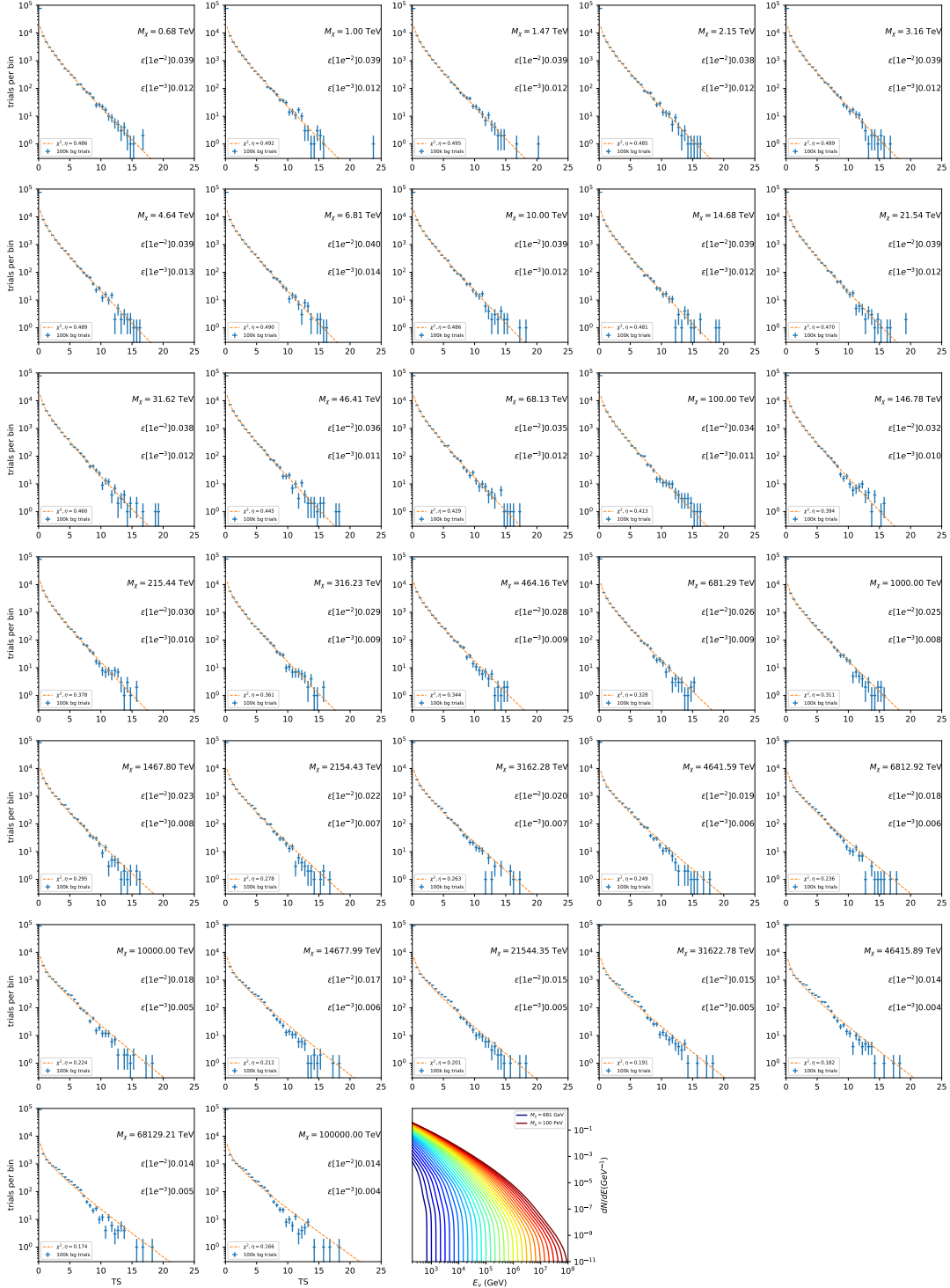


Figure 6.6 Test statistic (TS) distributions for Segue 1 and $\chi\chi \rightarrow b\bar{b}$. Each subplot, except the final, is the TS distribution for a specific DM mass listed in the subplot. Orange dashed lines are the traces for a χ^2 distribution with 1 degree of freedom. $\epsilon[\cdot]$ is the fraction of trials smaller than the bracketed value. The final subplot features the all DM spectral models, similar to Fig. 6.5, used as input for the TS distributions.

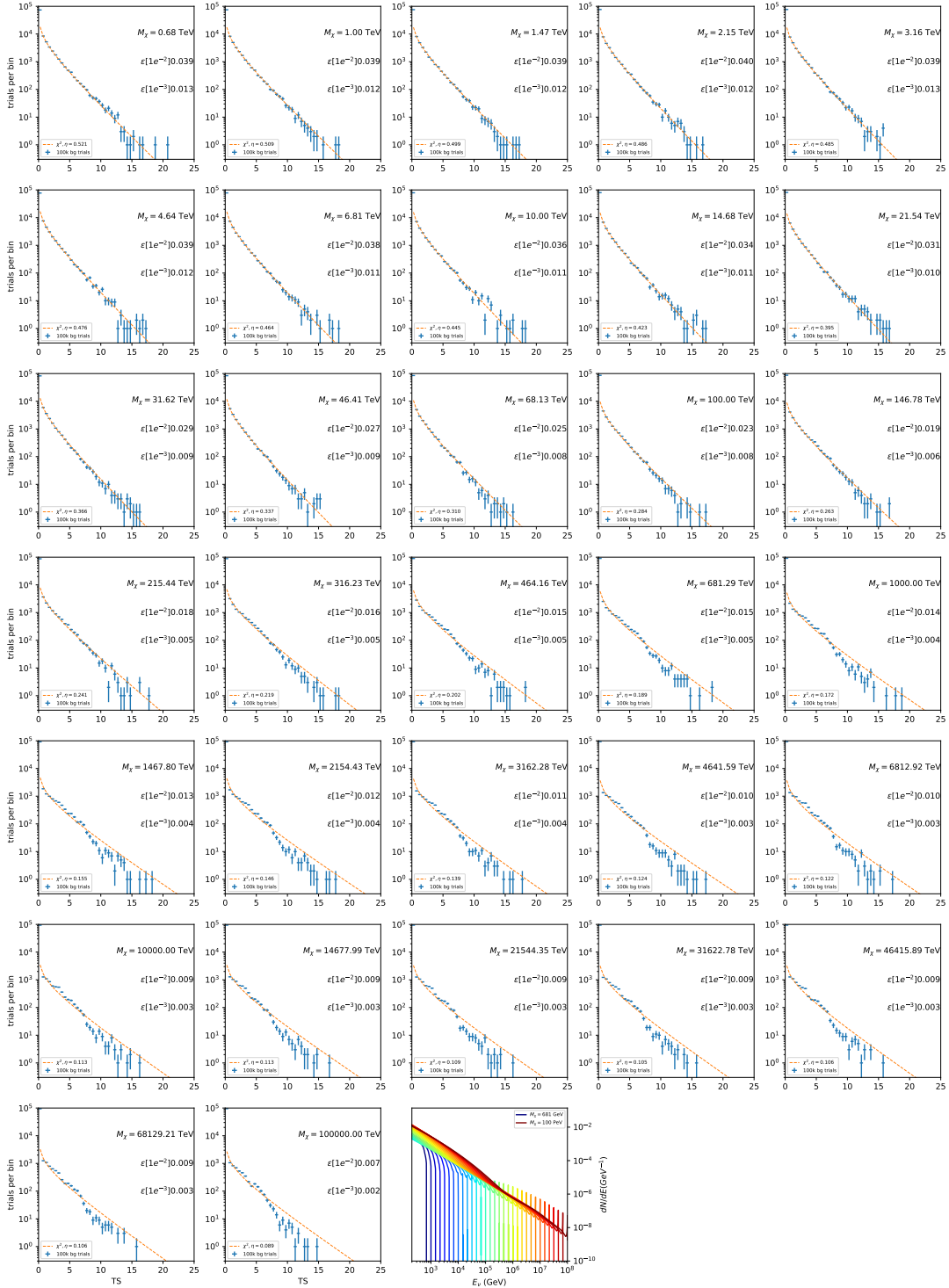


Figure 6.7 Same as Fig. 6.6 for Segue 1 $\chi\chi \rightarrow \tau\bar{\tau}$.

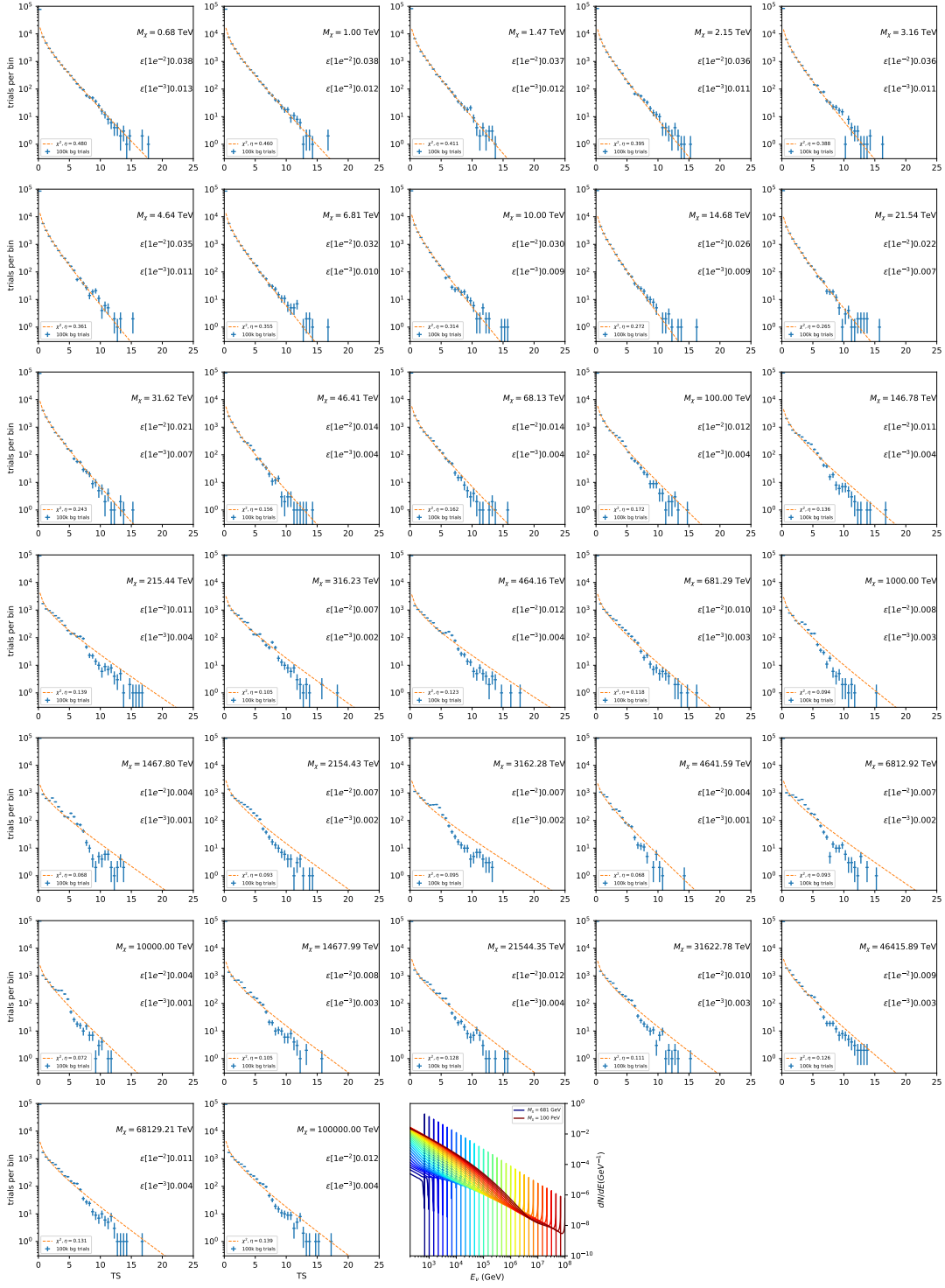


Figure 6.8 Same as Fig. 6.6 for Segue 1 $\chi\chi \rightarrow \nu_\mu\bar{\nu}_\mu$.

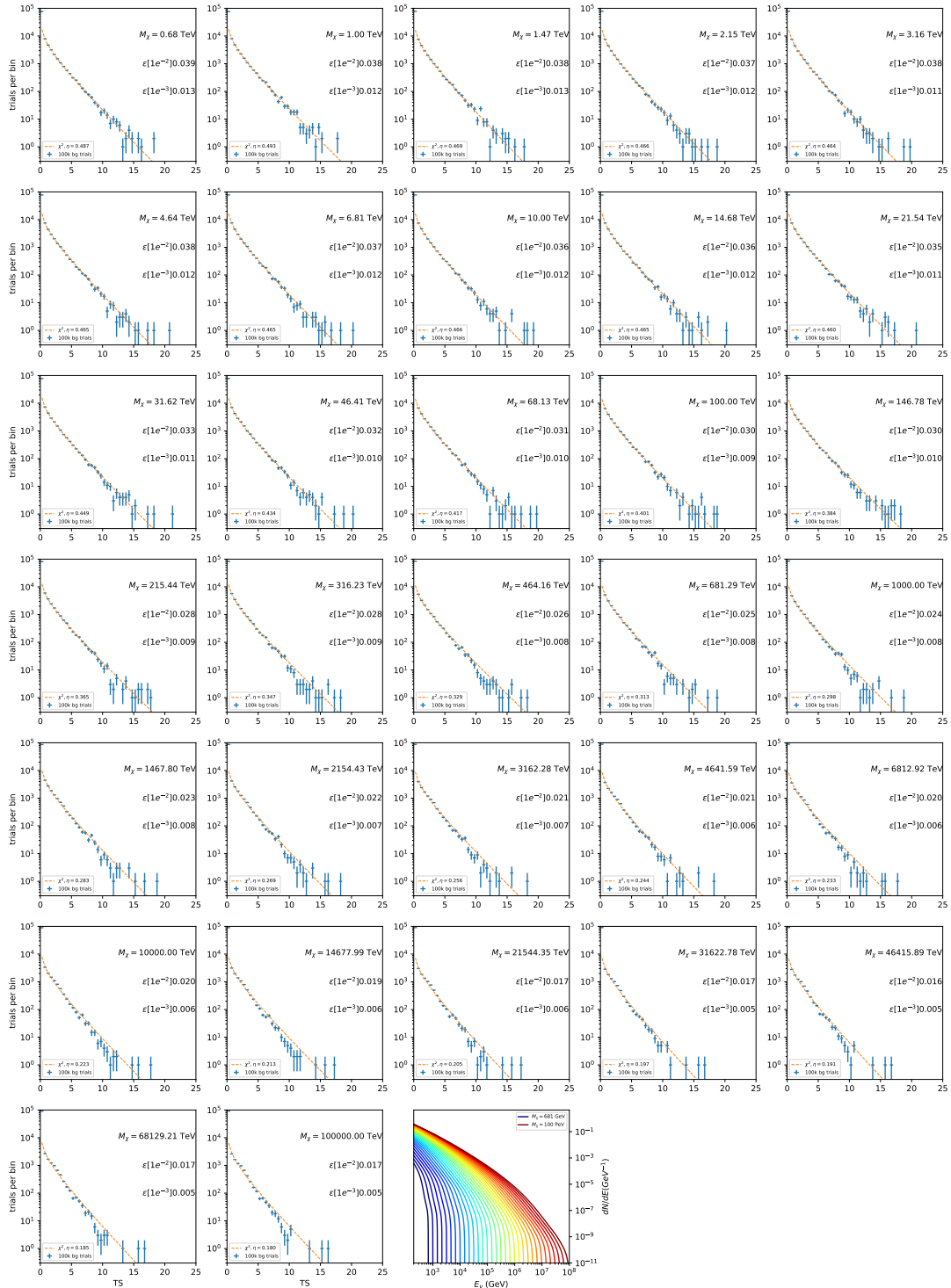


Figure 6.9 Same as Fig. 6.6 for Ursa Major II 1 $\chi\chi \rightarrow b\bar{b}$.

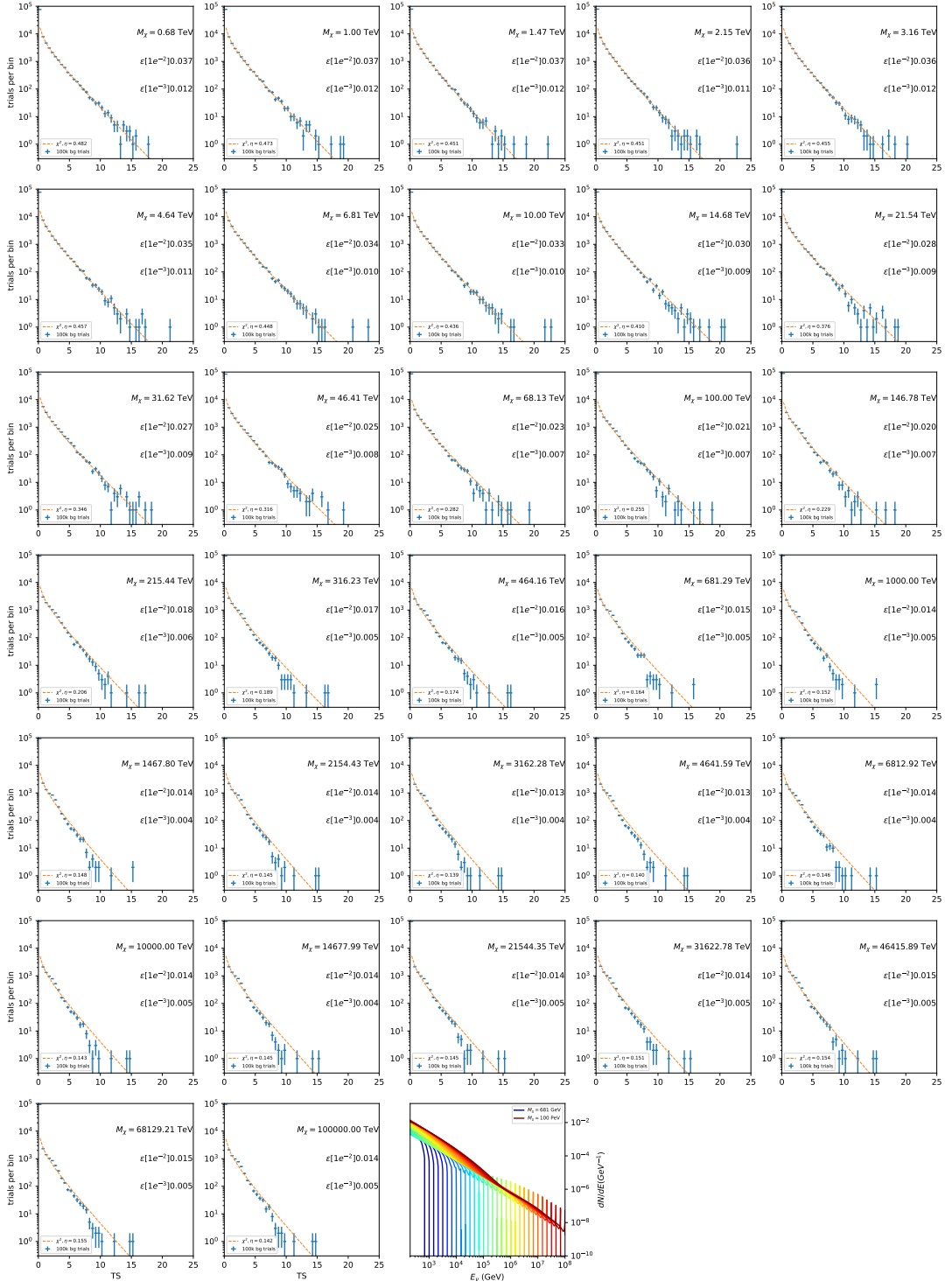


Figure 6.10 Same as Fig. 6.6 for Ursa Major II 1 $\chi\chi \rightarrow \tau\bar{\tau}$.

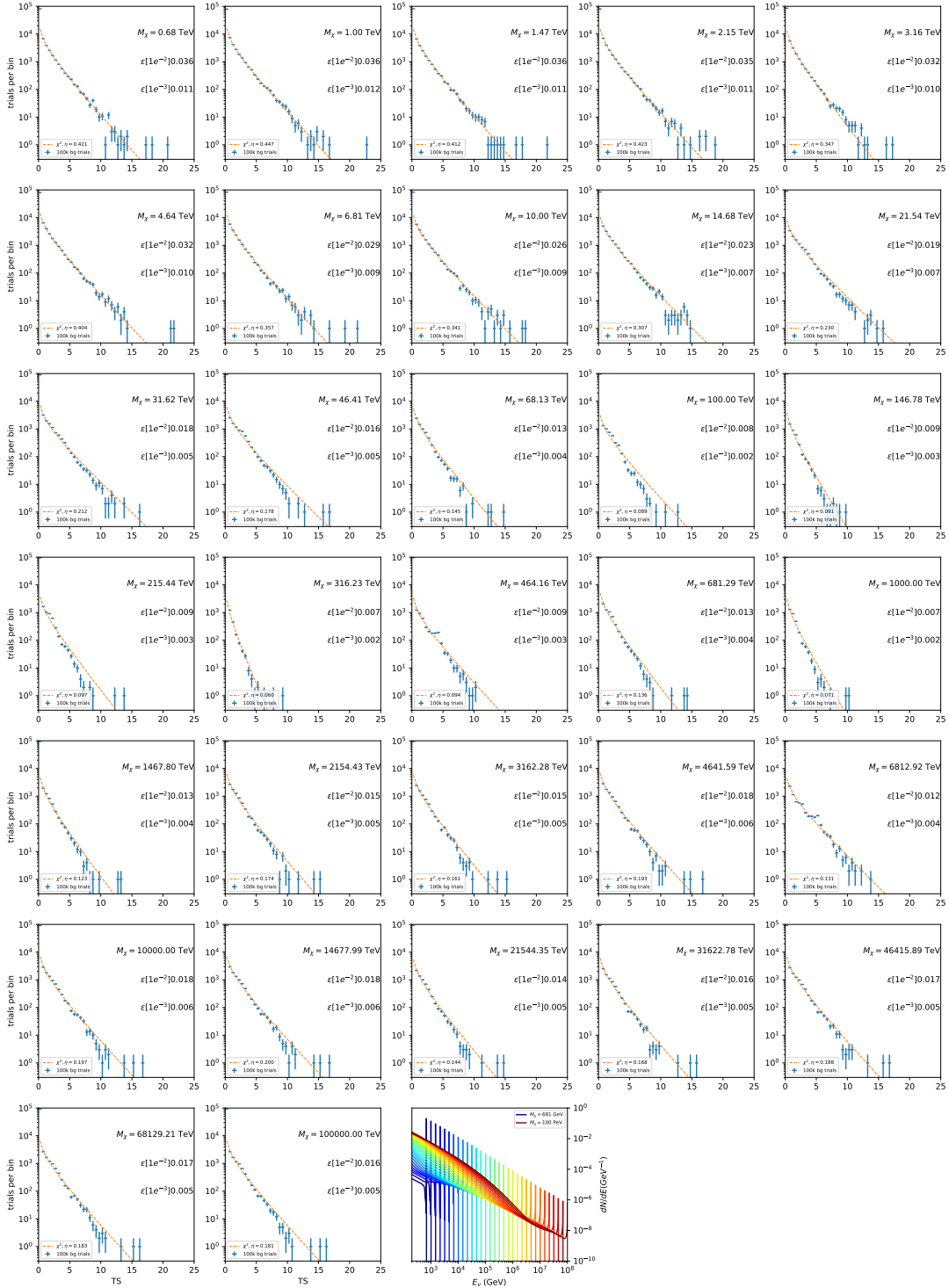


Figure 6.11 Same as Fig. 6.6 for Ursus Major II 1 $\chi\chi \rightarrow \nu_\mu \bar{\nu}_\mu$.

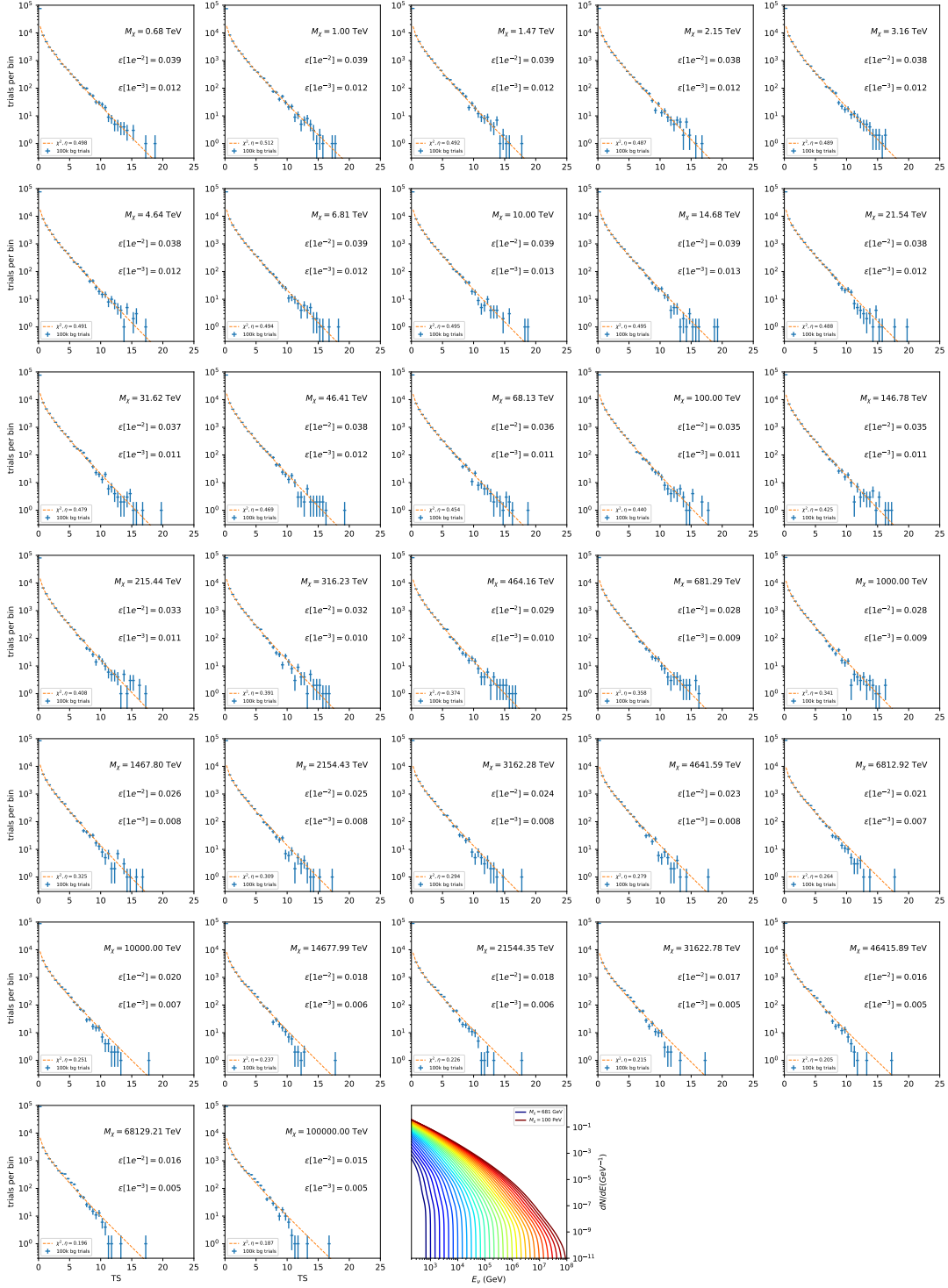


Figure 6.12 Same as Fig. 6.6 for 15, \mathcal{GS} J -factor, stacked sources and $\chi\chi \rightarrow b\bar{b}$.

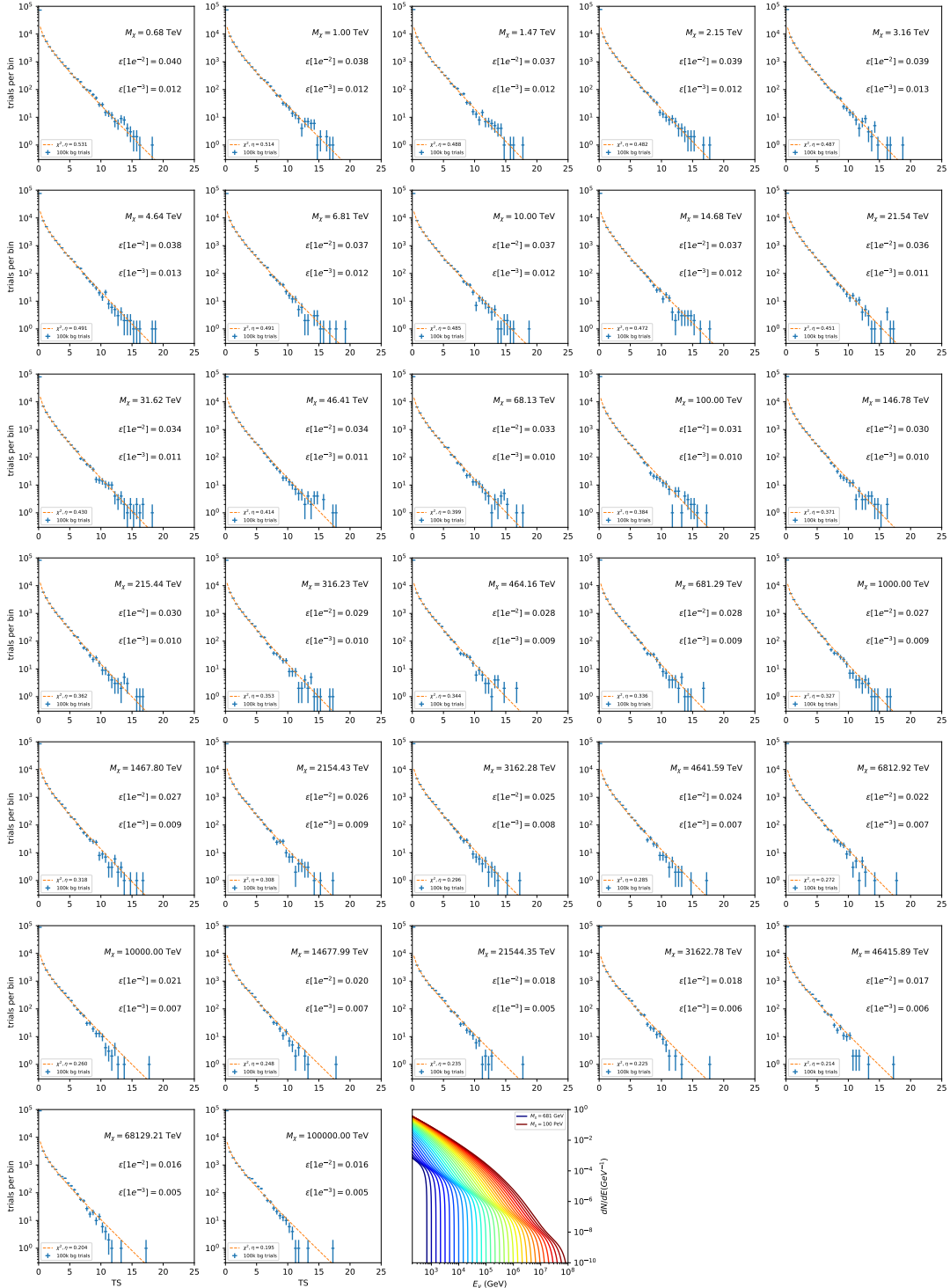


Figure 6.13 Same as Fig. 6.6 for 15, GS J-factor, stacked sources and $\chi\chi \rightarrow t\bar{t}$.

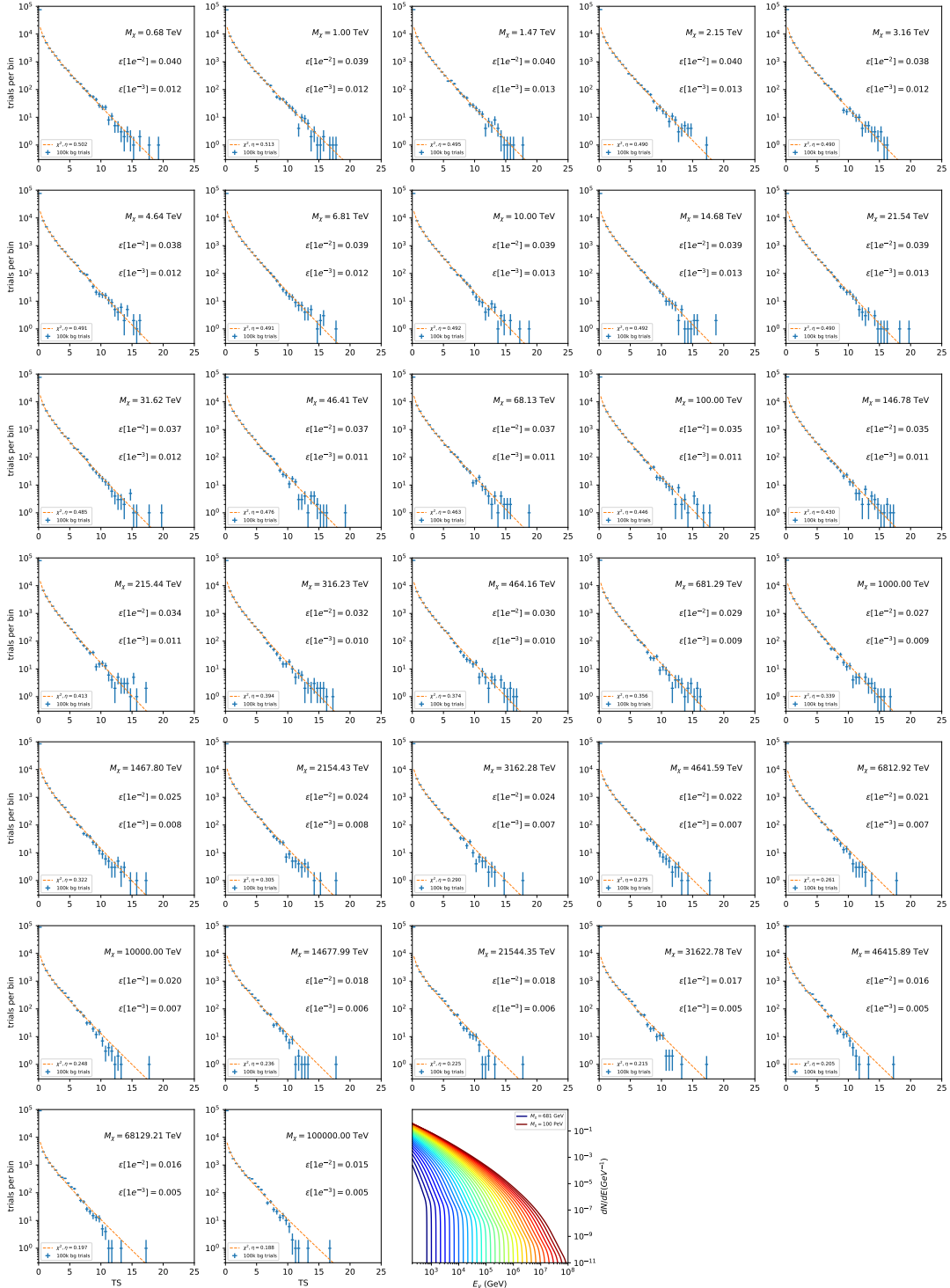


Figure 6.14 Same as Fig. 6.6 for 15, \mathcal{GS} J -factor, stacked sources and $\chi\chi \rightarrow u\bar{u}$.

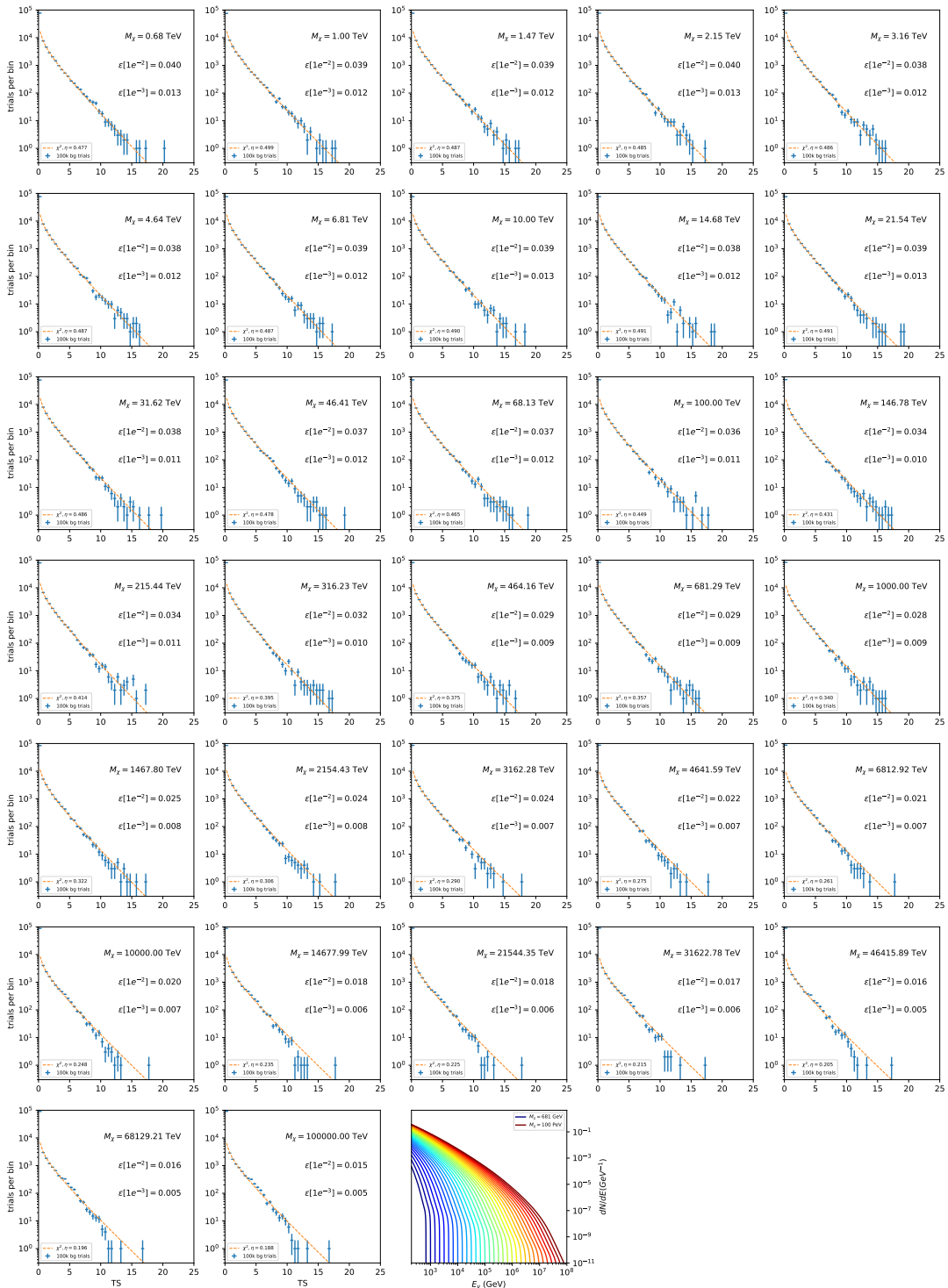


Figure 6.15 Same as Fig. 6.6 for 15, $\mathcal{G}\mathcal{S}$ J-factor, stacked sources and $\chi\chi \rightarrow d\bar{d}$.

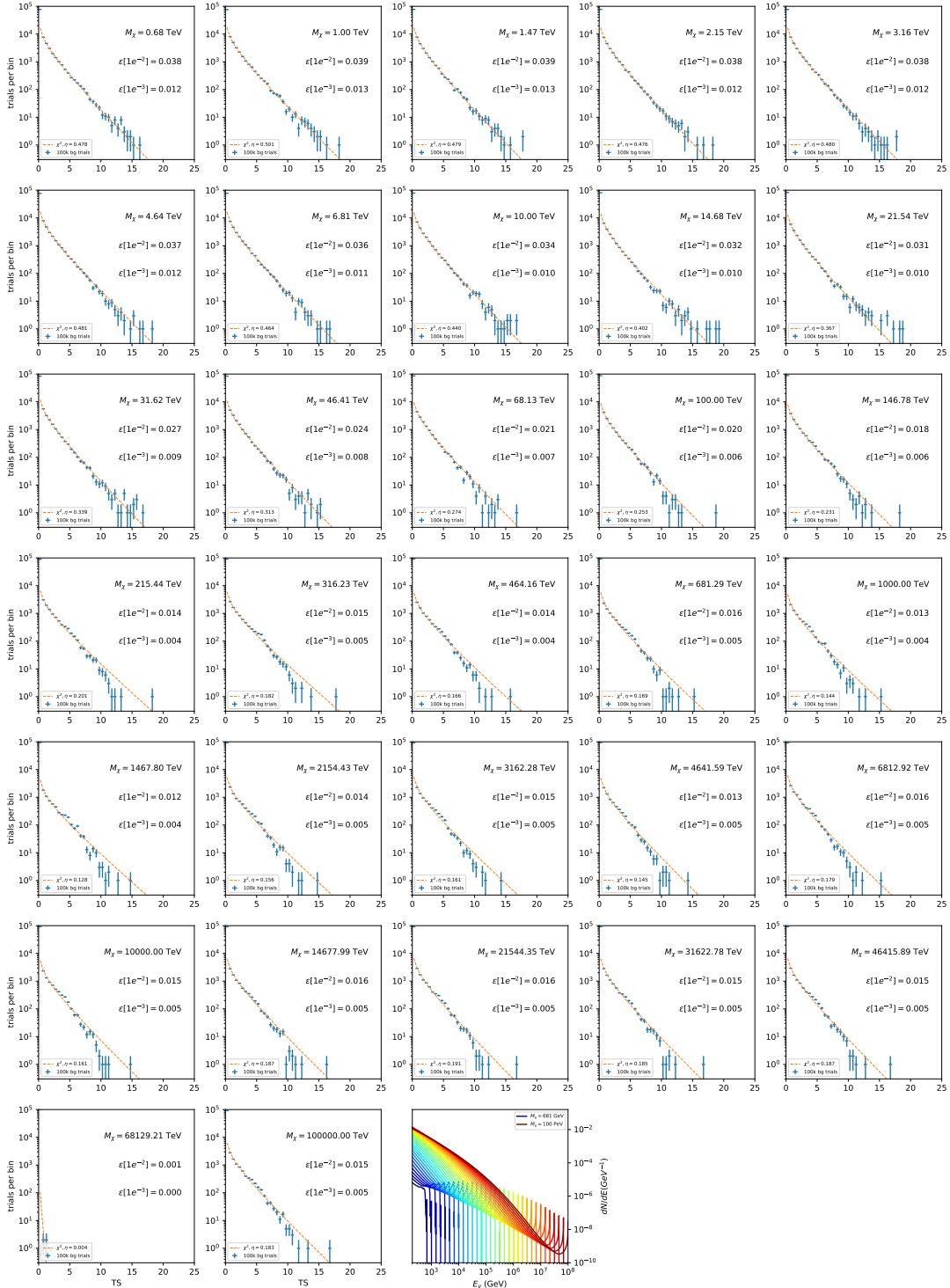


Figure 6.16 Same as Fig. 6.6 for 15, $\mathcal{G}\mathcal{S}$ J-factor, stacked sources and $\chi\chi \rightarrow e\bar{e}$.

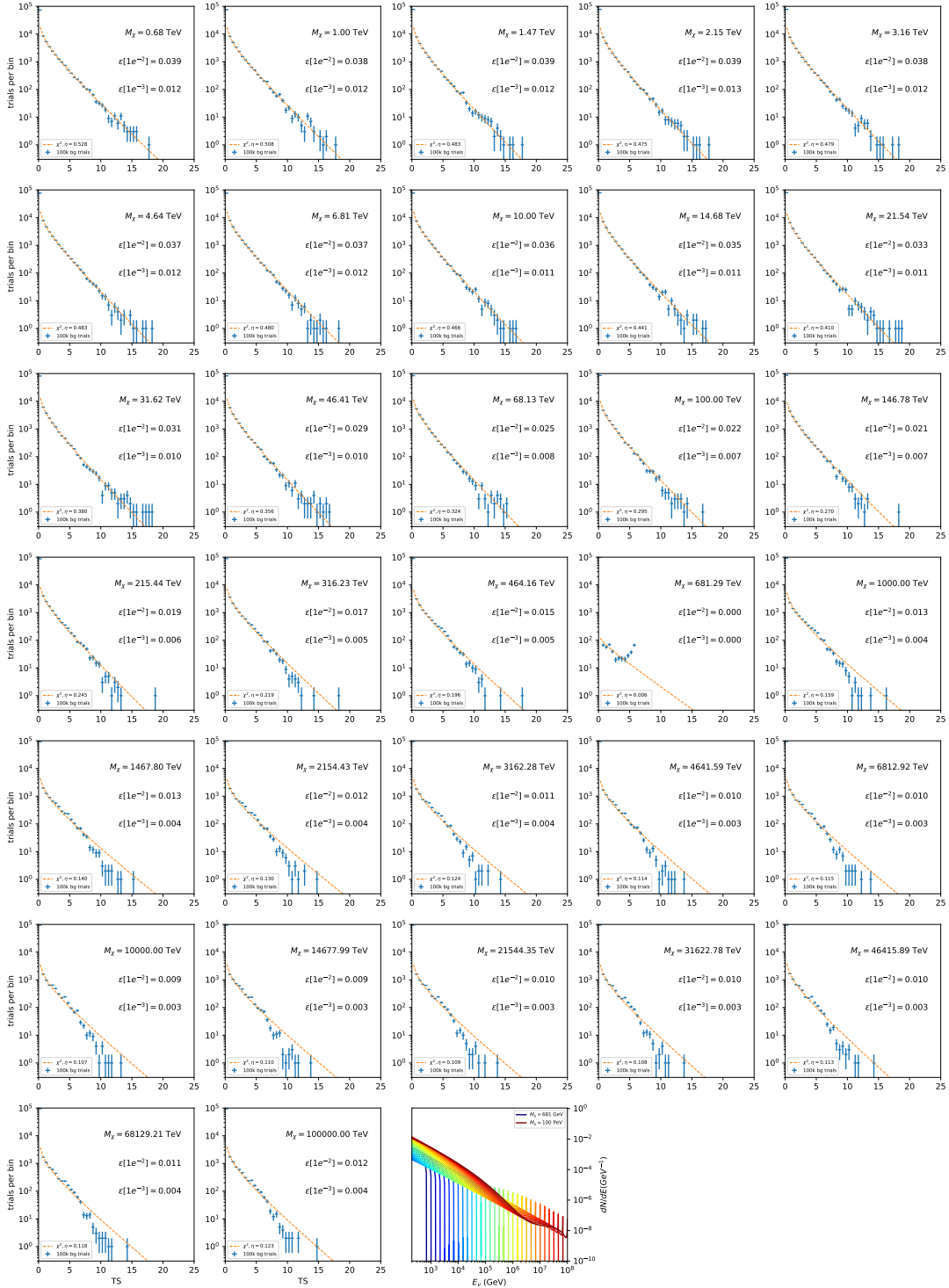


Figure 6.17 Same as Fig. 6.6 for 15, \mathcal{GS} J -factor, stacked sources and $\chi\chi \rightarrow \mu\bar{\mu}$.

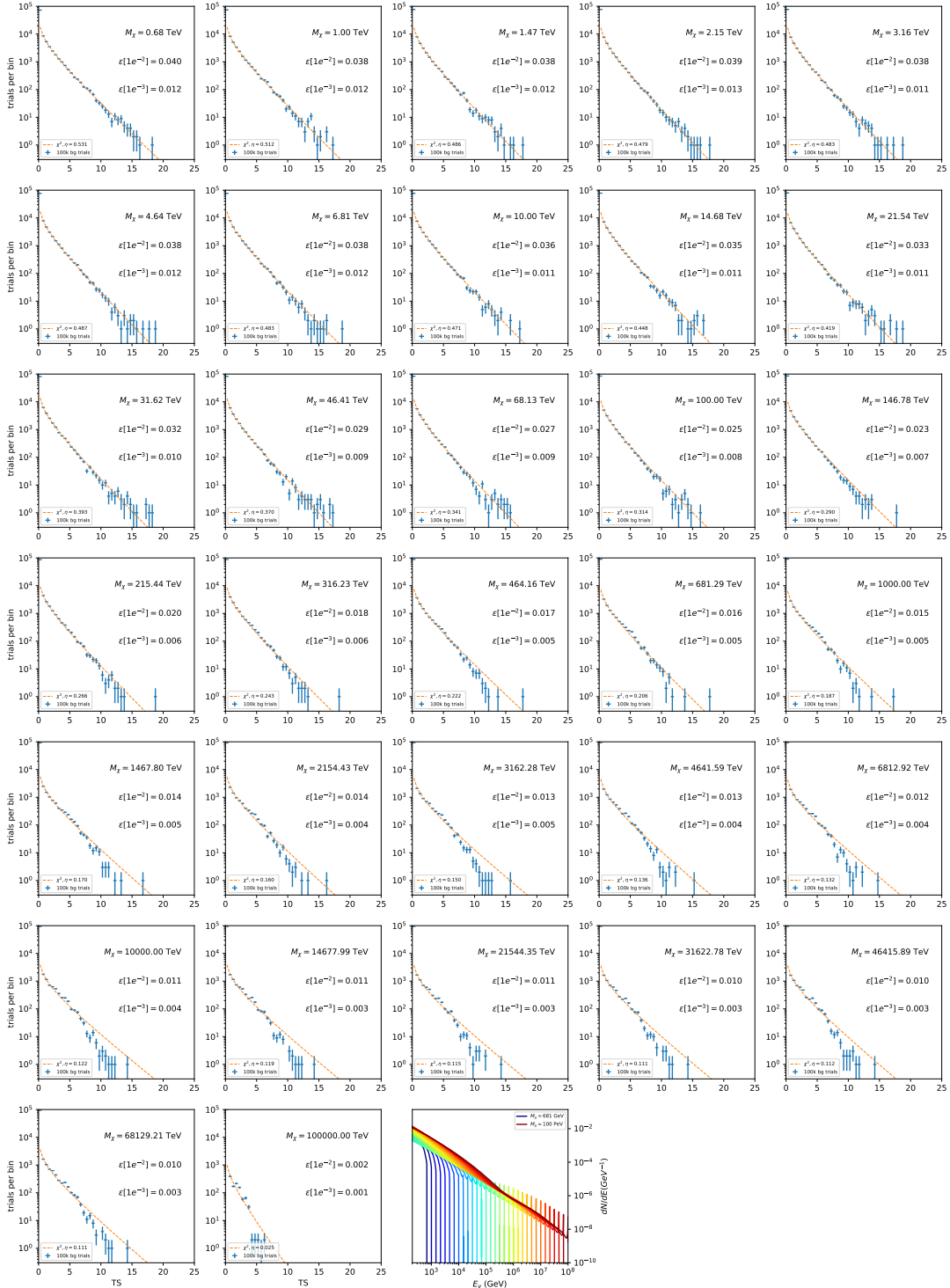


Figure 6.18 Same as Fig. 6.6 for 15, \mathcal{GS} J -factor, stacked sources and $\chi\chi \rightarrow \tau\bar{\tau}$.

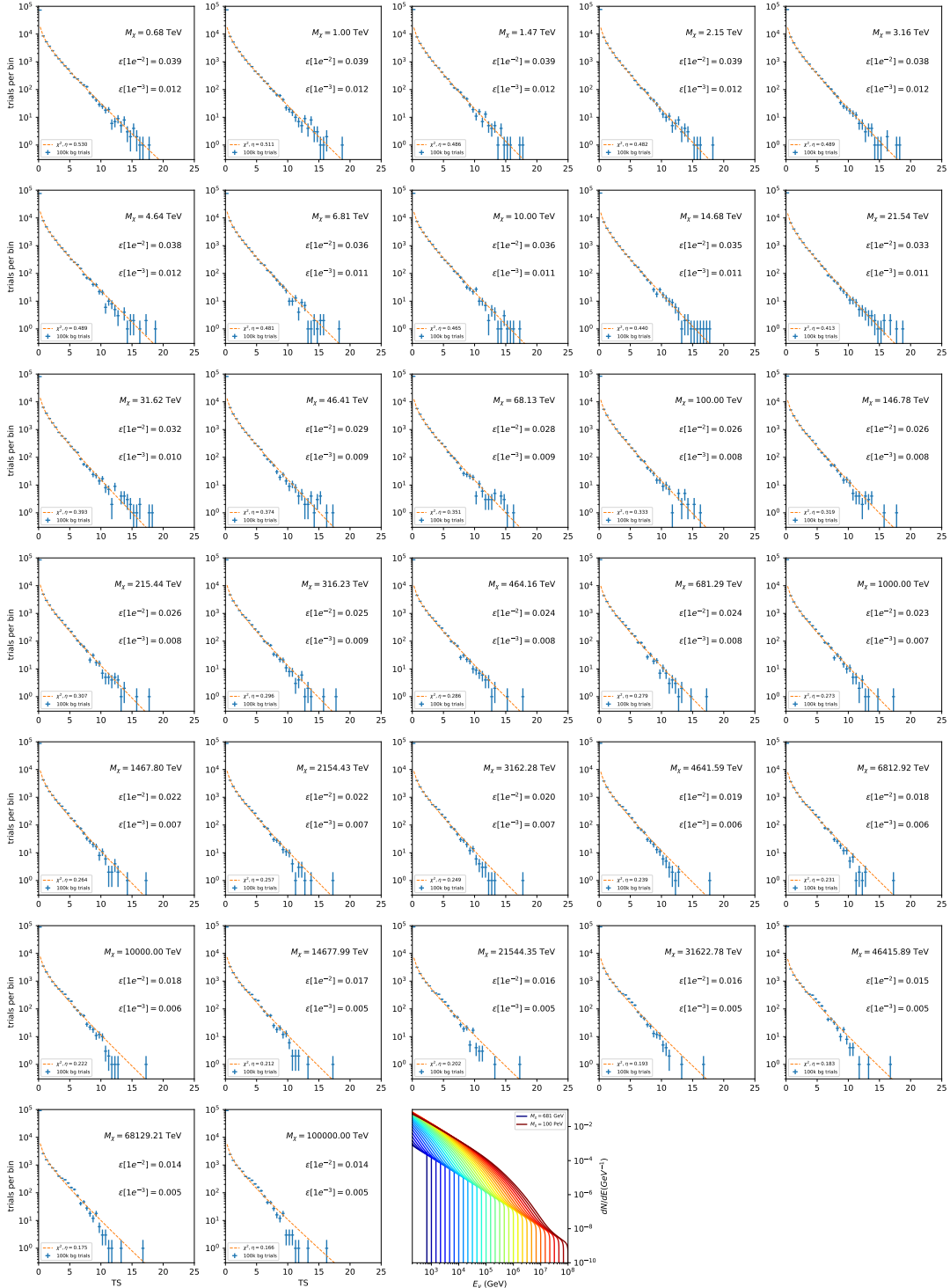


Figure 6.19 Same as Fig. 6.6 for 15, \mathcal{GS} J-factor, stacked sources and $\chi\chi \rightarrow W^+W^-$.

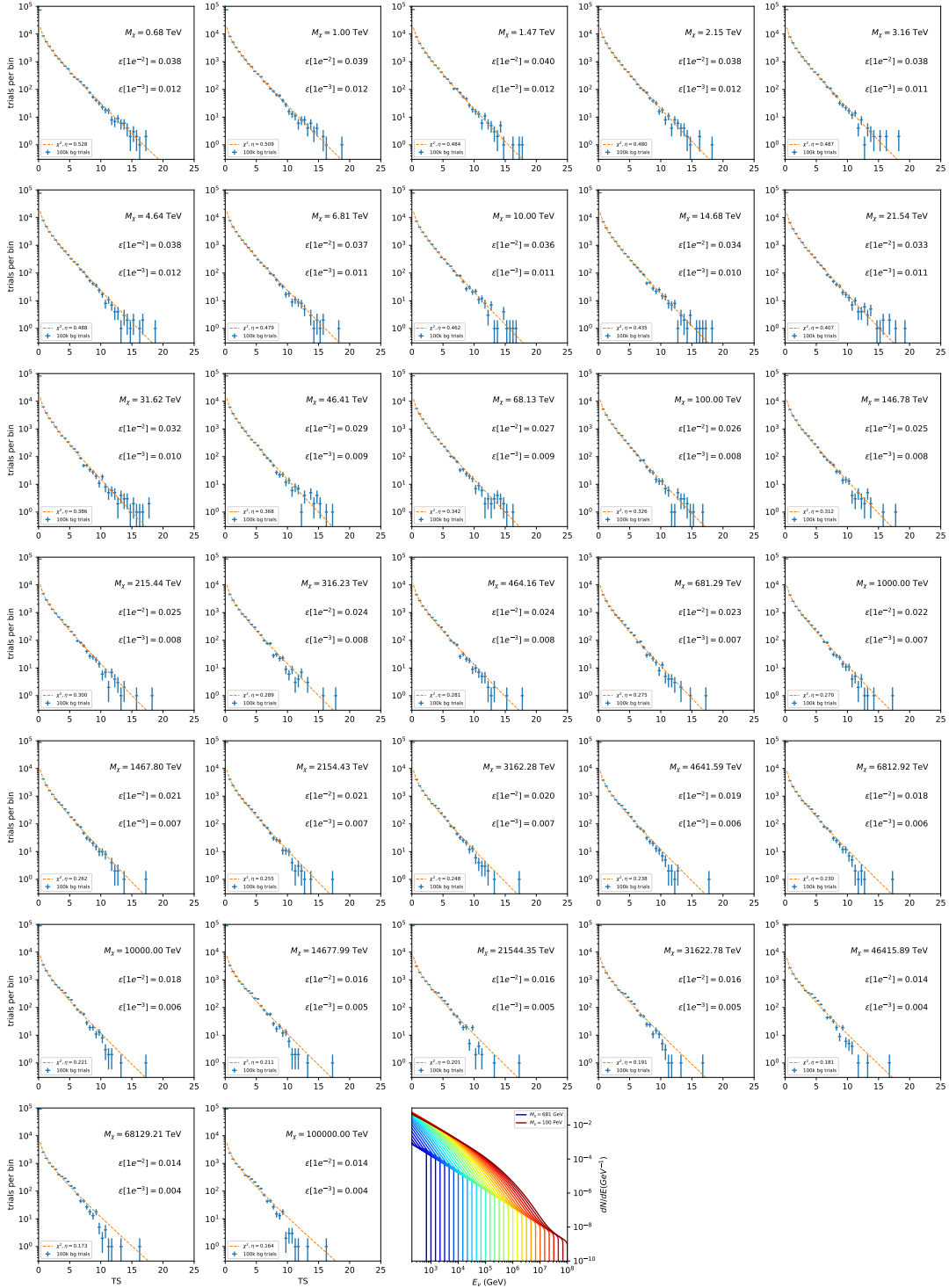


Figure 6.20 Same as Fig. 6.6 for 15, \mathcal{GS} J -factor, stacked sources and $\chi\chi \rightarrow ZZ$.

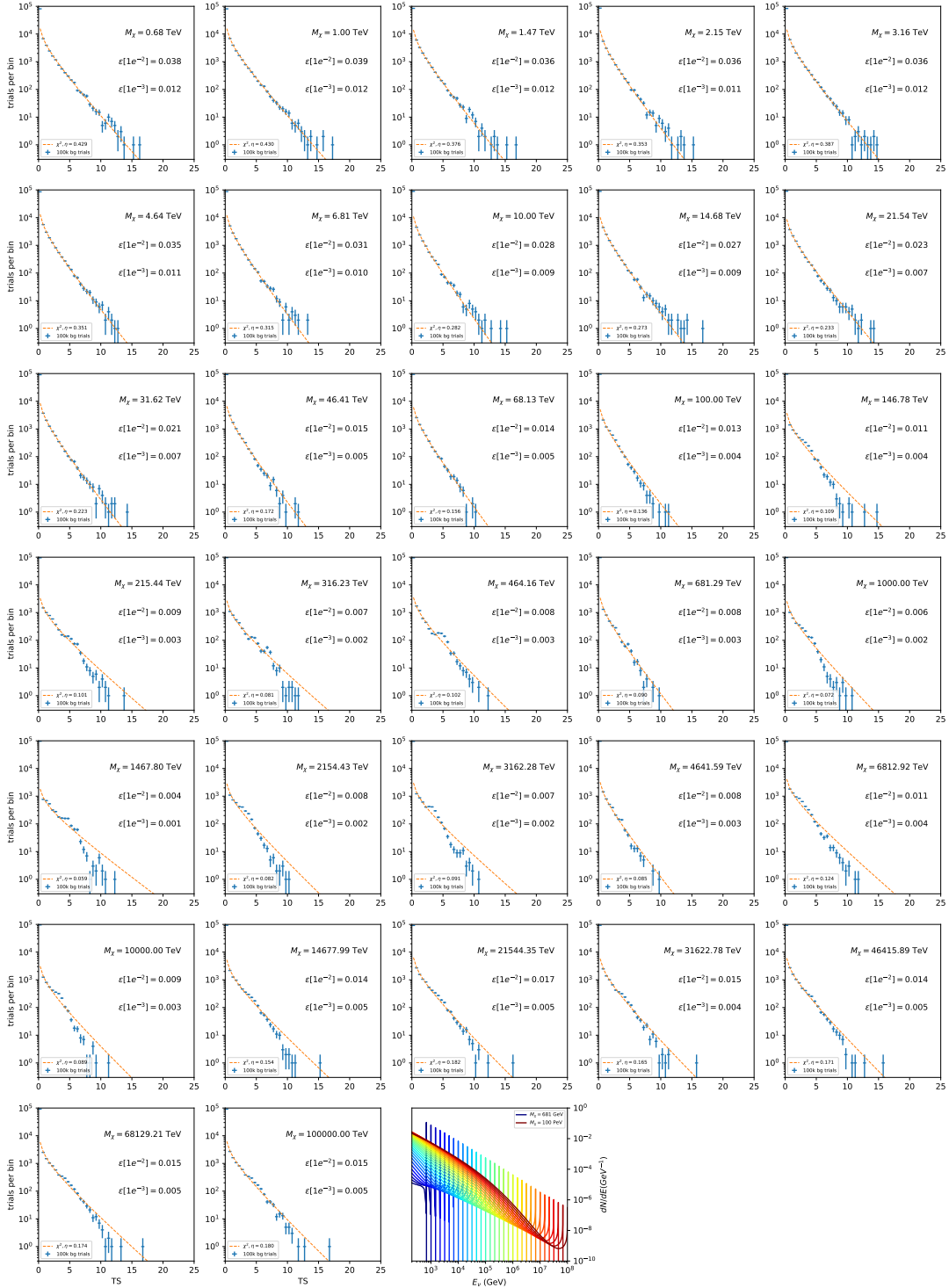


Figure 6.21 Same as Fig. 6.6 for 15, \mathcal{GS} J -factor, stacked sources and $\chi\chi \rightarrow \nu_e \bar{\nu}_e$.

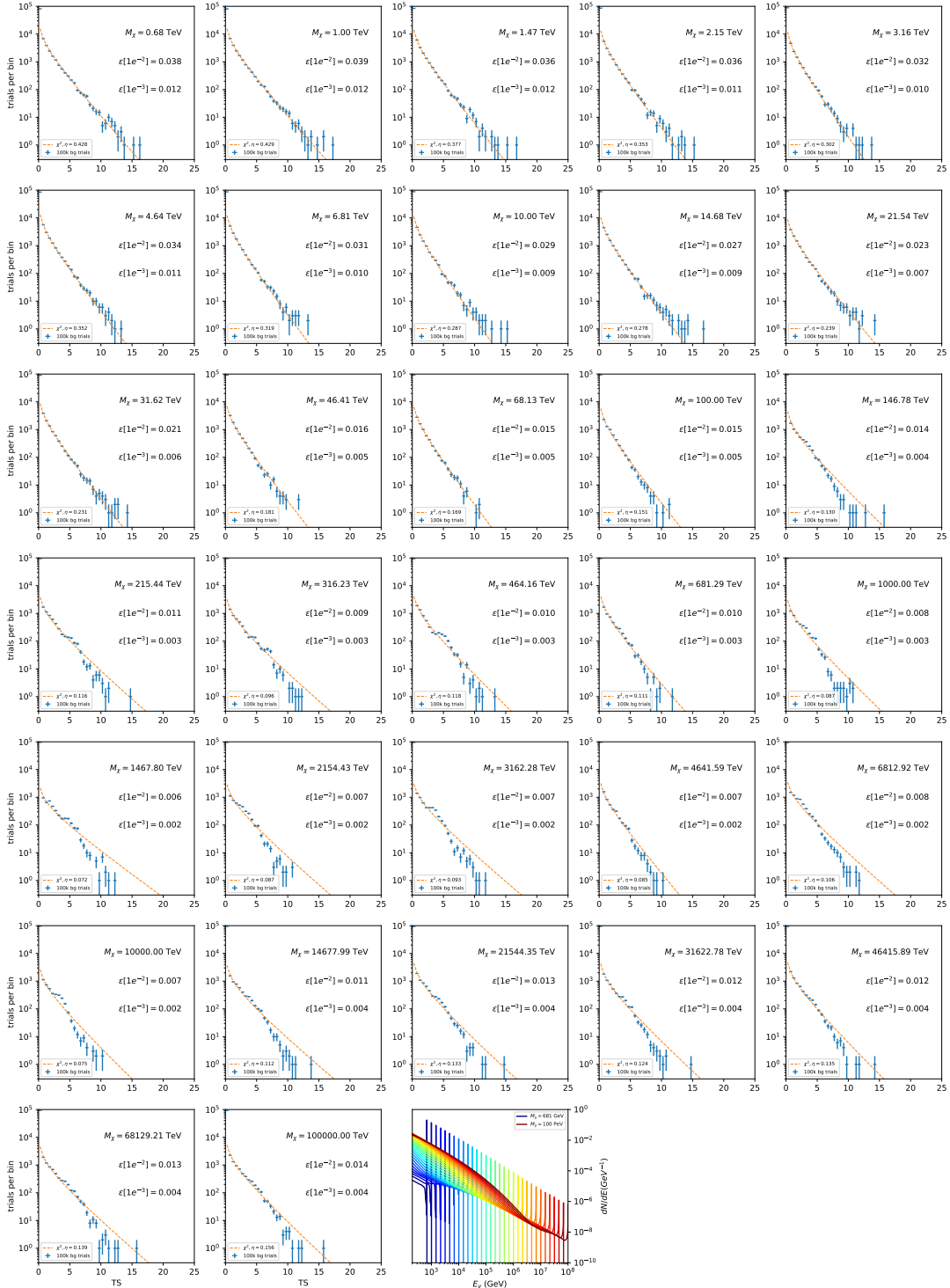


Figure 6.22 Same as Fig. 6.6 for 15, \mathcal{GS} J -factor, stacked sources and $\chi\chi \rightarrow \nu_\mu \bar{\nu}_\mu$.

2154 **6.5.1 TS per Source**

2155 Figure 6.6 to Figure 6.11 present the TS distributions for Segue 1 and Ursa Major II for 100,000
2156 trials. More studies for all annihilation channels and remaining 13 sources were also performed
2157 and are documented in IceCube’s internal wiki.

2158 Almost every distribution produced follows a χ^2 distribution with 1 degree of freedom. This is
2159 more true for low m_χ than high m_χ models. These observations are important for future assumptions
2160 made in Sec. 7 and may justify statistical calculations assuming our test statistics follow a χ^2 with
2161 1 degree of freedom.

2162 **6.5.2 Stacked TS**

2163 Figure 6.12 to Figure 6.22 present the TS distributions for a stacked study of 15 sources with
2164 \mathcal{GS} J -factors on 100,000 trials. The presentation of these plots are identical to the single source
2165 distributions in Section 6.5.1. We see similar behaviour in the stacked TS distributions compared
2166 to the single source studies.

2167 **6.6 Signal Recovery**

2168 We also wish to understand how well the analysis is able to reconstruct signal neutrinos. In
2169 order to test this, we inject neutrinos from our spectral models randomly then attempt to discern
2170 the number of signal neutrinos in the simulated data. Figure 6.23 and Figure 6.24 show this study
2171 for $\chi\chi \rightarrow b\bar{b}$, $t\bar{t}$, and $\nu_\mu\bar{\nu}_\mu$ for a stacked analysis of 15 sources. Figure C.3 to Figure C.8 show
2172 identical studies for Segue 1 and Ursa Major II. We see that the analysis is conservative at smaller
2173 m_χ , yet improves at larger m_χ . We also see that the uncertainty is small for the neutrino annihilation
2174 spectra, and the uncertainty is larger for softer channels like $b\bar{b}$.

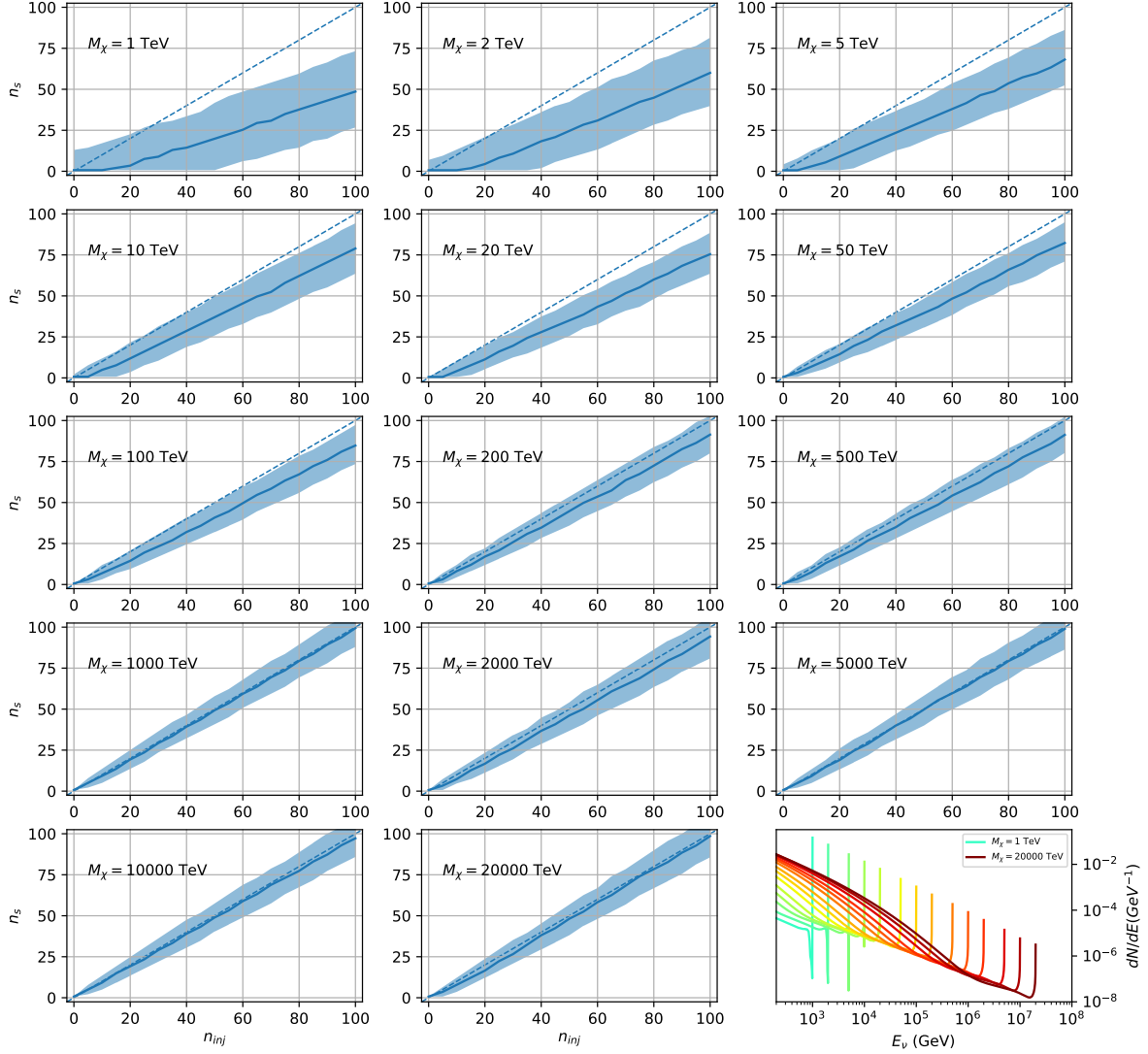


Figure 6.23 Signal Recovery study for an analysis with 15 stacked sources using the \mathcal{GS} J -factors [59]. Above shows 14 studies for DM mass ranging between 1 TeV and 20 PeV for $\chi\chi \rightarrow \mu_\mu\bar{\mu}_\mu$. The bottom right subplot features every spectral model used as input for the remaining subplots. The remaining subplots show n_{inj} as the number of signal events injected into background simulation. Whereas, n_s is the number of signal events recovered from analyzing the injected simulation. Blue line represents the median values of 100 simulations. Light blue bands show the 1σ statistical uncertainty around the median.

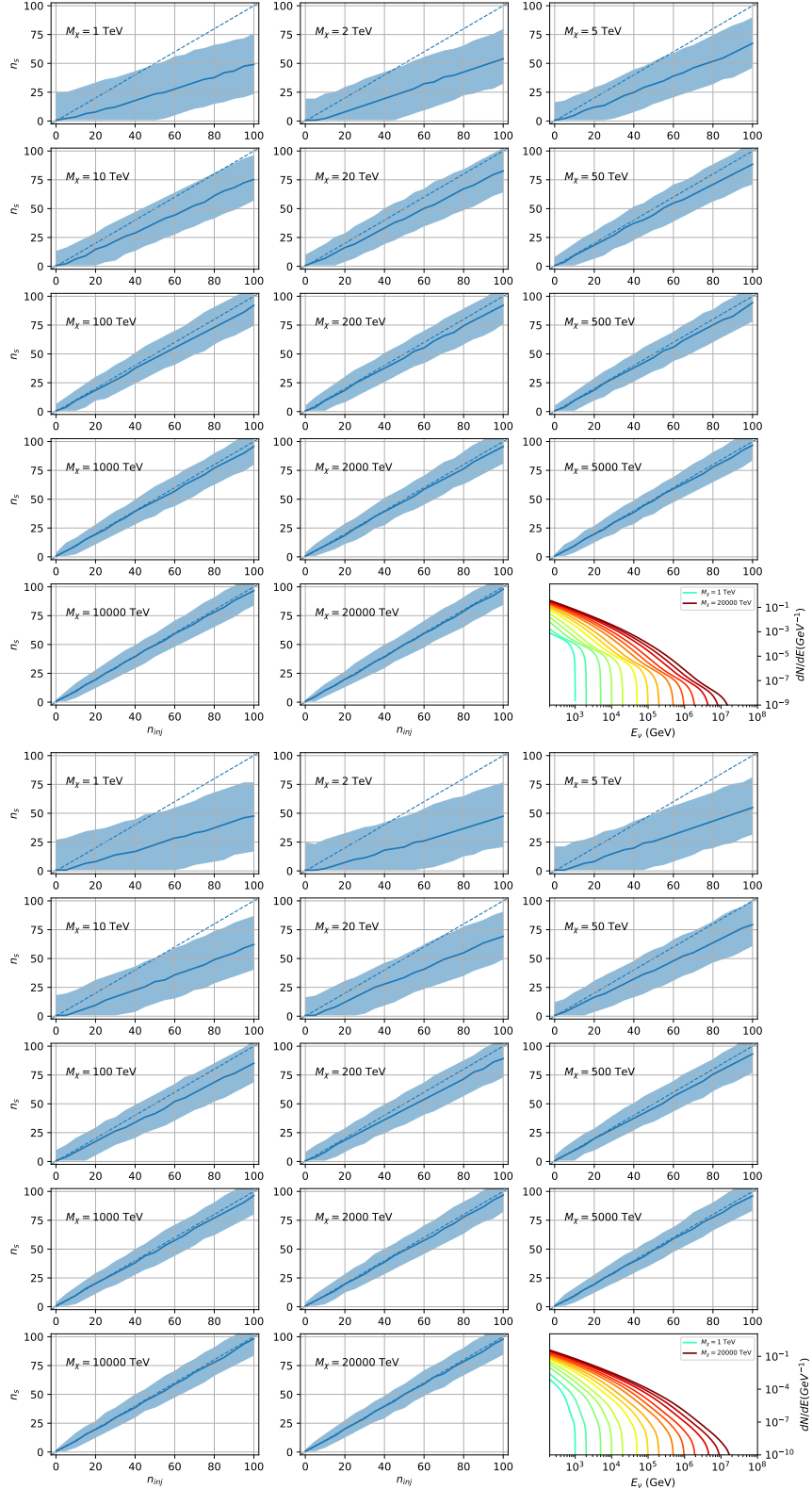


Figure 6.24 Same as Fig. 6.23 but for $\chi\chi \rightarrow t\bar{t}$ (top) and $b\bar{b}$ (bottom).

2175 **6.6.1 Sensitivities**

2176 In IceCube, we usually define the 90% confidence level (CL), as the minimum number of signal
2177 events (n_s) required to have a Type I error rate smaller than 0.5 and Type II error rate of 0.1. We
2178 compute n_s from the following equation

$$n_s = T_{\text{live}} \int_0^{\Delta\Omega} d\Omega \int_{E_{\min}}^{E_{\max}} dE_\nu A_{\text{eff}}(\hat{n}, E_\nu) \frac{d\Phi_\nu}{d\Omega dE_\nu}(\hat{n}, E_\nu), \quad (6.8)$$

2179 to extract the sensitivity on the dark matter velocity-weighted annihilation cross-section, $\langle\sigma v\rangle$. T_{live}
2180 is the detector live time, A_{eff} is the effective area of the detector, and E_{\min} , E_{\max} are the minimum,
2181 maximum energies of the expected neutrinos, respectively.

2182 Sensitivities are calculated for each source individually as if they were the only source and as a
2183 stack over 1000 trials. From Eq. (6.8) and Eq. (6.1) we can compute the $\langle\sigma v\rangle$ at a 90% confidence
2184 level. Figure 6.26 and Fig. 6.25 show the sensitivities for some DM annihilation channels. Not
2185 all channels computed successfully in time for the writing of this dissertation. Among channels
2186 missing include the charged leptons: e and τ .

2187 **6.7 Systematics**

2188 The current analysis plan is to compare these sensitivities to another J -factor catalog such as
2189 \mathcal{LS} [80] although this was not completed in time for this dissertation. Additionally, we set out to
2190 perform a standard suite of IceCube systematic studies which include: DOM efficiency, Hole ice,
2191 ice absorption, and photon scattering. We do study Earth attenuation, and Section 6.7.1 enumerates
2192 the impact of the Earth on our hardest neutrino spectra.

2193 **6.7.1 Earth Effects**

2194 We look to quantify the impact of the Earth on our sensitivity to $\chi\chi \rightarrow \nu_\mu \bar{\nu}_\mu$. This channel is
2195 expected to be among the significantly impacted annihilation channels because it has a significant
2196 contribution at PeV energies for $m_\chi \geq 1\text{PeV}$. The Earth is expected to attenuate these higher energy
2197 neutrinos. However, these neutrino spectra have significant low energy contributions, so we do not
2198 expect to entirely lose our sensitivity. This motivated a study examining our $\langle\sigma v\rangle$ sensitivity over
2199 all DM masses sampled for a selection of declinations.

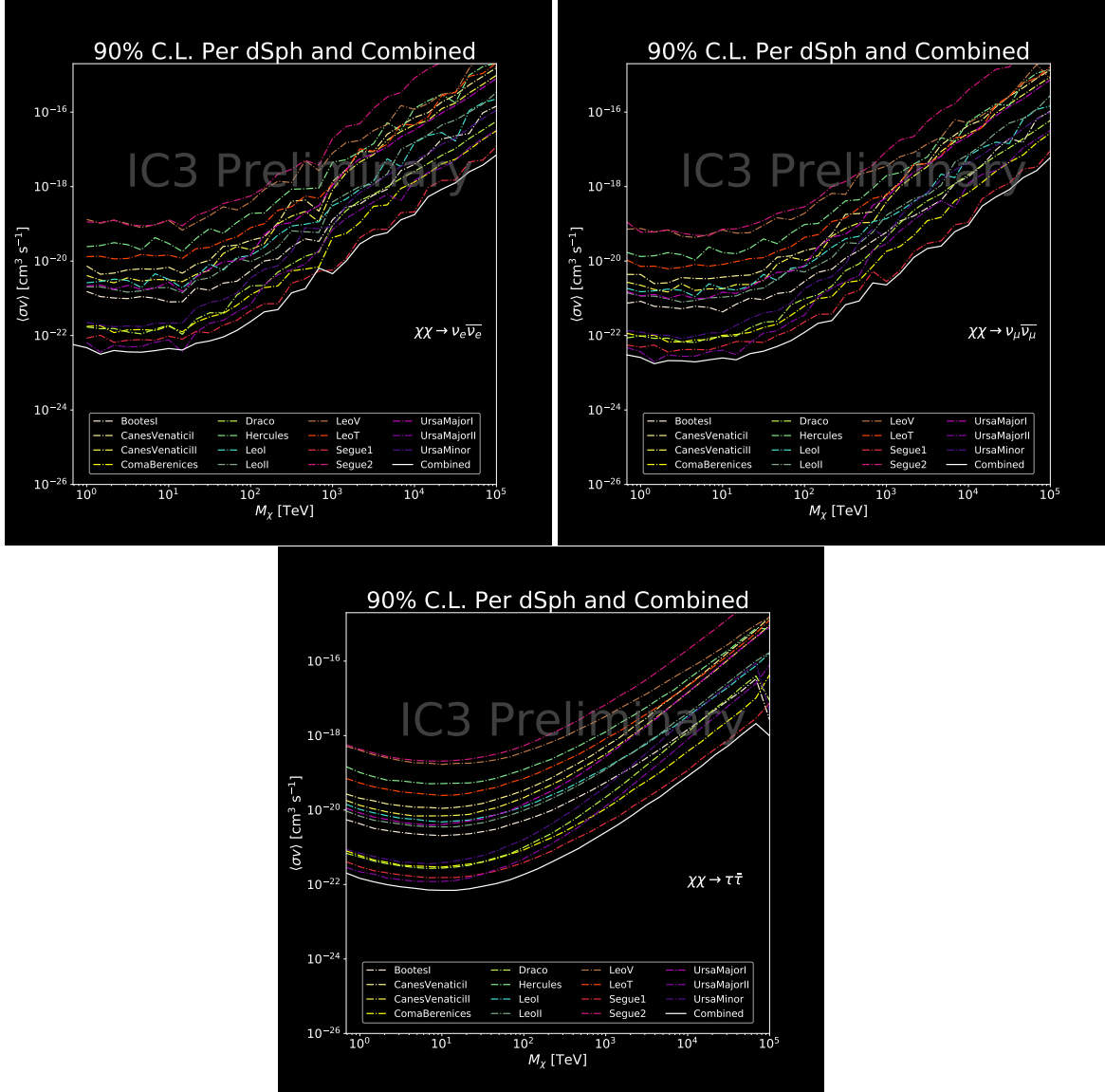


Figure 6.25 IceCube North Sky Track Sensitivities. Each panel shows sensitivity curves for various DM annihilation channels. Sensitivities are for the velocity-weighted cross-section $\langle\sigma v\rangle$ versus m_χ . Dotted, colored lines are sensitivities for individual sources. Solid white lines are for the combined sensitivity of all 15 \mathcal{GS} sources used in this study.

For this systematic study, I sample 6 DM masses per decade from 681 GeV to 100 PeV. I select declinations that are shared with sources in the \mathcal{GS} catalog: Boötes I, Canes Venatici II, Leo V, Ursa Major I, and Ursa Minor. I study a fake source who's J -factor is shared with Ursa Major II, but who's coordinates belong to the aforementioned list. The sensitivity studies performed for each source (Fig. 6.25 and Section C.5) provided n_s for 1000 trials which we extracted from Eq. (6.8). We derive $\langle\sigma v\rangle$ using $\log_{10} J = 19.42 \log_{10}(\text{GeV}^2 \text{cm}^{-5})$. Figure 6.28 shows the results.

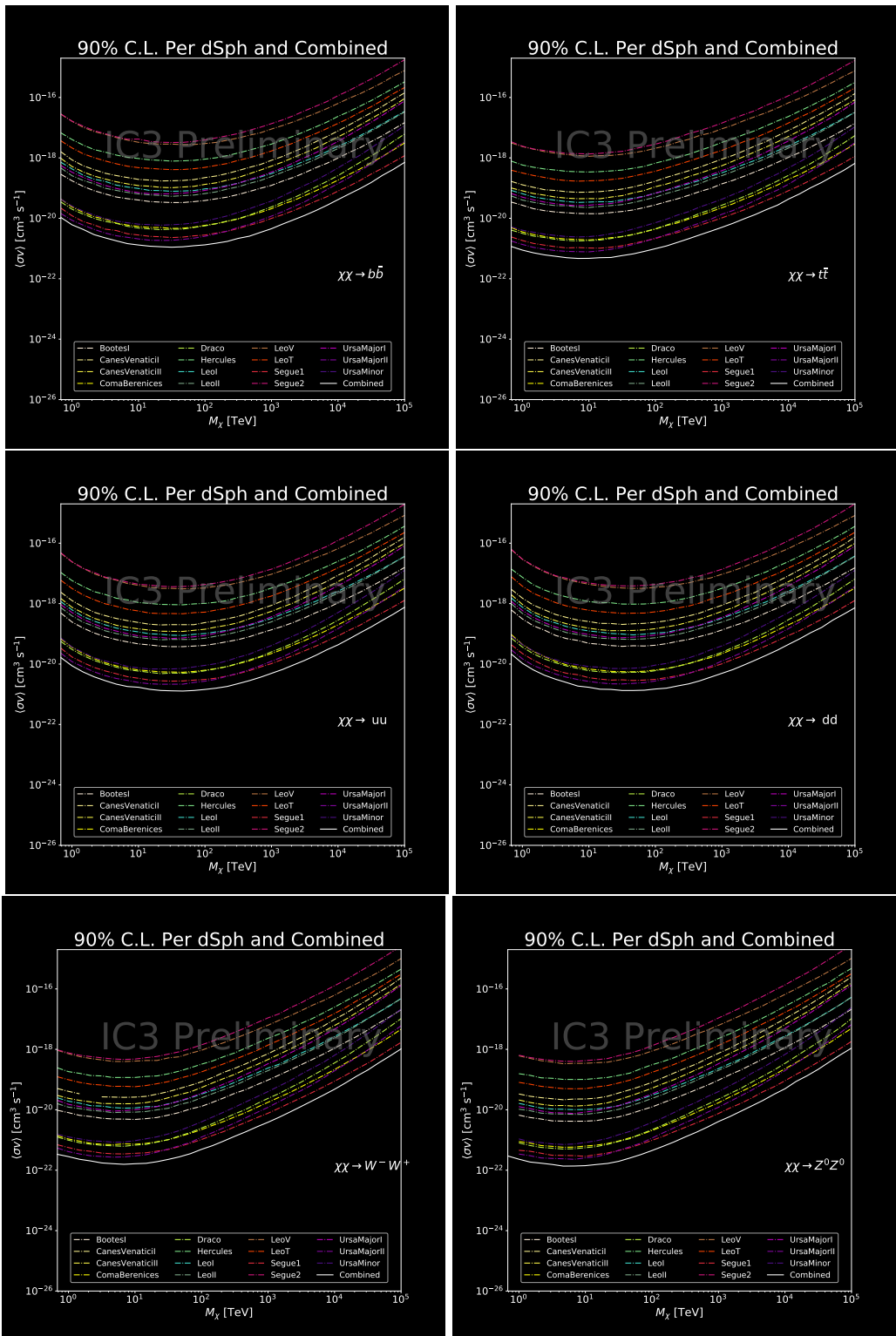


Figure 6.26 Same as Fig. 6.25 for three additional DM annihilation channels.

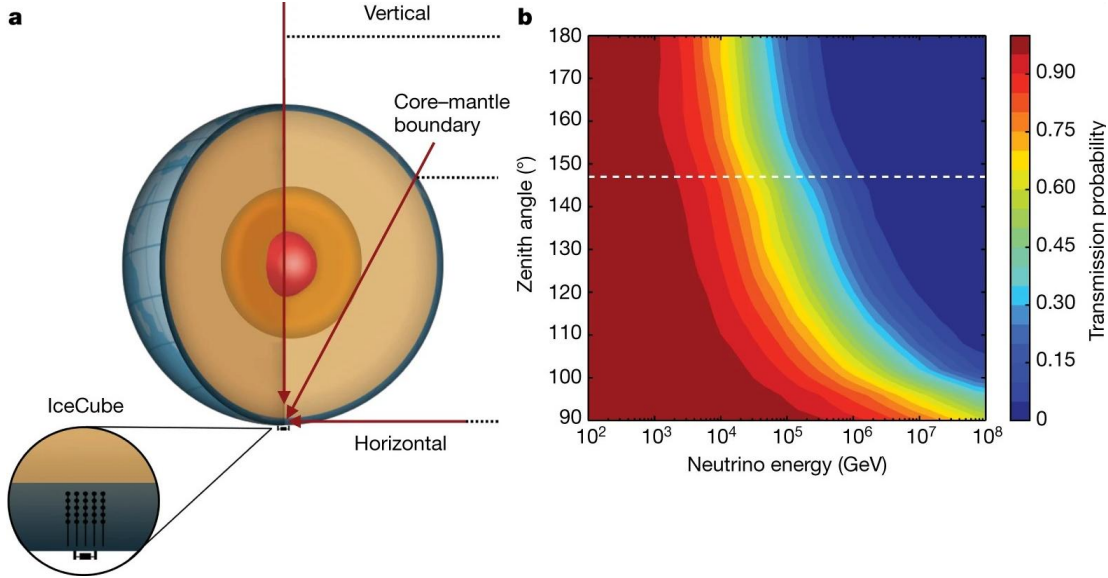


Figure 6.27 Panel A: Neutrino's from the Northern sky and incident on the IceCube detector will travel through the Earth. How much of the Earth these neutrinos travels is a function of zenith from the vertical axis. Panel B: SM prediction of neutrino transmission probabilities for neutrinos arriving at $90^\circ - 180^\circ$ zenith and with 100 GeV to 100 PeV energies. High-energy neutrinos traversing the whole Earth are completely absorbed, whereas low-energy neutrinos pass through unimpeded. Neutrinos coming from above the horizon will arrive unimpeded for all neutrino energies. Figure pulled from [102].

2206 Figure 6.28 shows that we have significant but diminishing sensitivity to sources at high
 2207 declination. We see in the worse case, the sensitivity at high declination is up to an order of
 2208 magnitude worse than at low declination. However, for $m_\chi < 1$ PeV, the sensitivities are very
 2209 similar. The comparable sensitivities imply that a stacking analysis with IceCube is most powerful
 2210 in the 500 GeV to 1 PeV region. Above 1 PeV, our limits and sensitivities are dominated by sources
 2211 near the horizon. When we additionally consider the J -factors, we expect Segue 1 to dominate
 2212 contributions to sensitivity and limits where $m_\chi > 1$ PeV.

2213 6.8 Conclusions

2214 We utilized advanced computing techniques like parallel programming and spline fitting of
 2215 particle physics Monte Carlo to greatly expand and refine IceCube's sensitivity to DM annihilation
 2216 from dSphs. Furthermore, we imported updated astrophysical and particle physics models that
 2217 better represent what we believe neutrino signals from DM annihilation should look like. We, for
 2218 the first time, build an analysis that is sensitive to PeV DM annihilation.

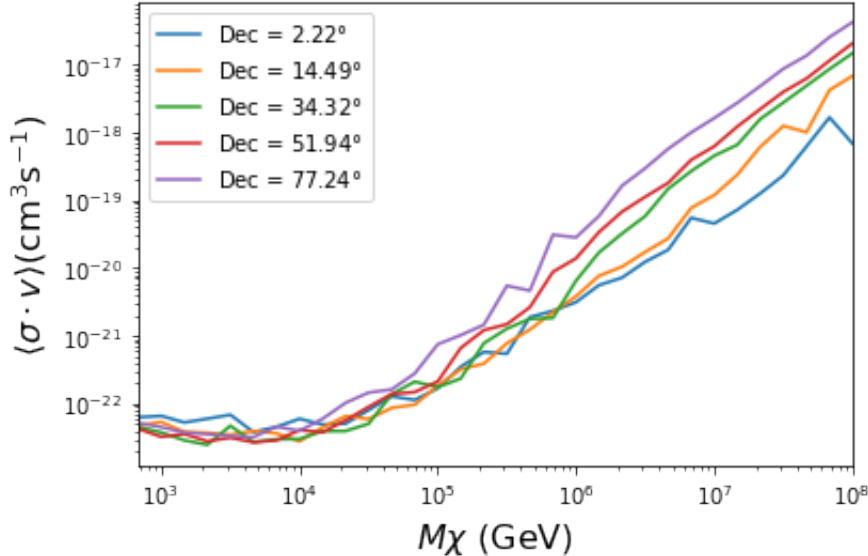


Figure 6.28 $\langle \sigma v \rangle$ sensitivities for 5 imaginary sources with $\log_{10} J = 19.42$ $\log_{10}(\text{GeV}^2 \text{cm}^{-5})$. Each imaginary source shares a declination with a source in Tab. 3.1

When we compare to previous IceCube publications of dSphs [93], we see an order of magnitude improvement to our sensitivity. This analysis has been working group approved within IceCube and is currently under collaboration review before unblinding. These processes did not complete in time for this dissertation. Therefore we do not show data for this thesis and is the clear next step.

The test statistic distributions in this analysis also demonstrate more characteristic behavior compared to previous DM analyses [97, 101]. With a 10-year dataset, we finally have enough statistics to almost trivially combine with other photon observatories, such as HAWC. The first groundwork for a multi-messenger DM search is provided with concluding remarks in chapter 7.

CHAPTER 7

2227 NU DUCK: CONCLUSIONS AND FUTURE DIRECTIONS

2228 7.1 Conclusions

2229 **TODO: Chat GPT the shit of everything below**In this work, three analyses were performed
2230 with data from the HAWC and IceCube observatories in order to explore some of the fundamental
2231 questions in particle astrophysics. The goal was to contribute to the understanding of the sources of
2232 cosmic rays, their acceleration mechanisms, and the nature of dark matter. The detection techniques
2233 and reconstruction methods for both observatories were described, along with the properties that
2234 make them ideal instruments to perform such searches.

2235 This dissertation used data from the HAWC detector to probe cutting-edge physics beyond
2236 the Standard Model. The techniques by which HAWC is able to detect cosmic gamma rays were
2237 demonstrated and the many advantages of HAWC in probing ultra-high energy gamma-ray physics
2238 were detailed. It was shown how HAWC data can be used to explore unanswered questions such as
2239 the nature of dark matter and the limits of Lorentz invariance. In particular, a search for evidence of
2240 WIMP dark matter in the Milky Way Galactic Halo was performed. To accomplish this, simulations
2241 of the dark matter density profile were combined with estimates of the HAWC sensitivity to dark
2242 matter-like energy spectra. This allowed strong constraints on dark matter annihilation and decay
2243 from the Galactic Halo to be derived that are insensitive to the large uncertainties arising from
2244 systematics in the dark matter spatial distribution. Multi-hundred TeV photon spectra were also
2245 significantly detected from HAWC sources within the Galactic Plane. These results lead to the
2246 strongest constraints on Lorentz invariance violation to be published at the time of writing.

2247 The work of this dissertation was made possible by the ongoing development of new algorithms
2248 and reconstruction techniques within the HAWC collaboration. Probing the Galactic Halo required
2249 the creation of a novel background estimation technique that relied on HAWC's wide field of view
2250 and strong ability to discriminate between gamma rays and cosmic rays. Meanwhile, the constraints
2251 on Lorentz invariance violation were enabled by the improved energy resolution from a machine
2252 learning technique. HAWC has recently completed a reprocessing of all archival data using an

updated set of algorithms that can lead to compelling follow-up work on these results. Combining the new background technique with the re-optimized energy estimators will allow for Galactic dark matter to be probed at even higher masses, as well as for analyses that require precise energy resolution such as gamma-ray line searches.

7.2 Future Directions: Multi-Messenger Dark Matter Search

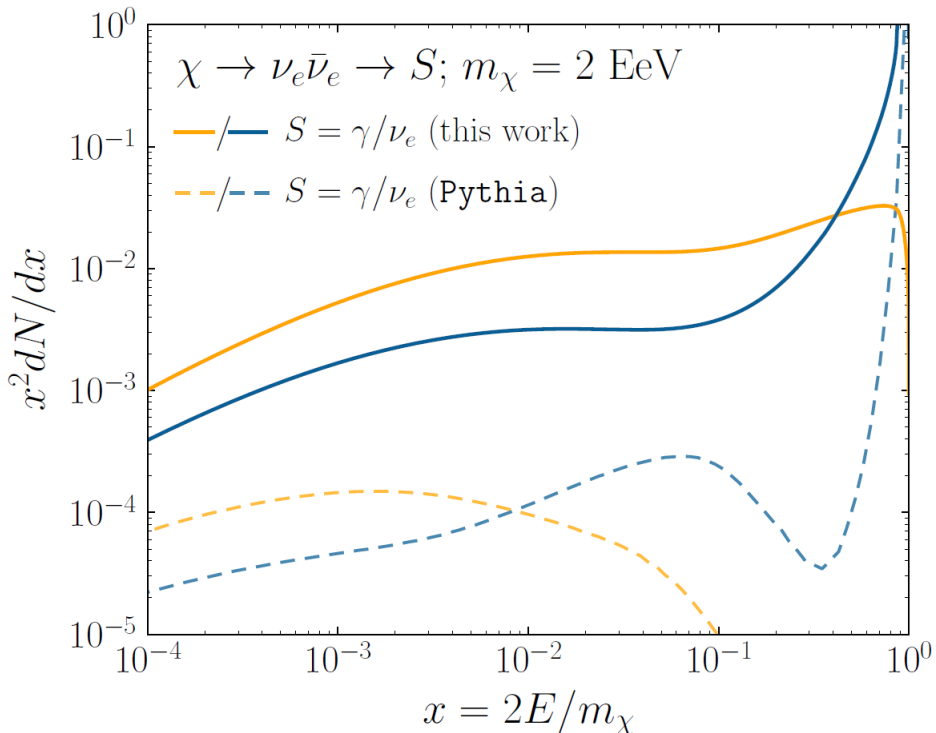


Figure 7.1 The prompt electron neutrino and photon spectrum resulting from the decay of a 2EeV DM particle to $\nu_e \bar{\nu}_e$, as currently being searched for at IceCube [5]. Solid curves represent the results of this work, and predict orders of magnitude more flux at certain energies than the dashed results of Pythia 8.2, one of the only existing methods to generate spectra at these masses. In both cases energy conservation is satisfied: there is a considerable contribution to a δ -function at $x = 1$, associated with events where an initial W or Z was never emitted and thus no subsequent shower developed. Large disagreements are generically observed at these masses for electroweak dominated channels, while the agreement is better for colored initial SM states.

As I have shown previously in Sec. 3 and Sec. 4, we can build a fast and robust analysis that shares tools with the field. The hope being that IceCube can eventually combine data with gamma-ray observatories.



Figure 7.2 TODO: neutrino and bb plot with nu Sensitivities[NEEDS A SOURCE][FACT CHECK THIS]

MULTI-EXPERIMENT SUPPLEMENTARY FIGURES

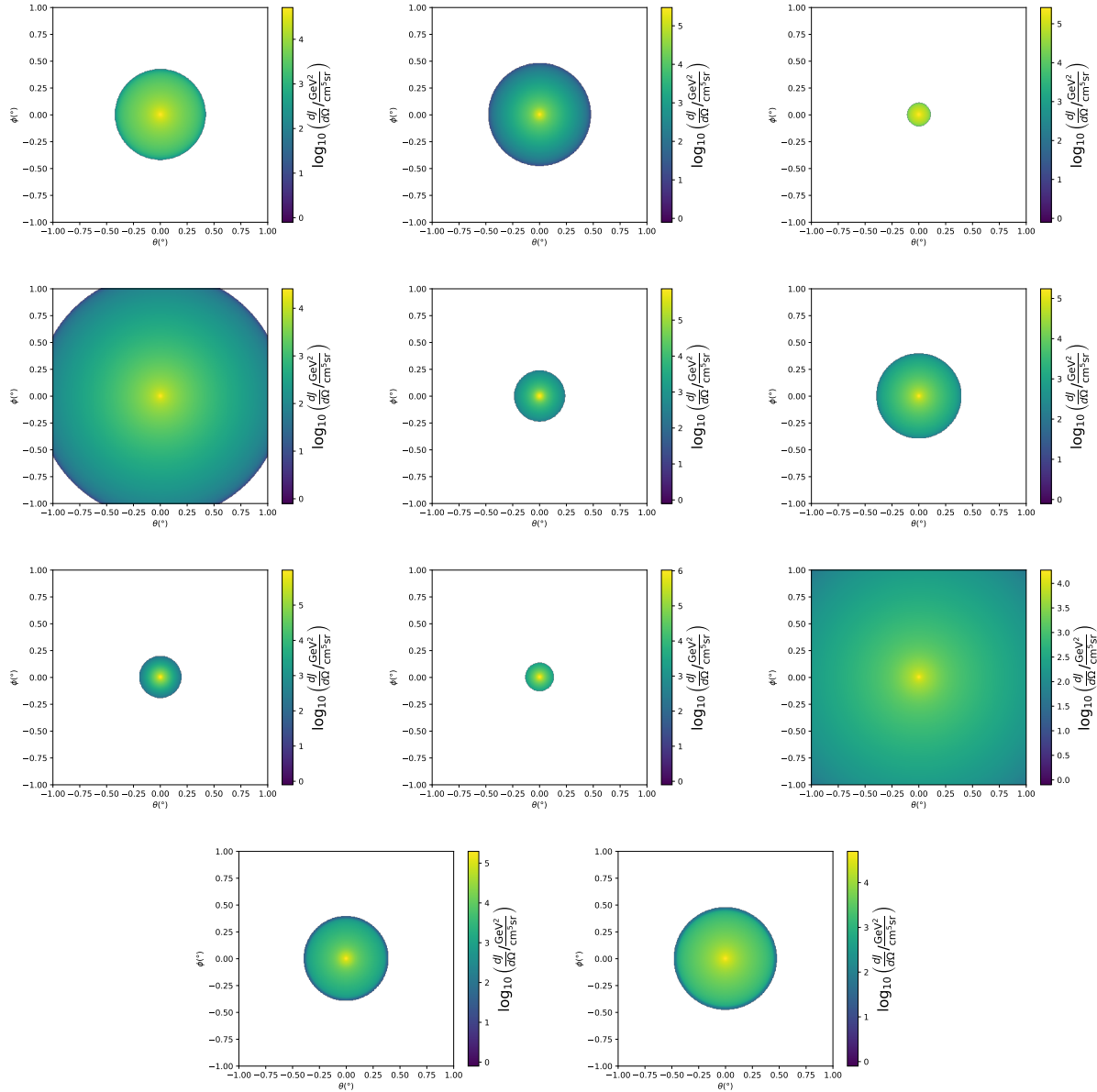


Figure A.1 Sister figure to Figure 3.3. Sources in the first row from left to right: Bootes I, Canes Venatici I, II. In second row: Draco, Hercules, Leo I. In the first row: Leo II, Leo IV, Sextans. In the final row: Ursa Major I, Ursa Major II.

APPENDIX B

2262 MULTITHREADING DARK MATTER ANALYSES SUPPLEMENTARY MATERIAL

2263 B.1 Remaining Spectral Models

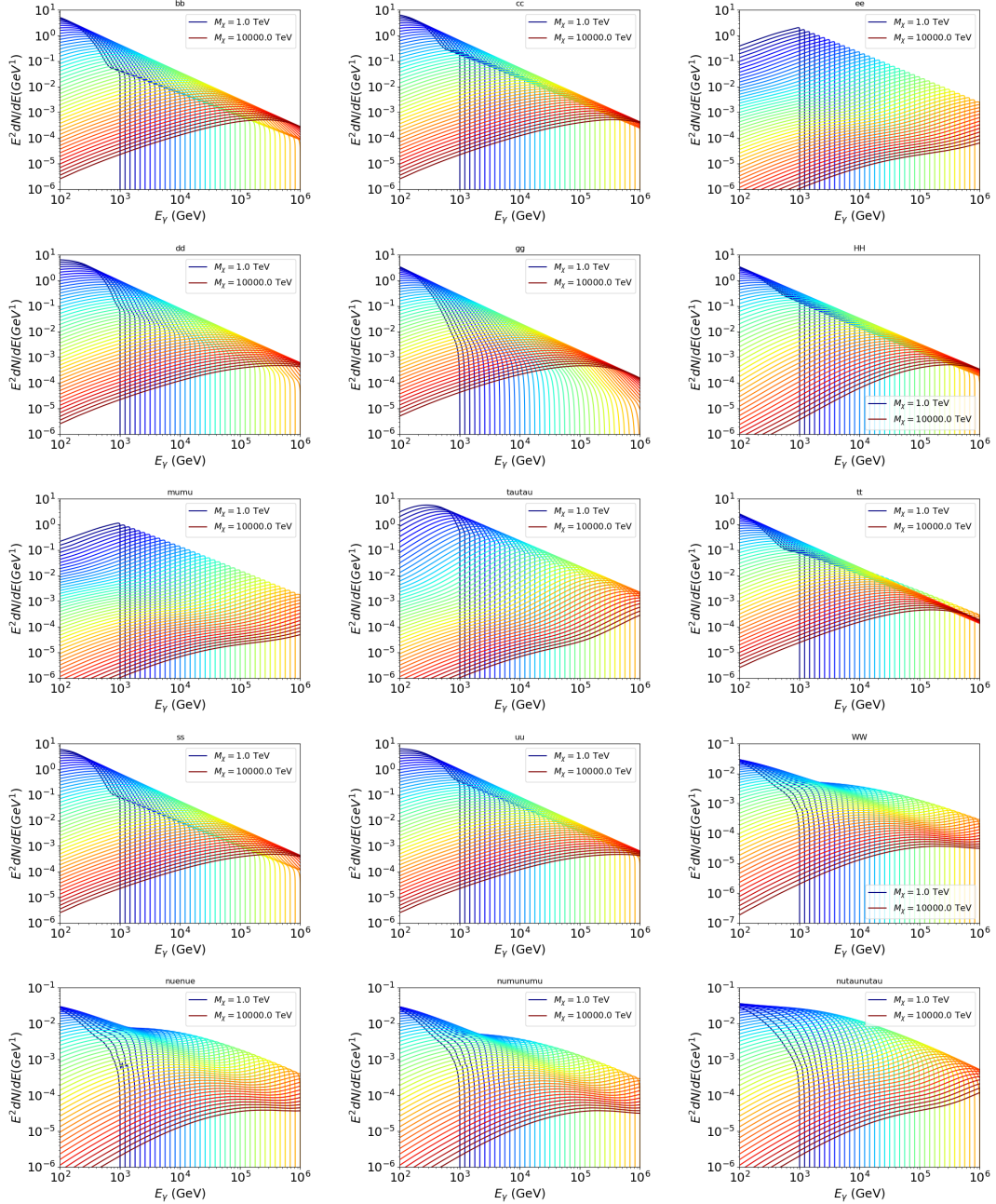


Figure B.1 Sister figure to Figure 4.2 for remaining SM primary annihilation channels studied for this thesis. These did not require any post generation smoothing and so are directly pulled from [79] with a binning scheme most helpful for a HAWC analysis.

2264 **B.2 mpu_analysis.py**

```
22651 import warnings
22662 with warnings.catch_warnings():
22673     warnings.simplefilter("ignore")
22684 # Python base libraries
22695 import os
22706 import sys
22717 import time
22728 # Import general libraries with namespace
22739 import matplotlib
22740 # Necessary for computing on cluster
22751 matplotlib.use("agg")
22762 import numpy as np
22773 import multiprocessing as mp
22784 # Import HAWC software
22795 sys.path.insert(1, os.path.join(os.environ['HOME'], 'hawc_software', 'threeML-
2280      analysis-scripts', 'fitModel'))
22816 from analysis_modules import *
22827 from threeML import *
22838 from hawc_hal import HAL, HealpixConeROI
22849 from threeML.minimizer.minimization import FitFailed
22850 # Import Dark Matter HAWC Libraries
22861 import analysis_utils as au
22872 import spectra as spec
22883 import sources as srcs
22894
22905 #* READ ONLY PATHS This block will change eventually
22916 MASS_LIST = './plotting/studies/nd/masses.txt'
22927 CHAN_LIST = './plotting/studies/nd/chans.txt'
22938
22949 #* WRITE PATHS, default location is to scratch
22950 OUT_PATH = os.path.join(os.environ["SCRATCH"], os.environ["USER"], 'New_duck')
```

```

22961 print('Our out path is going to be {}'.format(OUT_PATH))
22972
22983 # Define parallel Function. Can also be run serially
22994 def some_mass_fit(sigVs, datalist, shape, dSph, jfactor, mass_chan,
23005                 progress=None, log_file='', queue=None, i_job=0):
23016
23027     if progress is None:
23038         progress = [0]
23049     else: # Create log files for each thread
23050         log_file = log_file.replace('.log', '_ThreadNo_')
23061         log_file = log_file + str(i_job) + ".log"
23072         sys.stdout = open(log_file, "w")
23083
23094     fits = []
23105
23116     try:
23127         for m_c in mass_chan:
23138             print(f'Mass chan tuple: {m_c}')
23149             mass = int(m_c[0])
23150             ch = m_c[1]
23161             # Build path to output files
23172             outPath = os.path.join(OUT_PATH, ch, dSph)
23183             au.ut.ensure_dir(outPath)
23194
23205             if progress[i_job] < 0:
23216                 # If the master gets a Keyboard interrupt, commit suicide.
23227                 break
23238
23249                 ### Start Model Building for DM mass and SM channel #####
23250             spectrum = spec.DM_models.HDMSpectra()
23261             spectrum.set_channel(ch)
23272
23283             myDwarf = ExtendedSource(dSph, spatial_shape=shape,

```

```

23294                     spectral_shape=spectrum)
23305
23316             spectrum.J = jfactor * u.GeV**2 / u.cm**5
23327             spectrum.sigmav = 1e-24 * u.cm**3 / u.s
23338             spectrum.set_dm_mass(mass * u.GeV)
23349
23350             spectrum.sigmav.bounds = (1e-30, 1e-12)
23361             model = Model(myDwarf)
23372             ##### End model Building #####
23383
23394             jl = JointLikelihood(model, datalist, verbose=False)
23405
23416             try:
23427                 result, lhdf = jl.fit(compute_covariance=False)
23438                 ts = -2.* (jl.minus_log_like_profile(1e-30) - jl.
2344 _current_minimum)
23459                 # Also profile the LLH vs sv
23460                 ll = jl.get_contours(spectrum.sigmav, sigVs[0],
23471                                     sigVs[-1], len(sigVs),
23482                                     progress=False, log=['False'])
23493
23504                 sigv_ll = au.ut.calc_95_from_profile(ll[0], ll[2])
23515                 # Write results to file
23526                 outFileLL = outPath+f"/LL_{dSph}_{ch}_mass{int(mass)}_GD.txt"
23537                 np.savetxt(outFileLL, (sigVs, ll[2]),
23548                             delimiter='\t', header='sigV\tLL\n')
23559
23560                 with open(outPath+f"/results_{dSph}_{ch}_mass{int(mass)}_GD.
2357 txt", "w") as results_file:
23581                     results_file.write("mDM [GeV]\tsigV_95\tsigV_B.F.\n")
23592
23603                     results_file.write("%i\t%.5E\t%.5E\t%.5E"%(mass, sigv_ll,
23614                                         ts, result.value[0]))

```

```

23625         # End write to file
23626
23627     except FitFailed: # Don't kill all threads if a fit fails
23628         print("Fit failed. Go back and calculate this spectral model
23629             later")
23630
23631         fits.append((ch, mass, -1, -1))
23632
23633         with open(log_file+'.fail', 'w') as f_file:
23634             f_file.write(f'{ch}, {mass}\n')
23635
23636
23637         progress[i_job] += 1
23638
23639         matplotlib.pyplot.close() # Prevent leaky memory
23640
23641
23642         fits.append((ch, mass, result.value[0], ts))
23643
23644         progress[i_job] += 1
23645
23646         matplotlib.pyplot.close()
23647
23648     except KeyboardInterrupt:
23649         progress[i_job] = -1
23650
23651
23652     fits = np.array(fits)
23653
23654     if queue is None:
23655         return fits
23656
23657     else:
23658
23659         queue.put((i_job, fits))
23660
23661
23662 def main(args):
23663
23664     masses = np.loadtxt(MASS_LIST, dtype=int)
23665
23666     chans = np.loadtxt(CHAN_LIST, delimiter=',', dtype=str)
23667
23668     mass_chan = au.ut.permute_lists(chans, masses)
23669
23670
23671     print(f"DM masses for this study are: {masses}")
23672
23673     print(f"SM Channels for this study are XX -> {chans}")
23674
23675     print(mass_chan)
23676
23677
23678     # extract information from input argument

```

```

23957 dSph = args.dSph
23968 data_mngr = au.ut.Data_Selector('P5_NN_2D')
23979 dm_profile = srcts.Spatial_DM(args.catalog, dSph, args.sigma, args.decay)
23980
23991 ##### Extract Source Information #####
24002 if dm_profile.get_dec() < -22.0 or dm_profile.get_dec() > 62.0:
24013     raise ValueError("HAWC can't see this source D: Exitting now...")
24024
24035 print(f'{dSph} information')
24046 print(f'jfac: {dm_profile.get_factor()}\tRA: {dm_profile.get_ra()}\tDec: {dm_profile.get_dec()}\n')
2405
24067
24078 shape = SpatialTemplate_2D(fits_file=dm_profile.get_src_fits())
24089 ##### Finish Extract Source Information #####
24090
24101 ##### LOAD HAWC DATA #####
24112 roi = HealpixConeROI(data_radius=2.0, model_radius=8.0,
24123                         ra=dm_profile.get_ra(), dec=dm_profile.get_dec())
24134 bins = choose_bins.analysis_bins(args, dec=dm_profile.get_dec())
24145
24156 hawc = HAL(dSph, data_mngr.get_datmap(), data_mngr.get_detres(), roi)
24167 hawc.set_active_measurements(bin_list=bins)
24178 datalist = DataList(hawc)
24189 ##### FINISH LOAD HAWC DATA #####
24190
24201 # set up SigV sampling. This sample is somewhat standardized
24212 sigVs = np.logspace(-28,-18, 1001, endpoint=True) # NOTE This will change
2422 with HDM
24233
24244 if args.n_threads == 1:
24255     # No need to start || programming just iterate over the masses
24266     kw_arg = dict(sigVs=sigVs, datalist=datalist, shape=shape, dSph=dSph,
24277                     jfactor=dm_profile.get_factor(), mass_chan=mass_chan,

```

```

24288                 log_file=args.log)
24299             some_mass_fit(**kw_arg)
24300         else:
24311             # I Really want to suppress TQMD output
24322             from tqdm import tqdm
24333             from functools import partialmethod
24344             tqdm.__init__ = partialmethod(tqdm.__init__, disable=True)
24355
24366             x = np.array_split(mass_chan, args.n_threads)
24377             n_jobs = len(x)
24388
24399             print("Thread jobs summary by mass and SM channel")
24400             for xi in x:
24411                 print(f'{xi}')
24422
24433             queue = mp.Queue()
24444             progress = mp.Array('i', np.zeros(n_jobs, dtype=int))
24455
24466             # Define task pool that will be split amongsts threads
24477             kw_args = [dict(sigVs=sigVs, datalist=datalist, shape=shape,
24488                             dSph=dSph, jfactor=dm_profile.get_factor(),
24499                             mass_chan=mass_chan, progress=progress,
24500                             queue=queue, i_job=i, log_file=args.log)
24511                 for i, mass_chan in enumerate(x)]
24522
24533             # Define each process
24544             procs = [mp.Process(target=some_mass_fit, kwargs=kw_args[i]) \
24555                 for i in range(n_jobs)]
24566
24577             ### Start MASTER Thread only code block ###
24588             # Begin running all child threads
24599             for proc in procs: proc.start()
24600

```

```

24611     try:
24612
24613         # In this case, the master does nothing except monitor progress of
24614         # the threads
24615
24616         # In an ideal world, the master thread also does some computation.
24617
24618         n_complete = np.sum(progress)
24619
24620         while_count = 0
24621
24622
24623         while n_complete < len(mass_chan):
24624
24625             if np.any(np.asarray(progress) < 0):
24626
24627                 # This was no threads are stranded when killing the script
24628
24629                 raise KeyboardInterrupt()
24630
24631             if while_count%1000 == 0:
24632
24633                 print(f'{np.sum(progress)} of {len(mass_chan)} finished')
24634
24635             n_complete = np.sum(progress)
24636
24637             time.sleep(.25)
24638
24639             while_count += 1
24640
24641
24642         except KeyboardInterrupt:
24643
24644             # signal to jobs that it's time to stop
24645
24646             for i in range(n_jobs):
24647
24648                 progress[i] = -2
24649
24650                 print('\nKeyboardInterrupt: terminating early.')
24651
24652             ### End MASTER Thread only code block ###
24653
24654
24655             fitss = [queue.get() for proc in procs]
24656
24657             print(fitss)
24658
24659             print(f'Thread statuses: {progress[:]}')
24660
24661
24662             # putting results in a file
24663
24664
24665             print("QUACK! All Done!")

```

```

24943
24954
24965 if __name__ == '__main__':
24976     import argparse
24987
24998     p = argparse.ArgumentParser(description="Run a DM annihilation analysis on
2500         a dwarf spheroidal for a specific SM channel for DM masses [1 TeV to 10
2501             PeV]")
25029
25030     # Dwarf spatial modeling arguements
25041     p.add_argument("-ds", "--dSph", type=str,
25052                     help="dwarf spheroidal galaxy to be studied", required=
2506             True)
25073     p.add_argument("-cat", "--catalog", type=str, choices=['GS15', 'LS20'],
25084                     default='LS20', help="source catalog used")
25095     p.add_argument("-sig", "--sigma", type=int, choices=[-1, 0, 1], default=0,
25106                     help="Spatial model uncertainty. 0 corresponds to the
2511             median. +/-1 correspond to the +/-1sigma uncertainty respectively.")
25127
25138     # Arguements for the energy estimators
25149     p.add_argument("-e", "--estimator", type=str,
25150                     choices=['P5_NHIT', 'P5_NN_2D'],
25161                     default="P5_NN_2D", required=False,
25172                     help="The energy estimator choice. Options are: P5_NHIT,
2518             P5_NN_2D. GP not supported (yet).")
25193     p.add_argument("--use-bins", default=None, nargs="*",
25204                     help="Bins to use for the analysis", dest="use_bins")
25215     p.add_argument('--select_bins_by_energy', default=None, nargs="*",
25226                     help="Does nothing. May fill in later once better
2523             understood")
25247     p.add_argument('--select_bins_by_fhit', default=None, nargs="*",
25258                     help="Also does nothing see above")
25269     p.add_argument( '-ex', '--exclude', default=None, nargs="*",

```

```

25270         help="Exclude Bins", dest="exclude")

25281

25292     # Computing and logging arguements.

25303     p.add_argument('-nt', '--n_threads', type=int, default=1,
2534                 help='Maximum number of threads spawned by script. Default
2532                 is 4')

25335     p.add_argument('-log', '--log', type=str, required=True,
2534                 help='Name for log files. Especially needed for threads')

25357

25368     p.add_argument('--decay', action="store_true",
25379                 help='Set spectral DM hypothesis to decay')

25380

25391     args = p.parse_args()

25402     print(args.decay)

25413     if args.exclude is None: # default exclude bins 0 and 1
25424         args.exclude = ['B0C0Ea', 'B0C0Eb', 'B0C0Ec', 'B0C0Ed', 'B0C0Ee']

25435

25446     if args.decay: OUT_PATH += '_dec'
25457     else: OUT_PATH += '_ann'

25468

25479     OUT_PATH = OUT_PATH + '_' + args.catalog
25480     if args.sigma != 0: OUT_PATH += f'_{args.sigma}sig'

25491

25502     main(args)

```

2551 B.3 Comparison with Glory Duck

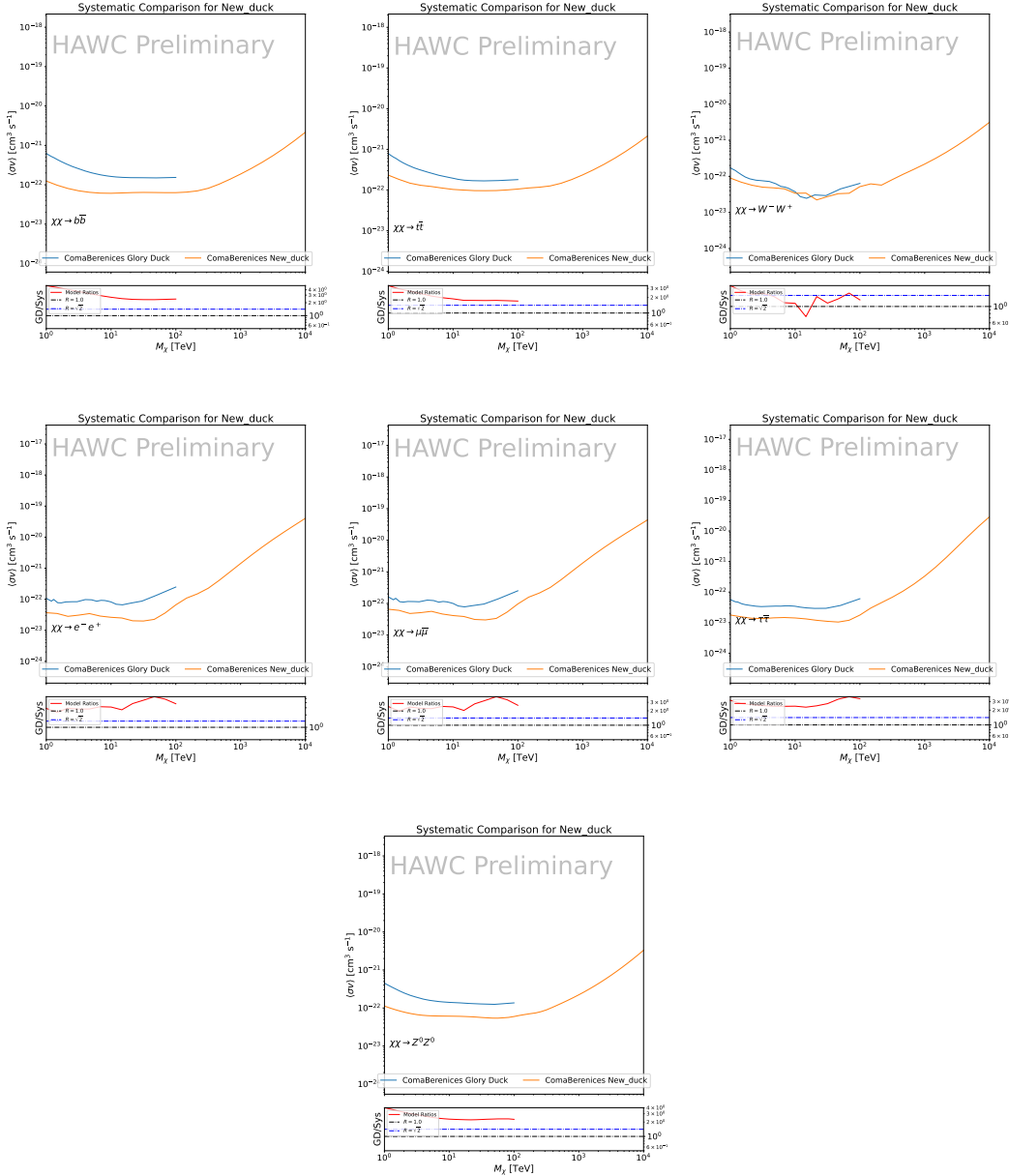


Figure B.2 Comparison of HAWC limits from this analysis to Glory Duck (Fig. 3.5) for Coma Berenices and 7 DM annihilation channels.

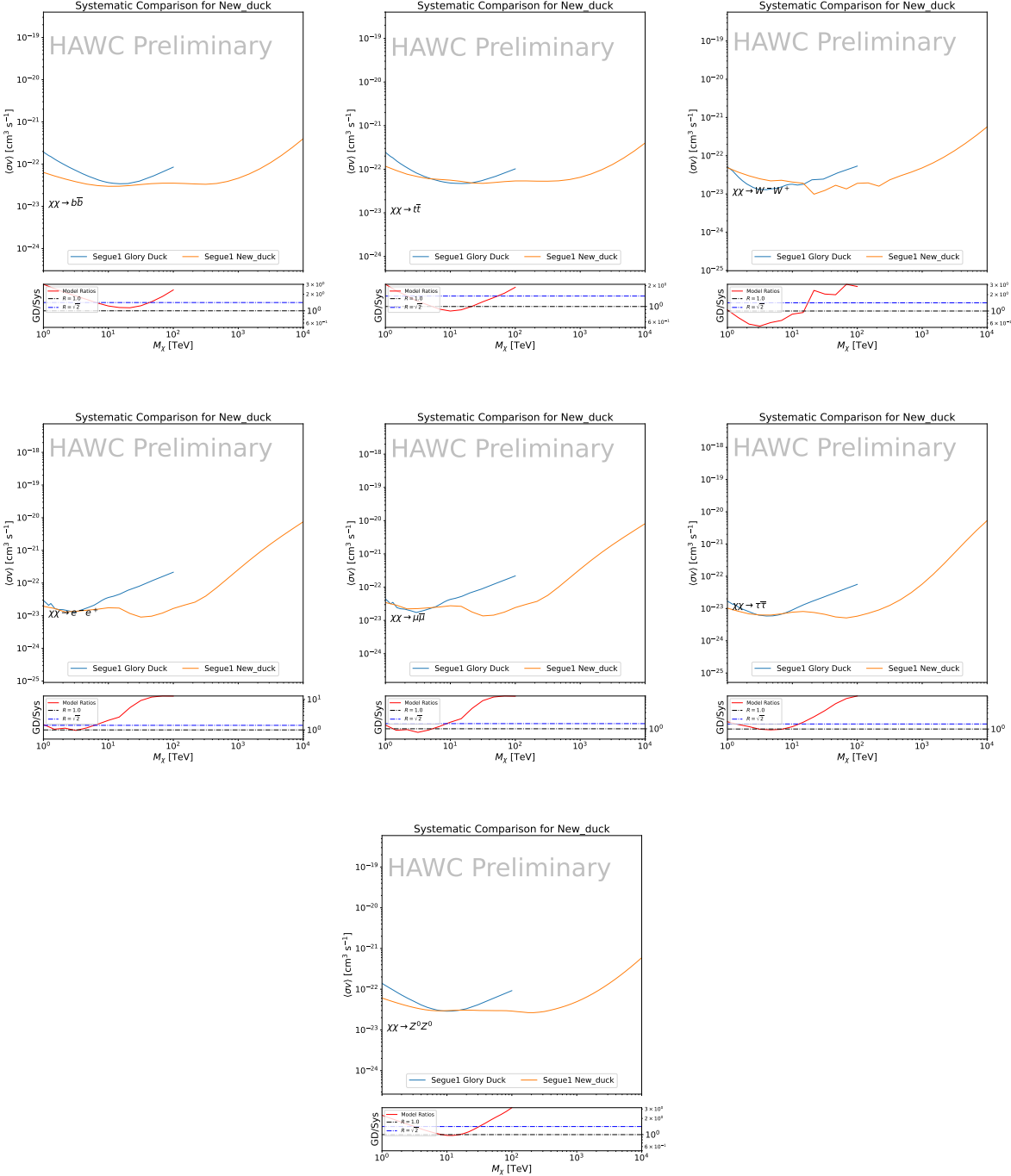


Figure B.3 Same as Fig. B.2 but for Segue 1.

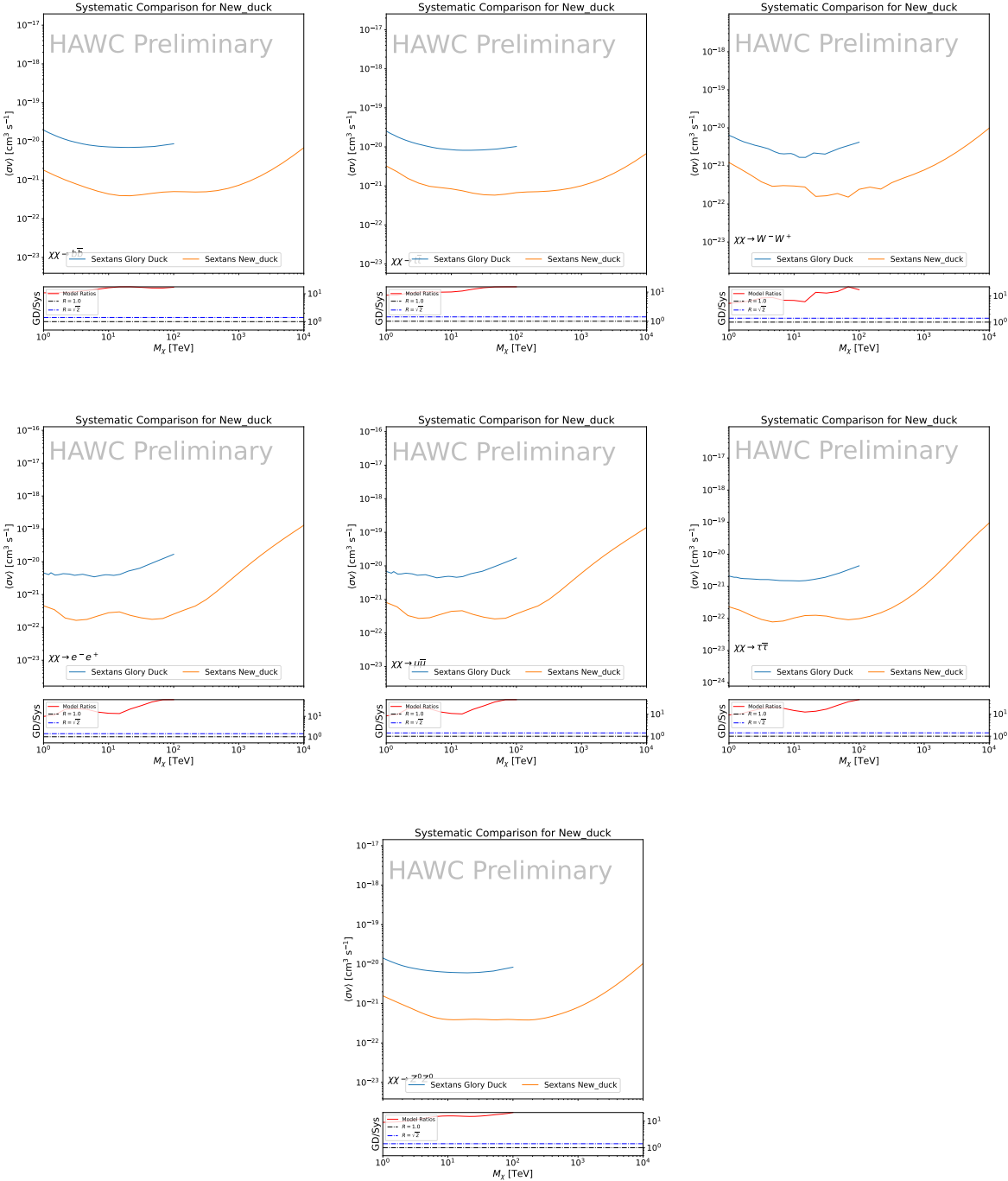


Figure B.4 Same as Fig. B.2 but for Sextans.

APPENDIX C

ICECUBE HEAVY DARK MATTER ANALYSIS SUPPLEMENTARY MATERIAL

C.1 Docker Image for Oscillating Neutrino Spectra

```
25541 FROM ubuntu:18.04
25552
25563 # Execute commands to install software packages
25574 RUN apt -y update
25585
25596     # Install utility programs
25607 RUN apt -y install vim wget git cmake
25618
25629 ARG DEBIAN_FRONTEND=noninteractive
25630
25641     # Install python
25652 RUN apt -y install python python-dev python-pip libjpeg-dev zlib1g-dev
25663
25674     # We need Python2 for installing Charon.
25685 RUN apt -y install python-numpy python-sympy python-matplotlib \
25696             python-sympy python-h5py python-astropy python-ipython
25707
25718     # Install dependencies of Charon : SQuIDS, NuSQuIDS
25729 RUN apt -y install libgsl-dev libgslcblas0 libgsl23 gsl-bin pkg-config
25730     # Install SQuIDS
25741 RUN mkdir /home/SQuIDS /home/SQuIDS_install
25752 WORKDIR /home/SQuIDS
25763 RUN git clone https://github.com/jsalvado/SQuIDS.git
25774 WORKDIR /home/SQuIDS/SQuIDS
25785 RUN git checkout 7ad9ba7c6ad06d1f0fa8418f937ebf1a403fef90
25796     # Before executing "make install" an environmental variable has to be set.
25807 ENV PKG_CONFIG_PATH=/home/SQuIDS/SQuIDS/lib
25818 RUN ./configure --prefix=../SQuIDS_install \
```

```

25829     && make
25830 RUN make install
25841
25852     # Set up an environmental variable that is required to install nuSQuIDS..
25863 ENV SQuIDS=/home/SQuIDS/SQuIDS
25874 ENV LD_LIBRARY_PATH=$SQuIDS/lib:$LD_LIBRARY_PATH
25885
25896     # Install NuSQuIDS
25907 RUN mkdir /home/nuSQuIDS
25918 WORKDIR /home/nuSQuIDS
25929 RUN git clone https://github.com/qrliu/nuSQuIDS.git
25930 WORKDIR /home/nuSQuIDS/nuSQuIDS
25941 RUN git checkout 072d8ef740e2fc7330f1fabaea94f0f4540c46f9
25952 RUN apt -y install libhdf5-dev hdf5-tools
25963 RUN apt -y install libboost1.65-all-dev
25974 RUN ./configure --with-squids=$SQuIDS --with-python-bindings --prefix=../
2598     nuSQuIDS_install \
25995     && make \
26006     && make install
26017
26028     # Set up an environmental variable for nuSQuIDS.
26039 ENV nuSQuIDS=/home/nuSQuIDS/nuSQuIDS
26040 ENV LD_LIBRARY_PATH=$nuSQuIDS/lib:$LD_LIBRARY_PATH
26051
26062     # Build the python bindings
26073 WORKDIR /home/nuSQuIDS/nuSQuIDS/resources/python/src
26084 RUN make
26095
26106     # Set up an environmental variable for the python bindings.
26117 ENV PYTHONPATH=$nuSQuIDS/resources/python/bindings/:$PYTHONPATH
26128
26139     # Install Charon in the /home/Charon/charon directory.
26140 RUN mkdir /home/Charon

```

```
26151 WORKDIR /home/Charon
26162 RUN git clone https://github.com/icecube/charon.git \
26173     && apt -y install unzip python-scipy
26184 WORKDIR charon
26195 RUN git checkout c531efe4e01dc364a60d1c83f950f04526ccd771
26206 RUN unzip ./charon/xsec/xsec.zip -d charon/xsec/ \
26217
26228 # Download neutrino spectra tables in the /home/Charon/charon/data directory
2623 .
26249 && mkdir ./charon/data
26250 WORKDIR ./charon/data
26261 RUN wget --no-check-certificate https://icecube.wisc.edu/~qliu/charon/
2627     SpectraEW.hdf5 \
26282 && wget --no-check-certificate https://icecube.wisc.edu/~qliu/charon/
2629     Spectra_PYTHIA.hdf5 \
26303 && wget --no-check-certificate https://icecube.wisc.edu/~qliu/charon/
2631     Spectra_noEW.hdf5
26324
26335 WORKDIR ../..
26346 RUN python setup.py install
26357 WORKDIR /home
```

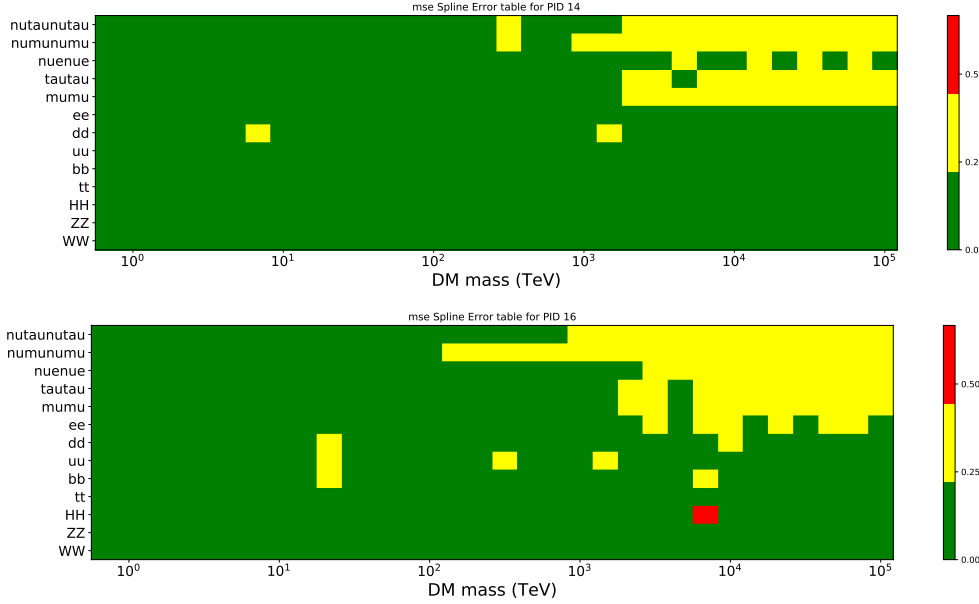


Figure C.1 Current status of spline tables according to constraints defined by Tab. 6.1. Green splines are splines that passed under the GOOD tolerance. Yellow are splines that are OK. Red are splines that FAIL. All yellow splines were inspected individually before running the analysis. Splines were made for the μ (PID 14; top panel) flavor and τ (PID 16; bottom panel) neutrino flavors.

2637 C.3 Neutrino Composite Spectra

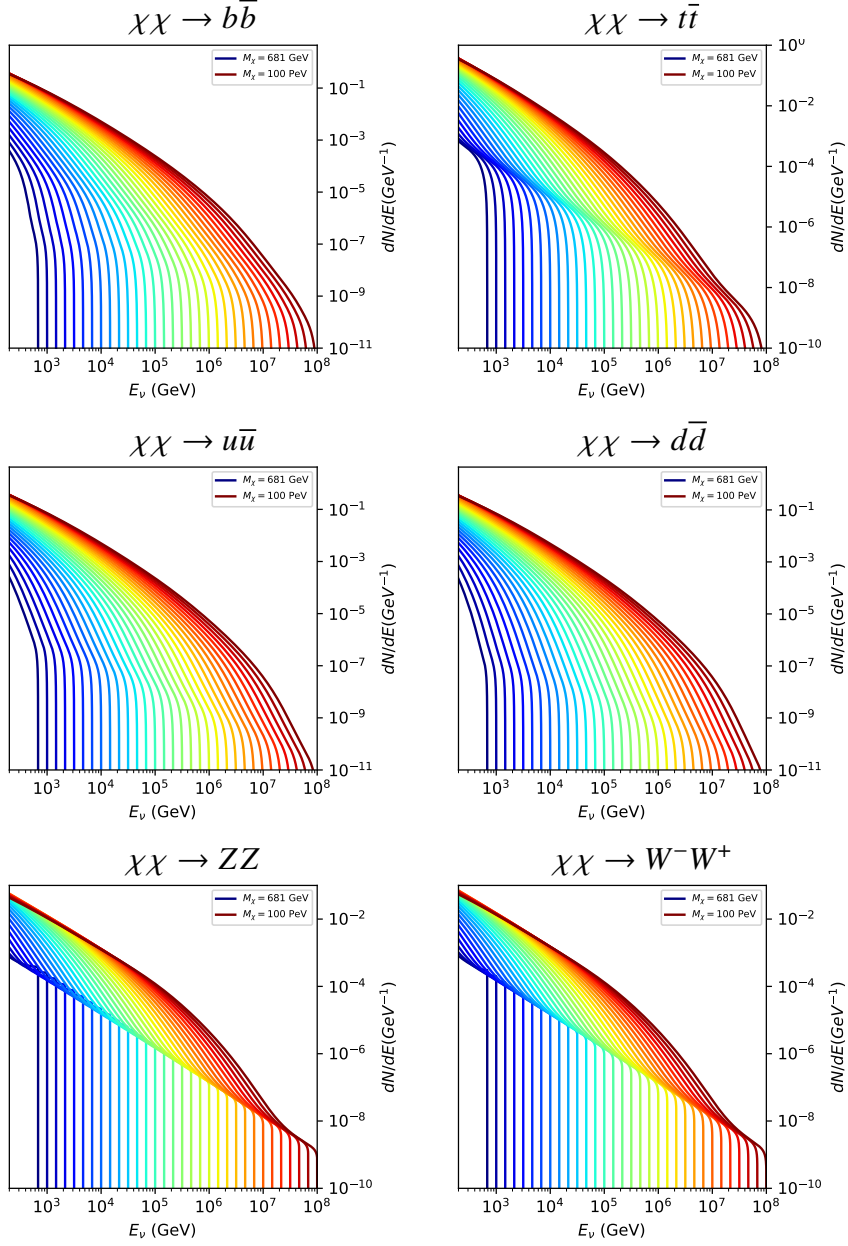


Figure C.2 Sister figure to Fig. 6.5 for annihilation channels that did not require kernel smoothing. These spectra are the composite ($\nu_\mu + \nu_\tau$) of neutrino flavors. Every spectral model used for this analysis is featured as a colored solid line. Bluer lines are for lower DM mass spectral models. DM masses range from 681 GeV to 100 PeV.

2638 C.4 Segue 1 And Ursa Major II Signal Recovery

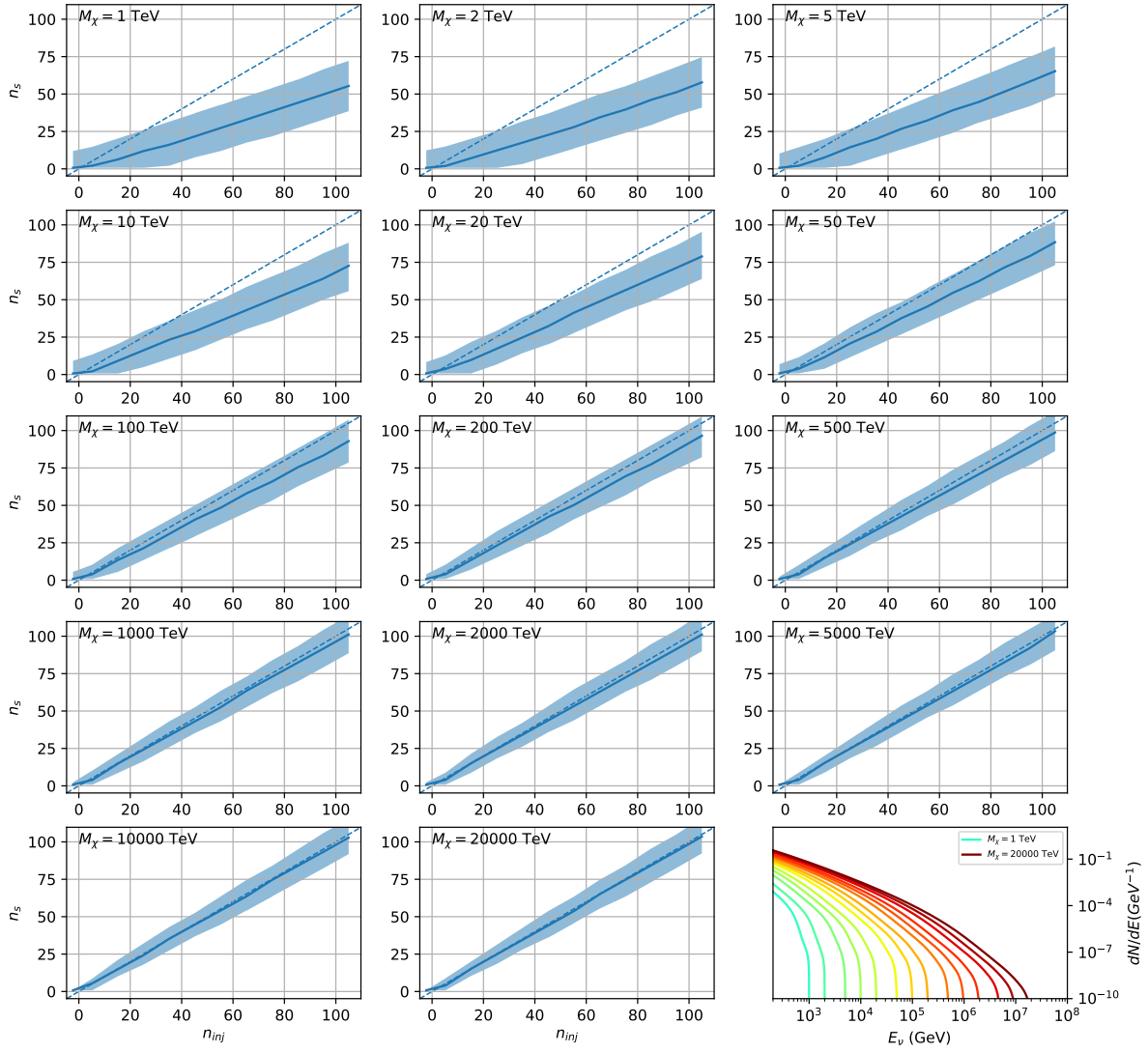


Figure C.3 Same as Fig. 6.23 but for Segue 1 and $\chi\chi \rightarrow b\bar{b}$.

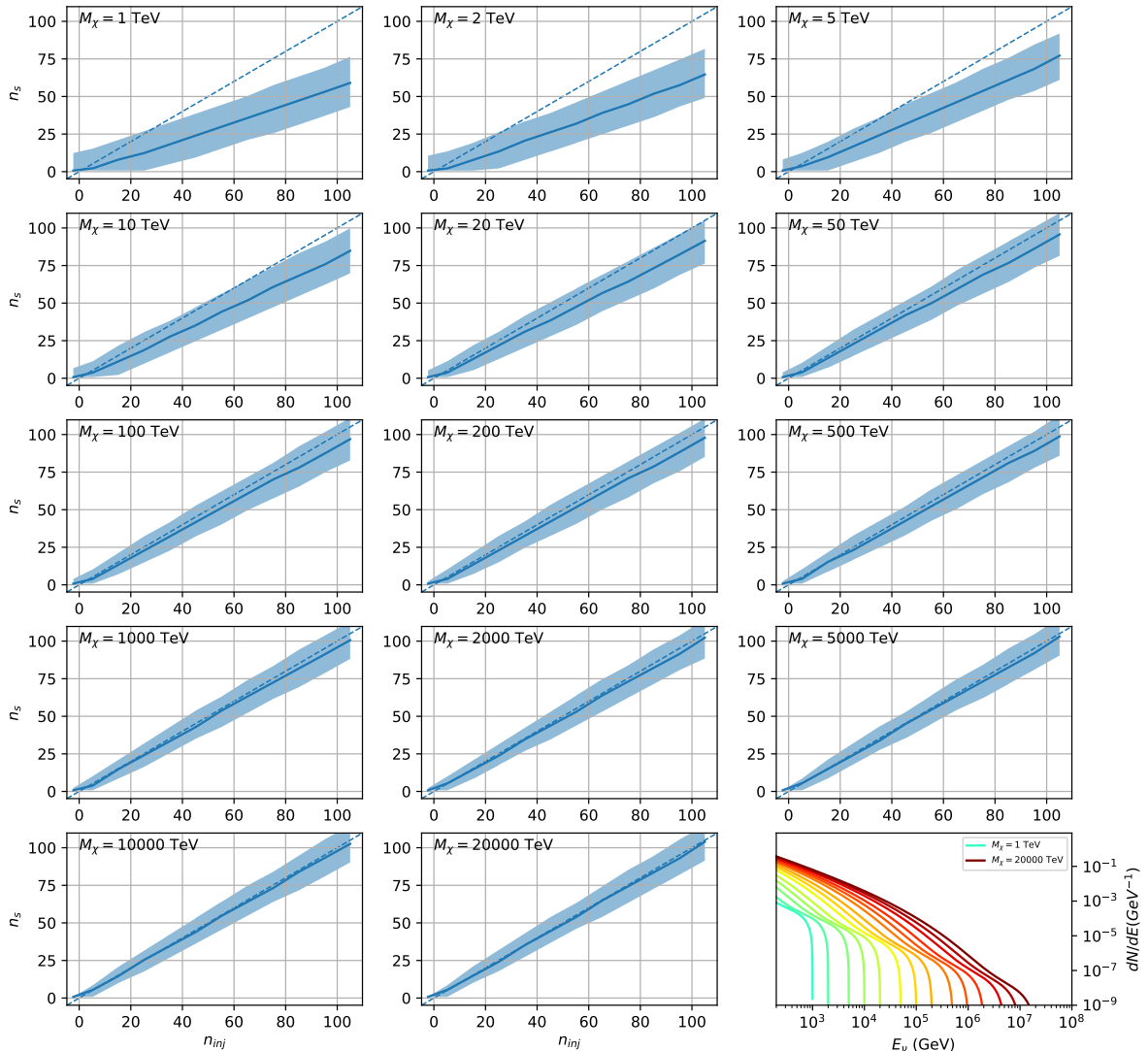


Figure C.4 Same as Fig. 6.23 but for Segue 1 and $\chi\chi \rightarrow t\bar{t}$.

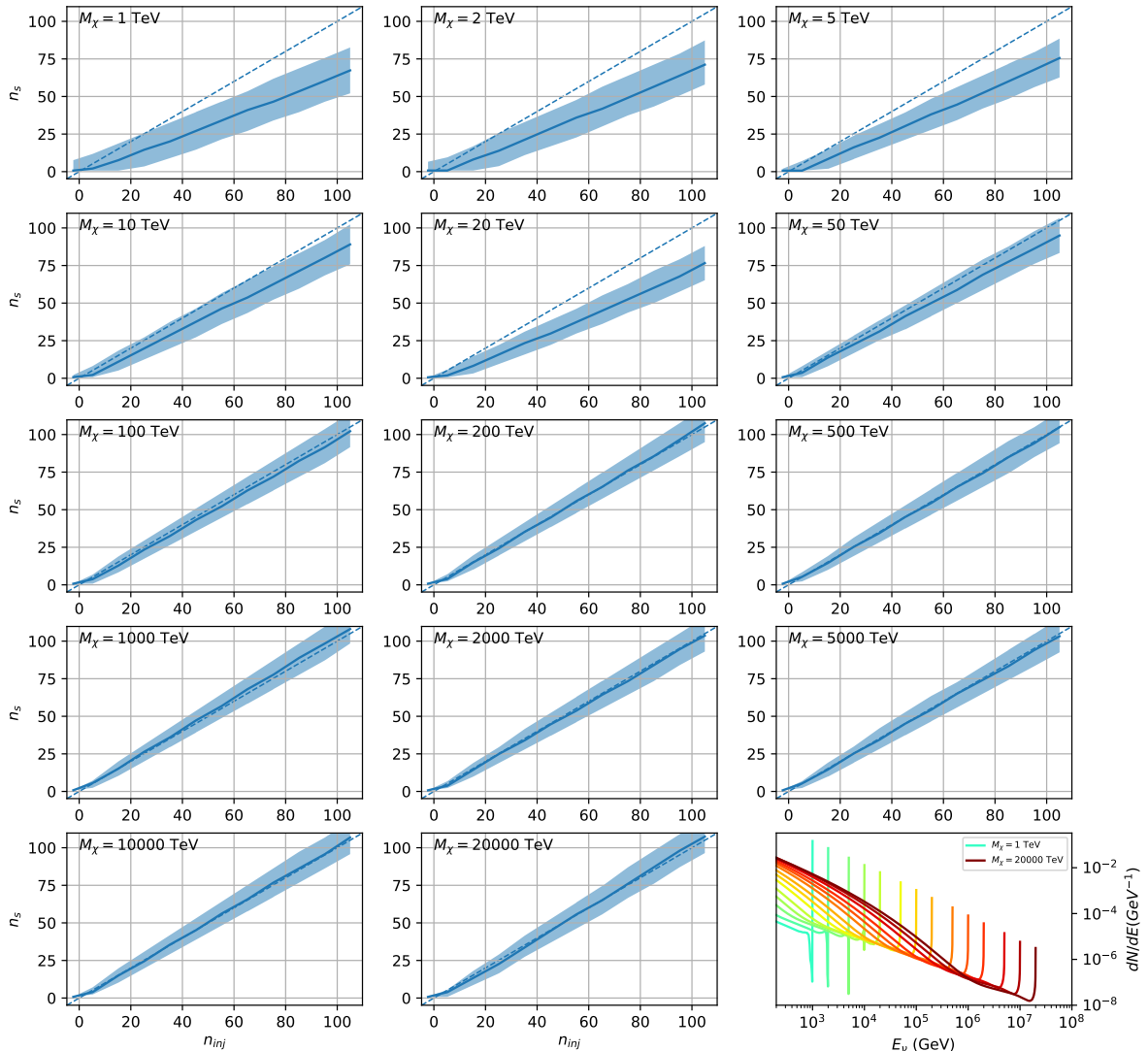


Figure C.5 Same as Fig. 6.23 but for Segue 1 and $\chi\chi \rightarrow \nu_\mu \bar{\nu}_\mu$.

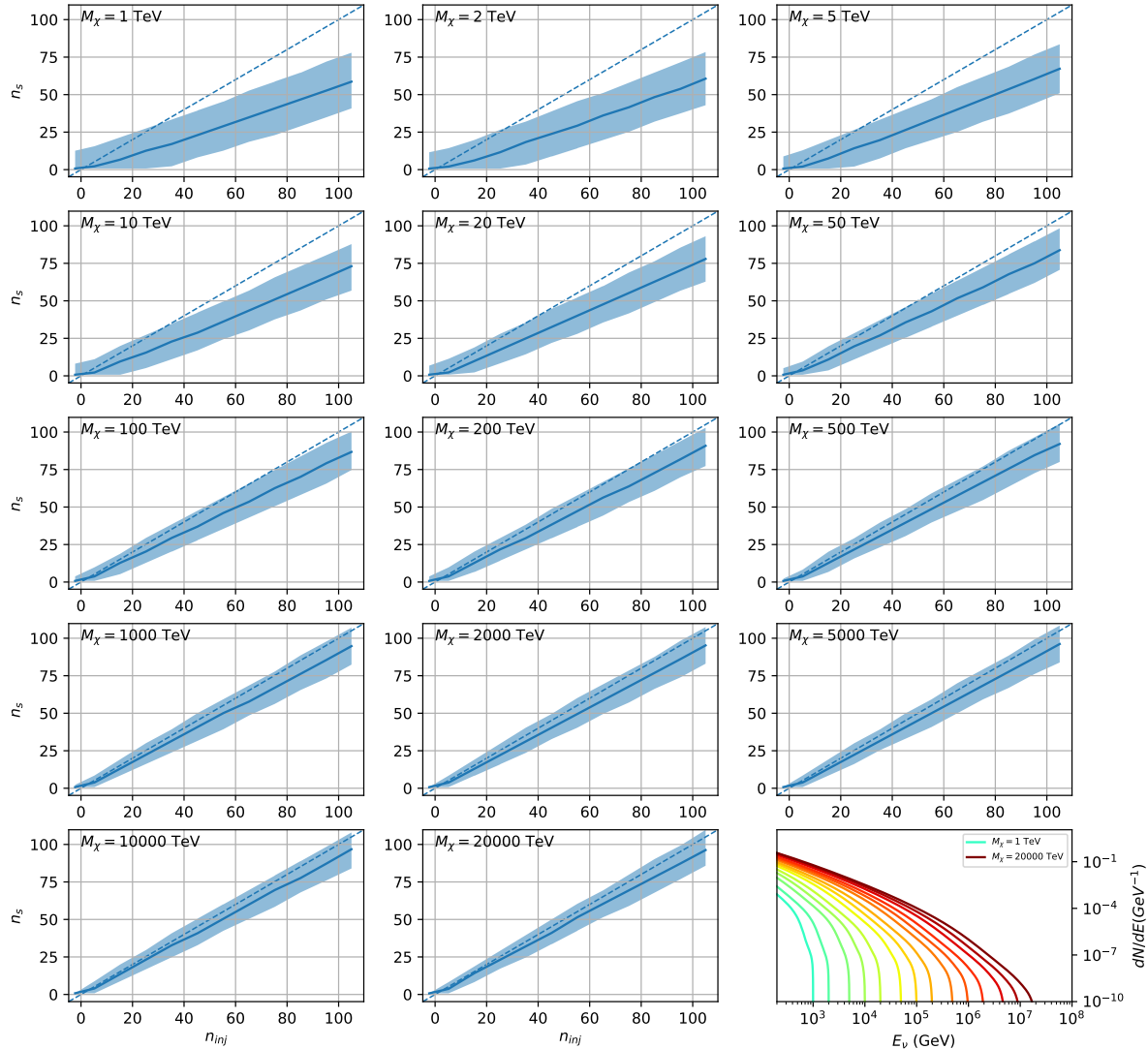


Figure C.6 Same as Fig. 6.23 but for Ursa Major II and $\chi\chi \rightarrow b\bar{b}$.

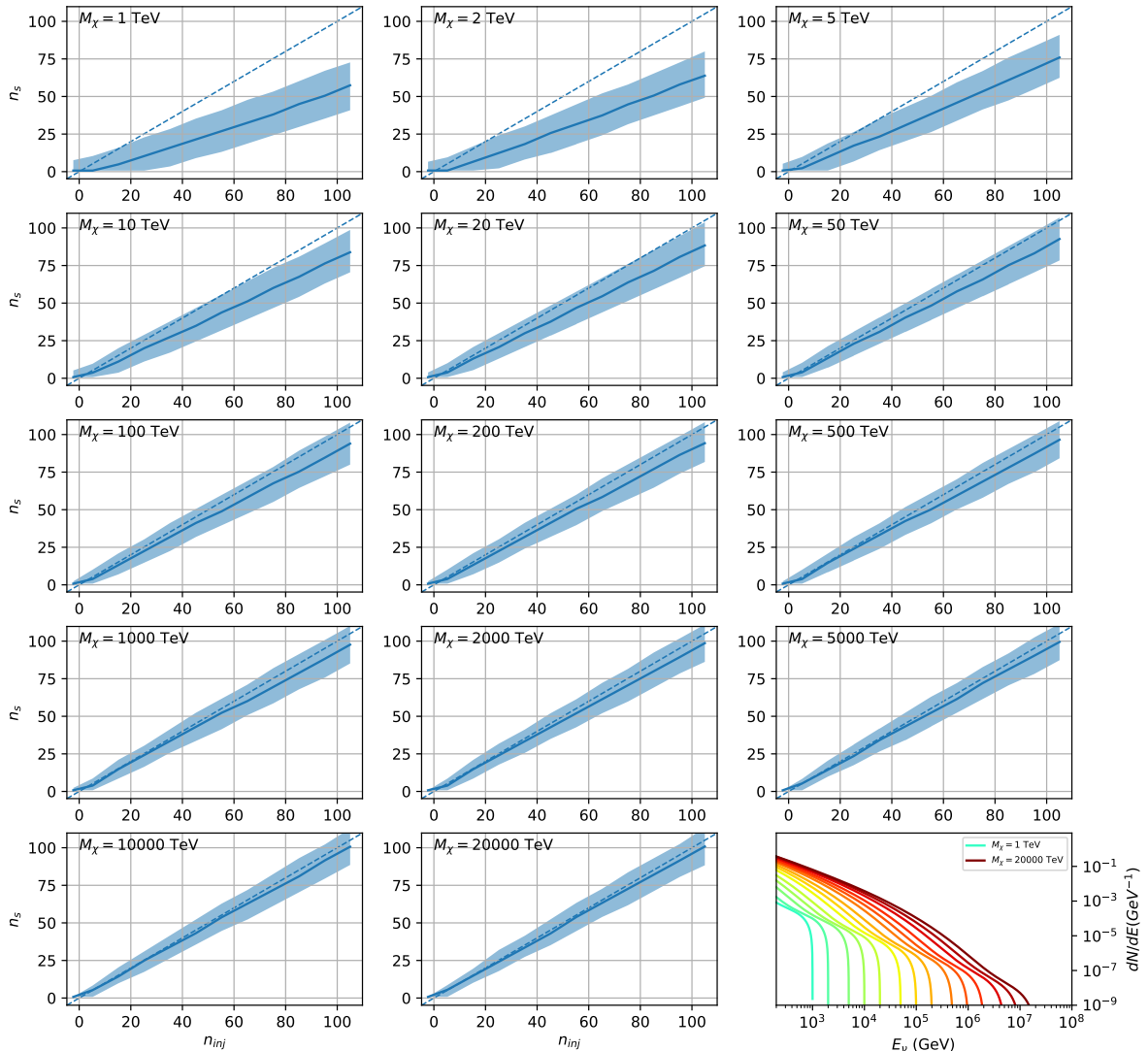


Figure C.7 Same as Fig. 6.23 but for Ursa Major II and $\chi\chi \rightarrow t\bar{t}$.

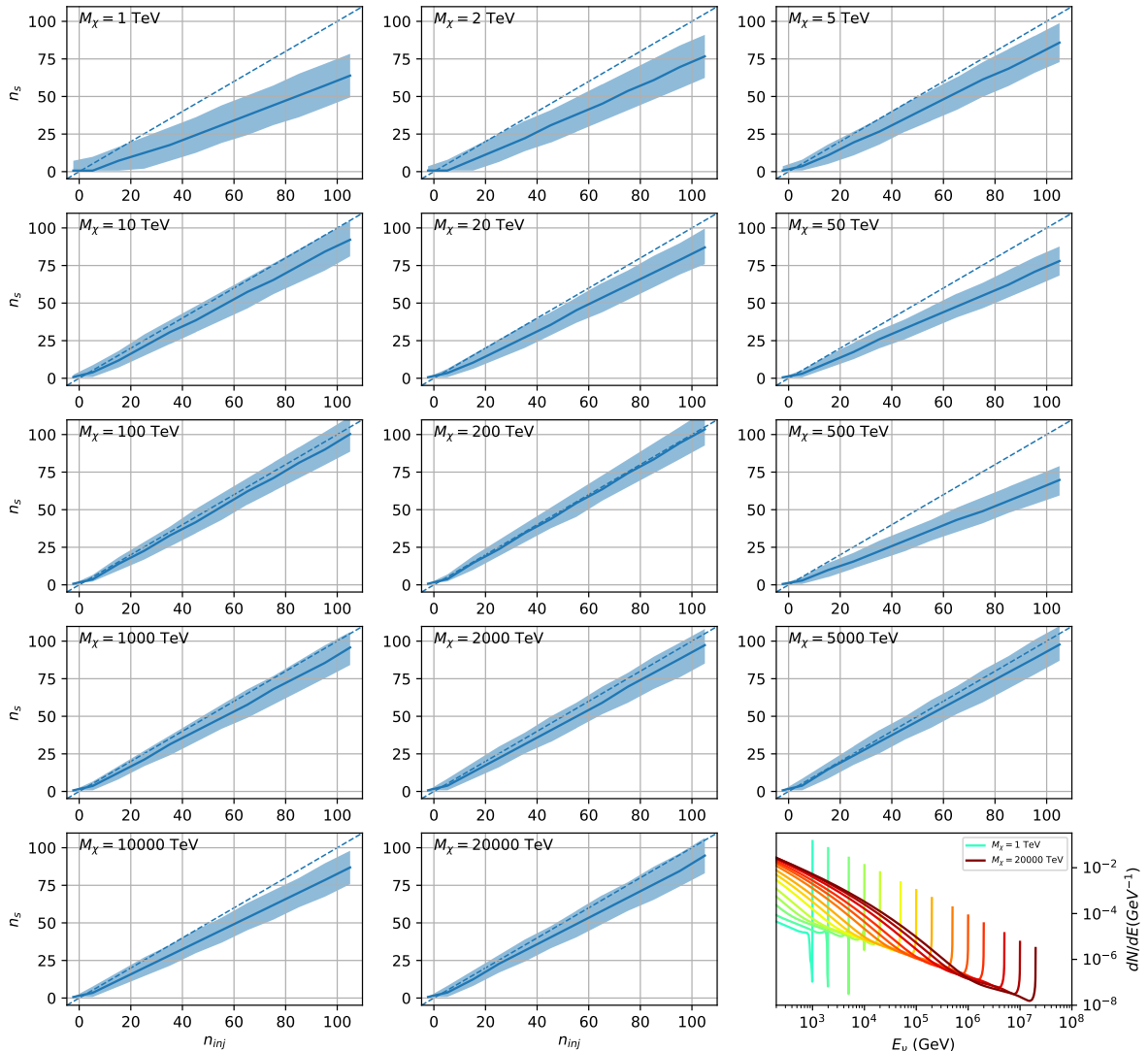


Figure C.8 Same as Fig. 6.23 but for Ursa Major II and $\chi\chi \rightarrow \nu_\mu \bar{\nu}_\mu$.

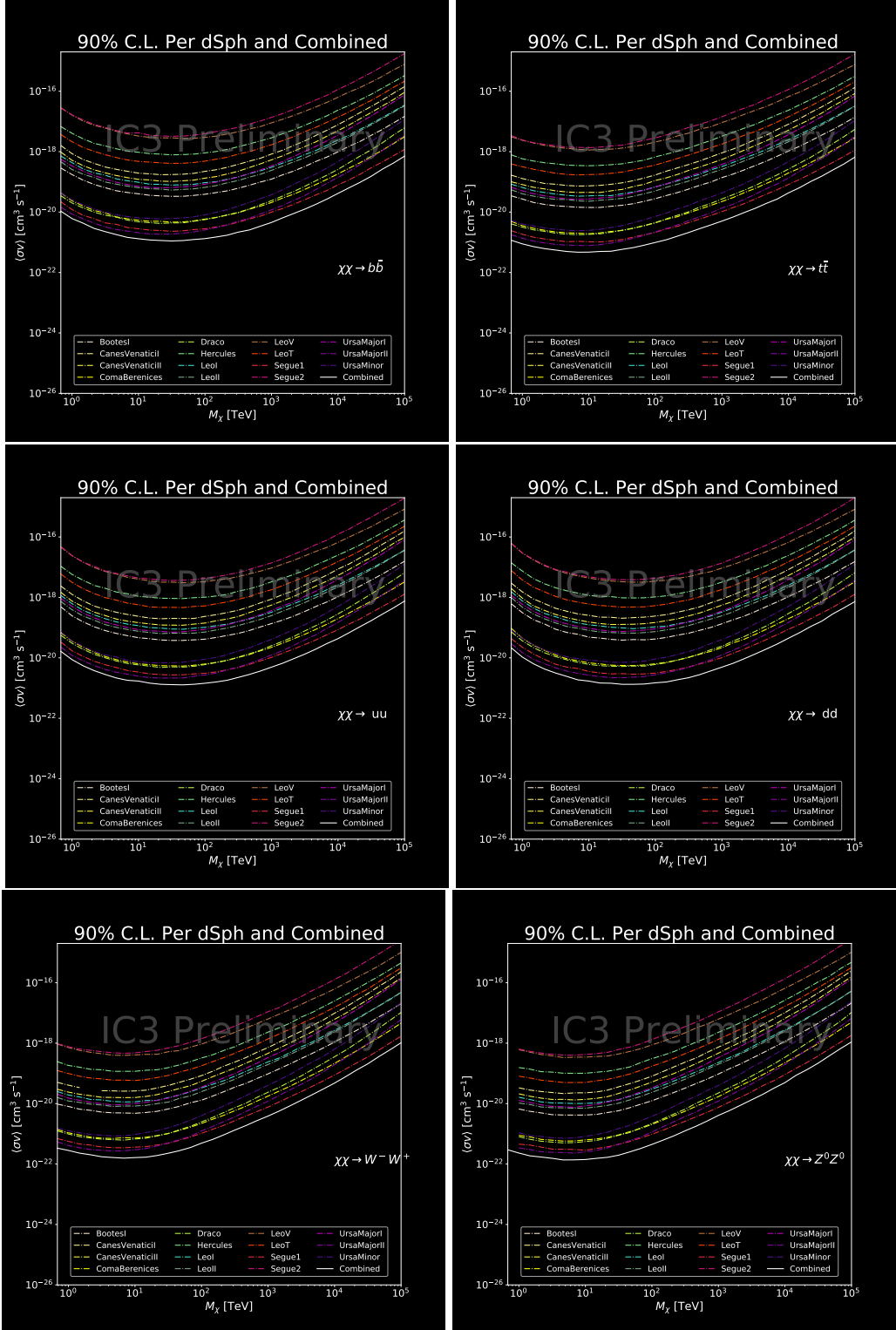


Figure C.9 IceCube North Sky Track Sensitivities for $n_s/\langle N \rangle$. n_s values are the counts fed into Eq. (6.8) to produce Fig. 6.26 and Fig. 6.25.

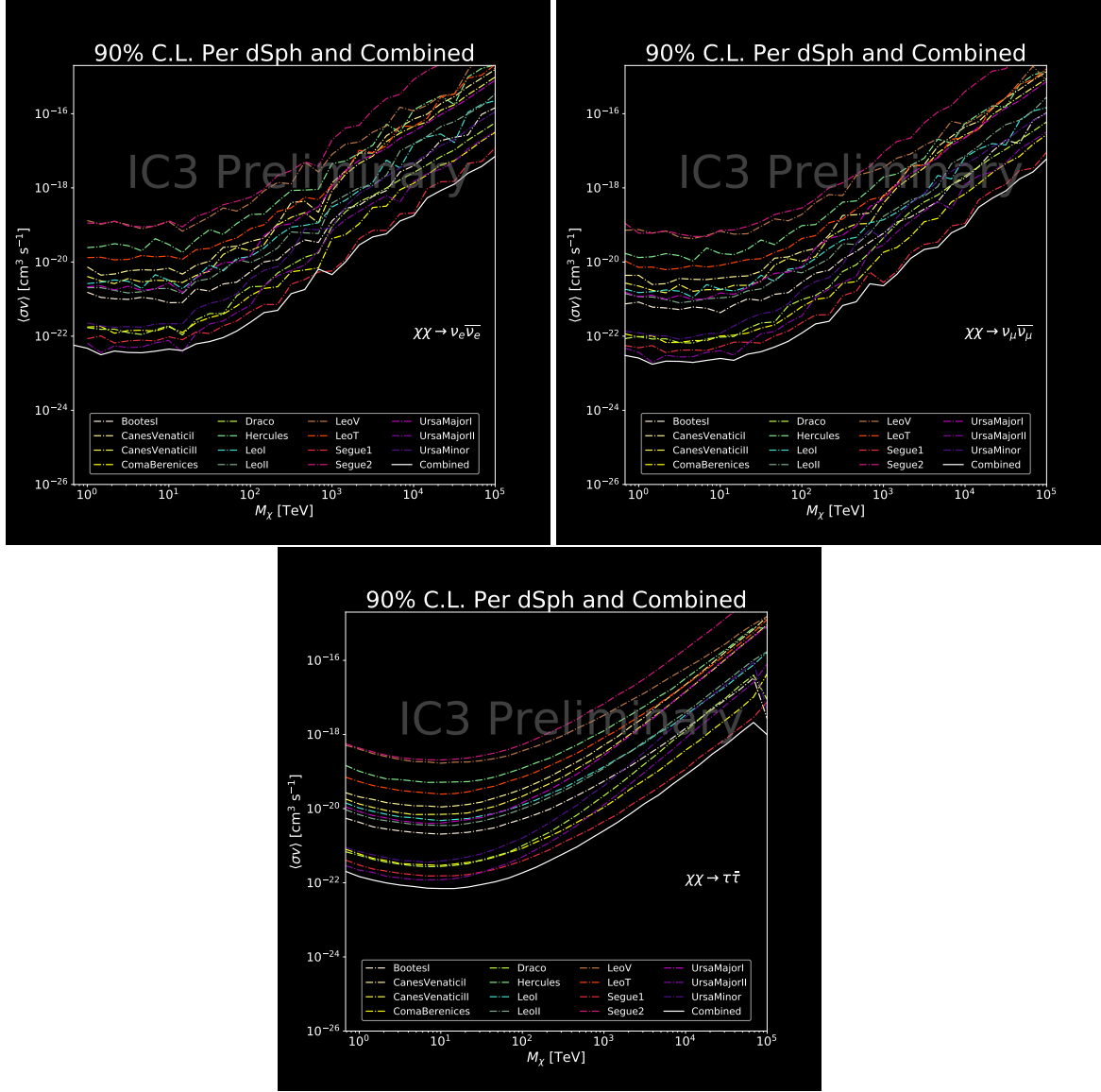


Figure C.10 Same as Fig. C.9 for three additional DM annihilation channels.

2640

BIBLIOGRAPHY

- 2641 [1] Anne M. Green. “Dark matter in astrophysics/cosmology”. In: *SciPost Phys. Lect.*
 2642 *Notes* (2022), p. 37. doi: [10.21468/SciPostPhysLectNotes.37](https://doi.org/10.21468/SciPostPhysLectNotes.37). URL: <https://scipost.org/10.21468/SciPostPhysLectNotes.37>.
- 2644 [2] Bing-Lin Young. “A survey of dark matter and related topics in cosmology”. In: *Frontiers*
 2645 *of Physics* 12 (Oct. 2016). doi: <https://doi.org/10.1007/s11467-016-0583-4>.
 2646 URL: <https://doi.org/10.1007/s11467-016-0583-4>.
- 2647 [3] Gianfranco Bertone, Dan Hooper, and Joseph Silk. “Particle dark matter: evidence,
 2648 candidates and constraints”. In: *Physics Reports* 405.5 (2005), pp. 279–390. ISSN: 0370-
 2649 1573. doi: <https://doi.org/10.1016/j.physrep.2004.08.031>. URL: <https://www.sciencedirect.com/science/article/pii/S0370157304003515>.
- 2651 [4] Gianfranco Bertone and Dan Hooper. “History of dark matter”. In: *Rev. Mod. Phys.*
 2652 90 (4 Aug. 2018), p. 045002. doi: [10.1103/RevModPhys.90.045002](https://doi.org/10.1103/RevModPhys.90.045002). URL: <https://link.aps.org/doi/10.1103/RevModPhys.90.045002>.
- 2654 [5] Fritz Zwicky. “The Redshift of Extragalactic Nebulae”. In: *Helvetica Physica Acta* 6.
 2655 (1933), pp. 110–127. doi: [10.5169/seals-110267](https://doi.org/10.5169/seals-110267).
- 2656 [6] Vera C. Rubin and Jr. Ford W. Kent. “Rotation of the Andromeda Nebula from a
 2657 Spectroscopic Survey of Emission Regions”. In: *ApJ* 159 (Feb. 1970), p. 379. doi:
 2658 [10.1086/150317](https://doi.org/10.1086/150317).
- 2659 [7] K. G. Begeman, A. H. Broeils, and R. H. Sanders. “Extended rotation curves of
 2660 spiral galaxies: dark haloes and modified dynamics”. In: *Monthly Notices of the*
 2661 *Royal Astronomical Society* 249.3 (Apr. 1991), pp. 523–537. ISSN: 0035-8711. doi:
 2662 [10.1093/mnras/249.3.523](https://doi.org/10.1093/mnras/249.3.523). eprint: <https://academic.oup.com/mnras/article-pdf/249/3/523/18160929/mnras249-0523.pdf>. URL: <https://doi.org/10.1093/mnras/249.3.523>.
- 2665 [8] *Different types of gravitational lenses*. website. Feb. 2004. URL: <https://esahubble.org/images/heic0404b/>.
- 2666 [9] Douglas Clowe et al. “A Direct Empirical Proof of the Existence of Dark Matter”. In: *apjl*
 2667 648.2 (Sept. 2006), pp. L109–L113. doi: [10.1086/508162](https://doi.org/10.1086/508162). arXiv: [astro-ph/0608407](https://arxiv.org/abs/astro-ph/0608407)
 2668 [[astro-ph](#)].
- 2670 [10] Planck Collaboration and N. et. al. Aghanim. “Planck 2018 results I. Overview and the
 2671 cosmological legacy of Planck”. In: *A&A* 641 (2020). doi: [10.1051/0004-6361/201833880](https://doi.org/10.1051/0004-6361/201833880). URL: <https://doi.org/10.1051/0004-6361/201833880>.
- 2673 [11] Wayne Hu. *Matter Density Animation*. web. 2024. URL: <http://background.uchicago.edu/MatterDensityAnimation>

- 2674 o.edu/~whu/animbut/anim2.html.
- 2675 [12] Wenlong Yuan et al. “A First Look at Cepheids in a Type Ia Supernova Host with JWST”. In:
2676 *The Astrophysical Journal Letters* 940.1 (Nov. 2022). doi: [10.3847/2041-8213/ac9b27](https://doi.org/10.3847/2041-8213/ac9b27).
2677 URL: <https://dx.doi.org/10.3847/2041-8213/ac9b27>.
- 2678 [13] Wendy L. Freedman. “Measurements of the Hubble Constant: Tensions in Perspective”. In:
2679 *The Astrophysical Journal* 919.1 (Sept. 2021), p. 16. doi: [10.3847/1538-4357/ac0e95](https://doi.org/10.3847/1538-4357/ac0e95).
2680 URL: <https://dx.doi.org/10.3847/1538-4357/ac0e95>.
- 2681 [14] Jodi Cooley. “Dark Matter direct detection of classical WIMPs”. In: *SciPost Phys.
2682 Lect. Notes* (2022), p. 55. doi: [10.21468/SciPostPhysLectNotes.55](https://doi.org/10.21468/SciPostPhysLectNotes.55). URL:
2683 <https://scipost.org/10.21468/SciPostPhysLectNotes.55>.
- 2684 [15] “Search for new phenomena in events with an energetic jet and missing transverse mo-
2685 mentum in pp collisions at $\sqrt{s} = 13$ TeV with the ATLAS detector”. In: *Phys. Rev.
2686 D* 103 (11 July 2021), p. 112006. doi: [10.1103/PhysRevD.103.112006](https://doi.org/10.1103/PhysRevD.103.112006). URL:
2687 <https://link.aps.org/doi/10.1103/PhysRevD.103.112006>.
- 2688 [16] *Jetting into the dark side: a precision search for dark matter*. website. July 2020. URL:
2689 <https://atlas.cern/updates/briefing/precision-search-dark-matter>.
- 2690 [17] Celine Armand et. al. “Combined dark matter searches towards dwarf spheroidal galaxies
2691 with Fermi-LAT, HAWC, H.E.S.S., MAGIC, and VERITAS”. in: *Proceedings of Science*.
2692 Vol. 395. Mar. 2022. doi: <https://doi.org/10.22323/1.395.0528>.
- 2693 [18] Tracy R. Slatyer. “Les Houches Lectures on Indirect Detection of Dark Matter”. In:
2694 *SciPost Phys. Lect. Notes* (2022), p. 53. doi: [10.21468/SciPostPhysLectNotes.53](https://doi.org/10.21468/SciPostPhysLectNotes.53).
2695 URL: <https://scipost.org/10.21468/SciPostPhysLectNotes.53>.
- 2696 [19] Christian W Bauer, Nicholas L. Rodd, and Bryan R. Webber. “Dark matter spectra from
2697 the electroweak to the Planck scale”. In: *Journal of High Energy Physics* 2021.1029-8479
2698 (June 2021). doi: [https://doi.org/10.1007/JHEP06\(2021\)121](https://doi.org/10.1007/JHEP06(2021)121).
- 2699 [20] Riccardo Catena and Piero Ullio. “A novel determination of the local dark matter density”.
2700 In: *Journal of Cosmology and Astroparticle Physics* 2010.08 (Aug. 2010), p. 004. doi:
2701 [10.1088/1475-7516/2010/08/004](https://doi.org/10.1088/1475-7516/2010/08/004). URL: <https://dx.doi.org/10.1088/1475-7516/2010/08/004>.
- 2702 [21] B. P. Abbott et al. “Observation of Gravitational Waves from a Binary Black Hole Merger”.
In: *Phys. Rev. Lett.* 116 (6 Feb. 2016), p. 061102. doi: [10.1103/PhysRevLett.116.061102](https://doi.org/10.1103/PhysRevLett.116.061102). URL: <https://link.aps.org/doi/10.1103/PhysRevLett.116.061102>.
- 2703 [22] R. Abbasi et. al. “Observation of high-energy neutrinos from the Galactic plane”. In:
2704 *Science* 380.6652 (June 2023), pp. 1338–1343.

- 2708 [23] NASA Goddard Space Flight Center. *Fermi's 12-year view of the gamma-ray sky*. website.
2709 2022. URL: <https://svs.gsfc.nasa.gov/14090>.
- 2710 [24] Marco Cirelli et al. "PPPC 4 DM ID: a poor particle physicist cookbook for dark matter
2711 indirect detection". In: *Journal of Cosmology and Astroparticle Physics* 2011.03 (Mar.
2712 2011), p. 051. doi: [10.1088/1475-7516/2011/03/051](https://doi.org/10.1088/1475-7516/2011/03/051). URL: <https://dx.doi.org/10.1088/1475-7516/2011/03/051>.
- 2714 [25] The HAWC Collaboration. "The High-Altitude Water Cherenkov (HAWC) observatory in
2715 México: The primary detector". In: *Nuclear Instruments and Methods in Physics Research*
2716 *Section A: Accelerators, Spectrometers, Detectors and Associated Equipment* 1052 (2023),
2717 p. 168253. ISSN: 0168-9002. doi: <https://doi.org/10.1016/j.nima.2023.168253>.
2718 URL: <https://www.sciencedirect.com/science/article/pii/S0168900223002437>.
- 2720 [26] Alicia Lopez Oramas. "Multi-year Campaign of the Gamma-Ray Binary LS I +61° 303
2721 and Search for VHE Emission from Gamma-Ray Binary Candidates with the MAGIC
2722 Telescopes". PhD thesis. Instituto de Astrofísica de Canarias, 2014. doi: <http://dx.doi.org/10.13140/RG.2.1.4140.4969>.
- 2724 [27] A.U. Abeysekara et. al. "The High-Altitude Water Cherenkov (HAWC) observatory in
2725 México: The primary detector". In: *Nuclear Instruments and Methods in Physics Research*
2726 *Section A: Accelerators, Spectrometers, Detectors and Associated Equipment* 1052 (2023),
2727 p. 168253. ISSN: 0168-9002. doi: <https://doi.org/10.1016/j.nima.2023.168253>.
2728 URL: <https://www.sciencedirect.com/science/article/pii/S0168900223002437>.
- 2730 [28] Hamamatsu Photonics KK. *Large Photocathode Area Photomultiplier Tubes*. 2019. URL:
2731 https://www.hamamatsu.com/content/dam/hamamatsu-photonics/sites/documents/99_SALES_LIBRARY/etd/LARGE_AREA_PMT TPMH1376E.pdf.
- 2733 [29] The HAWC Collaboration. "Data acquisition architecture and online processing system
2734 for the HAWC gamma-ray observatory". In: *Nuclear Instruments and Methods in Physics*
2735 *Research Section A: Accelerators, Spectrometers, Detectors and Associated Equipment* 888
2736 (2018), pp. 138–146. ISSN: 0168-9002. doi: <https://doi.org/10.1016/j.nima.2018.01.051>. URL: <https://www.sciencedirect.com/science/article/pii/S0168900218300688>.
- 2739 [30] The Milagro Collaboratio. "Milagrito, a TeV air-shower array". In: *Nuclear Instruments*
2740 *and Methods in Physics Research Section A: Accelerators, Spectrometers, Detectors and*
2741 *Associated Equipment* 449.3 (2000), pp. 478–499. ISSN: 0168-9002. doi: [https://doi.org/10.1016/S0168-9002\(00\)00146-7](https://doi.org/10.1016/S0168-9002(00)00146-7). URL: <https://www.sciencedirect.com/science/article/pii/S0168900200001467>.
- 2744 [31] Ian Gabriel Wisher. "Real-time Transient Monitoring With the HAWC Detector: Design

- 2745 and Performance”. PhD thesis. The University of Wisconsin - Madison, 2016.
- 2746 [32] The ZeroMQ authors. “ZeroMQ An open-source universal messaging library”. In: (2021).
2747 URL: <https://zeromq.org>.
- 2748 [33] Zigfried Hampel-Archisman. “Cosmic Ray Observations at the TeV Scale with the HAWC
2749 Observatory”. PhD thesis. University of Wisconsin-Madison, 2017.
- 2750 [34] A. U. Abeysekara et al. “Observation of the Crab Nebula with the HAWC Gamma-Ray
2751 Observatory”. In: *The Astrophysical Journal* 843.1 (June 2017), p. 39. doi: [10.3847/1538-4357/aa7555](https://doi.org/10.3847/1538-4357/aa7555). URL: <https://doi.org/10.3847/1538-4357/aa7555>.
- 2753 [35] Kenneth Greisen. “Cosmic Ray Showers”. In: *ANNUAL REVIEW OF NUCLEAR AND
2754 PARTICLE SCIENCE* 10 (1960), pp. 63–108.
- 2755 [36] The HAWC Collabortion. “Sensitivity of the high altitude water Cherenkov detector to
2756 sources of multi-TeV gamma rays”. In: *Astroparticle Physics* 50-52 (2013), pp. 26–32.
2757 ISSN: 0927-6505. doi: <https://doi.org/10.1016/j.astropartphys.2013.08.002>. URL: <https://www.sciencedirect.com/science/article/pii/S0927650513001230>.
- 2760 [37] The HAWC Collaboration. “Measurement of the Crab Nebula Spectrum Past 100 TeV with
2761 HAWC”. in: *The Astrophysical Journal* 881.2 (Aug. 2019), p. 134. doi: [10.3847/1538-4357/ab2f7d](https://doi.org/10.3847/1538-4357/ab2f7d). URL: <https://dx.doi.org/10.3847/1538-4357/ab2f7d>.
- 2763 [38] Samuel Miranelli. “CONSTRAINTS ON LORENTZ-INVARIANCE VIOLATION WITH
2764 THE HAWC OBSERVATORY”. PhD thesis. Michigan State University, 2019.
- 2765 [39] A. A. Abdo et al. “OBSERVATION AND SPECTRAL MEASUREMENTS OF THE
2766 CRAB NEBULA WITH MILAGRO”. in: *The Astrophysical Journal* 750.1 (Apr. 2012),
2767 p. 63. doi: [10.1088/0004-637X/750/1/63](https://doi.org/10.1088/0004-637X/750/1/63). URL: <https://dx.doi.org/10.1088/0004-637X/750/1/63>.
- 2769 [40] Javier Rico. “Gamma-Ray Dark Matter Searches in Milky Way Satellites—A Comparative
2770 Review of Data Analysis Methods and Current Results”. In: *Galaxies* 8.1 (Mar. 2020),
2771 p. 25. doi: [10.3390/galaxies8010025](https://doi.org/10.3390/galaxies8010025). arXiv: [2003.13482 \[astro-ph.HE\]](https://arxiv.org/abs/2003.13482).
- 2772 [41] W. B. Atwood et al. “The Large Area Telescope on the Fermi Gamma-Ray Space Telescope
2773 Mission”. In: *apj* 697.2 (June 2009), pp. 1071–1102. doi: [10.1088/0004-637X/697/2/1071](https://doi.org/10.1088/0004-637X/697/2/1071). arXiv: [0902.1089 \[astro-ph.IM\]](https://arxiv.org/abs/0902.1089).
- 2775 [42] M. Ackermann et al. “Searching for Dark Matter Annihilation from Milky Way Dwarf
2776 Spheroidal Galaxies with Six Years of Fermi Large Area Telescope Data”. In: *prl* 115.23,
2777 231301 (Dec. 2015), p. 231301. doi: [10.1103/PhysRevLett.115.231301](https://doi.org/10.1103/PhysRevLett.115.231301). arXiv:
2778 [1503.02641 \[astro-ph.HE\]](https://arxiv.org/abs/1503.02641).

- 2779 [43] Mattia Di Mauro, Martin Stref, and Francesca Calore. “Investigating the effect of Milky
2780 Way dwarf spheroidal galaxies extension on dark matter searches with Fermi-LAT data”.
2781 In: *Phys. Rev. D* 106 (12 Dec. 2022), p. 123032. doi: [10.1103/PhysRevD.106.123032](https://doi.org/10.1103/PhysRevD.106.123032).
2782 URL: <https://link.aps.org/doi/10.1103/PhysRevD.106.123032>.
- 2783 [44] F. et al. Aharonian. “Observations of the Crab Nebula with H.E.S.S.”. In: *Astron.
2784 Astrophys.* 457 (2006), pp. 899–915. doi: [10.1051/0004-6361:20065351](https://doi.org/10.1051/0004-6361:20065351). arXiv:
2785 [astro-ph/0607333](https://arxiv.org/abs/astro-ph/0607333).
- 2786 [45] J. Albert et al. “VHE γ -Ray Observation of the Crab Nebula and its Pulsar with the
2787 MAGIC Telescope”. In: *The Astrophysical Journal* 674.2 (Feb. 2008), p. 1037. doi:
2788 [10.1086/525270](https://doi.org/10.1086/525270). URL: <https://dx.doi.org/10.1086/525270>.
- 2789 [46] N. Park. “Performance of the VERITAS experiment”. In: *Proceedings, 34th International
2790 Cosmic Ray Conference (ICRC2015): The Hague, The Netherlands, July, 30th July - 6th
2791 August.* Vol. 34. 2015, p. 771. arXiv: [1508.07070 \[astro-ph.IM\]](https://arxiv.org/abs/1508.07070).
- 2792 [47] A. Abramowski et al. “H.E.S.S. constraints on Dark Matter annihilations towards the
2793 Sculptor and Carina Dwarf Galaxies”. In: *Astropart. Phys.* 34 (2011), pp. 608–616. doi:
2794 [10.1016/j.astropartphys.2010.12.006](https://doi.org/10.1016/j.astropartphys.2010.12.006). arXiv: [1012.5602 \[astro-ph.HE\]](https://arxiv.org/abs/1012.5602).
- 2795 [48] A. Abramowski et al. “Search for dark matter annihilation signatures in H.E.S.S. obser-
2796 vations of Dwarf Spheroidal Galaxies”. In: *Phys. Rev. D* 90 (2014), p. 112012. doi:
2797 [10.1103/PhysRevD.90.112012](https://doi.org/10.1103/PhysRevD.90.112012). arXiv: [1410.2589 \[astro-ph.HE\]](https://arxiv.org/abs/1410.2589).
- 2798 [49] H. Abdalla et al. “Searches for gamma-ray lines and ‘pure WIMP’ spectra from Dark
2799 Matter annihilations in dwarf galaxies with H.E.S.S”. in: *JCAP* 11 (2018), p. 037. doi:
2800 [10.1088/1475-7516/2018/11/037](https://doi.org/10.1088/1475-7516/2018/11/037). arXiv: [1810.00995 \[astro-ph.HE\]](https://arxiv.org/abs/1810.00995).
- 2801 [50] J. Aleksić et al. “Optimized dark matter searches in deep observations of Segue 1 with
2802 MAGIC”. in: *JCAP* 1402 (2014), p. 008. doi: [10.1088/1475-7516/2014/02/008](https://doi.org/10.1088/1475-7516/2014/02/008).
2803 arXiv: [1312.1535 \[hep-ph\]](https://arxiv.org/abs/1312.1535).
- 2804 [51] V.A. Acciari et al. “Combined searches for dark matter in dwarf spheroidal galaxies observed
2805 with the MAGIC telescopes, including new data from Coma Berenices and Draco”. In: *Physics of the Dark Universe* (2021), p. 100912. ISSN: 2212-6864. doi: <https://doi.org/10.1016/j.dark.2021.100912>. URL: <https://www.sciencedirect.com/science/article/pii/S2212686421001370>.
- 2809 [52] M. L. Ahnen et al. “Indirect dark matter searches in the dwarf satellite galaxy Ursa Major
2810 II with the MAGIC Telescopes”. In: *JCAP* 1803.03 (2018), p. 009. doi: [10.1088/1475-7516/2018/03/009](https://doi.org/10.1088/1475-7516/2018/03/009). arXiv: [1712.03095 \[astro-ph.HE\]](https://arxiv.org/abs/1712.03095).
- 2812 [53] S. et al. Archambault. “Dark matter constraints from a joint analysis of dwarf Spheroidal
2813 galaxy observations with VERITAS”. in: *prd* 95.8 (Apr. 2017). doi: [10.1103/PhysRevD.95.083008](https://doi.org/10.1103/PhysRevD.95.083008).

- 2814 . 95.082001. arXiv: 1703.04937 [astro-ph.HE].
- 2815 [54] Louise Oakes et al. “Combined Dark Matter searches towards dwarf spheroidal galaxies
2816 with Fermi-LAT, HAWC, HESS, MAGIC and VERITAS”. in: *Proceedings of Science*.
2817 2019.
- 2818 [55] Celine Armand et al. on behalf of the Fermi-LAT, HAWC, HESS, MAGIC, VERITAS.
2819 “Combined Dark Matter searches towards dwarf spheroidal galaxies with Fermi-LAT,
2820 HAWC, HESS, MAGIC and VERITAS”. in: *Proceedings of Science*. 2021.
- 2821 [56] Daniel Kerszberg et al. on behalf of the Fermi-LAT, HAWC, HESS, MAGIC, and VER-
2822 TIAS collaborations. “Search for dark matter annihilation with a combined analysis of
2823 dwarf spheroidal galaxies from Fermi-LAT, HAWC, H.E.S.S., MAGIC and VERITAS”. in:
2824 *Proceedings of Science*. 2023.
- 2825 [57] Giacomo Vianello et al. *The Multi-Mission Maximum Likelihood framework (3ML)*. 2015.
2826 arXiv: 1507.08343 [astro-ph.HE].
- 2827 [58] Marco Cirelli et al. “PPPC 4 DM ID: a poor particle physicist cookbook for dark matter
2828 indirect detection”. In: *Journal of Cosmology and Astroparticle Physics* 2011.03 (Mar.
2829 2011). ISSN: 1475-7516. doi: 10.1088/1475-7516/2011/03/051. URL: <http://dx.doi.org/10.1088/1475-7516/2011/03/051>.
- 2831 [59] Alex Geringer-Sameth, Savvas M. Koushiappas, and Matthew Walker. “DWARF
2832 GALAXY ANNIHILATION AND DECAY EMISSION PROFILES FOR DARK MAT-
2833 TER EXPERIMENTS”. in: *The Astrophysical Journal* 801.2 (Mar. 2015), p. 74. ISSN:
2834 1538-4357. doi: 10.1088/0004-637x/801/2/74. URL: <http://dx.doi.org/10.1088/0004-637x/801/2/74>.
- 2836 [60] A. Albert et al. “Dark Matter Limits from Dwarf Spheroidal Galaxies with the HAWC
2837 Gamma-Ray Observatory”. In: *The Astrophysical Journal* 853.2 (Feb. 2018), p. 154. ISSN:
2838 1538-4357. doi: 10.3847/1538-4357/aaa6d8. URL: <http://dx.doi.org/10.3847/1538-4357/aaa6d8>.
- 2840 [61] HongSheng Zhao. “Analytical models for galactic nuclei”. In: *Mon. Not. Roy. Astron.*
2841 *Soc.* 278 (1996), pp. 488–496. doi: 10.1093/mnras/278.2.488. arXiv: astro-ph/95
2842 09122 [astro-ph].
- 2843 [62] Julio F. Navarro, Carlos S. Frenk, and Simon D. M. White. “The Structure of Cold Dark
2844 Matter Halos”. In: *ApJ* 462 (May 1996), p. 563. doi: 10.1086/177173. eprint:
2845 astro-ph/9508025 (astro-ph).
- 2846 [63] V. Bonnivard et al. “Spherical Jeans analysis for dark matter indirect detection in dwarf
2847 spheroidal galaxies - Impact of physical parameters and triaxiality”. In: *Mon. Not. Roy.*
2848 *Astron. Soc.* 446 (2015), pp. 3002–3021. doi: 10.1093/mnras/stu2296. arXiv:

- 2849 1407.7822 [astro-ph.HE].
- 2850 [64] M. Ackermann et al. “Searching for Dark Matter Annihilation from Milky Way Dwarf
2851 Spheroidal Galaxies with Six Years of Fermi Large Area Telescope Data”. In: *prl* 115.23,
2852 231301 (Dec. 2015), p. 231301. doi: [10.1103/PhysRevLett.115.231301](https://doi.org/10.1103/PhysRevLett.115.231301). arXiv:
2853 [1503.02641](https://arxiv.org/abs/1503.02641) [astro-ph.HE].
- 2854 [65] M. L. Ahnen et al. “Limits to Dark Matter Annihilation Cross-Section from a Combined
2855 Analysis of MAGIC and Fermi-LAT Observations of Dwarf Satellite Galaxies”. In: *JCAP*
2856 1602.02 (2016), p. 039. doi: [10.1088/1475-7516/2016/02/039](https://doi.org/10.1088/1475-7516/2016/02/039). arXiv: [1601.06590](https://arxiv.org/abs/1601.06590)
2857 [astro-ph.HE].
- 2858 [66] Javier Rico et al. *gLike: numerical maximization of heterogeneous joint
2859 likelihood functions of a common free parameter plus nuisance parameters.*
2860 <https://doi.org/10.5281/zenodo.4601451>. Version v00.09.03. Mar. 2021. doi:
2861 [10.5281/zenodo.4601451](https://doi.org/10.5281/zenodo.4601451). URL: <https://doi.org/10.5281/zenodo.4601451>.
- 2862 [67] Tjark Miener and Daniel Nieto. *LklCom: Combining likelihoods from different ex-
2863 periments.* <https://doi.org/10.5281/zenodo.4597500>. Version v0.5.3. Mar. 2021. doi:
2864 [10.5281/zenodo.4597500](https://doi.org/10.5281/zenodo.4597500). URL: <https://doi.org/10.5281/zenodo.4597500>.
- 2865 [68] T. Miener et al. “Open-source Analysis Tools for Multi-instrument Dark Matter Searches”.
2866 In: *arXiv e-prints*, arXiv:2112.01818 (Dec. 2021), arXiv:2112.01818. arXiv: [2112.01818](https://arxiv.org/abs/2112.01818)
2867 [astro-ph.IM].
- 2868 [69] Alex Geringer-Sameth and Matthew Koushiappas Savvas M. and Walker. “Dwarf galaxy
2869 annihilation and decay emission profiles for dark matter experiments”. In: *Astrophys.
2870 J.* 801.2 (2015), p. 74. doi: [10.1088/0004-637X/801/2/74](https://doi.org/10.1088/0004-637X/801/2/74). arXiv: [1408.0002](https://arxiv.org/abs/1408.0002)
2871 [astro-ph.CO].
- 2872 [70] Gianfranco Bertone, Dan Hooper, and Joseph Silk. “Particle dark matter: evidence,
2873 candidates and constraints”. In: *Physics Reports* 405.5-6 (Jan. 2005), pp. 279–390. ISSN:
2874 0370-1573. doi: [10.1016/j.physrep.2004.08.031](https://doi.org/10.1016/j.physrep.2004.08.031). URL: <http://dx.doi.org/10.1016/j.physrep.2004.08.031>.
- 2876 [71] V. Bonnivard et al. “Dark matter annihilation and decay in dwarf spheroidal galaxies: The
2877 classical and ultrafaint dSphs”. In: *Mon. Not. Roy. Astron. Soc.* 453.1 (2015), pp. 849–
2878 867. doi: [10.1093/mnras/stv1601](https://doi.org/10.1093/mnras/stv1601). arXiv: [1504.02048](https://arxiv.org/abs/1504.02048) [astro-ph.HE].
- 2879 [72] A. et al. Albert. “Searching for Dark Matter Annihilation in Recently Discovered Milky
2880 Way Satellites with Fermi-LAT”. in: *Astrophys. J.* 834.2 (2017), p. 110. doi: [10.3847/1538-4357/834/2/110](https://doi.org/10.3847/1538-4357/834/2/110). arXiv: [1611.03184](https://arxiv.org/abs/1611.03184) [astro-ph.HE].
- 2882 [73] Mattia Di Mauro and Martin Wolfgang Winkler. “Multimessenger constraints on the dark
2883 matter interpretation of the Fermi-LAT Galactic Center excess”. In: *prd* 103.12, 123005

- 2884 (June 2021), p. 123005. doi: [10.1103/PhysRevD.103.123005](https://doi.org/10.1103/PhysRevD.103.123005). arXiv: [2101.11027](https://arxiv.org/abs/2101.11027) [astro-ph.HE].
- 2885
- 2886 [74] H. C. Plummer. “On the Problem of Distribution in Globular Star Clusters: (Plate 8.)”
2887 In: *Monthly Notices of the Royal Astronomical Society* 71.5 (Mar. 1911), pp. 460–470.
2888 ISSN: 0035-8711. doi: [10.1093/mnras/71.5.460](https://doi.org/10.1093/mnras/71.5.460). eprint: <https://academic.oup.com/mnras/article-pdf/71/5/460/2937497/mnras71-0460.pdf>. URL:
2890 <https://doi.org/10.1093/mnras/71.5.460>.
- 2891 [75] Daniel R. Hunter. “Derivation of the anisotropy profile, constraints on the local velocity
2892 dispersion, and implications for direct detection”. In: *JCAP* 02 (2014), p. 023. doi:
2893 [10.1088/1475-7516/2014/02/023](https://doi.org/10.1088/1475-7516/2014/02/023). arXiv: [1311.0256](https://arxiv.org/abs/1311.0256) [astro-ph.CO].
- 2894 [76] Barun Kumar Dhar and Liliya L. R. Williams. “Surface mass density of the Einasto family
2895 of dark matter haloes: are they Sersic-like?” In: *Mon. Not. Roy. Astron. Soc.* (2010). doi:
2896 [10.1111/j.1365-2966.2010.16446.x](https://doi.org/10.1111/j.1365-2966.2010.16446.x).
- 2897 [77] M. Baes and E. Van Hese. “Dynamical models with a general anisotropy profile”. In:
2898 *Astron. Astrophys.* 471 (2007), p. 419. doi: [10.1051/0004-6361:20077672](https://doi.org/10.1051/0004-6361:20077672). arXiv:
2899 [0705.4109](https://arxiv.org/abs/0705.4109) [astro-ph].
- 2900 [78] Matthew G. Walker, Edward W. Olszewski, and Mario Mateo. “Bayesian analysis of
2901 resolved stellar spectra: application to MMT/Hectochelle observations of the Draco dwarf
2902 spheroidal”. In: *mnras* 448.3 (Apr. 2015), pp. 2717–2732. doi: [10.1093/mnras/stv099](https://doi.org/10.1093/mnras/stv099).
2903 arXiv: [1503.02589](https://arxiv.org/abs/1503.02589) [astro-ph.GA].
- 2904 [79] Nicholas L. Rodd et al. “Dark matter spectra from the electroweak to the Planck scale”.
2905 In: *J. High Energy Physics* 121.10.1007 (June 2021).
- 2906 [80] Pace, Andrew B and Strigari, Louis E. “Scaling relations for dark matter annihilation and
2907 decay profiles in dwarf spheroidal galaxies”. In: *Monthly Notices of the Royal Astronomical
2908 Society* 482.3 (Oct. 2018), pp. 3480–3496. ISSN: 0035-8711. doi: [10.1093/mnras/sty2839](https://doi.org/10.1093/mnras/sty2839).
- 2909
- 2910 [81] Albert, A. et al. “Search for gamma-ray spectral lines from dark matter annihilation in
2911 dwarf galaxies with the High-Altitude Water Cherenkov observatory”. In: *Phys. Rev. D* 101 (10 May 2020), p. 103001. doi: [10.1103/PhysRevD.101.103001](https://doi.org/10.1103/PhysRevD.101.103001). URL:
2912 <https://link.aps.org/doi/10.1103/PhysRevD.101.103001>.
- 2913
- 2914 [82] Victor Eijkhout and Edmund Show and Robert van de Geijn. *The Science of Computing. The Art of High Performance Computing*. Vol. 3. Open Copy published under CC-BY 4.0
2915 license, 2023, pp. 63–66.
- 2916
- 2917 [83] The IceCube Collaboration. “The IceCube Neutrino Observatory: instrumentation and
2918 online systems”. In: *Journal of Instrumentation* 12.03 (Mar. 2017), P03012. doi: [10.1088/1748-0221/12/03/P03012](https://doi.org/10.1088/1748-0221/12/03/P03012)

- 2919 8/1748-0221/12/03/P03012. URL: [https://dx.doi.org/10.1088/1748-0221/12
2920 /03/P03012](https://dx.doi.org/10.1088/1748-0221/12/03/P03012).
- 2921 [84] IceCube Gallery. 2019. URL: [https://gallery.icecube.wisc.edu/internal/v/
2922 SPIImages/weekly/winteroverweeklyphotos2019/icl.JPG.html?g2_imageView
2923 sIndex=1](https://gallery.icecube.wisc.edu/internal/v/SPIImages/weekly/winteroverweeklyphotos2019/icl.JPG.html?g2_imageView).
- 2924 [85] Ahlers, Markus and Helbing, Klaus and Pérez de los Heros, Carlos. “Probing particle
2925 physics with IceCube”. In: *The European Physical Journal C* 78.11 (Nov. 2018). ISSN:
2926 1434-6052. DOI: [10.1140/epjc/s10052-018-6369-9](https://doi.org/10.1140/epjc/s10052-018-6369-9). URL: <http://dx.doi.org/10.1140/epjc/s10052-018-6369-9>.
- 2928 [86] Rene Reimann. “Search for the Sources of the Astrophysical High-Energy Muon-Neutrino
2929 Flux with the IceCube Neutrino Observatory”. PhD thesis. Aachen University in Erlan-
2930 gung, 2019.
- 2931 [87] IceCube Collaboration. *Detecting Neutrinos*. Web. 2024.
- 2932 [88] IceCube Collaboration. “Energy reconstruction methods in the IceCube neutrino tele-
2933 scope”. In: *Journal of Instrumentation* 9.03 (Mar. 2014), P03009. DOI: [10.1088/1748-0221/9/03/P03009](https://doi.org/10.1088/1748-0221/9/03/P03009). URL: <https://dx.doi.org/10.1088/1748-0221/9/03/P03009>.
- 2936 [89] The IceCube Collaboration. “Detection of astrophysical tau neutrino candidates in Ice-
2937 Cube”. In: *The European Physical Journal C* 82.11 (Nov. 2022). ISSN: 1434-6052. DOI:
2938 [10.1140/epjc/s10052-022-10795-y](https://doi.org/10.1140/epjc/s10052-022-10795-y). URL: <http://dx.doi.org/10.1140/epjc/s10052-022-10795-y>.
- 2940 [90] J. Ahrens et al. “Muon track reconstruction and data selection techniques in AMANDA”.
2941 in: *Nuclear Instruments and Methods in Physics Research Section A: Accelerators,
2942 Spectrometers, Detectors and Associated Equipment* 524.1 (2004), pp. 169–194. ISSN:
2943 0168-9002. DOI: <https://doi.org/10.1016/j.nima.2004.01.065>. URL:
2944 <https://www.sciencedirect.com/science/article/pii/S0168900204001871>.
- 2945 [91] Peter J. Huber. “Robust Estimation of a Location Parameter”. In: *The Annals of Math-
2946 ematical Statistics* 35.1 (1964), pp. 73–101. DOI: [10.1214/aoms/1177703732](https://doi.org/10.1214/aoms/1177703732). URL:
2947 <https://doi.org/10.1214/aoms/1177703732>.
- 2948 [92] IceCube Collaboration. “Calibration and characterization of the IceCube photomultiplier
2949 tube”. In: *Nuclear Instruments and Methods in Physics Research Section A: Accelerators,
2950 Spectrometers, Detectors and Associated Equipment* 618.1 (2010), pp. 139–152. ISSN:
2951 0168-9002. DOI: <https://doi.org/10.1016/j.nima.2010.03.102>. URL: <https://www.sciencedirect.com/science/article/pii/S0168900210006662>.
- 2953 [93] Aartsen, M. et al. “IceCube search for dark matter annihilation in nearby galaxies and galaxy

- 2954 clusters". In: *Phys. Rev. D* 88 (12 Dec. 2013), p. 122001. doi: [10.1103/PhysRevD.88.122001](https://doi.org/10.1103/PhysRevD.88.122001). URL: <https://link.aps.org/doi/10.1103/PhysRevD.88.122001>.
- 2955
- 2956 [94] Pearl Sandick et al. "Sensitivity of the IceCube neutrino detector to dark matter annihilating
2957 in dwarf galaxies". In: *Phys. Rev. D* 81 (8 Apr. 2010), p. 083506. doi: [10.1103/PhysRevD.81.083506](https://doi.org/10.1103/PhysRevD.81.083506). URL: <https://link.aps.org/doi/10.1103/PhysRevD.81.083506>.
- 2958
- 2959
- 2960 [95] Qinrui Liu and Jeffrey Lazar and Carlos A. Argüelles and Ali Kheirandish. " χ aro: a tool
2961 for neutrino flux generation from WIMPs". In: *Journal of Cosmology and Astroparticle
2962 Physics* 2020.10 (Oct. 2020), p. 043. doi: [10.1088/1475-7516/2020/10/043](https://doi.org/10.1088/1475-7516/2020/10/043). URL:
2963 <https://dx.doi.org/10.1088/1475-7516/2020/10/043>.
- 2964
- 2965 [96] Tessa Cerver. "Time Integrated searches for Astrophysical Neutrino Sources using the
2966 IceCube Detector and Gender in Physics studies for the Genera Project". PhD thesis.
2967 UNIVERSITE DE GEN ´ EVE, 2019, pp. 57–64.
- 2968
- 2969
- 2970 [97] Minjin Jeong on behalf of the IceCube Collaboration. "Search for Dark Matter Decay in
2971 Nearby Galaxy Clusters and Galaxies with IceCube". In: *Proceedings of Science* 444.38
2972 (2023).
- 2973
- 2974
- 2975 [98] IceCube Collaboration. "Evidence for neutrino emission from the nearby active galaxy
2976 NGC 1068". In: *Science* 378.6619 (2022).
- 2977
- 2978 [99] Nathan Whitehorn and Jakob van Santen. *Photospline*. IceCube: GitHub.
2979
- 2980
- 2981 [100] Paul H. C. Eilers and Brian D. Marx. "Flexible smoothing with B-splines and penalties".
2982 In: *Statistical Science* 11.2 (1996), pp. 89–121. doi: [10.1214/ss/1038425655](https://doi.org/10.1214/ss/1038425655). URL:
2983 <https://doi.org/10.1214/ss/1038425655>.
- 2984
- 2985
- 2986 [101] The IceCube Collaboration. *Search for neutrino lines from dark matter annihilation and
2987 decay with IceCube*. 2023. arXiv: [2303.13663 \[astro-ph.HE\]](https://arxiv.org/abs/2303.13663).
- 2988
- 2989 [102] The IceCube Collaboration. "Measurement of the multi-TeV neutrino interaction cross-
2990 section with IceCube using Earth absorption". In: *Nature* 551 (2017).